# THERMOPHYSICAL AND THERMOCHEMICAL BEHAVIOUR OF COAL AND BIOMASS DURING CHEMICAL LOOPING COMBUSTION

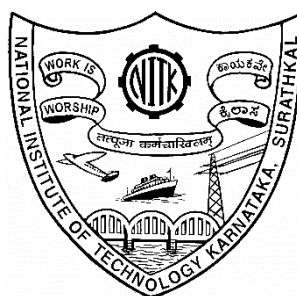Thesis

Submitted in partial fulfilment of the requirements for the degree of

## DOCTOR OF PHILOSOPHY

by

## PRAGADEESH K S



**DEPARTMENT OF CHEMICAL ENGINEERING**

**NATIONAL INSTITUTE OF TECHNOLOGY KARNATAKA**

**SURATHKAL, MANGALORE, INDIA - 575025**

**JULY, 2021**

# *D E C L A R A T I O N*

I hereby *declare* that the Research Thesis entitled "**Thermophysical and thermochemical behaviour of coal and biomass during chemical looping combustion**" which is being submitted to the National Institute of Technology Karnataka, Surathkal in partial fulfillment of the requirements for the award of the Degree of **Doctor of Philosophy** in the Department of Chemical Engineering, is a *bonafide report of the research work carried out by me*. The material contained in this Research Thesis has not been submitted to any University or Institution for the award of any degree.

Place: Surathkal, India

Date: 20th July 2021
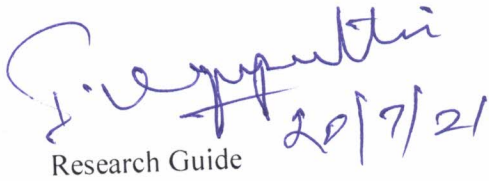
K. S. Pragadeesh
20-07-2021

Pragadeesh K S

145028CH14F03

Department of Chemical Engineering

# CERTIFICATE

This is to *certify* that the Research Thesis entitled "**Thermophysical and thermochemical behaviour of coal and biomass during chemical looping combustion**" submitted by **Mr. Pragadeesh K S (Register Number: 145028CH14F03)** as the record of the research work carried out by him, is *accepted as the Research Thesis submission* in partial fulfillment of the requirements for the award of degree of **Doctor of Philosophy**.

20/7/21

Research Guide

Dr. I. Regupathi
Associate Professor
Dept. of Chemical Engineering
NITK, Surathkal

20-07-2021

Research Guide

Dr. Ruben Sudhakar D.
Assistant Professor
Dept. of Energy and Environment
NIT, Tiruchirappalli

Chairman-DRPC
Dept. of Chemical Engineering
HEAD OF THE DEPARTMENT
CHEMICAL ENGINEERING
National Institute of Technology Karnataka, Surathkal
P.O. Srinivasnagar - 575 025, D.K., Mangalore

## ACKNOWLEDGEMENT

DEDICATED

TO

MY GURUS

and

THE SCIENTIFIC

COMMUNITY

**ABSTRACT**

Thermal power plants burning fossil fuels are the major anthropogenic sources of carbon dioxide emissions into the atmosphere. Chemical Looping Combustion (CLC) is a promising fuel conversion technology for inherent carbon capture with a low energy penalty. The present way of using pulverized coals in a fluidized bed (FB)-CLC has drawbacks like loss of unconverted char and gaseous combustibles. The utilization of large solid fuel particles (in mm-sizes) potentially overcomes these problems and also reduces the energy involved in size reduction. The thermophysical and thermochemical changes involved during the conversion of these large-sized particles are large in magnitude and of greater significance. Thus, they along with the fuels' thermochemical changes become critical inputs for the effective design of process equipment. This study is aimed at (i) gaining a qualitative understanding of the progressive thermophysical and thermochemical changes during fuel conversion and (ii) quantifying the influence of various operating parameters on the same. Thermochemical changes, namely devolatilization, char conversion, carbon transformations, and the thermophysical behaviour in terms of primary and secondary fragmentation, shrinkage, and microstructural changes are studied using single-particle experiments in fluidized bed insitu-gasification CLC conditions. Two types of Indian coals, one type of Indonesian coal and one type of carbon-neutral biomass (fuel wood), of three different sizes in the range of +8-25 mm are used in this study. Natural hematite is the oxygen carrier bed material used (in the size range of +250-425 µm), with steam as the fluidization-cum-gasification agent at 2.5 times the minimum fluidization velocity. The experiments are conducted at three different bed temperatures of 800, 875 and 950 ºC.

This work is comprised of six different experimental programs, viz. (i) development of a new method to determine devolatilization time in flameless FB-CLC conditions, called 'Colour Indistinction Method (CIM)', (ii) devolatilization and char yield experiments, (iii) experiments of primary fragmentation during devolatilization (iv) char conversion and char fragmentation (secondary) experiments, (v) char reactivity experiments using thermogravimetry, and (vi) char structural analysis using instrumental techniques. CIM is developed based on the observation of particle disappearance in the bed at the end of devolatilization and validated using standard

diagnostic methods such as residual-volatile measurements and particle-centre temperature profilometry. CIM produced reliable results within the error range of -7.57 to +3.70 %. The devolatilization experiments revealed that the larger particles have a relatively lower amount of volatile release. However, increasing the bed temperature enhances the volatile release rate as well as the quantity of release (up to 12% in coals; 30% in biomass). With the decrease in sphericity (seen in flake coal particles), a maximum of 56% reduction in devolatilization time is noticed. A correlation for determining devolatilization time under the CLC environment is developed, with a coefficient of determination of 0.95. Char yield is found to be strongly influenced by operating bed temperature, but it is a weak function of particle size and shape. Shrinkage in biomass is witnessed for all sizes, with an effective reduction of 31-52% in initial particle volume. Char conversion times of fuels increase by 60 to 170% when particle size is increased by 2 to 2.5- folds, while an increase in bed temperature by 150 $^{\circ}$C caused a reduction of 42 to 86%. It is also understood that if the fixed carbon content is higher than the ash content in fuel, intensive fragmentation occurs and brings down the char conversion time.

Primary and secondary fragmentation phenomena are quantified using various indicators such as probability of fragmentation events, frequency and timing of fragmentation, number of fragments, fragmentation index and particle size distribution of fragments at different residence times. The intensity of primary fragmentation increases with the increase in particle size and bed temperature, while it decreases with the increase in compressive strength. Only a maximum of 60% of the tested particles undergo fragmentation, irrespective of fuels. High-volatile Indian coal and biomass, respectively, are the most and least susceptible fuels to primary fragmentation irrespective of particle size and bed temperature. Indian coals are found to fragment in the earlier stages of conversion, thus becoming a dominant factor in shortening the overall fuel conversion time. Unlike during devolatilization, the largest sized particles of all the tested fuels experience secondary fragmentation. Among the different bed temperatures studied, 950 $^{\circ}$C is found to be the most favourable for char conversion and fragmentation. Regardless of fuel type and feed size, the inception of char fragmentation is noticed in the very first quarter of conversion time, indicating its

substantial effect on the char conversion time, and therefore, it becomes necessary to carefully incorporate this size reduction with respect to time in the char conversion models. Percolative mode of fragmentation is noticed in the final quarter of char conversion, except for high-ash Indian coal particles. A minimum critical char size exists below which char weakening does not yield breakage, whose values vary between 4.4 and 14.2 mm, depending on fuel type and feed size. Fuel type is found to be the prime influencer of fuel conversion and comminution phenomena, followed by particle size and operating bed temperature. This study establishes that large fuel particles up to 25 mm can be used in CLC systems without any prior size reduction, except in the case of high-ash Indian coal.

Isothermal char reactivity studies using TGA show that samples exhibit high reactivity if char preparation is done at low temperatures for high-volatile fuels and at high temperatures for low-volatile fuels. Peak reactivity is noticed during the initial stages of char conversion regime for all coals and in later stages for biomass samples. Char micrographs show mesoporous char formation with pore size of about 2-4 nm in all fuels, during the course of char conversion. Electron dispersive studies indicate that the high volatile Indian coal retains Ca throughout the conversion period, whereas biomass chars retain the catalytic species like K and Ca. Raman spectroscopic analyses show that graphitic carbon structures are selective towards the steam atmosphere, while defective carbon structures are relatively more selective towards $CO_2$.

# CONTENTS

# Abbreviations and acronyms

| | |
|---|---|
| CCS | Carbon Capture and Sequestration |
| CLC | Chemical Looping Combustion |
| CLOU | Chemical Looping with Oxygen Uncoupling |
| CLOC | Chemical Looping Oxy Combustor |
| iG-CLC | integrated Gasification- Chemical Looping Combustion |
| CDCL | Coal Direct Chemical Looping |
| OC | Oxygen Carrier |
| FR | Fuel Reactor |
| AR | Air Reactor |
| TGA | Thermo-Gravimetric Analyser/Analysis |
| IC1 | high volatile Indian Coal |
| IC2 | high ash Indian coal |
| IDC | Indonesian coal |
| BM | firewood Biomass |
| FET | Flame Extinction Technique |
| PCT | Particle Centre Temperature |
| PF | Percentage or Probability of Fragmentation events |
| NF | Number of Fragments |
| TF | Timing of Fragmentation |
| FF | Frequency of Fragmentation |
| FI | Fragmentation Index |
| PSD | Particle Size Distribution |
| SEM | Scanning Electron Microscope |
| EDX | Energy Dispersive X-ray spectroscopy |

**Symbols and notations**

| | |
|---|---|
| $\tau_d$ | Devolatilization time |
| $\tau_{cc}$ | Char conversion time |
| $\varphi$ | Particle sphericity |
| d or $d_p$ | Mass equivalent diameter of particle |
| $\sigma_c$ | Compressive strength |
| A | proportionality constant |
| T | Operating bed temperature |
| t | time |
| $R^2$ | Coefficient of determination in regression analysis |
| kW | kilo Watt |
| MPa | Mega Pascals |
| Mt | Mega or Million tonnes |
| m/s | metres per second |

## Definitions of general terms used in this thesis

*Fuel:* It always refers to a solid fuel (coal and/or biomass).

*Devolatilization:* A phase of fuel conversion, where the volatile matter present in the fuel gets released.

*Char:* Char is the residue leftover at the end of devolatilization.

*Comminution:* The process of particle size reduction and it can be in two forms namely, fragmentation and attrition.

Fragmentation: The phenomenon of particle structure breaking down into several numbers of fragments due to many causes during combustion and gasification.

*Primary fragmentation:* Fragmentation that happens during the devolatilization phase of fuel conversion.

*Secondary fragmentation:* Fragmentation events during the char conversion phase.

*Attrition:* The events of fines generation from fuel particles as a result of wear of fuel particles due to collisions and abrasions during conversion of fuel.

*Oxygen carrier (OC):* It is a reactive bed material, usually metal oxides, used in the fluidised bed – Chemical Looping Combustion. They carry oxygen molecules from air reactor to fuel reactor.

*Sintering:* The process of coalescence of microstructures in a matter (for e.g. oxygen carrier), leading to loss of active surface area.

*iG-CLC:* integrated Gasification- Chemical Looping Combustion – In this type of CLC, the oxygen carrier does not release the oxygen directly. Rather, the gaseous fuels or gaseous product from gasification of solid fuel reacts with oxygen carrier to get oxidised.

*CLOU:* Chemical Looping with Oxygen Uncoupling – In this type of CLC, the oxygen carrier directly releases oxygen in the fuel reactor, which oxidises the fuel.

# CHAPTER 1

# 1 INTRODUCTION

## 1.1 Carbon emissions and chemical looping combustion

Carbon dioxide is the major anthropogenic greenhouse gas that is emitted out from various man-made activities. Currently, the atmospheric $CO_2$ level is about 416.39 ppm and is increasing at an average rate of 2.19 ppm $yr^{-1}$ in the past 20 years, as reported by National Oceanic & Atmospheric Administration, USA. In 2017, world $CO_2$ emissions from fuel combustion were about 32840 Mt, out of which 41.4% was from electricity and heat generation. At the same time, India's contribution was 2162 Mt, of which 51% came from electricity and heat sectors (International Energy Agency 2019). Compared to other countries, developing countries like India will be worst affected by the overage effects of greenhouse gases. Presently, coal is the major fuel consumed (48.7 % as of 2017) in the Indian energy sector (International Energy Agency 2020). It would continue to be a dominant fuel in India with its demand expected to grow by +107% in the period of 2017-2040 (BP p.l.c. 2019).

Internationally, a lot of efforts are being directed towards the reduction of $CO_2$ emission into the atmosphere from the power plants. Especially in developing countries like India, extensive research is necessary to reduce carbon emissions by means of improving the efficiency of the existing technologies and retrofitting the $CO_2$ capture technologies with them. As the reserve levels of high-grade coals (high calorific value and low ash) are limited, the future may demand the use of Indian coals, which are of low grade in terms of low carbon content (calorific value), high ash content and moderate sulphur content. This unique nature of Indian coals invites the necessity for systematic research on the various aspects of its utilisation in the present and future carbon capture technologies. In addition, India's abundant bioresources could supplement the burning of coal to a greater extent, in terms of co-firing. Co-firing biomass with coal enriches the fuel calorific value in power generation and bring down the carbon emission to a significant level.

## 1.2 Development of carbon capture technologies

Although combustion of coal with co-firing of carbon-neutral fuel like biomass indirectly reduces the $CO_2$, the use of biomass has a conflict of interest and availability

issue. So, there is a necessity to explore other carbon mitigation technologies. In carbon mitigation, there are two steps, namely the carbon capture step and the sequestration step. CCS increases the electricity production cost by 50%, and the capture of $CO_2$ alone contributes 75% to the overall CCS cost (Feron and Hendriks 2005). Thus, the high cost makes the research on the $CO_2$ capture step, more important.

Globally, several techniques have been proposed for capturing $CO_2$. Based on the modes of capture, carbon capture technologies can be classified under two major groups namely,

- In-situ mode
- Ex-situ mode (pre and post-combustion modes)
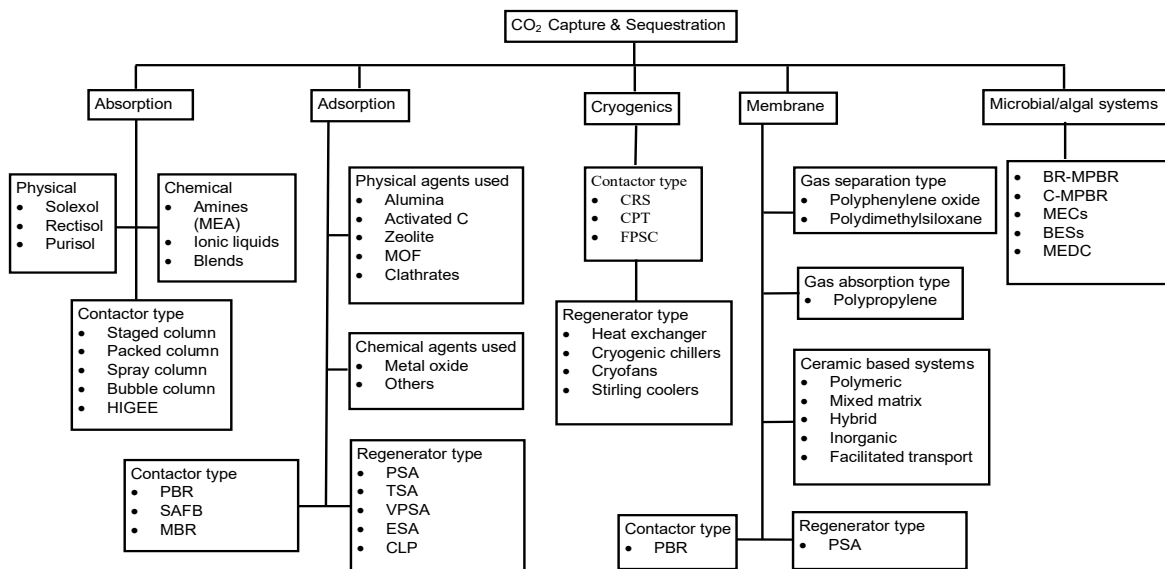


*Figure 1.1 Various carbon capture methods (Sreenivasulu et al. 2015)*

A chart of various $CO_2$ capture methods is presented in Figure 1.1. In situ methods are oxy-fuel combustion, Chemical Looping Combustion (CLC) and Chemical Looping with Oxygen Uncoupling (CLOU). Ex-situ capture techniques include adsorption, physical and chemical absorption, membrane separation (based on the molecular weight cut off), Integrated Gasification Combined Cycle (IGCC-Gasification followed by combustion) and cryogenic separations (Sreenivasulu et al. 2015). Pre-combustion capture involves three stages (Basile et al. 2011). The initial stage is the partial oxidation or gasification of solid fuel to form CO, $H_2$, $CO_2$ (and small quantities of gases such as methane), followed by the secondary stage of water gas-shift reaction of

CO to form $CO_2$. The tertiary stage is the separation of $CO_2$ and other impurities from hydrogen by using solvents, sorbents, membranes etc. Though post-combustion methods have easier retrofitting options than pre-combustion methods, the energy penalty involved is almost double than the later. So, from the penalty viewpoint, pre-combustion or in-situ technologies are better compared to other technologies for carbon capture. The energy penalty of various carbon capture technologies is summarised in Table 1.1.

*Table 1.1 Energy penalty of carbon capture technologies*

| *Technology* | *Energy penalty* | *Reference* |
|---|---|---|
| *Ex-situ* | 6 - 30 % | |
| Membranes | 30 % | NETL (2012) |
| Amine sorption | 9.5 - 12.5 % | Xu et al. (2010) |
| Calcium looping | 6 - 8 % | Blamey et al. (2010) |
| IGCC | 6 - 7 % | NETL (2011) |
| *In-situ* | 0 - 9.5 % | |
| Oxyfuel combustion | 9.5 % | Mukherjee et al. (2015) |
| CLC | *2.5 % or even nil* | Lyngfelt (2014) |

Thus, among the in-situ methods, CLC is found to be an attractive option with the least energy penalty of 2.5%. CLC, a next generation method uses the oxidised material (termed "oxygen carrier") to selectively carry oxygen from Air Reactor (AR) to the Fuel Reactor (FR). So, one may call this method indirect oxy-fuel combustion. The oxygen carrier reacts with the gasification products formed in the fuel reactor to emit a pure stream of $CO_2$. Following are the reactions involved in CLC and the schematic diagram is given in Figure 1.2.
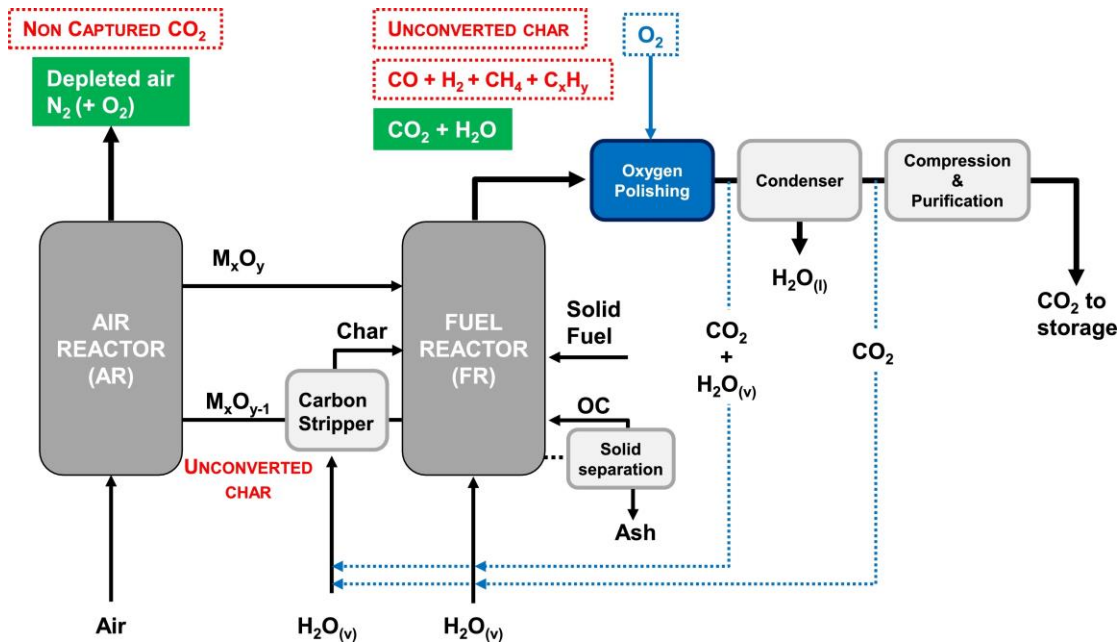
*Figure 1.2 Schema of chemical looping process of solid fuel (Adánez et al. 2018).*

$$\text{Reduced metal oxide (MeO}_{x-1}\text{)} + \text{Air} \xrightarrow{\text{Oxidation @ AR}} \text{Oxidised metal oxide (MeO}_x\text{)}$$

$$\text{Solid fuel} \xrightarrow{\text{devolatilization @ FR}} \text{Volatiles} + \text{Char}$$

$$\text{MeO}_x + \text{Volatiles} \xrightarrow{\text{Combustion}} CO_2 + \text{MeO}_{x-1}$$

$$\text{Char} \xrightarrow{\text{gasification}} \text{Producer gas (CO} + CH_4 + H_2\text{)} + \text{ash}$$

$$\text{MeO}_x + \text{Producer gas} \xrightarrow{\text{Combustion}} CO_2 + \text{MeO}_{x-1}$$
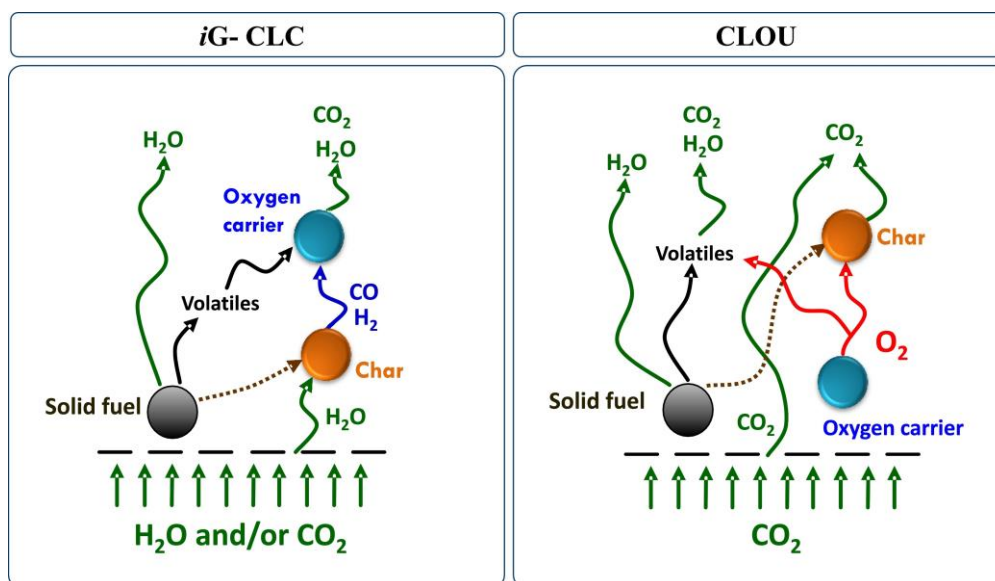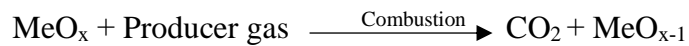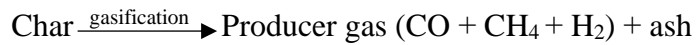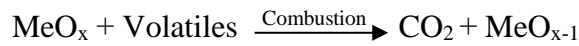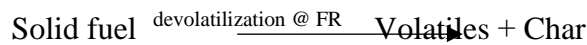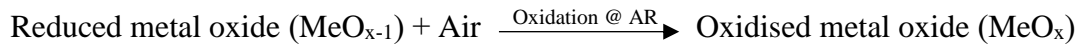


*Figure 1.3 Reaction scheme of iG-CLC and CLOU (Adánez et al. 2018).*

The reactions of combustible gases with the oxygen carrier involve the initial diffusion through the pores of the surface followed by adsorption and then the chemical reaction in the surface region within the OC (Fennell and Anthony, 2015). Based on the oxygen carrier used, CLC can be classified into iG-CLC (insitu Gasification-CLC), CLOU (Chemical Looping with Oxygen Uncoupling) and CLaOU (CL assisted by Oxygen Uncoupling) (Adánez et al. 2018). As visualised from Figure 1.3, the solid fuel is pyrolyzed initially in all the cases, and the volatiles and combustible gases from the gasification process react with oxygen carrier in iG-CLC to form $CO_2$ and $H_2O$ (Adanez et al. 2012), whereas CLOU fastens the oxidation process by providing nascent oxygen from oxygen carriers to char as well as volatiles (Leion et al. 2009), and the CLaOU uses a mixture of iG-CLC and CLOU oxygen carrier materials (Adánez et al. 2018), forming similar end products. The overall reaction nature is exothermic, thus avoiding a huge energy penalty. With lesser alterations to the existing industrial infrastructure, industries could adopt this technology, once it becomes available for deployment in a large scale.

## 1.3 Development of Chemical Looping Combustion technology

The idea of using metal oxides as oxygen carriers was first patented by Lewis and Gilliland (1954), for the production of pure $CO_2$ (Lyngfelt 2010). Following this, a thermodynamic study by Richter and Knoche (1983) suggested the use of oxygen-carrying metal oxide as reactants with combustion intermediates in order to increase efficiency. Another thermodynamic study by Ishida et al.(1987) introduced the term, 'Chemical Looping Combustion' and later introduced this technology for carbon dioxide separation (Ishida and Jin 1994). In 1990s, the studies on chemical looping processes have been intensified on call from various world councils on pollution control. The work on $CO_2$ capture gained pace from a study on a twin fluid-bed reactor by Shimizu et al.(1999).

The early 2000s saw various initial studies focussed on the development of CLC, all around the world. Since its inception, studies on CLC are focused much on its application with gaseous fuel conversion and only since 2007, investigations on solid fuels have started and been advanced. The other variant of CLC known as Chemical looping combustion with oxygen uncoupling (CLOU) was introduced to the scientific

community by Mattisson et al.(2009), which was originally patented by the same authors in 2005. As of 2017, the technology readiness level (TRL) of CLC is low compared to other carbon capture (Kanniche et al. 2017), but it is of interest to industries due to their energy performance. Thus, chemical looping technology must be explored enough to improve its TRL and commercial deployment. In parallel lines, chemical looping is seen as a potential technology for energy-conserving, emission-reducing (particularly $CO_2$) and profitable industrial chemical production processes and their process intensification (Zhu et al. 2020).

**1.4 Fluidised beds for CLC technology**

Conventionally, fluidised bed (FB) systems in the energy sector are used for fuel conversion in combustion and gasification modes. These systems typically consist of a vertical reactor column containing bed material and fuel particles which are fluidised using a gas stream (generally air), with the help of a gas distribution arrangement at the bottom of the reactors. The FB systems came into the industrial application for the following advantages.

    (i)      Reduce the pollutants ($NO_X$ and $SO_X$) concentration in the flue gas.

    (ii)     Flexibility of using a variety of fuels including low-grade solid fuels.

    (iii)    Better fuel conversion efficiency than certain conventional systems.

Based on their operating fluidisation velocity, they can be classified into two types namely,

    a)  Bubbling fluidised beds (BFB)    - fluidization velocity of 1.5 to 2.5 m/s

    b)  Circulating fluidised beds (CFB) - fluidization velocity of 3 to 5 m/s

Based on the fuel particle nature and its size, either BFB or CFB is selected. Circulating Fluidized Beds (CFBs) are the preferred type of fuel reactor for gaseous fuels due to the better gas-solid mixing (Basu 2006), whereas, bubbling fluidized beds (BFBs) are preferred as fuel reactors for solid fuels (Berguerand and Lyngfelt 2009; Fan 2010; Huijun et al. 2015; Nandy et al. 2016). The advantage of BFBs over CFBs for solid fuels lies in the longer residence times of fuel particles, which ensure the complete conversion of char by preventing the loss of carbon out of the reactor. Particularly, the fuels that are difficult to pulverise (like biomass) are preferable to be used in larger forms (mm-size), and they would require more residence time in the

reactor for complete conversion. In this case, a BFB can be utilised, and mostly low-grade fuels are preferred to be used in these sizes, to cut pulverization costs. Also, a BFB reactor as a fuel reactor aids fuel flexibility and prevents the unconverted char from escaping into the air reactor, whereas the cost-intensive CFB as air reactor helps to oxidise the reduced oxygen carrier and quickly transport it back to the fuel reactor (DeFusco et al. 2010).

### 1.4.1 Fuel conversion process in fluidized beds

During the solid fuel conversion process, fuel particles undergo thermochemical changes accompanied by thermophysical changes. The thermochemical changes involve two major phases namely, devolatilization and char conversion. The devolatilization phase is a combined heat and mass transfer process that involves particle heating, removal of moisture, and release of light hydrocarbons (volatile) due to the fuel's exposure to a high-temperature environment (Oka 2003). During this process, the volatiles may tend to condense and polymerise to form heavier hydrocarbons molecules (tar). Some of the heavier hydrocarbons contribute to carbon deposition over the inner layers of fuel particles and add to the fixed carbon (Anthony and Howard 1976; Borah et al. 2011; Demirbas 2004). Following the volatile release, the volatiles gets ignited in the presence of a strong oxidation medium like air/oxygen, during conventional combustion. In the case of chemical looping combustion, the fluidization medium (steam/$CO_2$) acts as a gasification agent and cracks the heavier hydrocarbons in the released volatiles. The lighter hydrocarbons and permanent gases get oxidised by the oxygen carrier (iG-CLC case) or the nascent gaseous oxygen released by the oxygen carrier (CLOU case).

The char conversion phase involves the oxidation of fixed carbon in both combustion and gasification operations. The by-product of combustion is generally $CO_2$, oxides of nitrogen and sulphur, and the heat transfer occur from the fuel particle to the fluidized bed. In contrast to combustion, the heat transfer process in gasification occurs from fluidised bed to fuel particle due to the endothermic nature of the reactions involved. The by-products of gasification are collectively called as syngas consisting of gases like CO, $H_2$, $CH_4$, $CO_2$, oxides of nitrogen and sulphur, tar components, and so on (Figure 1.4).
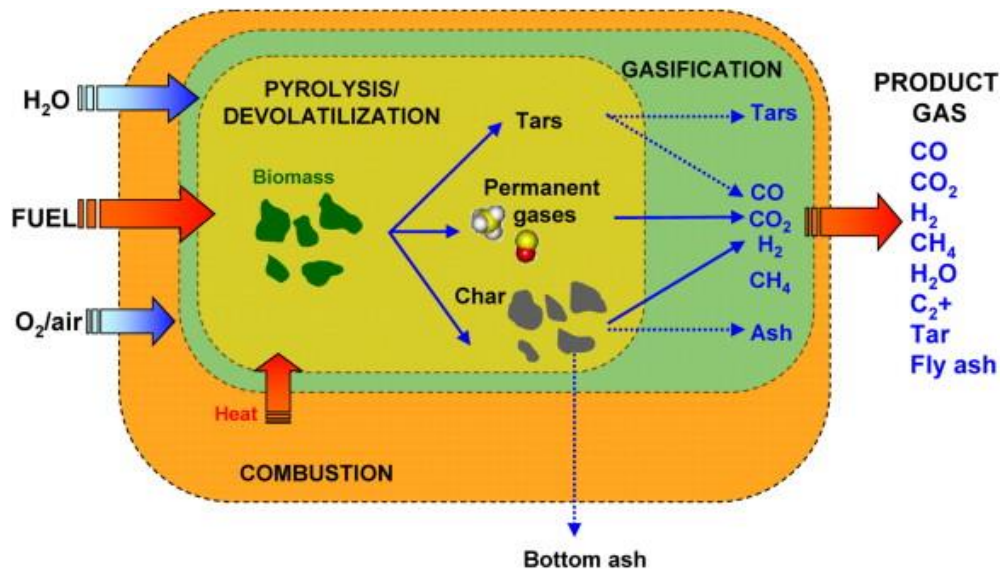
***Figure 1.4 Schematic representation of biomass conversion process via gasification***
***(Gómez-Barea and Leckner 2010).***

Concurrent to the thermochemical processes, changes to the fuel particles' physical structure are evidenced (Figure 1.5). These thermophysical changes include swelling/shrinkage, fragmentation, and attrition. Swelling could be witnessed during devolatilization of caking coals, whereas, shrinkage is observed in moisture-rich fuels like lignite and biomass(Coetzee et al. 2014; Kumar et al. 2006; Saxena 1990). Primary fragmentation involves the fuel particle breakage due to thermal stresses and internal overpressures generated by the release of volatiles during the early stages of the conversion process (Bareschino et al. 2020; Senneca et al. 2013, 2017b; a; Stubington et al. 1991). Thermal stress developed due to thermal shock is reported to be greater than the mechanical stress from the pressure developed during volatile evolution(Senneca et al. 2017a). As the char conversion progresses, consumption of carbon leads to the loss of carbon bridges and subsequent particle weakening that results in comminution referred to as secondary fragmentation. Percolative fragmentation occurs when a weak char particle with very high porosity is formed (when fixed carbon conversion exceeds 50 %), making way for the generation of char fines of easily elutriable sizes (Feng and Bhatia 2000).

8

| | Devolatilization | Char combustion | Char gasification |
|---|---|---|---|
| **Chemical and microtextural changes** | Coal depolymerization, Tar/gas release, Metaplast cross-linking and resolidification | Oxidation by $O_2$ | Oxidation by $H_2O$, $CO_2$, $H_2$ |
| | | Thermal annealing (change of turbostratic carbon structure, ash sintering/melting) | |
| **Size and morphological changes** | Swelling, Primary fragmentation | Shrinkage, Secondary fragmentation | |

Lifetime in a combustor/gasifier →

*Figure 1.5 Thermophysical and thermochemical changes experienced by a fuel particle (Senneca et al. 2017b).*

Attrition is the generation of fines by means of mechanical, thermal and chemical stresses over the particle surface(Scala et al. 2013). Divided into two types viz. mechanical and combustion-assisted attrition, mechanical attrition is caused by the surface wear due to abrasion of char with bed material and low-energy collisions against reactor surfaces, while the combustion-assisted attrition is due to the chemical and thermal stresses experienced by the particles. Mechanical attrition mostly results in loss of ash layer, whereas, generation of carbon fines in low-reactive fuels is evidenced from combustion-assisted type(Senneca et al. 2017b). Attrition behaviour primarily affects the balance of fly ash and bottom ash discharges from the reactor (Canò et al. 2007; Chirone et al. 2000; Scala et al. 2013). Understanding these comminution phenomena provides clear insights on the fuel size changes, consequent changes in conversion kinetics, effects of fuel particles on bed hydrodynamics and maintenance of solids inventory during the reactor operations.

## 1.5 Key challenges in chemical looping technology

To achieve high carbon capture efficiency, one has to have a suitable oxygen carrier material and a suitable reactor design either to deploy as a retrofit or as a standalone installation (Fennell and Anthony 2015). To date, research on producing a suitable oxygen carrier and optimal reactor designs for specific conditions is ongoing. An ideal oxygen carrier is expected to possess the following important characteristics.

(i)   High oxygen transport capacity to pick oxygen from air reactor and to deliver in the fuel reactor.

(ii)  High selectivity towards oxidation of combustibles in the fuel reactor.

(iii) High stability in terms of the number of redox cycles and mechanical strength.

(iv)  Low/no agglomeration property at high-temperature fluidization conditions

(v)   Good availability and low cost

(vi)  Environmentally benign nature

In general, a material having good oxygen-carrying capacity usually lacks mechanical strength and at the same time, there are oxygen carriers that have good mechanical strength but less oxygen-carrying capacity. For example, an iG-CLC material like iron oxide has better mechanical strength than the better oxygen-carrying CLOU material like copper oxide, which enables fuel conversion rates of about 3 to 15 times faster than the iG-CLC oxygen carriers (Leion et al. 2009). In terms of availability, low cost and environmentally benign nature, iG-CLC materials have an upper hand. Though having the fore-mentioned advantages, they have to be improved for oxygen-carrying capacity without compromising on its strength.

For achieving an industry-ready chemical looping technology, the following criteria have to be satisfied (Fennell and Anthony 2015).

(i)   Excellent gas-solids contact for better conversion,

(ii)  Better separation and circulation of oxygen carrier between fuel and air reactors

(iii) Effective gas separation system to avoid the escape of combustible matter or $CO_2$ into air reactor,

(iv)  Best heat extraction system

(v)   Better in-bed ash separation (specific for solid fuels)

(vi)  Best control system for stable operation.

Another major challenge is solid fuel feed characteristics when using specific solid fuels such as high-ash coals, lignite, biomass residues, pet coke, municipal solid wastes etc. The complexity increases when mixed fuels are considered in power generation, as they are expected to cause problems in moisture handling, density variation, proper size for feed etc.

**1.6 Research direction**

Apparently, studies on oxygen carriers and reactor designs are available in large numbers when compared to other aspects specific to CLC. Various aspects of solid fuel behaviour during chemical looping combustion is important to be studied, as they form a critical input for the conservative design of CLC systems. As mentioned earlier, since the Indian coals are not much explored for application in CLC, the present study will pave a path for the development of this carbon capture technology for the Indian power industry. In terms of imports, Indonesian coals hold the major share to source the Indian thermal power industry and the underutilized inland resources are the largely available biomass. Hence, this thesis aims to take one other step along with the peer researchers, towards the sustainable utilization of these solid fuel resources in CLC systems for better carbon management.

**1.7 Contents of the thesis**

*Chapter 2* delivers the **literature review and project outline**, where the critical review on chemical looping combustion literature, various specific research gaps in the mentioned research direction, scope and objectives of the thesis are discussed.

*Chapters 3* contains the **materials and methods**, in which details of the experimental setup and the procedures followed in various investigations over specific research objectives are detailed.

*Chapters 4 – 8 presents the results and discussions on investigations over specific research objectives.*

*Chapter 4* introduces **a new method for the determination of devolatilization time in CLC atmosphere** and presents the validation and comparison of CIM using established diagnostic methods.

*Chapter 5* discusses the results of **devolatilization studies under chemical looping conditions** and the associated **char yield** when varying the operating parameters such as particle size, bed temperature, and particle shape.

*Chapter 6* presents the detailed investigation on **primary fragmentation of solid fuels during chemical looping combustion**, using various indicators such as percentage of

fragmentation events, number of fragments, timing and frequency of fragmentation events, fragmentation index, and the particle size distribution.

*Chapter 7* discusses the results of the experiments on **char conversion and secondary fragmentation behaviour of solid fuels under chemical looping conditions**, using the same indicators applied in the primary fragmentation study.

*Chapter 8* discusses the results of the **analyses of char reactivity and structural aspects of chars** obtained at different operating conditions of fuel reactor, using thermogravimetric analysis, and the structural as well as chemical variations in chars using various instrumental characterization techniques.

*Chapter 9* **summarises** the significant observations and **major conclusions** of all the studies carried out towards the research objectives of the present work and the scope for future work.

# CHAPTER 2

## 2 LITERATURE REVIEW AND RESEARCH OUTLINE

### 2.1 Research aspects of Chemical Looping Combustion

Multiple aspects of Chemical looping combustion technology are currently being investigated e.g., oxygen carriers, different forms of fuels, fuel conversion levels, $CO_2$ capture efficiency, combustion efficiency, operating conditions, gasification agents, scale-up of reactor designs etc. The essence of the various study aspects are discussed in this chapter, and various research gaps are identified. From the given set of research gaps, a few of them are focused in this study.

### 2.1.1 Oxygen carriers in CLC

About 42% of the total oxygen carriers tested for chemical looping processes are ores of the transition elements like Iron, Manganese, Cobalt, Nickel, Copper etc. Iron oxide contributes to another 36%, owing to its low cost and availability (Mattisson et al. 2018). Table 2.1. shows the maximum oxygen-carrying capacity ($R_O$) of few oxygen carriers based on Equation 2.1 by Lyngfelt et al. (2001).

$$R_O = \frac{m_{ox} - m_{red}}{m_{ox}} \ldots\ldots\ldots\ldots\ldots\ldots..\ldots\ldots\ldots\ldots\ldots.(2.1)$$

Here, $m_{ox}$ is mass of oxidized carrier and $m_{red}$ is the mass of reduced carrier.

*Table 2.1 Oxygen transport capacity of pure oxygen carrier systems*

| System | $R_O$ (-) | System | $R_O$ (-) |
|---|---|---|---|
| $CaSO_4/CaS$ | 0.4701 | $CuO/Cu_2O$ | 0.1006 |
| $Co_3O_4/Co$ | 0.2658 | $Fe_2O_3/FeO$ | 0.1002 |
| $NiO/Ni$ | 0.2142 | $Mn_3O_4/MnO$ | 0.0699 |
| $CuO/Cu$ | 0.2011 | $Fe_2O_3/Fe_3O_4$ | 0.0334 |

Though calcium sulphate has the highest oxygen-carrying capacity, sulphur release in fuel reactor make it unsuitable, and its reactivity is greatly lost with the number of cycles (Tian et al. 2010). Oxides of nickel and cobalt are also not preferred citing the low physical strength & health hazards of nickel (Kuo et al. 2013), and cobalt's lower decomposition temperature (Mattisson et al. 2009). Iron oxides have been widely studied for their application in CLC (Lyngfelt 2014). Lyngfelt and his team

mostly used ilmenite, a titanium ore containing 37 % of $Fe_2O_3$ which was also found to be an attractive OC for CLC (Linderholm et al. 2012).

For chemical looping with oxygen uncoupling systems, three metal oxides such as $CuO/Cu_2O$, $Mn_2O_3/Mn_3O_4$, and $Co_3O_4/CoO$ have been identified by Mattisson et al. (2009). The overall endothermic reaction of cobalt oxide system with fuel in the fuel reactor makes the cobalt oxides less attractive for CLOU. Whereas the oxide systems of copper and manganese demonstrate overall exothermic reactions, which make them the most promising materials for CLOU application (Mattisson et al. 2009).

Another class of oxygen carrier is the combined oxide materials which are composed of two or more oxides (Fennell and Anthony 2015), for example, $Cu_{0.95}Fe_{1.05}AlO_4$, $Co_{0.5}Ni_{0.5}FeAlO_4$, $CoFeAlO_4$, $CuFeGaO_4$, $NiFeAlO_4$ etc. Another types of oxides called Perovskites ($ABO_{3-\delta}$) find their use as CLOU and CLaOU materials within the operating temperature range of 950-1000 °C (e.g. $SrFeO_{3-\delta}$). But the oxygen-carrying capacity is not consistent since it mainly depends on the reoxidation partial pressure of $O_2$. Perovskite-based OCs are partially substituted with transition metal ions having a similar oxidation state, at B sites to improve CLOU property in delivering oxygen at high temperatures (Imtiaz et al. 2013).

Low-cost oxygen carriers are the ore-based oxides such as ores of iron, titanium, magnesium etc. and few industrial wastes, which are tested widely. Bauxite waste (otherwise called red mud) is turning out to be a promising candidate as a low-cost oxygen carrier material (Chen et al. 2015; Mendiara et al. 2013b; c; a). It shows a high reactivity, stability and high oxygen-carrying capacity due to the minimal interaction between the active content ($Fe_2O_3$) and the inert supports. Regeneration tests showed that the OCs could be reoxidized completely without particle degradation (Chen et al. 2015). In the same way, other low-grade ores and unexplored industrial waste can be used in addressing the cost concern. As of now, the reported total operational experience with oxygen carriers is nearly about 11746 hours (Lyngfelt 2020), in various pilot-scale operations.

### 2.1.2 *Improvement of oxygen carrier properties*

In general, OCs are not sustainable for longer runs as they are subject to a series of damage when used directly in their raw form. Also, loss of particle fines in fly ash (due to attrition, fragmentation) and loss of OC reactivity (due to agglomeration, sintering, irreversible formation of oxides) are the frequent problems with materials employed in the redox operations. On the other hand, fragmentation and attrition are seen to have a beneficial effect on OC reactivity with the increase in cycle number as a result of the increase in surface area and exposure of unreacted core (Huang et al. 2014).

So, it is observed that the lesser the particle strength, the higher the reactivity, but the greater loss of fines, and sintering over cycles (as in the case of copper oxides). For oxygen carriers with high particle strength, the reactivity would be low (as in the case of iron oxides). To improve the reactivity and strength of OC, stoichiometric amounts of other OC materials are added to the main OC used and improvement in $CO_2$ capture efficiency has been achieved (Imtiaz et al. 2013; Rajendran et al. 2015). Impregnation of CLOU materials helped combustion at relatively low temperatures such as 500 °C thereby reducing the conversion period (Xu et al. 2014). With CLOU capable OC, secondary metal oxides like $Fe_2O_3$ are added to increase the decomposition temperature (Shafiefarhood et al. 2015). The use of inerts such as $Al_2O_3$ helps in improving the mechanical strength of the oxygen carriers, which reduces the attrition and fragmentation (Jin et al. 1999, Rydén et al. 2008). OC modified by sintering at high temperatures increased the crushing strength of the particles (De Diego et al. 2004; Mattisson et al. 2014). Sometimes mechanical strength is also improved by sintering, leading to stable reactivity (Chen et al. 2015; Gu et al. 2015).

Some of the methods employed to enhance their physical and mechanical properties are spray-drying, freeze granulation, solution combustion, extrusion, co-precipitation, sol-gel method, mechanical mixing etc. Also, while preparing the modified OCs, one needs to take into account the Tammann (half the melting point) and Hüttig temperature (one-third of the melting point) to prevent sintering of the support material. There needs much understanding about both the OC selected to fuse/dope with and the support material used. Most materials used for support have the property of fusing with OC at temperatures above Tammann temperature, with a risk

of sintering as well. Also, another disadvantage observed commonly is the decrease in reactivity with an increase in resistance to sintering (Imtiaz et al. 2013). Although modified OCs possess superior properties, they tend to deteriorate in activity with the increase in redox cycles due to the sintering effects, the formation of irreversible inert compounds (Ge et al. 2015a; Mei et al. 2015). Also, altering the composition of raw OC reduces the quantity of active oxygen release considerably.

### 2.1.3   *Operating conditions on oxygen carrier performance*

The temperature of the fuel reactor is one of the most important parameters influencing the overall reaction. Increase in the reaction temperature resulted in the decrease of carbon deposition during reduction but with increased reduction time (de Diego et al. 2008). In the case of OCs whose reduction can occur even at temperatures around 800 °C, a stable reactivity was demonstrated at operating temperatures more than 900 °C (Cuadrat et al. 2011; Song et al. 2013). Oxygen transfer capacity is also enhanced with increasing concentration of reduction agent (i.e. fuel) (Campos et al. 2013). Studies by Rydén et al. (2011a; b) state that $O_2$ uncoupling is higher at higher temperatures, resulting in faster fuel conversion rates. CLOU materials tend to agglomerate, affecting the reoxidation capacity to a substantial extent. Also, it is recommended to limit the temperature to less than 950 °C, to minimize sintering and agglomeration (Luo et al. 2014a). In the fuel front, higher bed temperatures (of around 1000 ºC) enhance char gasification rate, promoting greater char conversion in the fuel reactor and thus reduces the amount of char reaching the air reactor (Adánez et al. 2018).

Zhang et al. (2014) has found that operation at elevated pressures below 0.5 MPa has a positive effect in avoiding sintering/agglomeration of oxygen carriers and in making the oxygen carrier porous (Xiao et al. 2010). Although the pyrolytic process is suppressed at elevated pressures, the char reactivity and gasification rate are found to be improved at pressurized conditions below 0.5 MPa (Chen et al. 2017; Zhang et al. 2014). The overall reaction rate of CLC is also improved at limited elevated pressure in the pressurized CLC of coal (Huang et al. 2014).

Regarding the fluidization velocity, formation of large bubbles occurs at higher gas velocities reducing the contact area between fuel and gaseous oxygen, thereby leading to a lower reaction rate and less gas residence time  (Zhao et al. 2014). Higher

16

velocities lead to unconverted volatiles. Fluidization velocity is also related to attrition and fragmentation of OC particles, where the increase in this parameter leads to an increase in particle degradation due to collisions at high temperatures.

### 2.1.4   Nature of fuel used

For gaseous fuels like methane, syngas and natural gas, the oxygen carrier requirements are low as the complete oxidation mostly occurs in a single cycle without affecting much of the OC properties (Pans et al. 2015). Also, gas fuel conversion rates are higher than solid fuel conversion rates, in general, though some solid fuels containing high volatiles show higher conversion rates at higher temperatures (Mei et al. 2013). The experience on gaseous fuels in pilot-scale operations of up to 200 kW are recorded in literature, with at least 6191 hours of operation (Fennell and Anthony 2015; Mattisson et al. 2018).

As with gaseous fuels, liquid fuels could be directly injected into the fluidized bed, depending on their form and viscosity(de Diego et al. 2016; Moldenhauer et al. 2017). Reportedly 7% of the total CLC research operations had been carried out with easily devolatilizable liquid hydrocarbons and heavy oils(Mattisson et al. 2018). The CSIC group in Spain has performed investigations on various liquid fuels such as ethanol, diesel, synthetic oil, and mineral oil with different oxygen carrier materials (García-Labiano et al. 2014; Serrano et al. 2017). The major problems faced while operating with liquid fuels are

(i)    expanding volume of liquid fuels at high temperatures, causing mixing problem between fuel and oxygen carrier

(ii)   With the growth of bubbles in the fluidised bed, most of the fuel conversion occurs around the fuel feed region, demanding high oxygen carrier solid inventory.

Possible remedies suggested in the literature are using multiple feed points, fuel atomization, in-bed fuel injection /distribution system, and multi-stage fuel reactors (Mattisson et al. 2018).

In the case of solid fuels like coal, the OC suffers a lot of thermo-physical change along with the coal particles like sintering due to ash and sometimes ash fusion with

OC forming inerts, leading to its reduction in oxygen-carrying capacity. The presence of ash is inevitable in the fuel reactor since its removal causes loss of oxygen carrier. To make up for the oxygen carrier loss, one needs to select a low-cost OC material. Carry away of char particles to the air reactor is another problem since this will leave the $CO_2$ from combustion in the air reactor uncaptured.

From the particle size point of view, all the types of fuel which are used in FB-CLC studies are in the sizes as small as 45 µm (Linderholm et al. 2012) to a bit coarser particles and few studies used fuels up to 8 mm/~ 3108 µm (Ohlemüller et al. 2016). Smaller fuel particles have the advantage of getting converted at faster rates, but at the same time, all the released volatiles and gasification products may not be readily converted because of the slow rates of conversion with oxygen carriers. Carryover of char particles to the air reactor is one other problem since this will leave the $CO_2$ from combustion in the air reactor uncaptured. Longer residence time is required for complete conversion of the fuel sometimes requiring increased OC to fuel ratio, for better oxygen availability. Also, there is a need to avoid the escape of unconverted combustible volatiles which would then require an oxygen polishing step, where oxygen is introduced just before the FR exit, to oxidize all volatiles (Lyngfelt 2014). This problem can be avoided by using larger particles in the mm-size, which also has the benefit of minimization of size reduction operation (Dacombe et al. 1999). When larger fuel particles are used, the changes in the reactor operations should be made accordingly. On that front, fuel conversion times, fragmentation, other particle size changes, heat release, and recovery rate need to be investigated for optimal design and operation.

### 2.1.5 *Ash formations in fuel reactor specific to solid fuels*

Solid fuels like coal and biomass tend to produce ash as a final product which is usually an undesirable component in combustion. The formation of ash is unavoidable, and the removal of OC from ash from the system is also a challenging task since fine OC and char particles tend to get lost along with ash. Ash of coals are generally rich in Si, Ti, Fe, Ca, Mg, Na and K (Fennell and Anthony 2015). Biomass, though being an environmentally benign fuel, performs poorly in combustion processes because of their aggressive ash components such as chlorine and alkali like potassium, sodium

etc.(Lyngfelt 2020). Ash components have both catalytic benefits as well as the corrosive tendency towards the reactor parts. Studies on the effect of ash show that it is detrimental to OC activity except for lignite ash which had a beneficial effect on the ability of OC to oxidize carbon. A study by Rubel et al. (2012) showed a notable enhancement in the oxygen carrier reduction when ash is used in concentrations <75 wt.% in a mixture of char/OC/ash.

Gu et al. (2015b) observed that $SiO_2$-rich ash resulted in particle sintering with subsequent reactivity loss of iron ore, whereas $K_2O$-rich ash promoted the reduction reactivity of oxygen carrier, reportedly due to the K-Fe-O compound presence in ash. OCs such as $CuO/MgAl_2O_4$ and $Mn_3O_4/ZrO_2$ tend to react well with mineral matter in the fuel reactor. These reactions of OC have a good side of improving the mechanical strength but have a drawback of pore losses while coming to the re-oxidation capacity. The formation of pyrites and inert silicates give a heavy loss to OC inventory, requiring a continuous supply of fresh feed. Over a certain period of time, the sintered oxygen carrier particles that lack oxygen-carrying capacity stay along with the fresh supply of OC. This leads to problems associated with the overall solid circulation system and also poses difficulty in separation (Keller et al. 2014). The magnetic method of separation is proposed to separate ash from the oxygen carrier in a study conducted by Abián et al. (2017).

### 2.1.6 Gasification agents for solid fuels

Since gasification is an important step for carbon conversion in CLC, there is a significant role for gasification agents. Both the char gasification rate and the combustion efficiency increase as the percentage of steam in the feeding increases (Cuadrat et al. 2012a). A feasibility study of using $H_2O:CO_2$ mixtures as gasification agent showed that some of $H_2O$ could be replaced by $CO_2$, without affecting much of carbon capture efficiency while using bituminous coals and lignite (Cuadrat et al. 2012b; c).

The conversion rates of coal chars are reported to decrease while using $CO_2$ as a gasification agent, except for lignite char (Mendiara et al. 2013b). A molar ratio 70:30 was found to be sufficient to reach combustion efficiencies higher than 0.95 at

temperatures ranging between 900 °C and 980 °C (Mendiara et al. 2013c). The use of steam as the gasification agent reduced the risk of agglomeration/sintering when the oxygen carrier reduction was carried out at high temperature (1050 °C)  but reduced the oxygen-carrying capacity  (Chen et al. 2015). Gu et al. 2015a found that an elevated fuel reactor temperature and the use of steam as a gasification agent are beneficial to reduce fuel NO release in the CLC system.

Overall, the proportions of steam and $CO_2$ in the gasification medium depend on the nature of the fuel (Cuadrat et al. 2012c). For high volatile and reactive fuels like biomass, lignite etc., there is no significant difference reported in the gasification performance while using either steam or $CO_2$.

### 2.1.7   Reactor system design

The various configurations of reactors used in CLC research are two-reactor systems (AR and FR), coal-direct CLC system (moving bed system), and two-stage fuel reactor system. The two-reactor system of CLC is the regular type which uses a fast-fluidized circulating fluidized bed (CFB) air reactor and a fuel reactor of either fast or bubbling or spouting bed type. The solid circulation to the fuel reactor is handled by a high-velocity air reactor, and the solid return flow to the air reactor is achieved through overflow exit, fluidized loop seals, separate risers, or using the fuel reactor itself as a riser (Mattisson et al. 2018). The solids circulation rate is generally maintained by controlling the gas velocities in the reactors. Over choosing the fluidization mode for fuel reactor operations, bubbling fluidized beds (BFB) has the advantage of limiting the carry-over of unconverted char and volatiles exiting FR, by offering longer residence times for fuel particles. Nevertheless, they need a large solids inventory to reach high combustion efficiency, and the fuel feed point governs the complete conversion of carbon within BFB fuel reactors. Meanwhile, circulating beds have high char carry over to the air reactor, requiring an efficient carbon stripper in between AR and FR. CFBs are preferred for CLOU mode of operations, which have larger circulation rates; however, BFBs could also be used if there are no limitations on solids circulation rates(Adánez et al. 2018). The spouted bed could minimize the loss of material due to elutriation, but, the gas-solid contact was even inferior to the bubbling fluidized bed (Shen et al. 2009).

The moving bed system of the fuel reactor in coal-direct chemical looping (CDCL) uses a counter-current flow of oxygen carrier descending by gravity, fuel supply in the middle, and the gasification agent supplied from the bottom (Bayham et al. 2015; Kim et al. 2013). This kind of reactor system is claimed to offer high combustion efficiency. Although larger-sized solids are required to avoid any fluidization in the fuel reactor (Kim et al. 2013). As the co-current operation of solids and gases is preferred for high volatile fuels, the counter-current moving beds can be well utilized for low-volatile and high carbon fuels (Luo et al. 2014b).

The two-stage fuel reactor systems are proposed to enhance the conversion of gaseous combustibles using an upper stage containing freshly regenerated oxygen carriers (Thon et al. 2014). The lower stage could act as a carbon stripper when fine fuel particles are used. Almost complete conversion of combustibles is reported after passing the upper stages. However, a high pressure drop is noticed across the distributor plate of the upper stage, causing the leak of gases from the fuel reactor to the air reactor (Haus et al. 2016).

Regarding the use of oxygen carrier in fuel reactor, CLOU mode offers advantages in requiring a less efficient carbon stripper and has almost no oxygen demand in the freeboard, when compared to iG-CLC mode (Adánez et al. 2018).

## 2.2 Current status of Chemical Looping Combustion

Internationally, the work on looping combustion is more concentrated in the European countries, United States, China, Australia, and a few other countries. Around 3500+ research articles have been published worldwide on looping combustion in various levels such as evaluating the capture materials, modelling, using a variety of oxygen carrier materials, and modification of these materials for suitability in looping studies and tried with many types of fuels sourced from various parts of their locations.

For the utilization of CLC in the conversion of gaseous fuels like sungas, natural gas, methane, etc., Vienna University of Technology has successfully conducted a wide range of studies in a 140 kW CLC pilot reactor. Lyngfelt and Linderholm (2014) claim that a 100-kW unit at Chalmers University of Technology, Sweden, could operate with high $CO_2$ capture of more than 98% achieved using pulverized coal, with the attachment

of carbon stripper. Gas conversion of 84% is reached with bituminous coal, using the low-cost oxygen carrier ilmenite and a higher conversion of 95 % was reached with low-volatile fuels like wood char. Currently, the world's largest pilot-scale operation with solid fuel is successfully demonstrated with a 1 $MW_{th}$ chemical looping plant at Technische Universität Darmstadt by Ströhle et al. (2014). Another technology called Coal Direct Chemical Looping (CDCL) of 25-kWth capacity moving bed reactor designed by Fan et al. (2012) and Kim et al. (2013) at Ohio State University showed 97% conversion of sub-bituminous coal conversion with a $CO_2$ concentration of >99%. This technology claims to eliminate the need for a solid recirculation device and an additional carbon separation unit such as a carbon stripper. Recent works are seen to be concentrating much on modification of oxygen carriers for better cost-benefit, performance in carbon capture and durability. Other aspects of CLC like scale-up operations, fuel-based design optimization etc. have still a long way to hit industrial levels and therefore, have to be focussed much.

## 2.3 Critical summary of literature review on Chemical Looping Combustion

From the comprehensive survey of research articles, a comparison between CLC and CLOU is made in Table 2.2 and a list of various fuels and oxygen carriers studied in CLC technology development is presented in Table 2.3. Numerous works have been reported using gaseous fuels like natural gas, syngas but studies on solid fuels like coal, petroleum coke, biomass, and sewage sludge are only recently concentrated. Oxygen carriers like $Fe_2O_3$, NiO, Ilmenite, CuO are proved to be successful, but with some shortcomings during high temperature operation. The major difference between CLC and CLOU lies with the property of oxygen-releasing mechanism of the oxygen carrier particles.

As discussed in earlier sections, it is observed that an OC material with good oxygen-carrying capacity does not last long in a CLC process, and an OC which has good duty life does not possess a good oxygen-carrying characteristic. Despite having a relatively poor oxygen-carrying capacity of iG-CLC materials, they provide an economic advantage owing to their low cost. In two ways of approach, a better oxygen carrier can be developed. A CLOU material can be improved by imparting good mechanical strength by using a support material like alumina, magnesia, etc. The

oxygen-carrying capacity of an iG-CLC material can be improved by incorporating CLOU capable materials. It is also quite interesting that mixed metal oxides like Manganese/iron oxides, copper ferrites are showing good oxygen release properties (Evdou et al. 2016; Rydén et al. 2011a; Shafiefarhood et al. 2015).

*Table 2.2 Overview of CLC and CLOU*

| *Parameters* | *CLC* | *CLOU* |
|---|---|---|
| *Fuels used* | Gaseous fuels and solid fuels | Gaseous fuels and solid fuels |
| *Oxygen carriers* | Based on Fe, Ni, Co, Mg | Mostly based on Cu, Mn and perovskites |
| *Overall heat change* | -494 kJ/mol $O_2$ (max for Fe based OC) | -263 kJ/mol $O_2$ (max for Cu based OC) |
| *ART* | 800 - 1000 ˚C | 600 – 950 ˚C |
| *FRT* | 800 - 1200 ˚C | 750 – 1200 ˚C |
| *Particle degradation* | Moderate | Severe |
| *Solids inventory* | 500-1500 kg/MW (>3000 units in CSIC system) | 50 - 500 kg/MW (888 units in CSIC) |
| *Conversion rate* | 1 unit | 3-15 units |
| *OC* | 100 -500 μm | |
| *Fuel* | 37 μm to 100 μm (coal) Around 1000 μm (biomass) | |

Note: Few values are obtained from Fennell and Anthony (2015)

Scaling up the pilot-scale operations to commercial scale need this technology well-proven in all aspects. The present technology readiness level (TRL) of CLC for commercial deployment is 6. The operating experience with solid fuel amounts to more than 2700 h in 19 pilot plants ranging from 0.5 kWth to 4 MWth. For achieving higher carbon capture efficiency, the recommended options are (i) using highly reactive fuels like lignite, biomass etc., (ii) using efficient carbon stripper, and (iii) utilizing CLOU capable oxygen carriers(Adánez et al. 2018). One of the least focussed aspects of research in chemical looping combustion is the fuel nature and its thermophysical behaviour during conversion. The major issues found with CLC and CLOU systems in

the fuel front are the loss of unconverted char, solids handling, and ash removal when it comes to pilot-scale operation. Particularly, handling high ash coals like Indian coals will be a challenging process, owing to their fixed carbon intersperse in the ash skeleton and are not investigated to a good extent. Globally, only a few research articles presented research work on chemical looping combustion of high-ash coals like Indian coals (Bhui and Vairakannu 2019; Dubey et al. 2014; Suresh et al. 2015). Also, it can be noticed that only fuel particles of smaller sizes, i.e. pulverized coals are investigated in CLC studies till now.

*Table 2.3 List of solid fuels and OCs studied*

| *Fuels studied* | OC *studied* |
|---|---|
| South African coal and char | Iron Oxide |
| Mexican pet coke | Nickel Oxide |
| Shenhua bituminous coal (China) | Copper oxide |
| Colombian bituminous coal | Calcium sulphate |
| Spanish lignite and anthracite | Ilmenite |
| Chinese Huaibei anthracite | $Mn_3O_4$ |
| Kentucky coal char, Metallurgical coke (USA) | Hematite |
| Hambach & Rhenish lignite (Germany) | Copper ferrite |
| Chinese lignite | Bauxite waste (Red mud) |
| Dewatered sludge in China | Perovskite |
| Indonesian coal | Modified OCs |
| Swedish wood char | |
| Milled pine wood chips | |

## 2.4 Identified research gaps

- CLC studies of Indian coals and other solid fuels like biomass are very few.
- Devolatilization of solid fuels during CLC is not studied much, which assumes greater significance, especially with the volatiles-rich biomass.
- The thermophysical behaviour of coal and biomass during CLC is one of the least studied areas.
- CLC studies used only pulverized fuel particles less than 1.5 mm till now. However, it is important to study larger particle sizes as is the industrial case, typically with fluidized bed combustors.
- Solids inventory is a critical part and still lacks a good understanding of oxygen carriers.

## 2.5 Research needs and motivation towards the choice of objectives

Current research on CLC systems includes studies on the use of varieties of coal available worldwide, reactor system design, optimization of various operational parameters, oxygen carrier development, and performance studies. Copious amounts of CLC studies on gaseous fuels are available, while the studies on coal and biomass are very limited. Most of the published work on CLC of coal and biomass have used micron-sized fuel particles, and only a few studies using mm-sized particles are reported. Ohlemüller et al. (2016) report the use of coarse coal particles of sizes up to 8 mm in a pilot-scale FB-CLC for the following reasons.

(i)     To reduce carbon losses from the fuel reactor,

(ii)    To have a longer residence time of fuel in the fuel reactor.

The use of large (mm-sized) fuel particles can also be beneficial in the CLC systems for the following reasons.

(i)    The future CLC systems would prefer to minimize auxiliary power consumption by avoiding pulverization of fuel particles, especially in the case of high ash (e.g. Indian coals) and high moisture fuels (e.g. energy-intensive agro-residual biomass), as pulverization is difficult, energy- and maintenance-intensive (Dacombe et al. 1999; Zhang et al. 1990).

(ii)  Since volatiles and gasification products are converted at relatively lower rates in the case of in-situ Gasification-CLC (iG-CLC), they are preferred to be released at comparable rates at which they can be combusted/oxidised by the available OC.

(iii) Unlike in the case of pulverized coal, the volatiles and gasification products are gradually released when large-sized coal particles are used, resulting in the reduced requirement of oxygen carrier inventory in the bed. This would also reduce the gaseous oxygen requirement in the oxygen polishing step or eliminate the oxygen polishing step (Lyngfelt et al. 2016).

(iv) In the case of high carbon content coals, a high degree of fragmentation is witnessed during fluidized bed combustion (Chirone and Massimilla 1991), leading to the formation of smaller char particles in the bed, improving the char combustion rate. This moderate reduction in the size happens without any explicit addition of energy as unlike in the case of the use of pulverized fuel, thus reducing the overall auxiliary energy requirements of the system.

In support of the above, the literature on conventional air combustions shows that the majority of the studies used fuels in the size range of 1.5 -12 mm (Arena et al. 1992; Dacombe et al. 1994; Rangel and Pinho 2010; Scala et al. 2006). Nevertheless, the fluidized beds can comfortably operate with fuel particles of sizes up to 30 mm (Sarkar 2015) in bubbling mode.

### 2.5.1   *Thermophysical and thermochemical behaviour of solid fuels in CLC*

When the particle sizes are larger than 0.5 - 1 mm in coals (Agarwal et al. 1984; Cui and Stubington 2001; J.-T., Yang et al. 1990; Jüntgen and Van Heek 1979; Ross et al. 2000; Scala et al. 2006) and 2 mm in cellulosic biomass (Raman et al. 1981), the thermochemical conversion processes are primarily controlled by heat and mass transfer rather than only the intrinsic chemical kinetics. The thermophysical changes associated with thermochemical conversion include swelling, shrinkage, fragmentation, attrition, pore size changes etc. The initial conversion phase of devolatilization becomes a significant phenomenon, which affects the physical behaviour of fuel and has implications on the design of fuel reactor in FB-CLC (Lyngfelt and Leckner 2015), particularly when dealing with large fuel particles (Jia et al. 1993). It is to be noted that CLC environment is different from the conventional combustion environment (air) due

to the presence of steam and solid OC. The influence of steam environment on the devolatilization behaviour of coal has been demonstrated by Khan and Hshieh (1989) and Xu et al. (2016). Khan and Hshieh (1989) reported that the devolatilization of coal in the presence of steam atmosphere increases the volatile yield and produces a more reactive char. Xu et al. observed that the char yield during devolatilization in the oxy-steam environment is lower than that in the nitrogen environment. Apparently, the above studies indicate that the atmosphere in which the fuel get devolatilized makes a considerable influence on the devolatilization behaviour of the fuel. Thus, it becomes important to understand the devolatilization behaviour of fuels in a strong steam environment (absence of gaseous oxygen/air) present in CLC systems, as it is expected to be different compared to conventional FBCs.

The rate of volatile release (i) signifies the severity of mixing required between oxygen carrier and the volatiles and (ii) determines the fuel feeding rate (Fennell and Anthony 2015; Linderholm et al. 2014). Devolatilization studies help in determining the oxygen demand profiles across the reactor (since high volatile fuels such as wood and solid wastes devolatilize at a faster rate and volatiles quickly escape the reactor without conversion) and the oxygen carrier as well as the fuel loading in the bed. Thus, devolatilization time is an important design input for chemical looping combustors, especially in the case of moderate to high volatile fuels. In a similar way, char conversion becomes equally important to investigate, since it is the longest step of CLC process involving fixed carbon conversion in char by gasification (Scala et al. 2006; Senneca et al. 2017b). More importantly, the char conversion phase involves the fixed carbon conversion step, which is the slowest and therefore, the rate-determining step of the overall fuel conversion process.

While considering thermo-physical changes in fuel particles, the role of comminution on fuel conversion rates is vital. Particle comminution can be associated with one or more of the following causes (Chirone et al. 1991).

i. Development of high pressures inside fuel particles due to the generation of volatile gases (leads to primary fragmentation)

ii. Weakening of the fuel structure and breakage of C-C bridges (leads to secondary fragmentation)

iii.    Pore enlargement by percolation (Pore evolution/devolution)

iv.    Particle wear due to thermal stress or as a result of hitting/abrasion with other solid boundaries (Attrition)

These causes can prevail simultaneously, contributing combinedly to particle comminution. During the rapid phase of devolatilization, the volatiles present in the fuel particle tend to expand at high temperatures and tries to come out with high pressure. By doing so, the volatiles either find a passage through the pore structure or create stress leading to cracks/ sudden fragmentation at weak points in the fuel structure and also follow the combination of these two pathways. This, in turn, results in increased surface area for reaction and heat transfer. Depending on the degree of conversion, the density and thermal properties of the fuel particle keeps changing during combustion.

Char conversion and secondary fragmentation (char fragmentation) are equally important as devolatilization and primary fragmentation. Percolative fragmentation typically succeeds char fragmentation when any of the fragments are critically weakened, mostly in the later stages of char conversion (conversions >50 %). Though this phenomenon can be considered for studying the generation of char fines hand in hand with attrition (Senneca et al. 2017b), it does not have a well-known influence over char fragmentation. In combustion environments like CLC, a relatively long residence time of char in the absence of direct oxygen promotes char fragmentation. Hence, the majority of the conversion factors are largely influenced by the particle size changes, thus affecting the optimum configuration of a reactor that can be built upon(Walsh and Li 1994). This forms a motivation to study the larger sizes under CLC environment, exploring the possibility of using them without pulverization, resulting in lower penalty cuts in the process economy.

### 2.5.2    *Necessity of a new method to determine devolatilization time during CLC*

Several methods are available for the determination of devolatilization time of solid fuels in a fluidized bed, as detailed by Solimene et al. (2012). The visual techniques (Prins et al. 1989; Sreekanth et al. 2008b; Stubington et al. 1997; Urkan and Arikol 1994; Zhang et al. 1990) include flame period (which consider the time of flame

visibility) and flame extinction techniques (which consider the time between fuel introduction and flame disappearance). The instrumental techniques include,

(i) Mass loss history and thermogravimetric analysis of residual volatiles (de Diego et al. 2002; Thunman et al. 2004) in fuel particles sampled at regular time intervals during devolatilization,

(ii) time-resolved exhaust gas concentration of methane (Morris and Keairns 1979; Stubington and Sumaryono 1984) (in pyrolysis conditions) or carbon dioxide/oxygen (Chirone et al. 2008; de Diego et al. 2002, 2003; Jand and Foscolo 2005; Salam et al. 1988; Scott et al. 2007; Stubington et al. 1997).

(iii) particle centre temperature history (Di Blasi and Branca 2003; Heidenreich and Zhang 1999; Ross et al. 2000; Sasongko and Stubington 1996; Stubington and Sasongko 1998; Zhang et al. 1990), where the time at which the centre of the fuel particle reaches the bed temperature is considered as the devolatilization time,

(iv) time-resolved overboard pressure measurements (Solimene et al. 2012) to find the determine the devolatilization rates and correspondingly the devolatilization time.

Among the available methods, visual flame techniques are the simplest, easiest and quickest. However, these flame techniques cannot be applied for cases of flameless combustion as occurring in chemical looping combustion (Anheden and Svedberg 1996), where steam is a fluidizing medium. Similar conditions are observed during the conversion of high moisture fuels in an oxidizing atmosphere (Urciuolo et al. 2012).

Mass loss history experiments could present only approximate estimations of devolatilization time and require a large number of samples. The thermogravimetric analysis of residual volatiles, though considered to be a precise technique, consumes a relatively long time to determine devolatilization time and sometimes, requires more number of samples, in case of heterogeneity occurring within samples. where the particles of the same size vary in volatile matter composition. The application of time-resolved gas concentration measurement becomes cumbersome in CLC conditions due to the presence of high moisture in the gas stream. Also, continuous emission of gas species like CO, $H_2$, and $CO_2$ is evident throughout the pyrolysis phase and extends into the char conversion regime, making it difficult to recognize the endpoint of devolatilization. This condition worsens further when fuel fragmentation occurs, where

the smaller fragments reach an early char conversion stage emitting CO and $H_2$ that overlaps the concentration of gases from the larger fragments. Hence, a level of uncertainty and inaccuracy arises in the exhaust gas concentration method and its application becomes less reliable. Particle centre temperature (PCT) measurement is reasonably more accurate since the devolatilization time is noted when the centre reaches bed temperature and by that time, all the volatiles could be driven off from the particle. In PCT, the original nature of the particle gets manipulated while drilling the particle which generates high temperatures locally and creating cracks in the particle, and sample preparation to obtain non-cracked ones becomes a tedious process. The time-resolved pressure (TRP) measurement method is another diagnostic technique that could determine devolatilization time relatively more accurate. This method requires sophisticated instrumentation to monitor the pressure variations and a suitable mathematical model to serve the purpose. Most of the instrumental techniques need sample preparation, sophisticated devices and consume a longer time to analyse the results to determine the devolatilization time. Hence, an alternative, a reliable method is needed to determine the devolatilization time in flameless combustion conditions like FB-CLC and conventional FB-combustion involving high-moisture fuels.

### 2.5.3   *Char reactivity and the associated structural variations in char*

Along with the data on devolatilization, comminution and the char conversion rates from experiments, more detailed kinetic information is essential for developing reliable predictive models of fuel conversion in iG-CLC conditions. Gasification reactions being slow plays an important role in the char conversion stage of iG-CLC. Thus, exploring the char reactivity becomes significant in knowing the kinetic parameters.

The conversion rates of char depend not only on the origin, rank, and composition of coal (Czechowski and Kidawa 1991) but also on the preparation conditions like temperature, pressure, particle size, rate of heating, gaseous environments etc.(Czechowski and Kidawa 1991; Dutta et al. 1977). As the heterogenous char oxidation (by gasification) proceeds, internal factors like morphology, pore characteristics, and inherent carbon reactivity determine the conversion rates (Lorenz et al. 2000; Tsai and Scaroni 1987). Bulk diffusion of gas species is governed by the comminution phenomenon (particularly in large fuel particles), whereas the pore

diffusion depends on the microstructural formations. Further, diffusion is influenced by the operating bed temperature, i.e. gaseous species entering and exiting the internal structures differ, subsequently altering the rates of various reactions. Thus, obtaining reactivity data and structural information of chars, under various operating conditions is important.

Char reactivity studies consider either the fastest reaction of direct char oxidation by oxygen or the slowest reaction of char with steam or $CO_2$ (Li et al. 2017, 2018; Rathnam et al. 2009). Mostly, char reactivity has been studied using a thermogravimetric analyser (TGA) or in a furnace with a microbalance (Bouraoui et al. 2015; Jayaraman and Gokalp 2015; Kök and Yildirim 2020; Yan et al. 2020). Few studies report the use of fixed/fluidized beds or horizontal tube reactors for reactivity measurements using online gas chromatography and (or) mass spectrometry until certain reaction time or at varying burn-off levels (say 20%, 50% conversion of char) or until zero concentration of carbon monoxide(CO) is recorded (Aranda et al. 2016; Morin et al. 2018b; Wang and Bell 2017). Physisorption experiments of $CO_2$ in char at low temperature are also carried out and outgassing at the same or higher temperature, i.e. temperature-controlled desorption (TCD), where the measured weight change is used to indicate char reactivity(Gupta et al. 2018; Liu et al. 2003; Morin et al. 2018a). Variants of these experiments include carbon deposition (using methane) on char, fumigation of char with pyrolysis gas (mostly volatiles) using TGA/two-stage reactors (Chen et al. 1997). Out of several techniques available to determine char reactivity, thermogravimetric analysis is found to be more advantageous owing to the lesser sample size and quantity requirement, relatively more realistic approach in determining char reactivity and the continuous measurement of weight loss in a temperature controlled environment (Russell et al. 1998; Zolin et al. 1998). Further, thermogravimetric method of reactivity analysis eliminates the molecular diffusion limitations due to the high temperature operation (Tsai and Scaroni 1987). Although TGA is known to have problems associated with external diffusion limitations, these limitations could be eliminated by altering the gas flow rates, crucible dimensions, reacting char bed height etc.(Babinski et al. 2018; Russell et al. 1998).

In the mainstream reactivity studies available in the open literature, catalytic effects of inorganic alkali/alkaline earth metallic species (AAEM) found in fuel samples on char reactivity are focussed. Most studies involve complete demineralization of fuel samples by treating with HCl and HF mixture to remove all inorganics, either with or without the introduction of other ionic species (Hippo et al. 1979; Wang et al. 2016). Few researchers carried out partial leaching of AAEM to reduce ash content in char and examined their effect on reactivity (Wang et al. 2015c). These studies found the presence of alkali species improve reactivity in high ash coals, whereas in low ash fuels, the influence is less prominent or even absent. Reactivity of char is generally found to increase with the increase in reaction temperature (Jayaraman et al. 2017). Whereas, at low temperature operations, the ash formed (with Si as the major component) encapsulates active char sites due to ash melting and sintering (Bouraoui et al. 2015; Guizani et al. 2016; Lahijani et al. 2015), thus resulting in low char reactivity. The observations towards particle size show that the smaller particles have lower activation energy (which aids faster conversion), but they experience a reduction in reaction rates as the alkali catalytic species is lost during conversion. On the other hand, larger particles experience diffusion restrictions, and higher activation energy is required for conversion. But they could hold the catalytic species longer than the smaller particles (Asadullah et al. 2009; Jayaraman et al. 2017).

On the carbon structural aspects, studies find that the higher the maturity of coal, the higher the aromaticity and the higher the amount of carbon held in the aromatic structure. At higher reaction temperatures, larger and condensed aromatic rings are formed (Keown et al. 2007). These larger aromatic rings are found to be less accessible for reactions since only a few edge C atoms are available for reaction. The increase in char preparation temperature, as well as low heating rates, favour the increase in crystallite size of carbon formations (Lu et al. 2002; Schuepfer et al. 2020). An increase in the crystallite size decreases the ratio of edge C atoms (active sites) to basal carbon atoms (inactive sites), which makes the char less amorphous. These structural variations in carbon formations that affect the char reactivity are studied using Raman spectroscopy (Li et al. 2006; Sekine et al. 2006; Sheng 2007; Wang et al. 2014), Fourier-Transformation Infra-Red spectroscopy (Guizani et al. 2017; Min et al. 2011; Xu et al. 2013) and supplemented by X-Ray diffraction analysis in few studies.

**2.6 Research aim and objectives**

Based on the observations from the literature survey and from the motivation to test solid fuels in larger forms, the following aims were set out.

1. To gain a qualitative understanding of the thermophysical behaviour of solid fuels in large-sized particles and their thermochemical changes during chemical looping combustion.

2. To develop a quantitative relationship among the important variables involved in chemical looping combustion of solid fuels in a bubbling fluidized bed fuel reactor, through experiments.

*2.6.1   Objectives*

The following specific research objectives are framed to achieve the above set out aims:

 (i)    To develop a new method to determine the devolatilization time of a fuel particle in a fuel reactor of a chemical looping combustion system, validate and compare that with other available methods.

 (ii)   To quantify the various parameters characterizing devolatilization in CLC environment and develop an appropriate correlation for devolatilization time as a function of fuel particle size, shape, and bed temperature.

(iii)   To determine the primary fragmentation parameters of fuel particles at different operating conditions during chemical looping combustion conditions.

(iv)   To determine the char conversion time and quantitate the secondary fragmentation behaviour and the influence of operating conditions on the same.

 (v)    To assess the reactivity of chars during the char conversion phase of fuels in chemical looping environment.

*2.6.2   Scope of the research*

This research work brings out the necessary inputs for the conservative design of CLC systems that use mm-sized solid fuel particles. The scope of this work is listed as follows.

- Experimental determination of the devolatilization time, char combustion time, fuel particle swelling/shrinkage, primary and secondary fragmentation characteristics, char yield, char size distribution for three different varieties of Indian coals and one

biomass (*Casuarina equisetifolia*) of various sizes (+8-25 mm and +10-20 mm respectively), three bed temperatures (750, 850 and 950 °C) in fuel reactor, using one oxygen carrier as bed material (hematite) fluidized at 2.5 times the minimum fluidization velocity.

- Reactivity of char samples produced from fluidized bed at different discrete residence times during the char conversion regime, using thermogravimetric analysis accompanied by structural characterization techniques like SEM-EDX, BET and BJH pore analysis and Raman spectroscopy.

# CHAPTER 3

## 3 MATERIALS AND METHODS

### 3.1 Experimental setup

Figure 3.1 shows the fluidised bed combustor unit used in this study. The reactor is made of a stainless-steel cylinder of inner diameter 130 mm and height 600 mm, maintained at desired temperatures by a 12-kW silicon carbide heating arrangement. The fluidising media are preheated using a set of 3 pre-heaters in series, with a capacity of 2.5 kW each.
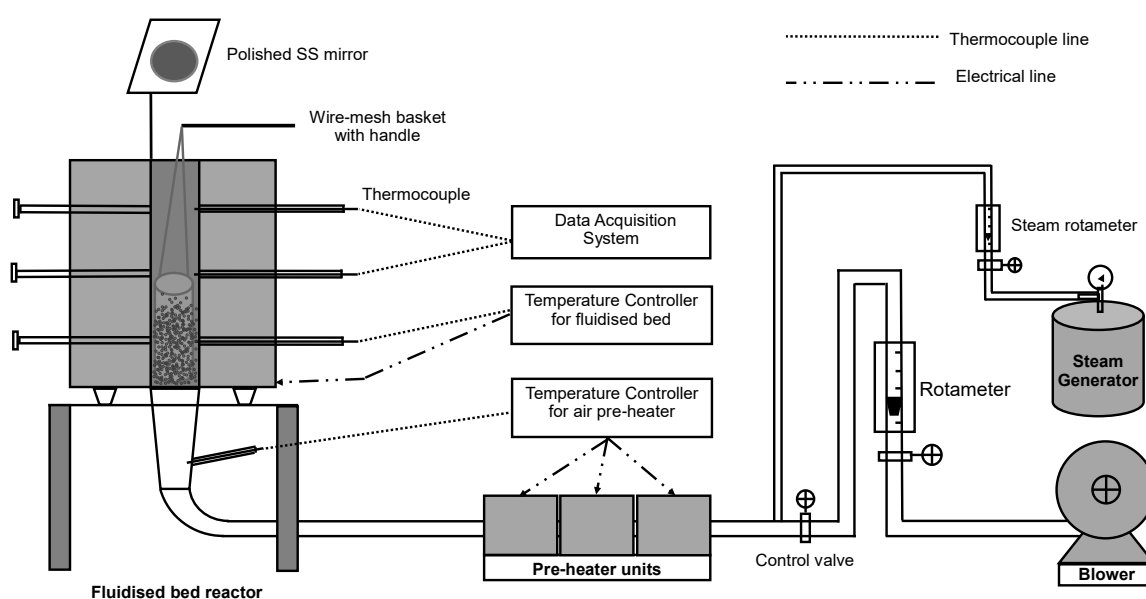


*Figure 3.1 Schematic of the FB-CLC unit.*

The fluid flow metering is done using calibrated air rotameter and steam rotameter for air and steam respectively. The air supply is provided by a centrifugal blower and a steam generator is used for the steam supply. Thermocouples are positioned at three different locations, specifically at the centre of the static bed (7 cm from the bottom of the bed), just above the static bed (15 cm) and at a point in the freeboard (50 cm), which are all connected to an Agilent data acquisition system. The in-bed thermocouples are connected to controllers to maintain the bed temperature at the desired level. A stainless-steel mesh basket of 2 mm mesh opening is used to hold the fuel particles during devolatilization and retrieve them at the end of devolatilization for analysis. Polished stainless steel (SS) plate is used as a mirror to see the in-bed events. The reactor is operated in a bubbling mode with a gas velocity of 2.5 times the minimum

fluidisation velocity at the respective bed temperatures. The minimum fluidization velocities are determined experimentally at different bed temperatures, by measuring the pressure drop across the bed while increasing the fluidization velocity (Oka 2003). The measured minimum fluidization velocities are 0.04, 0.038, and 0.036 m/s, corresponding to the operating bed temperatures of 800, 875, and 950 °C respectively.

## 3.2 Properties of materials used

The characterisation of solid fuels is carried out as per the following ASTM standards. The proximate analysis includes the determination of moisture content (D3173 – 11), volatile matter (D3175 – 11), ash content (D3174 – 12) and is carried out using the thermogravimetric procedure (D7582 – 12). The ultimate analysis involves the quantitative analysis of various elements such as carbon, hydrogen, nitrogen, and oxygen and it is carried out using Thermo Finnigan- FLASH EA 1112 series instrument at IIT Bombay, Mumbai. The composition and the properties of the fuels and the oxygen carrier used in the study are given in Tables 3.1 and 3.2 respectively.

*Table 3.1 Properties and compositions of fuels used*

| Composition (%wt.) | Indian Coal 1 (IC1) | Indian Coal 2 (IC2) | Indonesian Coal (IDC) | Biomass (BM) |
|---|---|---|---|---|
| Moisture | 8.2 | 4.5 | 6.3 | 8.9 |
| Volatile Matter | 33.5 | 23.2 | 40.4 | 79.8 |
| Fixed Carbon | 31.9 | 29.62 | 43.62 | 10.9 |
| Ash | 26.4 | 42.68 | 9.68 | 0.4 |
| *Elements (%wt.)* | | | | |
| Carbon | 53.53 | 43.62 | 60.74 | 43.76 |
| Hydrogen | 2.133 | 1.86 | 5.01 | 5.69 |
| Nitrogen | 0.64 | 1.04 | 0.89 | 0.16 |
| Oxygen | 8.98 | 5.88 | 17.18 | 41.02 |
| *Property* | | | | |
| Bulk density (kg/m$^3$) | 702 | 939 | 647 | - |
| Particle density (kg/m$^3$) | 1480 | 1917 | 1274 | 780 |

**Indian Coal 1    Indian Coal 2    Indonesian coal    Biomass**

*Figure 3.2 Samples of different fuels used in the study.*

Four different types of solid fuels namely, two types of sub-bituminous Indian coals, an Indonesian coal and *Casuarina equisetifolia* wood (henceforth referred to as IC1, IC2, IDC and BM respectively) are taken for this study (Figure 3.2). Iron ore (hematite) containing 64% Fe, which is used as the oxygen carrier in the present study is sourced from SLR Metaliks Ltd., Bellary, India. The size range of the iron ore used is +250-425 µm.

*Table 3.2 Characteristics of the oxygen carrier (iron ore)*

| **Physical properties** | | | | | | |
|---|---|---|---|---|---|---|
| Bulk density (kg/m$^3$) | | | 2186 | | | |
| Particle density (kg/m$^3$) | | | 4541 | | | |
| Mean particle diameter (µm) | | | 337.5 | | | |
| **Chemical composition** | | | | | | |
| Composition | LoI* | Fe(T)$^+$ | SiO$_2$ | Al$_2$O$_3$ | P | Mn |
| Mass % | 4.80 | 62.43 | 1.20 | 2.25 | 0.151 | 1.01 |

*\* Loss on Ignition; $^+$Total Iron*

Coal samples are prepared by crushing larger coal blocks using a jaw crusher, which consisted of a mix of both near-rounded and flaky particle shapes. The crusher product is sieved, and the near-rounded particles are selected for use in all the experimentations, while the flakes are used only for comparison purposes in a part of the research work. The sizes (average sieve diameters) of coal samples used are 9 mm (+8 mm -10 mm), 14.25 mm (+12.5 - 16 mm), and 22.5 mm (+20 mm - 25 mm). The woody biomass of *Casuarina equisetifolia* is sun-dried and sized in the form of cubes with sides measuring 10 mm, 15 mm, and 20 mm. While the particle sizes are expressed as average sieve diameters, the individual particles within the same sieve range vary in

sizes and weights slightly. To bring out the effect of these variations in particles within each of the average sieve diameters, the particle sizes are henceforth expressed in terms of mass equivalent diameters (Sudhakar and Kolar 2010) at appropriate places.

## 3.3 Experimental procedure

A static bed of 13 cm is formed inside the cylindrical reactor using 3.772 kg of hematite, resulting in a height to diameter (H/D) aspect ratio of 1. The fluidization medium (air/steam) is preheated to a temperature of 300 ºC before entering the reactor. Simultaneously, the bed is also heated using the silicon carbide rods placed around the reactor vessel. The bed is initially fluidized by air and when the desired operating temperature is reached, the fluidisation medium is switched to steam and maintained at the same temperature. The present study deals with experiments using single fuel particles, since this is an effective way of investigating fuel particle behaviour in the high temperature fluidised bed environments, as the fuel particles in real conditions are isolated physically, and do not influence the conversion of each other directly. For every test, a stainless-steel mesh basket is introduced into the reactor and a single fuel particle is carefully introduced into the mesh basket and allowed to devolatilize or undergo char conversion.

Depending on the type of experiments, the samples are retrieved after a certain residence time, by lifting the basket out of the reactor after immediate quenching with inert sand. For example, sample retrieval during devolatilization time and char conversion time experiments is done by following the respective visual techniques that are explained in Chapter 4 and Chapter 6 individually. The studies on thermophysical characteristics such as primary fragmentation and secondary fragmentation and the study of char reactivity are carried out at four different residence times, i.e. four quarters of either the devolatilization time or the char conversion time. Immediately after the sample retrieval, the sample is quenched in the sand to prevent conversion in the open atmosphere and stored in an air-tight container for further analyses. Mass of the individual particles/fragments is measured before and after the experiments. Mass loss with respect to initial sample mass is determined using fresh fuel samples, for each of the different residence times during the char conversion regime. Fuel particle sizes are expressed in terms of average sieve diameters or mass equivalent diameters (Sudhakar

and Kolar 2010), wherever appropriate. The mass equivalent diameters ($d_{eq,m}$) of the fuel particles are calculated using Equation 3.1, where 'm' and '$\rho$' are respectively the mass and density of the samples.

$$d_{eq,m} = \left(\frac{m}{\rho}\right)^{1/3} \ldots\ldots\ldots\ldots\ldots\ldots\ldots\ldots\ldots\ldots\ldots\ldots\ldots(3.1)$$

In addition to the above, procedures corresponding to specific experiments are detailed in the 'Experiments' sub-section of the respective chapters, for the convenience of readers. The uncertainties involved in the experimental and instrumental measurements are detailed in Appendix 2.

# CHAPTER 4

# 4 NEW METHOD FOR DETERMINATION OF DEVOLATILIZATION TIME IN CLC ENVIRONMENT

## 4.1 Introduction

Devolatilization is the initial phase of the fuel conversion process, and the measurement of devolatilization time becomes essential in assessing the behaviour of fuel particles during this phase. Flame Extinction Technique (FET) is the simplest and widely applied visual method to determine devolatilization time in conventional combustion environments, which is based on the volatile oxidization visualised in the form of flame. However, the devolatilization phase of chemical looping combustion is of flameless nature, owing to the unavailability of a direct oxidant such as air or oxygen in the combustion environment and also, the presence of steam as the fluidization agent. This necessitates a search for a new visual method for the measurement of devolatilization time in CLC conditions.

The first venture of this thesis is to develop a new method to determine the devolatilization time in flameless conditions. Irrespective of the combustion environment, the volatile gas species emanating out of the particle decreases the surface temperature and makes it appear black (Andrei et al. 1985; Prins et al. 1989; Saxena 1990) throughout the devolatilization phase, even in the high temperature environment. The surface of the fuel particle could attain the colour of the hot-bed only after the complete emission of volatiles which is relatively at low temperatures. Once the devolatilization or the char formation is complete, glowing char conversion occurs all over the particle surface (Andrei et al. 1985), rendering it almost the same colour as that of the hot bed, effecting the particle disappearance. Based on these events, a new method called "Colour Indistinction Method (CIM)" is proposed as a simple, quick and easy visual technique for the determination of devolatilization time of solid fuels in flameless combustion environments like FB-CLC. This method considers the completion of devolatilization phase based on the colour change of fuel particle from black to reddish-orange, attaining the bed colour and becoming indiscernible from the bed particles. The new method is validated and compared with the results from few existing devolatilization time determination methods, with the aid of the following experiments.

1. Devolatilization time ($\tau_d$) experiments by colour indistinction method (CIM)

2. Determination of devolatilization time by Flame Extinction Technique (FET) in conventional fluidized bed combustion using air.

3. Thermo-gravimetry experiments to determine the residual volatile content of the char (devolatilized fuel) to validate CIM.

4. Mass loss history experiments in CLC conditions to validate the devolatilization time obtained by CIM.

5. Particle centre temperature measurement as an additional diagnostic technique to validate the devolatilization time obtained by CIM.

## 4.2 Experiments and validation studies

The experiments presented in this chapter involves two fuels namely, IC2 (coal) and BM (biomass), whose properties are listed in Chapter 3. These two fuels are studied in three particle sizes ranging from 8 to 25 mm, at three bed temperatures of 800, 875, and 950 ºC.

### *4.2.1 Colour Indistinction Method (CIM) - methodology*

During devolatilization experiments conducted under CLC conditions, introduced coal particles are visible as such in black colour inside the bed and the wood particles become black in the CLC conditions as soon it is exposed to the hot bed. These black coloured particles are closely monitored for the colour change to reddish-orange (matching the colour of the hot bed), using a SS mirror. When the particle becomes indistinct from the hot bed material, immediately the particle is retrieved out of the bed and rapidly quenched in the sand to arrest further fuel conversion. After that, the particle is allowed to cool and then stored in an air-tight container. The residence time of the particle in the bed (time between the introduction of a fuel particle into the bed and its disappearance) is marked as the devolatilization time.

During the devolatilization in the fluidized bed, a fuel particle moves randomly in and out of the bed at a particular rate. As the fuel approaches the end of devolatilization, sometimes it takes a long time to show up at the bed surface, which may be construed to be the disappearance of the particle leading to the wrong estimate of the devolatilization time. To rule out this possibility and also to ensure the exact time

of colour indistinction between the particle and the bed, a set of preliminary devolatilization experiments for different sized particles are carried out. In these preliminary experiments, the particle is allowed to reside for an extended time period of around 20 times the average surfacing time from the point of time of colour indistinction and is continuously monitored. It is found that the disappeared char particle does not reappear even after the allowed residence time. A video in this connection is available as supplementary material from the published article (Pragadeesh and Sudhakar 2019), wherein a 15-mm biomass particle can be seen devolatilizing in the fluidized bed at 875 ⁰C. Thus, the moment of last immersion of the particle into the bed following the complete colour change is considered as the end of devolatilization in this method.

'Flame Extinction Technique': To establish the necessity of the CIM technique in flameless CLC conditions, conventional fluidized-bed air combustion experiments are conducted with the same fuels, employing a method called Flame Extinction Technique (FET). As reported in the literature (Borah et al. 2011; Ross et al. 2000; Stubington et al. 1991), this flame extinction corresponds to a 90 or 95% mass loss of the total volatile matter in the fuel particle. Thus, in FET, the devolatilization time is defined as the time interval between the introduction of the fuel particle in the reactor and the extinction of flames emerging from the particle.

### 4.2.2 Measurement of residual volatiles in char

The residual volatiles present in the char can reveal the extent of devolatilization that occurred in the fuel particle. To validate CIM, based on the retention of residual volatiles, char particles obtained from the $\tau_d$ determination experiments using CIM and FET are analysed. The residual volatile matter is determined as per ASTM D7582 – 15 standard test method, using a thermo-gravimetric analyser (TGA). In this part of the study, char is obtained from coal particles of average sieve size of 14.25 mm and biomass particles of 15 mm, devolatilized at three different bed temperatures (800, 875, and 950 ⁰C) are used. The samples are ground to $\leq 100$ μm and are analysed under a nitrogen (UHP) atmosphere. During the analysis, the moisture content is removed by the program hold of 10 minutes at 107±3 ⁰C and the volatile matter is measured from the mass loss that occurred while the temperature increased from 105 to 950 ⁰C. The

amount of residual volatiles is calculated from the ratio of the measured mass loss in devolatilized char using TGA to the mass loss expected from complete release of proximate volatile matter and expressed in percentage.

### 4.2.3   Mass loss history experiments

The history of mass loss experienced by fuel particles under CLC conditions show the time at which the particle has almost no mass loss, which could be deemed as the end of devolatilization. For obtaining mass loss profiles, the fuel particles of average sieve sizes of 14.25 mm (coal) and 15 mm (biomass) are selected with similar shapes and closer masses in the case of coal, and shaped biomass particles are used with equivalent masses. A fresh fuel sample (for each residence time) is introduced and allowed to devolatilize for a certain set of residence times, in the order of 20 seconds up to 200 seconds. At the end of the set residence time, the sample is drawn out from the bed and quenched in sand. The mass of every sample is noted before and after the devolatilization for each set residence time. In this study, the mass loss history is obtained for coal and biomass at a bed temperature of 950 ⁰C.

### 4.2.4   Particle centre temperature measurements

Devolatilization times determined using CIM are compared with an established diagnostic technique that considers the time at which the centre of the particle attains the operating bed temperature as devolatilization time(Ross et al. 2000). The particle centre temperature (PCT) experiments are conducted with both the fuels of all three particle sizes at bed temperatures of 800 and 950 °C. For the centre temperature measurements, representative fuel samples with known diameter are drilled with a 2-mm bit at the middle point towards the centre of the particle core, covering the radial distance. A 2 mm sheathed K-type (Chromel-Alumel) thermocouple is closely held in contact with the fuel particle using a high-temperature refractory cement as followed in the literature (Di Blasi and Branca 2003; Eatough and Douglas Smoot 1996). The particle centre temperature is continuously monitored by an Agilent data acquisition unit with a logging interval of 0.5s.

## 4.3 Results and discussion

### 4.3.1 Determination of devolatilization time using CIM

Figure 4.1 shows the photographs of a 15-mm biomass particle at different residence times during devolatilization at 875 °C, as visualized from the SS mirror mounted above the fluidized bed setup. The endpoint of devolatilization can be identified by the disappearance of the particle in the bed or by the indistinction between the particle and the bed at time 01 minute 43 seconds (103 seconds).

Initially, the wood particle appears black against the reddish-orange bed. After 20 s, the edges of the particle attained the bed colour, which then gradually extends towards the particle centre (on the outer sides). Over the course of devolatilization, the black region is limited to the particle centre irrespective of the sides. Finally, the black spot disappears resulting in a completely glowing particle at 103s and the particle becomes indistinct in the hot fluidizing bed. This point of time is marked as the end of devolatilization and so the devolatilization time.
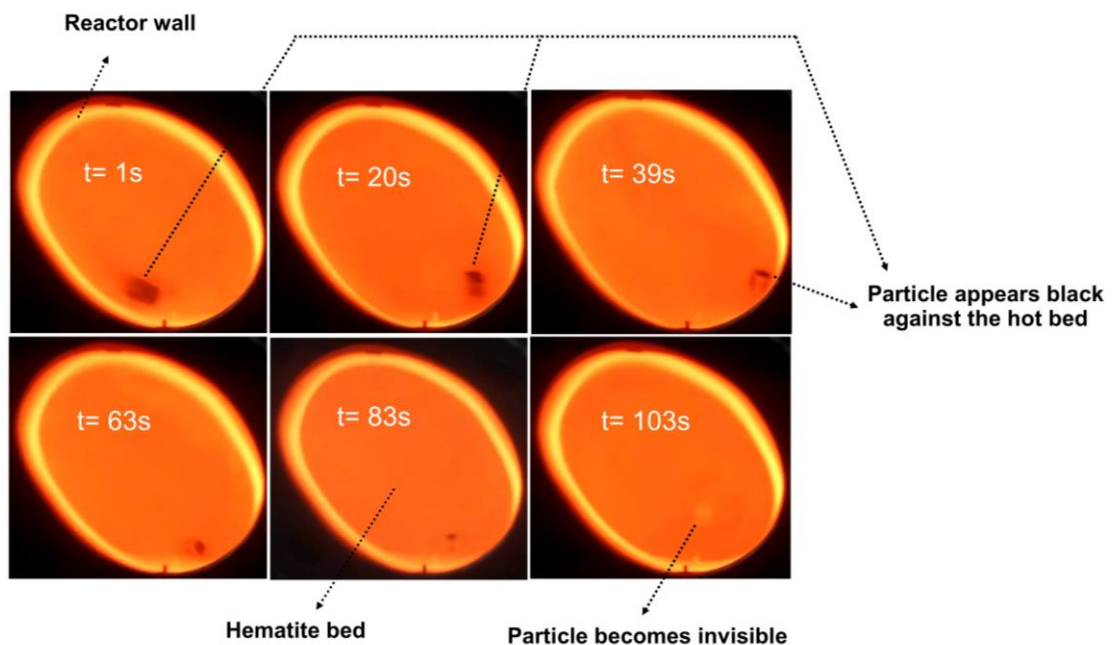


***Figure 4.1 Photographs of a 15-mm wood particle at different resident times during devolatilization under CLC conditions at 875 °C.***
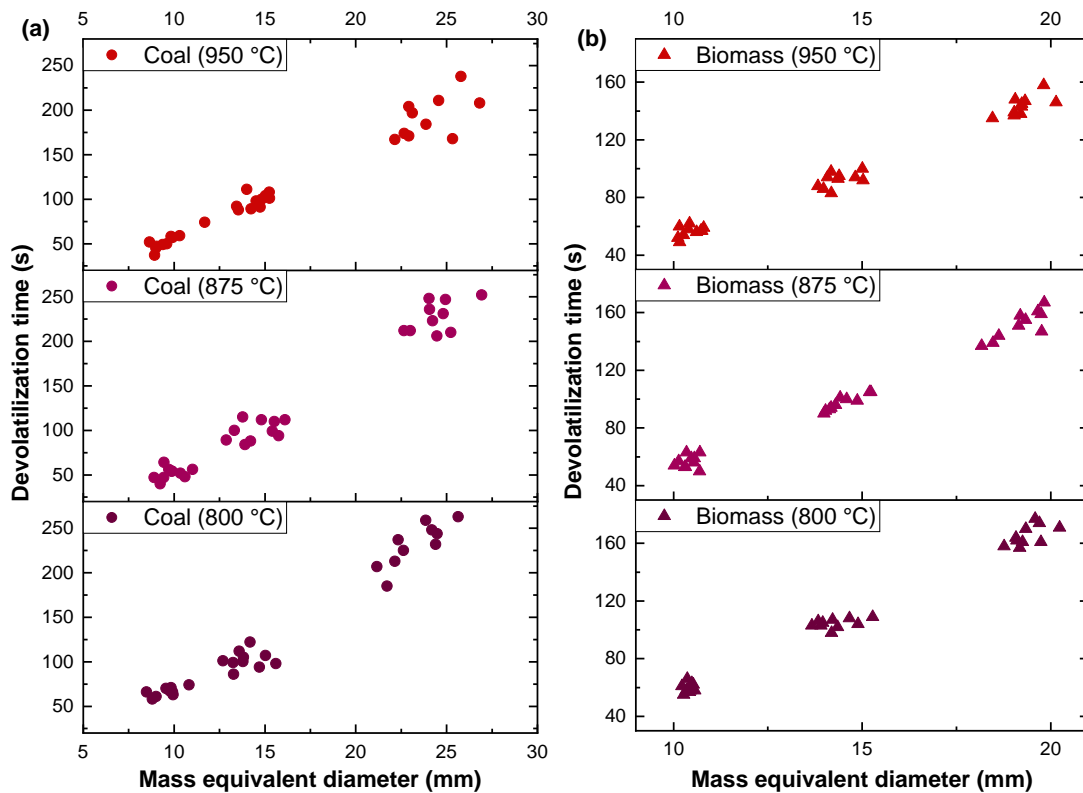
*Figure 4.2 Devolatilization time of (a) coal and (b) of biomass for different particle sizes at 800, 875 and 950 ºC.*

Figure 4.2 shows the devolatilization times of coal and biomass respectively at three different temperatures for various particle sizes studied, as determined by CIM. As observed in the case of conventional fluidized bed combustion systems (Stubington et al. 1991, 1992), the devolatilization time in CLC environment also increases with the increase in particle size (Ross et al. 2000; Saxena 1990), which is mainly governed by the heat transfer rates within the thermally thick particles (Prins et al. 1989; Stubington and Sumaryono 1984).

The devolatilization time is found to decrease with the increase in temperature (Stubington et al. 1991). However, there are few exceptions to this trend, especially in the large particles as seen in Figure 4.2. This may be due to the difference in the degree of inhomogeneity in the samples used for the study. In the smaller particle sizes studied, this degree of inhomogeneity between the samples is low and hence the observed devolatilization time of all the samples of the same or nearly the same size is not very different from each other. The scatter in the trend could also be due to the fragmentation

events happening due to the internal pressure developed by the volatile release. Fragmentation results in the generation of new surfaces, leading to increased devolatilization rate and thus reduced devolatilization times than the non-fragmenting particles with similar masses.

In the case of CLC of biomass particles (Figure 4.2), a similar pattern of devolatilization time is observed with the increase in particle size. Unlike in coal, the devolatilization behaviour of biomass particles is found to be consistent, which is reflected in the reduced scatter of data points (when compared to coal) corresponding to the different samples of the same or nearly the same size.
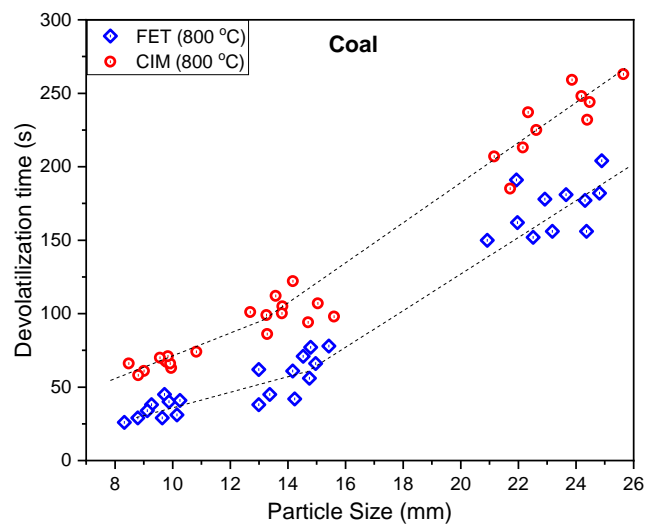


***Figure 4.3 Comparison of devolatilization time of coal obtained using FET (in air) and CIM (in steam CLC conditions).***

To compare the order of magnitude of devolatilization times found by CIM, the results are compared with devolatilization times obtained by FET method used in the conventional fluidized bed combustion environment. Figures 4.3 and 4.4 show the comparison of devolatilization times obtained from CIM with that of FET for coal and biomass particles respectively. It is clearly observed in Figure 4.3 that the devolatilization time measured by CIM in CLC environment is consistently and considerably different from the devolatilization times measured using FET method (in conventional FBCs), across a range of particle sizes. For smaller particle sizes (8-16 mm), the deviation ranges from 30 to 42 seconds, while it ranges from 42 to 67 seconds for larger sizes (20-25 mm), which translates to a minimum deviation of about 30%

from the corresponding FET values (Figure 4.3). This difference in the devolatilization times determined by FET and CIM can be attributed to the presence of steam and oxygen carrier in CLC environment.
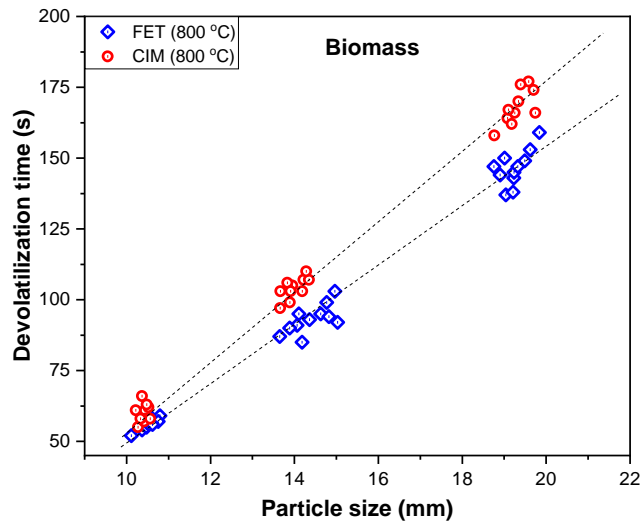


*Figure 4.4 Comparison of devolatilization time of biomass obtained from FET (in air) and CIM (in steam CLC conditions).*

Likewise, it can be noticed that the devolatilization time of biomass as determined by CIM lies well above that of FET and this shows that the time taken for devolatilization of the same fuel particle (biomass) under two different environments i.e. conventional FB and FB-chemical looping combustion varies significantly. For the smaller biomass particles (10 mm), the deviation in devolatilization time ranges from 2 to 13 seconds, whereas the larger particles (15 and 20 mm) have deviations in the ranges from 18 to 24 seconds. The deviation from the corresponding FET devolatilization times is about 15% for all sizes (Figure 4.4). This observation, as also inferred in the case of coal affirms the necessity of a new specific technique to determine the devolatilization times of fuel particles in FB-CLC environment.

### 4.3.2 *Validation of CIM using mass loss during devolatilization*

The total mass loss due to the release of volatiles during the observed devolatilization time can give an indirect measure of the correctness of the proposed method. The mass loss during devolatilization ($m_d$) is calculated using Equation 4.1 as,

$$m_d = \frac{m_i - m_f}{m_i} \; x \; 100 \; \%\dots\dots\dots\dots\dots\dots\dots\dots\dots\dots\dots\dots\dots(4.1)$$

where $m_i$ is the initial mass and $m_f$ is the final mass of the fuel particle.
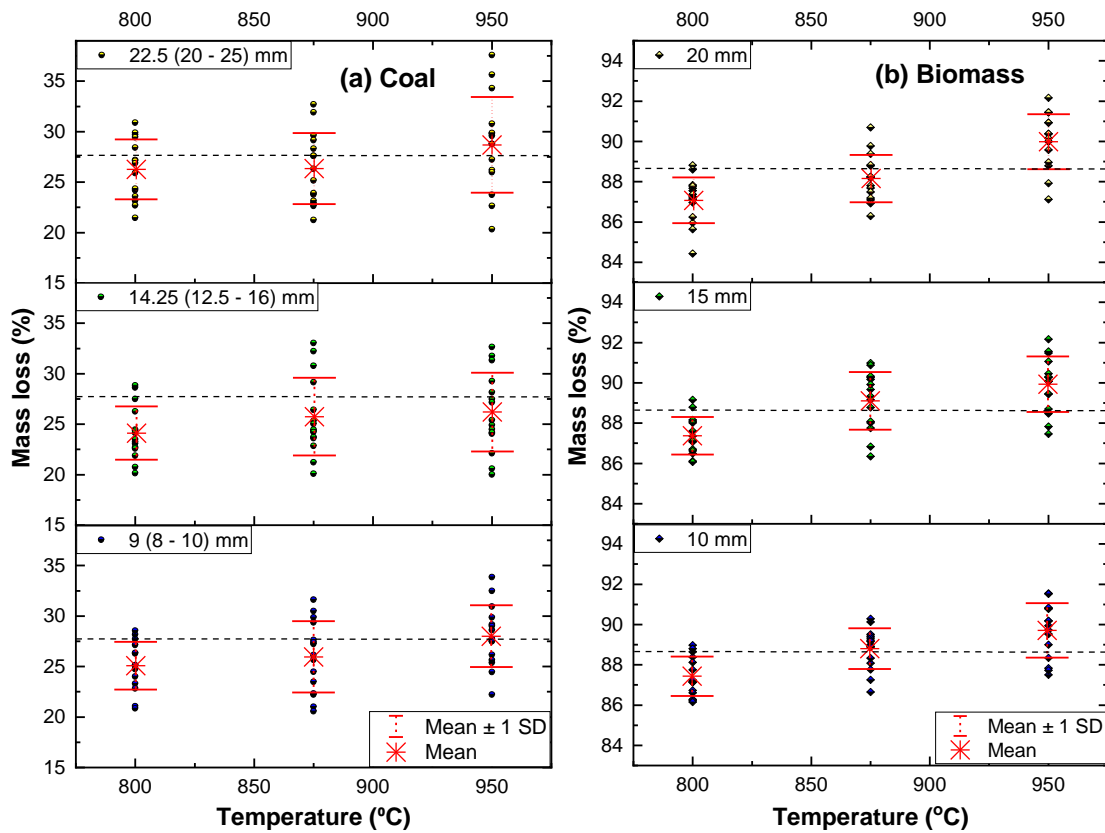


*Figure 4.5 Mass loss in (a) coal and (b) biomass for different sizes at bed temperatures of 800, 875 and 950 ºC (--- represents the expected mass loss due to the removal of proximate moisture and volatile matter of the parent fuel).*

The $m_d$ of coal and biomass of two different sizes at various temperatures of 800, 875- and 950 ºC are given in Figure 4.5. It can be observed that the percentage mass loss in fuel particles is not constant across the range of particle sizes and operating bed temperatures. The data points are spread around the dashed line representing the expected mass loss from the sum of proximate volatile and moisture content. Whereas most of the points are present below the marked line denoting that the mass losses are lesser than the expected value. In coal, the 22.5 mm particles exhibit more mass loss compared to the smaller ones, which may be related to the relatively larger comminution in higher-sized coal particles (Dacombe et al. 1999). For volatile-rich biomass particles, the percentage of mass loss is not affected much by the change in particle size. But mass loss is observed to be higher than the sum of proximate volatiles and moisture with the increase in temperature. This can be attributed to the mass loss

resulting from the extended conversion of biomass particles in the air, due to a lag in the quenching process (of about 5 to 7 seconds in between particle retrieval and quenching).

Overall, the mass loss increase with an increase in bed temperature, while it decreases with an increase in size, which is mainly governed by the internal heat transfer rate in the particle and is the reason why we observe the low amount of volatile losses for the particles of relatively bigger diameters (Prins et al. 1989). However, at individual particle levels, mass loss due to volatiles is found to vary noticeably, as seen from the standard deviation of the actual mass loss due to volatiles for individual particles relative to the proximate volatile content and moisture (dashed line). This is probably due to the fact that the actual volatile content of the coal particles might not always match the volatile content of the parent coal particles (the ones which are used for determining the proximate volatile content of a coal type) and also, not all the volatiles are removed during the observed devolatilization period (Borah et al. 2008; Zhang et al. 1990). Another cause of the deviation could be the fuel particle fragmentation. When fragmentation happens, higher mass loss is evident due to the excess conversion of smaller fragments as well as from the loss of fine particles escaping the basket. This kind of excess mass loss can be noticed in Figure 4.5.

From the mass loss experiments in FB-CLC conditions, it is seen that the coal and biomass particles exhibit mass losses due to volatiles, near equal to the proximate volatile content, which is about 20 to 30 % and 85 to 90 % respectively. This observation of the percentage mass losses of various fuel particles shows that the measurement by the proposed CIM is satisfactory.

### 4.3.3 Validation of CIM using residual volatile content in char

Typically, 95% of the volatiles present in the fuel particle is released during the devolatilization time determined by visual techniques like FET (Morris and Keairns 1979; Stubington and Sumaryono 1984). To validate the proposed visual technique, it is crucial to measure the residual volatile content present in the char obtained after the noted devolatilization time using this technique. The residual volatiles present in fuel chars obtained at the end of devolatilization in CLC (CIM) and air combustion environments (FET) are shown in Figure 4.6.

50
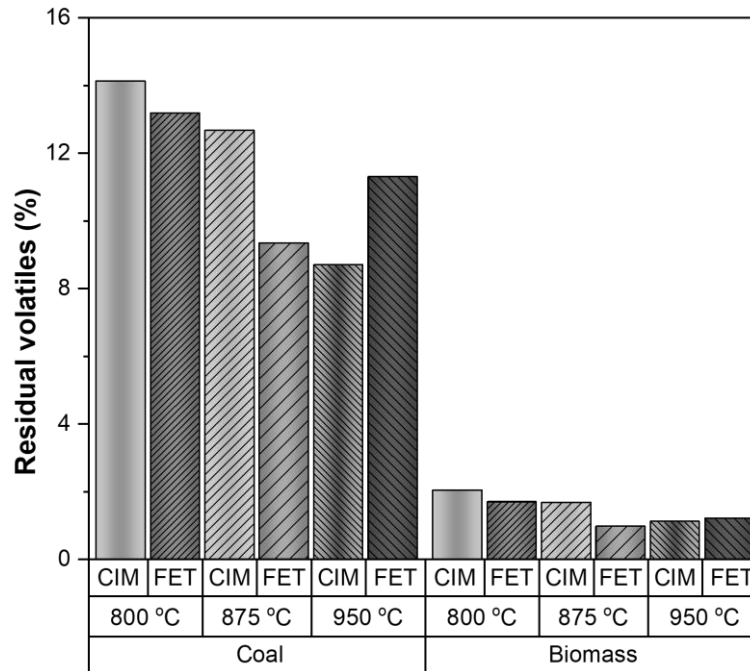
*Figure 4.6 Residual volatile content in char particles of coal and biomass as determined by TGA experiments.*

The residual volatiles present in char of coal and biomass particles is found to be decreasing with the increase in operating bed temperature. The residual volatiles found in the samples from FET method ranges from 9.3 to 13.2 % for coal and 0.9 to 1.7 % for biomass. Whereas the coal samples from CIM method have residual volatile content ranging from 8.7 to 14.1 % and for biomass samples, it is about 1.1 to 2 %. It is noticed that even the FET method yielded more residual volatiles (maximum volatile loss of only 90.7 %) for coal samples in contrast to the 95 % devolatilization definition. But at the same time, biomass samples have released more than 99.1 % of the volatiles present in them. It is also to be noted from Figure 4.6 that at 950 °C, the residual volatiles is lesser in the case of CIM which is probably due to the combined effect of steam and high temperature (Khan and Hshieh 1989).

For the particles studied by CIM, comparable results are obtained with a maximum volatile release of 91.3 % in coal samples and 98.9% in biomass particles during the devolatilization time. Moreover, the coals, particularly of bituminous types, are reported to form condensed volatile matter in char as much as 10% by weight (Kobayashi et al. 1977). Therefore, the observation of high residual volatiles (i.e. more than 5% of the total volatiles) in coal samples is expected naturally. But these methods

prove to conform well with the 95% devolatilization time definition for the case of biomass fuel particles. Hence, CIM can be regarded as an equivalent of FET for flameless conditions like CLC.

### 4.3.4 Validation of devolatilization time using particle mass loss history

An alternate way of validating the devolatilization time measurements obtained by CIM is by using the mass loss history of the particles during devolatilization in fluidized bed systems (Zhang et al. 1990). Figure 4.7 shows the mass loss history of coal and biomass particles respectively. It can be observed that the mass loss curve exhibits two different stages, namely (i) initial rapid mass loss (steep curve) and (ii) later very slow mass loss (near plateau).
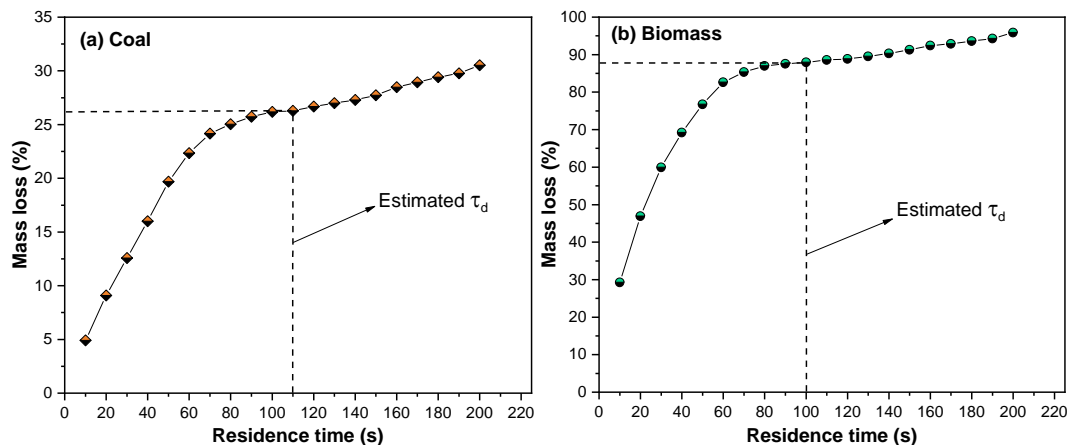


***Figure 4.7 Mass loss curves of (a) coal (14.25 mm) and (b) biomass particles (15 mm) at 950 ⁰C.***

The first rapid mass loss of the particle as indicated by the steep curve correspond to the mass loss due to loss of volatiles during devolatilization. At the end of the first stage, the fuel particle gets devoid (almost) of the volatiles. Followed by this, in the second stage, the mass loss is due to the slow conversion rate of char. This slow char conversion is indicated by a near plateau. The residence time at the inception of the plateau marks the end of devolatilization and can be inferred as the devolatilization time of the particle. The mass loss experiments of coal particles yielded scattered values because of the inhomogeneity among the coal samples used for the study. Averaged data points from repeat experiments yielded a smooth curve (Figure 4.7). But in the case of biomass, the curve is relatively smoother which is primarily due to the less non-uniformity in the composition of the different particles studied.

52

The devolatilization time of coal particles estimated from Figure 4.7 is around 110s, with about 93% of the total volatiles content released and that for biomass particles, it is about 100s, with about 98% of the total volatiles in biomass liberated. The observed average devolatilization time using CIM is about 108 and 104 seconds for coal and biomass respectively. Thus, it is found that devolatilization time obtained by CIM conducted at different temperatures compares well with the devolatilization time determined from the mass loss history study.

### 4.3.5    *Comparison of CIM using particle centre temperature measurements*

The particle centre temperature profiles of coal and biomass particles are presented in Figure 4.8, with the average devolatilization times determined using CIM marked by star notation. The obtained temperature profiles are in similar lines with the trends reported by Ross et al.(2000) for coal, and Di Blasi and Branca (2003) for wood particles. The devolatilization time of a fuel particle is calculated as the time at which the temperature of the particle centre matches the bed temperature (Ross et al. 2000). It can be observed that the devolatilization time determined by CIM is very close to the values determined using PCT measurements. The characteristic curves shown are obtained by arithmetic averaging of the data points from 3 repetitions. The slope of the curve gradually increases up to temperatures around 700 and 850°C respectively for 800 and 950 °C experiments and tends to decrease as it approaches the bed temperature. This change in the slope may be attributed to the completion of a major phase of volatile release which is followed by slow release of remaining gaseous products. The temperature profiles of wood particles show a shoulder in the curve and from that point, they follow a similar trend to that of coal particles.
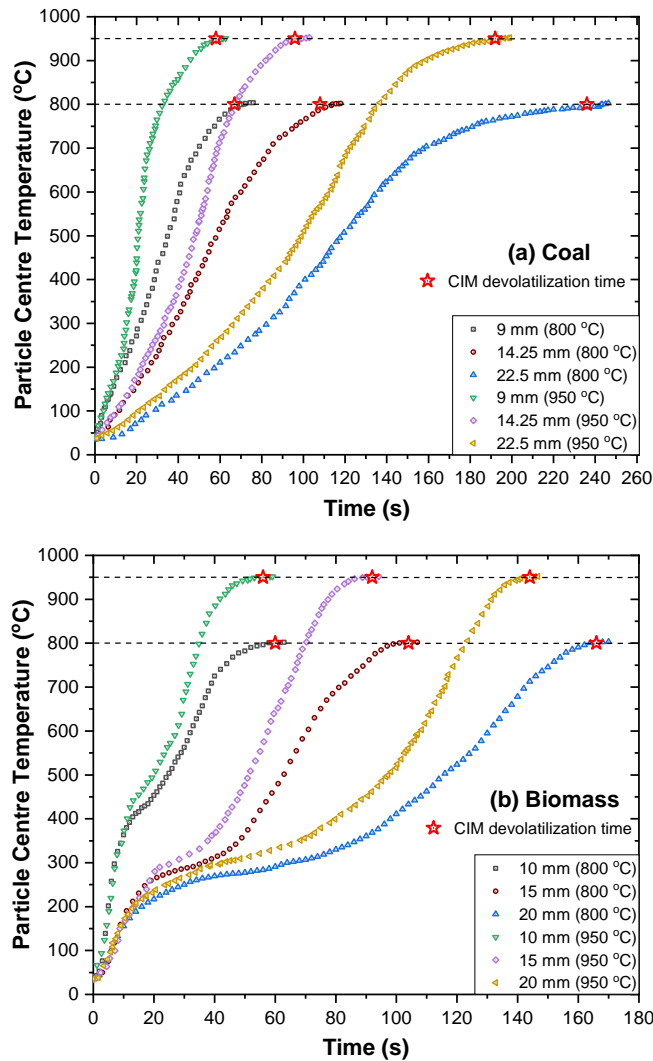
***Figure 4.8 Particle centre temperature profiles of (a) coal and (b) biomass particles
of three sizes at 800 and 950 °C.***

Table 4.1 compares the devolatilization time determined using CIM and particle centre temperature measurements. For coal particles, the deviation of devolatilization time as determined by CIM to that of PCT experiments ranges from -2.08 to -7.57%. For biomass particles, a positive deviation of PCT values is noticed in the range of +1.41 % to +3.70 %. This can be attributed to the low ash content and the porous nature of the wood particles, offering a relatively lesser resistance to heat transfer towards the particle core when compared to ash-rich coal particles.

54

*Table 4.1 Comparison of devolatilization times determined using CIM and PCT measurements.*

| Fuel - particle size | 800 °C | | | 950 °C | | |
|---|---|---|---|---|---|---|
| | CIM | PCT | Deviation (CIM to PCT) | CIM | PCT | Deviation (CIM to PCT) |
| **Coal** | | | | | | |
| +8-10 mm | 66 | 71 | -7.57 % | 58 | 61 | -5.17 % |
| +12.5-16 mm | 108 | 114 | -5.55 % | 96 | 99 | -3.12 % |
| +20-25 mm | 236 | 243 | -2.96 % | 192 | 196 | -2.08 % |
| **Biomass** | | | | | | |
| 10 mm | 60 | 58 | +3.45 % | 56 | 54 | +3.70 % |
| 15 mm | 104 | 101 | +2.97 % | 92 | 89 | +3.37 % |
| 20 mm | 166 | 163 | +1.84 % | 144 | 142 | +1.41 % |

From the comparisons made in Table 4.1, it can be inferred that the CIM devolatilization times are very close to the PCT devolatilization times with a maximum deviation of 7.57%. Thus, the CIM is found to produce comparable results to that of an accurate diagnostic technique and can be applied to determine the devolatilization time of large fuel particles at CLC conditions.

## 4.4 Closure

A new technique called 'Colour Indistinction Method (CIM)' for the determination of devolatilization times of coal and biomass in FB-CLC conditions is proposed, validated and compared with results obtained using similar methods, available in the open literature. The proposed CIM successfully determines the devolatilization time of different types of fuel particles, over a range of particle sizes at different bed temperatures. Hence, CIM is established as a valid, quick, easy and convenient technique for determining devolatilization times of fuel particles in FB-CLC environment as well as during the conversion of high moisture fuels even in oxidizing air atmospheres.

# CHAPTER 5

# 5   DEVOLATILIZATION STUDIES UNDER CLC CONDITIONS

## 5.1 Introduction

Devolatilization time of fuel is affected by parameters such as bed temperature, shape, and fuel properties. When devolatilization is accompanied by thermal fragmentation, it further influences the heat and mass transfer between the fuel and the reactor environment. It also becomes essential to study the effect of coal particle shape on devolatilization time, as the feed particles to industrial-scale combustors are irregularly shaped. This chapter deals with determination of devolatilization times and char yields of large fuel particles and analyses of the influence of operating parameters on them. The effect of particle sphericity of coal particles on devolatilization is also investigated.

## 5.2 Experiments

Devolatilization times of the fuel samples are determined by Colour Indistinction Method as detailed in Chapter 4. At the end of devolatilization, samples are retrieved using the basket technique and the individual samples are weighed. The char yield is defined as the ratio of the mass retained by the particle after devolatilization to the initial mass of particle introduced and the values are expressed in percentage.

## 5.3 Results and discussion

The devolatilization times ($\tau_d$) of various fuels tested are reported in this section and the operating parameters influencing devolatilization time are discussed in their order of influence (high to low). Generally, devolatilization of a fuel is controlled by the following processes in the combustor (Bliek et al. 1985; Oka 2003; Ross et al. 2000; Sasongko and Stubington 1996; Urkan and Arikol 1994), namely

i.   Intensity or rate of heat transfer from the surroundings to the surface of the fuel particle

ii.  Variation in thermal properties of the fuel which results in a temperature gradient within the fuel particle

iii. Kinetics of chemical reaction during devolatilization

iv.  Resistance to the mass diffusion from inside of the particle core towards the surface, through the porous structure in fuel.

The effect of temperature gradient and flow filtration on devolatilization can be noticed along with the changes in particle size. The effect of heat transfer intensity is associated with bed temperature variation. The influence of temperature gradient on the devolatilization process is also related to the fuel type, where density differences are the primary causes. The devolatilization time and the char yield of four different fuels with varying sample parameters (size, sphericity) at different bed temperatures are reported and discussed. Additional data points (of IC2 and BM) have been drawn from the previous chapter on CIM, for comparison purposes.

### 5.3.1 Effect of fuel type on devolatilization

The nature of fuel is the most significant factor influencing its devolatilization behaviour. The devolatilization times of different fuels of different sizes studied at different bed temperatures are given in Figure 5.1. Table 5.1 shows the magnitude of devolatilization time of fuels with their corresponding combination of mineral matter and volatile matter.

*Table 5.1 The magnitude of devolatilization time based on the composition of various fuels.*

| Fuel | Magnitude of devolatilization time | Composition (relative) |
|------|-----------------------------------|------------------------|
| IDC  | Highest | ● high VM, FC, and low MM |
| IC1  | High    | ● medium VM, FC and MM |
| IC2  | Low     | ● low VM, FC, and highest MM |
| BM   | Lowest  | ● highest VM and lowest FC, MM |

Note: MM – Mineral Matter; VM – Volatile Matter; FC – Fixed Carbon

Among the coal types studied, the fuel with the highest volatile content i.e. IDC takes more time to release the volatiles completely. Coals with higher volatile content have higher specific heat capacity (Table 5.2, Tomeczek and Palugniok (1996)), and this may be one of the reasons why IDC takes more time to acquire heat and devolatilize. Compared to other fuel particles, biomass particles rapidly devolatilize at any given temperature. This variation in the devolatilization time between coals and biomass is caused by the mineral matter and their effect on porosity of fuel particles,

i.e., more the mineral content, lesser the porosity i.e. more resistance to mass transfer and therefore, higher the devolatilization time. Specific to coals, the resistance offered by the mineral matter changes with respect to the level of porous network development, which is also dependant on the volatile content of the coal. As an example, the devolatilization time of the high ash IC2 is almost nearer to the value of IDC though there exists a big difference in the volatile matter content. This implies that, IC2 might not have developed a porous network upon volatile release, possibly owing to the existence of a rigid ash skeleton (refer Chapter 8).
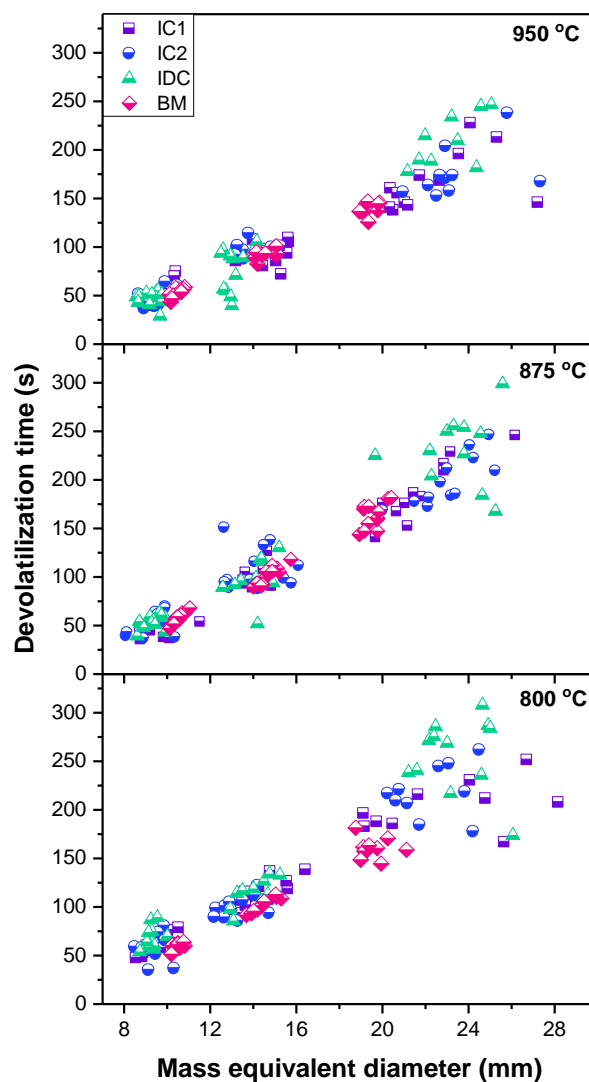


*Figure 5.1 Scatter plot of devolatilization time showing the influence of the fuel type at different bed temperatures.*

*Table 5.2 Heat of devolatilization of the fuels tested using TGA*

| Fuel | Heat of devolatilization ($Jg^{-1}$) | Net heat change |
|------|------|------|
| IC1 | 519.2 | Endothermic |
| IC2 | 247.5 | Endothermic |
| IDC | 328.3 | Endothermic |
| BM | 1477 | Endothermic |

Among all the fuel types studied, IDC has the highest devolatilization times, and biomass has the least devolatilization times for different particle sizes. From Figure 5.1, the following observations are made.

(i)    Fuel with a high mineral matter and volatile content take more time to devolatilize.

(ii)   Fuel with low mineral matter and high volatiles content devolatilize very quickly.

As mentioned earlier, for the fuels with low volatile content, a scattered pattern of devolatilization time is seen. The Indian coals are seen to have more scattered data points, which may be either due to the heterogeneity or the structural deformations leading to reduced devolatilization times. As expected, the IDC and biomass particles show less scatter in data points for a given size range, which can be explained by the relatively less heterogenous nature of the fuels. At 950 $^{\circ}$C, the scatter among the largest sized particles is reduced, which may be owing to the predominant crack formation or the fragmentation events occurring alongside the devolatilization process of the fuel particles. In addition to fragmentation, higher temperatures favour tar cracking (Stubington and Sumaryono 1984), resulting in a faster rate of volatile release.

### 5.3.2   Influence of particle size on devolatilization time

The devolatilization times of two Indian coals, Indonesian coal and biomass studied at three different bed temperatures, for various particle sizes are given in Figure 5.2. The dotted curves indicate the trend of devolatilization time with the increase in particle size. Across all temperatures studied, the coal particles have $\tau_d$ in the range of 23 to 89 s for +8-10 mm sizes, 56 to 139 s for +12.5-16 mm sizes and 102 to 309 s for +20-25

mm sizes. The biomass particles have $\tau_d$ of 44 to 68 s for 10 mm, 83 to 118 s for 15 mm and 126 to 182 s for 20 mm cubes.

All the coal types exhibit an increasing trend of devolatilization time with respect to particle size (represented in terms of particle diameter), irrespective of the bed temperatures studied (Figure 5.2). The particles in the smallest size range studied (9 mm) do not show much difference in their devolatilization time of the same/nearer particle sizes.
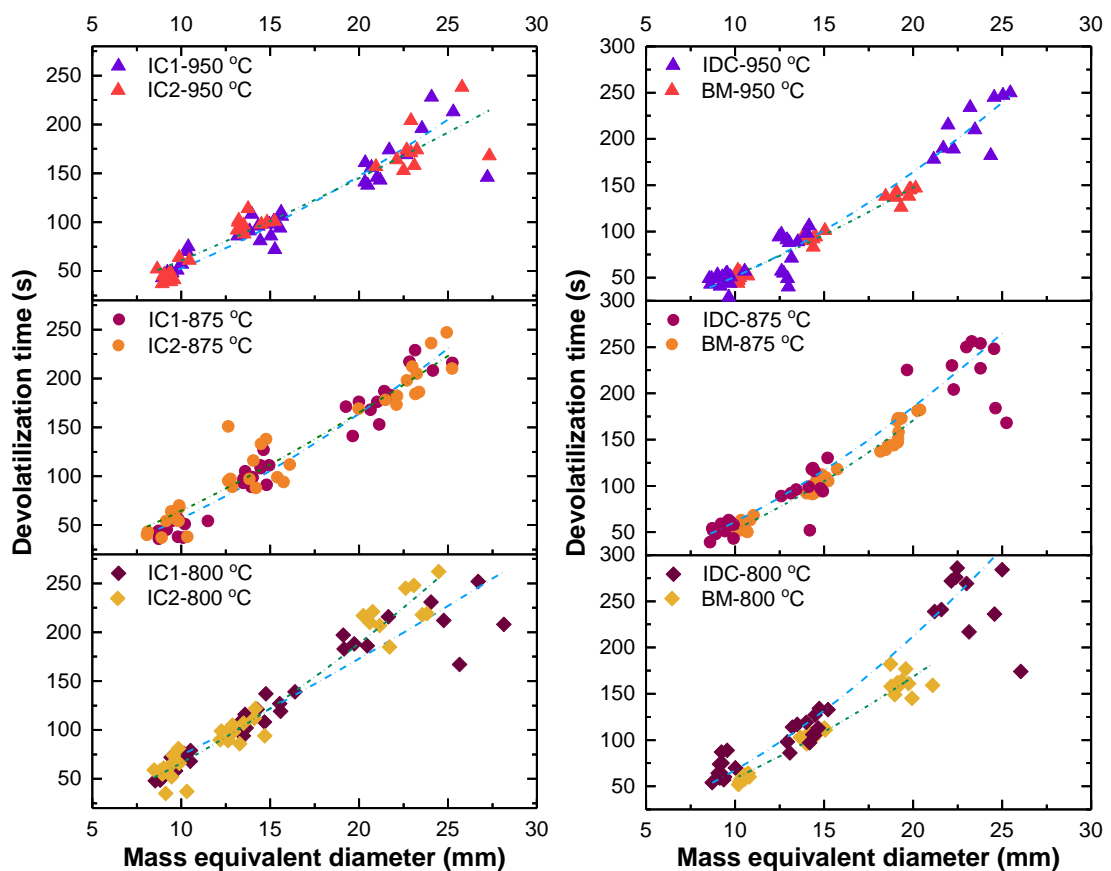


*Figure 5.2 Devolatilization times of different fuels with varying particle sizes.*

As the size increases, the spread (of datapoints in Figure 5.2) between the devolatilization times of the various samples of the same size range increases and observed to be highest in the case of largest particle sizes studied (22.5 mm). This spread is attributed to the effect of increased heterogeneity in the fuel samples.

The general devolatilization trend of the fuels tested under CLC environment (Figure 5.2) is similar to the case of the conventional FB combustion processes found in literature (Borah et al. 2010; Stubington and Sumaryono 1984), with respect to

changes in particle size and bed temperature. However, the order of magnitude of $\tau_d$ is relatively higher in CLC environment when compared to conventional air combustion (Figures 4.3 and 4.4). Particularly, the larger particles exhibit the advantage of gradual release of volatiles, as noticed by the increase in the slope of devolatilization trend line (Figure 5.2).

Comparison of devolatilization times of the Indian coals and Indonesian coal reveals a relatively larger scatter among the data points of Indian coals. This spread is due to the effect of different degrees of heterogeneity existing between the particles within the same size range. Heterogeneity among fuel particles within the same size range and across sizes may be due to one or more of the following characteristics of the fuels.

(i)     Difference in the amount of volatile matter present in individual particles.

(ii)    Distribution of mineral matter interspersed with the carbon framework.

(iii)   Structural variations developed during the formation of the fuel chunk.

Within the Indian coals, the coal with relatively higher volatile content (IC2) has a comparatively higher slope of the devolatilization trend, and the slope of IDC is the highest among the coals, which has the highest volatile matter among them. However, at the same time, biomass has a significantly different trend (relatively lower slope than IDC), despite having more volatiles. The difference in the rates of devolatilization is due to the relatively less dense and high porous nature of biomass. In detail, the volatiles generated at high temperatures in a biomass particle faces relatively less obstruction to get liberated, due to the porous nature of the fuel. Whereas, the denser coal particles have a gradual volatile release towards the surface of the particle due to the resistance to the mass transport created by the mineral matter as well as the fixed carbon matter, which makes them less porous.

The ratio of devolatilization time of the largest to the smallest sized particles is calculated using the devolatilization times at each bed temperature and the range of values are given (Table 5.3). The broader range of devolatilization time ratio of the largest particle to the smallest particle is found with IC1 and IDC has the least range. On average, the devolatilization time of coals increases by four to five folds when

particle size is increased from 8 mm to 25 mm. Biomass particles have a narrow range in the devolatilization time ratio and have about a 3-fold increase in devolatilization time with the increase in particle size from 8 mm to 25 mm.

*Table 5.3 The ratio of devolatilization times of largest to smallest particles tested across different bed temperatures*

| Fuel | Ratio of devolatilization time (largest to smallest size) |
|------|-----------------------------------------------------------|
| IC1  | 2.9 - 4.4 |
| IC2  | 4.4 - 5.7 |
| IDC  | 4.8 - 5.1 |
| BM   | 2.8 - 3.6 |

From these observations, it can be drawn that if a fuel has a broader range of this ratio, more the fuel heterogeneity and the effect of bed temperature. As Indian coals have wider ratios, they behave inconsistently and influences the reactor conditions, such as the rate of fuel feeding and ash retrieval, leading to tedious material handling. Relatively, the low ash biomass and IDC are easier to handle.

### 5.3.3 Effect of operating bed temperature on devolatilization

The effect of bed temperature on the devolatilization time of the fuels studied is presented in Figures 5.3 and 5.4. For all the fuels, the devolatilization time decreases with an increase in bed temperature, which is a trend observed in the literature on fuel devolatilization in conventional FBCs (Sasongko and Stubington 1996) as well as in CLC studies (Ge et al. 2015b; Mattisson et al. 2016; Niksa et al. 1985; Stainton et al. 2012) using micron-sized particles. The effect of bed temperature is evinced clearly with every type of fuel studied, being prominent in larger particles (in terms of actual values) when compared to the smaller ones. It implies that the high heat-transfer resistance offered by the fixed carbon and mineral matter is overcome by the increase in bed temperature.
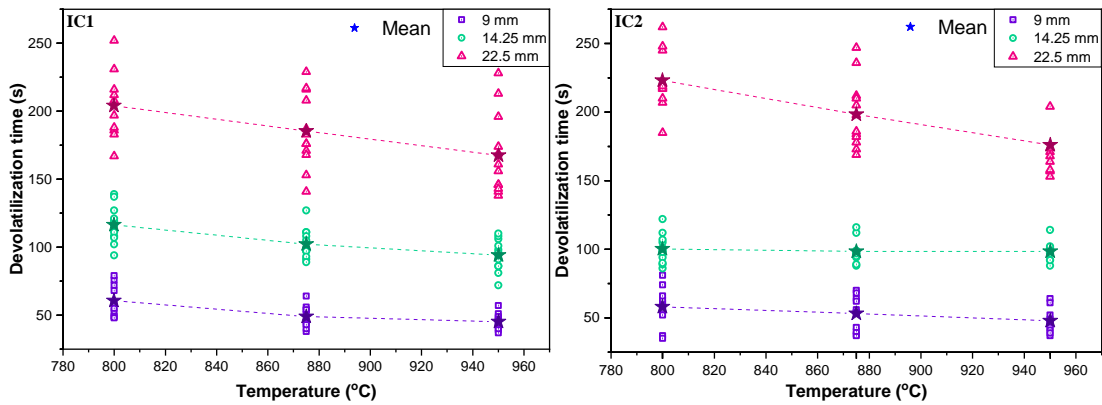
*Figure 5.3 Devolatilization time of IC1 and IC2 at different bed temperatures.*
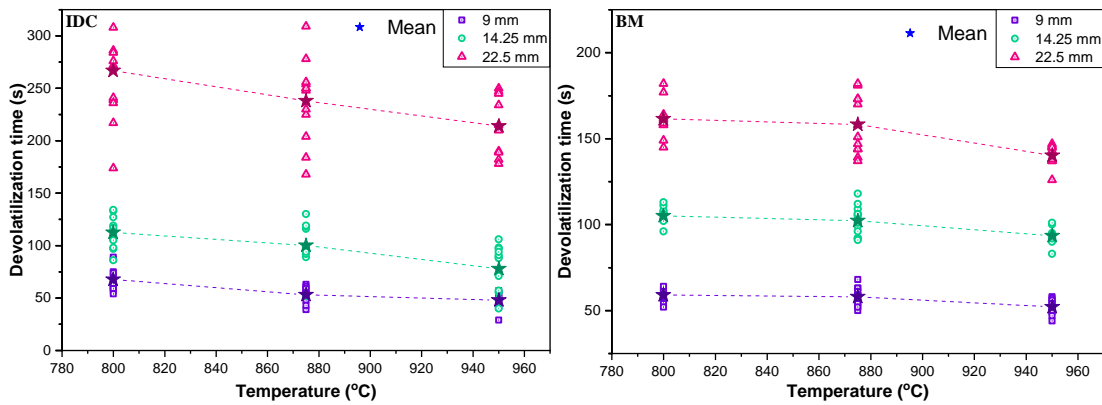


*Figure 5.4 Devolatilization time of IDC and BM at different bed temperatures.*

In terms of percentage reduction in $\tau_d$ with an increase in bed temperature from 800 to 950 ºC, biomass particles experience the least effect, having a reduction of only 10 to 14 % for all sizes. Coal samples show a decrease of 11 to 27 % in $\tau_d$ for smaller sizes (+8-16 mm) but a lesser reduction of 15 to 22 % in the case of the 22.5 mm particles. This kind of behaviour with coal particles is observed earlier in conventional combustion environments (Morris 1993), where the effect of bed temperature on volatile evolution is less pronounced in larger particles. This can be directly attributed to highly competitive volatilization reactions than the tar deposition over the sublayers of fuel particle core, at high temperatures (Bliek et al. 1985; Kobayashi et al. 1977). Partly, crack development in the larger particles can be a cause for this reduction. Influence of bed temperature is found to be slightly more in IDC particles (reduction in the range of 15 to 30 %) which is because of its low mineral matter.

During fuel devolatilization, two stages are known to be present (Oka 2003). In the initial phase, low-temperature reactions occur, leading to a huge and rapid evolution of volatile matter. This phase is followed by slow reactions when the particle attains a higher temperature close to the bed, resulting in a gradual release of hydrogen (Morris and Keairns 1979; Saxena 1990). When the particle sizes are large and thermally thick (Biot number > 0.1), the temperature gradient existing within the particle causes an overlap of the final stage of the devolatilization phase with the succeeding char conversion phase, during which small quantities of volatile gases continue to evolve gradually. Ideally, the devolatilization is said to be complete when the centre of fuel particle attains the bed temperature. For example, the heat-up times for 9 and 22.5 mm particles of IC2 to reach a bed temperature of 950 ℃ are found to be 59 and 189 s respectively, based on the Fourier number-based analysis (Redko et al. 2020). Whereas, the CIM measured devolatilization times corresponding to 9 and 22.5 mm particles are 48 and 171 s. On comparing the heat-up and devolatilization times, the overlapping period of the devolatilization and a possible char conversion phases is expected to be about 9.5-18.6% of the heat-up time. These findings reaffirm the thermally-thick property of the fuel particles and the dominance of internal heat-transfer processes during devolatilization.

### 5.3.4  *Effect of shape of fuel particles and fragmentation on devolatilization*

The coal particles, when crushed using jaw crusher before being fed to the combustors, produce particles of two groups based on shape (Figure 5.5), namely (i) near-rounded and (ii)flaky. Depending upon the coal type, they produce near-rounds and flakes in various proportions viz. flakes of 26 % in IC1, 34% in IC2 and 29% in IDC. Though the near-rounded ones form the larger group, it is essential to analyse the devolatilization performance of thin flakes, considering the vast quantities of coal used in thermal power stations.
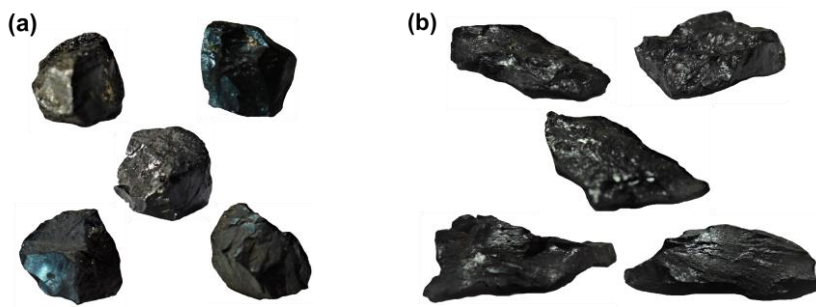
*Figure 5.5 IDC particles (+20-25 mm) exhibiting different shapes i.e. (a) near-rounded and (b) flaky.*
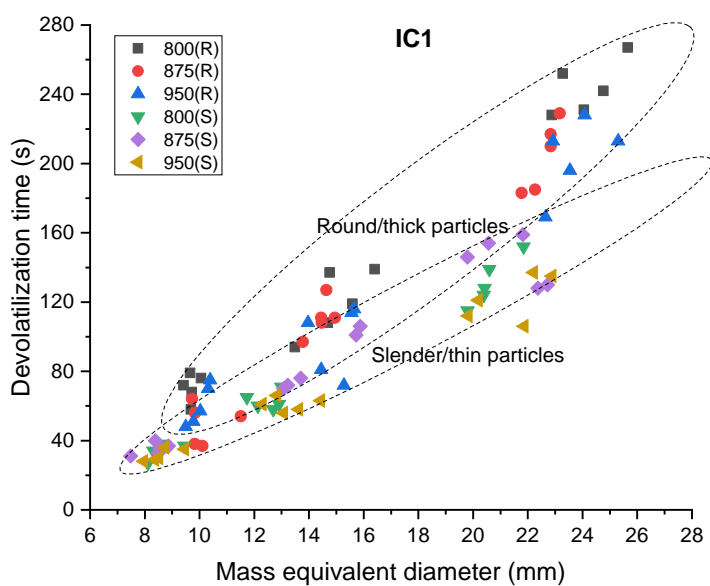


*Figure 5.6 Comparison of devolatilization times of near-rounded and flaky IC1 particles.*
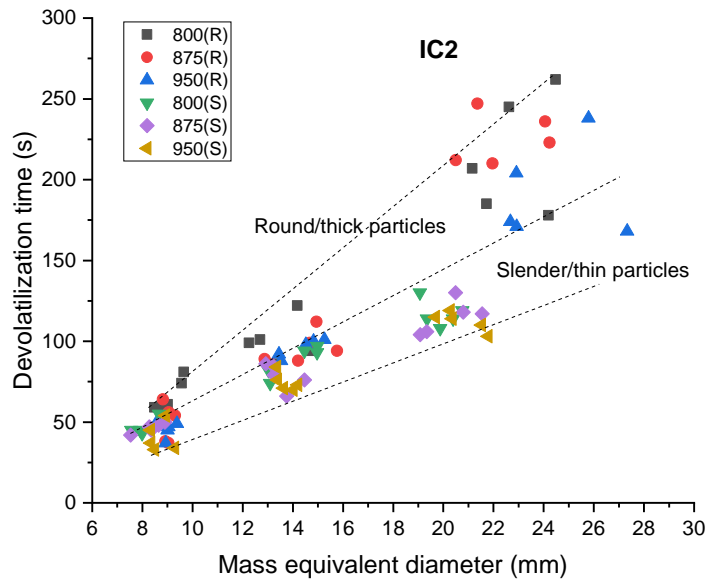
*Figure 5.7 Comparison of devolatilization times of near-rounded and flaky IC2 particles.*
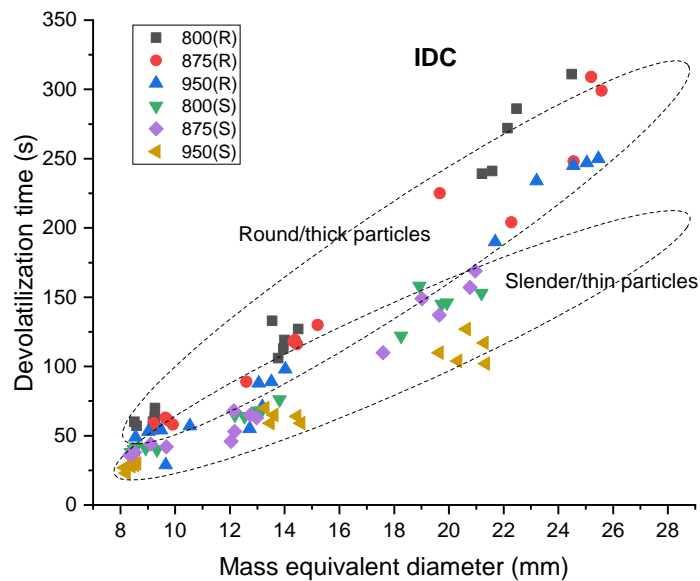


*Figure 5.8 Comparison of devolatilization times of near-rounded and flaky IDC particles.*

The devolatilization times of the near-rounded (R) and the slender flaky (S) particles are plotted in Figures 5.6, 5.7 and 5.8 for IC1, IC2, and IDC respectively. The near-rounded and slender particles produce segregated clusters of data points for all coals irrespective of particle size and bed temperature, as shown encircled in Figure 5.6 and 5.8. For the slender fuel particles in the +20 – 25 mm sieve range, the mass-equivalent diameters are found in the range of 17 to 23 mm because of their slender

forms. In the lower sieve ranges (+8 - 16 mm), the differences in the mass equivalent diameter of these two shape groups are relatively less.

The sphericity data of the coal samples estimated using the pressure drop data collected by permeation method in a fixed bed and applying the modified Ergun equation (Subramanian and Arunachalam 1980; Trahan et al. 2014) is shown in Table 5.4. The sphericity of near-rounded ones is in the range of 0.63 to 0.79, and that of thin flakes is found between 0.24 and 0.4, depending on the coal type and particle size.

*Table 5.4 Sphericity and surface area of the tested coal samples*

| *Sphericity of fuel particles* | | | | | | |
|---|---|---|---|---|---|---|
| | *+8-10 mm* | | *+12.5-16 mm* | | *+20-25 mm* | |
| *Coal* | *Near-rounded* | *Slender* | *Near-rounded* | *Slender* | *Near-rounded* | *Slender* |
| IC1 | 0.76 | 0.39 | 0.79 | 0.37 | 0.72 | 0.30 |
| IC2 | 0.69 | 0.35 | 0.73 | 0.26 | 0.63 | 0.24 |
| IDC | 0.71 | 0.40 | 0.74 | 0.35 | 0.76 | 0.31 |
| *Surface area of the fuel particles in mm²* | | | | | | |
| IC1 | 368 | 599 | 900 | 1495 | 2511 | 5650 |
| IC2 | 335 | 608 | 817 | 1599 | 2924 | 4951 |
| IDC | 371 | 565 | 704 | 1639 | 2520 | 4192 |

The $\tau_d$ of slender ones are 60% shorter (on average) than the near-rounded particles, which are 48-72% lesser in 9 mm, 52-79% in 14.25 mm, and 44-70% in 22.5 mm particles. The scatter in data points of IC2 slender particles is relatively very less than in IC1 and IDC, which might be due to either very low sphericity of IC2 flakes and their relatively uniform conversion or because of low particle-comminution. From the observations, slender flaky particles could impact the overall fuel conversion time in an industrial-scale continuous process, if their proportion in feed is significantly large. Since these flaky particles are observed to undergo lower comminution, the changes in the particle size distributions during the later stages of conversion would not be drastic. If near-rounded particles are of interest to the industrial scale operation, an

impact crusher could be used to generate particles with high sphericity, whereas a jaw or gyratory-type crusher could be used to generate flaky and elongated particles (Sims et al. 2019).

While modelling the particle heat-up time and devolatilization time, the particle sphericity needs to be accounted as it is known to alter the length of thermal diffusion. In a non-spherical coal particle, the shortest distance to the particle centre in the length scale of thermal diffusion is the height (in the direction perpendicular to bedding plane). For a near-rounded particle in the +20-25 mm size range, with a sphericity of 0.7 being related to particle length (15.75 mm) and the particle width being related to average sieve opening diameter (22.5 mm), the height is found to be 16.83 mm (on volumetric basis). Similarly, for a flaky particle in the same size group, the length, width and height respectively are 25.6, 20 and 25.6 mm. This resulted in a decrease of about 34 and 93% in the length of thermal diffusion of near-rounded and flaky particles correspondingly. While these particle dimensions are used for calculating the heat-up times using Fourier analysis, the near-rounded particle consumed 23% less time than the calculated value for a perfect sphere of 22.5 mm and 72% lesser for the flaky coal particles.
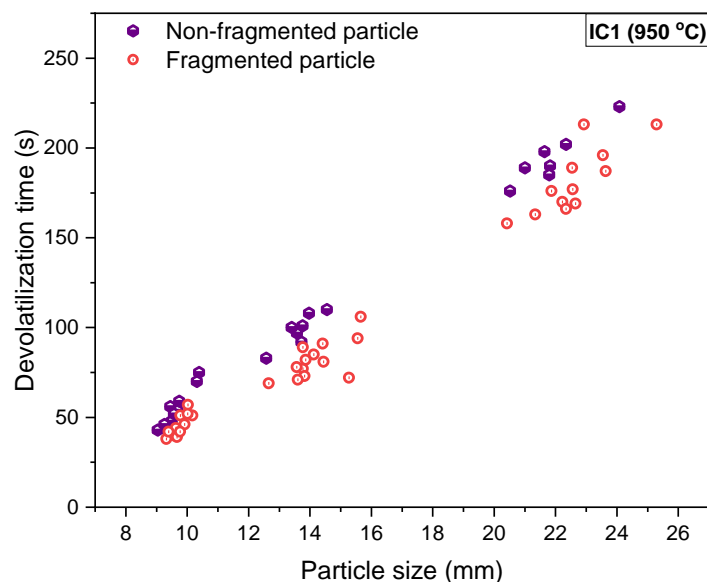


*Figure 5.9 Comparison of devolatilization times of fragmentating and non-fragmentating particles of IC1 at 950 ºC.*

For understanding the effect of fragmentation on devolatilization time, the case of IC1 is considered since it is reported to fragment more compared to the other two

coal types (Pragadeesh and Sudhakar 2018), resulting in widely scattered data points. Figure 5.9 compares the devolatilization times obtained for fragmenting and non-fragmenting particles. The fragmented particles are found to have lesser devolatilization time than the particles that do not fragment.

While the devolatilization process is in progress, the following events co-exist.

(i) Fragmentation of original fuel particle and consequent devolatilization of daughter particles at a faster rate.

(ii) Before the devolatilization is over, the daughter fragments (smaller ones) which eventually devolatilised will undergo char conversion process and may sometimes escape the reactor/basket.

(iii) The non-uniform crack formations across the particle structure, resulting in uneven conversion at different locations in the particle.

All these events influence the mass loss rate, consequently bringing down the devolatilization time. Among the coals, IC2 particles which are reported to fragment lesser (Pragadeesh and Sudhakar 2018), are observed to experience further low fragmentation in their slender forms, as seen from the less dispersed data points. Fragmentation events influence the particle residence time inversely and at the same time, they enable the availability of new surfaces for the subsequent char conversion by gasification in CLC. Thus, devolatilization time determination involving size changes due to fragmentation also becomes an important measurement for CLC using large-sized fuel particles.

### 5.3.5 *Char yield at the end of devolatilization*

Char yield is defined as the percentage of the fuel mass remaining at the end of devolatilization. Char yields for the fuels studied at different operating conditions are presented in Figures 5.10 and 5.11. The larger particles yield more char on average than the smaller particles at the end of devolatilization, due to the carbon deposition from extensive secondary reactions occurring at high pressures (Khan and Wang 2013; Saxena 1990; Yang et al. 2008). So, higher char yields are possible in cases of very low volatile matter, unavailability of the porous network extending to the surface and the intraparticle secondary reactions of condensation-polymerization. The char yields of 22.5 mm particles of all fuel types are almost equal to the difference of the initial weight

and the sum of proximate volatile content and moisture content. The smaller particles (+9-16 mm) show lesser char yield (below the dotted line in Figures 5.10 and 5.11) because of one of the likely causes of particle cracking or fragmentation events and the tar cracking at high temperatures (Stubington and Sumaryono 1984). On the other hand, particles show a high char yield than the sum of fixed carbon and ash, at lower bed temperatures.
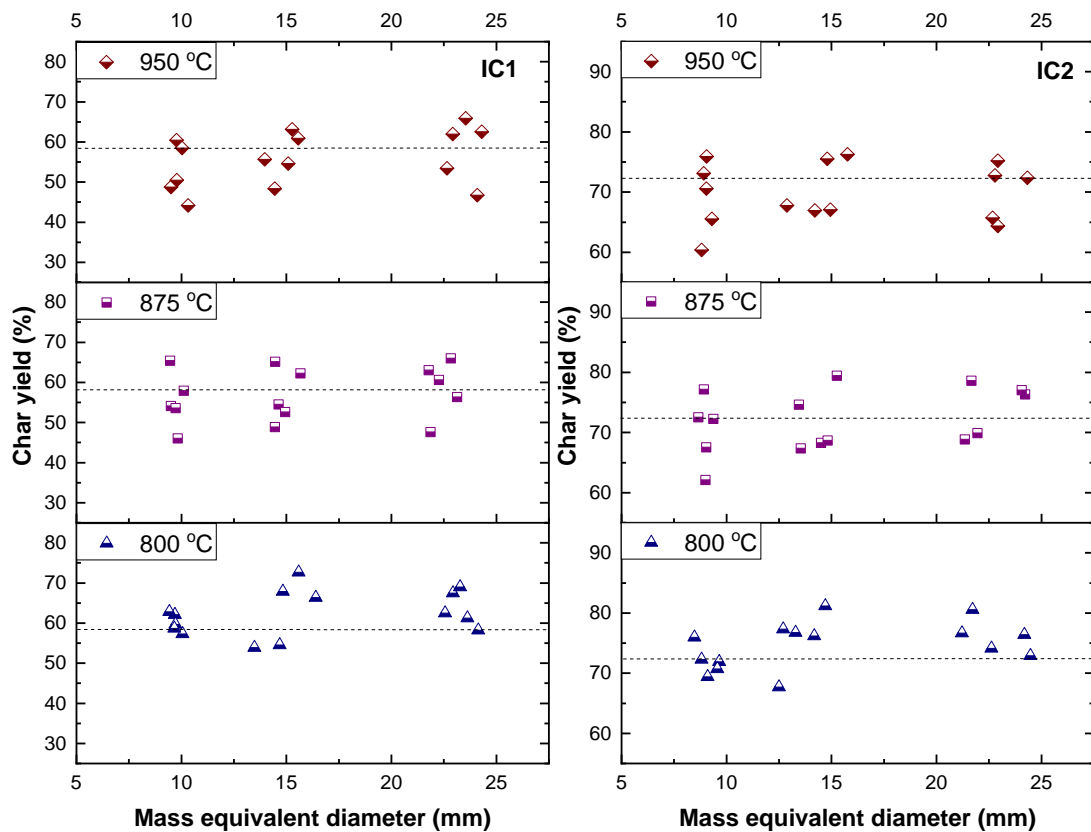


*Figure 5.10 Char yields of IC1 and IC2 of various particle sizes at different bed temperatures.*

IC2, when compared to IC1, shows a comparatively lesser impact of the increase in particle size over char yield. Two probable causes for this behaviour could be (i) the conversion of smaller particles in the air during the basket retrieval and quenching events (4-7s), (ii) incomplete release of volatiles from the innermost core of the larger particles. As observed from Figure 5.11, IDC and BM particles do not exhibit a remarkable influence of particle size on char yield. In the course of devolatilization, IDC particles tend to expand plastically, thus aiding the volatile release without much

obstruction. Similarly, biomass particles have good porosity compared to coal particles, resulting in relatively easier flow of volatiles irrespective of particle size.
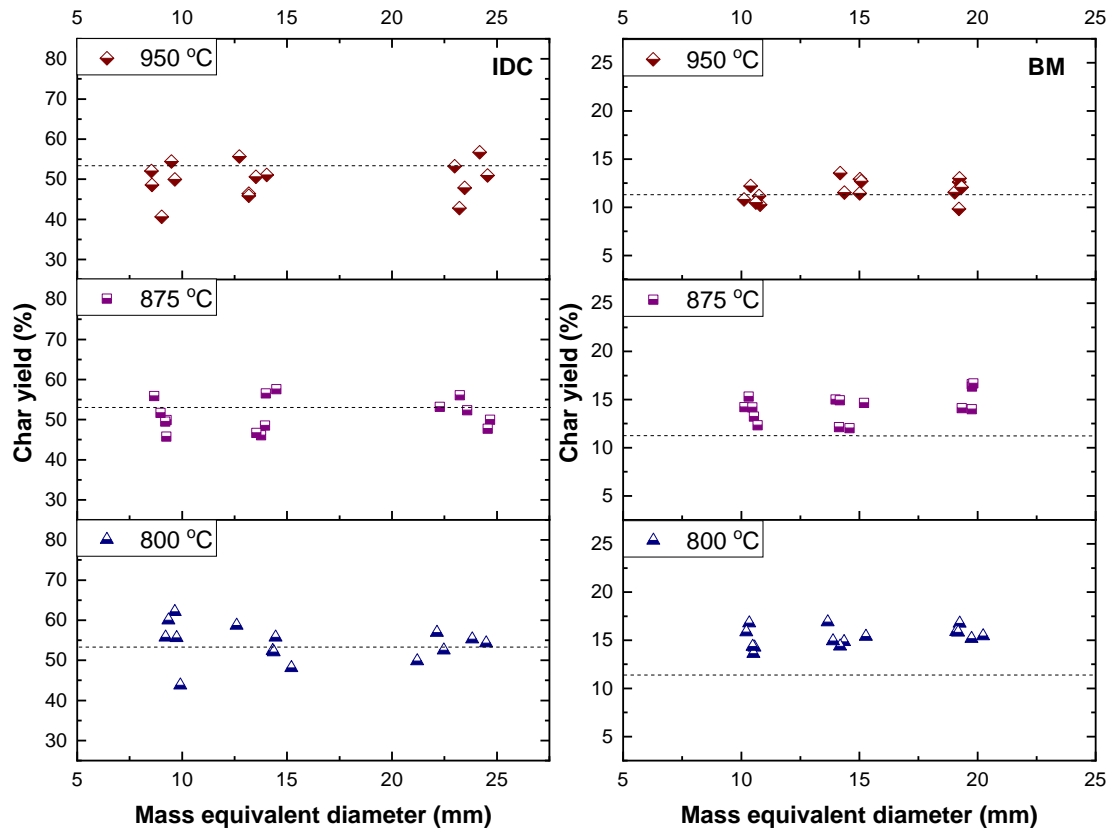


*Figure 5.11 Char yields of IDC and BM of various particle sizes at different bed temperatures.*

With the increase in temperature, the char yield is found to decrease for all fuels, ranging from a minimum of 3% to a maximum of 48 % depending on fuel type. However, this is in a bit contrary to the observation made by Borah et al.(2011), where the total volatile yield is invariable at a temperature above 727 °C in conventional air environment. Also, Di Blasi and Branca (2003) states that the effect of bed temperature on char yield becomes insignificant above 577 °C when devolatilized under nitrogen environment. The low char yield results in the present study can be corroborated by the char yields obtained by Xu et al. (2016) in oxy-steam environment. The presence of steam atmosphere affects the char composition in terms of formation of large aromatic rings by condensation of smaller aromatic groups (Xu et al. 2016). This process could possibly create free sites or voids in the char structure as earlier reported by Czechowski and Kidawa (Czechowski and Kidawa 1991), where the formation of mesoporous

72

structures and high surface roughness in char are noticed. This would further increase the volatile release rate at higher temperatures and as a result, shorter devolatilization times are noticed. Additionally, the consumption of smaller aromatic groups getting consumed is also likely, which could lead to a lower char yield. Thus, the influence of fluidizing medium on char yield is evident, and the char yield decreases with increasing bed temperatures in the iG-CLC environment.

In addition, higher volatile yields and thus low char yields are favoured by lesser tar deposition(Bliek et al. 1985) or tar cracking in internal layers of the fuel particles at high temperatures(Yang et al. 2008). Char yields are almost equal to their corresponding sum of fixed carbon and ash (as determined by proximate analysis) for all coals and biomass at 875 and 950°C respectively. Char yields of BM particles are clearly well above the sum of proximate fixed carbon and ash at 800 °C, probably due to tar deposition. The yield tends to decrease with the increase in bed temperature. At 950 °C, biomass is fully devoid of carbon deposition due to the cracking of tar into lighter molecules (Yang et al. 2008).

### 5.3.6   Effect of fuel shape on char yield

Since the fuel shape influences the devolatilization time, it is more likely to affect the char yield. The char yield data points for the near-rounded (R) and slender (S) particles are populated for each coal type, and the scatter plots are shown in Figure 5.12.

IC1 is the only coal type which exhibits a difference in char yield when the shape of the subjected coal particle changes (Figure 5.12). The primary cause could be the non-fragmenting nature of the thin flakes of IC1, unlike the near-rounded particles. The slender ones have about 15 to 20 % higher yield of char than the near-rounded particles. In the case of IC2, this kind of observation is less probable, since the near-rounded particles themselves do not undergo extensive fragmentation (Pragadeesh and Sudhakar 2018). Similarly, the difference in char yields between these two shapes is not noticed in IDC primarily because of the coal's plastic expansion during devolatilization regardless of the particle size.
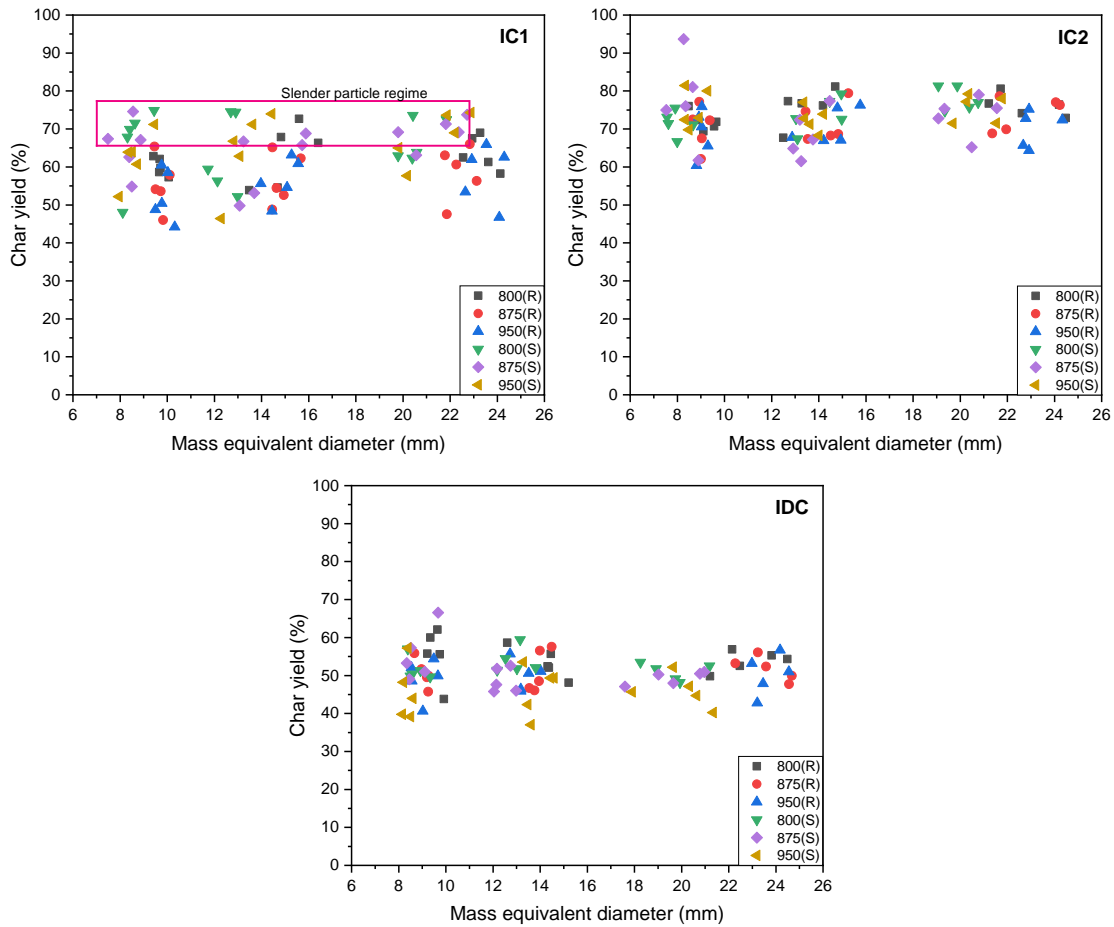
***Figure 5.12 Comparison of char yields of near-rounded and slender coal particles.***

The influence of particle size over the char yields of Indian coal flakes is noticed, whereas, IDC shape groups are not significantly affected by size changes. As observed in near-rounded ones, the char yield of these slender particles is maximum in the largest size tested. The effect of operating bed temperature is seen only in the Indonesian coal particles, i.e., char yields decrease with the increase in temperature. Therefore, the shape effect on char yield depends on the fuel type studied.

### 5.3.7  *Correlation of devolatilization time*

For conventional combustion conditions, the correlation provided in the literature (Ross et al. 2000; Stubington and Linjewile 1989; Zhang et al. 1990) represents devolatilization time as a function of only the particle size, in the form of Equation 5.1.

$$\boldsymbol{\tau_d = A.d_p^i}\dots\dots\dots\dots\dots\dots\dots..\dots\dots\dots\dots\dots\dots\dots.(\boldsymbol{5.1})$$

A new correlation embodying the effects of other parameters such as temperature and particle shape is presented in the form of Equation 5.2.

$$\tau_d = A.d_p^i.T^j.\varphi^k \ldots\ldots\ldots\ldots\ldots\ldots\ldots\ldots\ldots.(5.2)$$

where A is the proportionality constant accounting for the effects of transient heat and mass transfer within the particles as well as the devolatilization kinetics(Solimene et al. 2012), $d_p$ is the particle diameter in mm, T is the operating bed temperature in Celsius, and $\varphi$ is the sphericity of fuel particles and i,j,k are the exponents of the respective parameters. Since cube-shaped biomass particles are only investigated in the present study, the sphericity parameter is not included during the calculation for biomass. The correlation values are given in Table 5.5 for all the fuels studied, which cover three particle sizes, three bed temperatures and two different particle shapes for each coal. Correlations of devolatilization time for the coals and biomass under iG-CLC conditions are given as Equations 5.3 and 5.4 respectively.

$$\tau_{d,Coal} = 10421.d_p^{1.536}.T^{-1.266}.\varphi^{0.376}\ldots\ldots\ldots\ldots\ldots\ldots\ldots.(5.3)$$

$$\tau_{d,Biomass} = 293.d_p^{1.615}.T^{-0.799}\ldots\ldots\ldots\ldots\ldots\ldots\ldots\ldots.(5.4)$$

*Table 5.5 Values of correlation parameters for determining devolatilization time of different fuels*

| Fuels | A (Proportionality constant) | i (size factor) | j (temperature) | k (shape factor) | Coefficient of determination , $R^2$ |
|---|---|---|---|---|---|
| IC1 | 2449 | 1.489 | -1.042 | 0.349 | 0.959 |
| IC2 | 19997 | 1.39 | -1.298 | 0.362 | 0.956 |
| IDC | 9831 | 1.666 | -1.303 | 0.4 | 0.966 |
| BM | 293 | 1.615 | -0.799 | - | 0.973 |
| All tested coals | 10421 | 1.536 | -1.266 | 0.376 | 0.945 |

The constant A varying between 293 and 19997 seems to be an intrinsic property specific to each type of fuel and shows how strong is the intraparticular heat and mass transfer resistance and inversely represents the devolatilization kinetics. Indian coal

IC2, which is known to have the highest density, has the highest A value and exhibits a strong negative influence of bed temperature on devolatilization time.
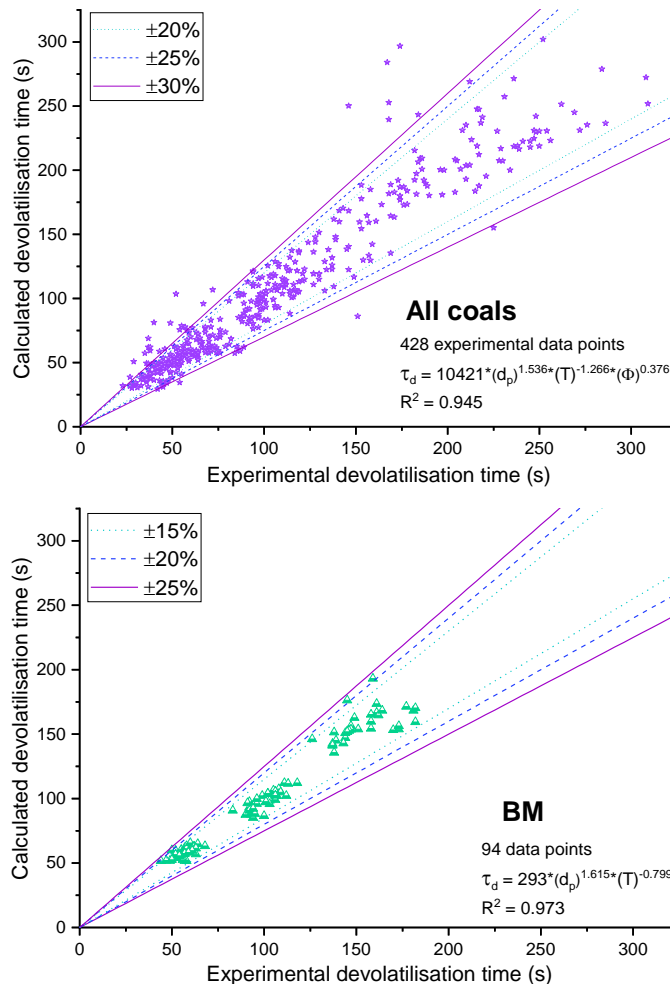


*Figure 5.13 Comparison of experimental and calculated values of devolatilization time of all coals and biomass tested in this study.*

Indonesian coal has the highest exponents for all the operating parameters, making it the most influenced fuel by the operating parameters. This implies that the combustion rate of IDC can be easily controlled by changing the operating conditions. Biomass particles with the least A and j values have the least resistance to heat and volatile transport across the particle. The power law correlations given as Equations 5.3 and 5.4 successfully fit the devolatilization times of various fuels at different operating conditions with a minimum $R^2$ value of 0.945 and 0.973 for coals and biomass respectively. Parity plots comparing the experimental and calculated values are given as in Figure 5.13 for coals and biomass. About 92.5% of the calculated data points are

within ±25% deviation from the experimental values. Most of the data points outside the 25% deviation line are found to be overestimated/underestimated values by the correlation, particularly for the +8-10 mm size range. Calculated values for larger particles are found to match well with the experimental data points. For devolatilization conditions in air, Prins et al. (1989) states that earlier researchers defined 'i' values varying from 0.3 to 1.8, whereas Agarwal et al.(Agarwal et al. 1984) defines i=2 (i.e. $d_p^2$ ) for coal particles larger than 1 mm and later they recognized that $d_p^2$ relation can be applied only for the case of external heat transfer controlled devolatilization. As commonly reported, the exponents of particle size ('i') in CLC conditions are found in the range of 1.39 to 1.66.

The values of intrinsic constant 'A' for conventional air combustion studies range between 1 and 6 (Solimene et al. 2012; Stubington et al. 1992). Since other influencing parameters such as temperature and sphericity are incorporated in the present correlation and the tested environment is CLC, 'A' becomes a sensitive and large value (specific to fuel type) among other correlation parameters. Calculated devolatilization times of biomass particles match very closely with measured values, i.e., more than 95% of the values lie within ±15% deviation zone. Thus, particle size is the most influencing parameter followed by operating bed temperature and sphericity, in the order of magnitude of effect.

## 5.4 Closure

The devolatilization times of various sized fuel particles at different operating bed temperatures are determined using CIM and their respective char yields are determined. New correlations for devolatilization time as a function of particle size, bed temperature and sphericity are developed separately for coals and biomass for a wide range of parameters. With further understanding of the associated events of fuel conversion such as primary fragmentation, char conversion and secondary fragmentation, the largest size of a particular fuel for its application in a continuous CLC process can be established.

# CHAPTER 6

# 6 THERMOPHYSICAL BEHAVIOUR OF FUELS DURING DEVOLATILIZATION UNDER CLC CONDITIONS

## 6.1 Introduction

Essentially, the thermophysical behaviour is characterised by the evolution of particle geometry caused by comminution and the volumetric changes such as swelling or shrinkage. Comminution during the devolatilization phase of fuel conversion is considered to be critical (Paprika et al. 2013; Senneca et al. 2009; Stubington and Moss 1995), since it affects the particle size distribution in the reactor and the conversion rates. Fragmentation during the devolatilization phase is termed as primary fragmentation.

The significance of primary fragmentation lies in the timing of fragmentation events wherein the particles fragmenting earlier during devolatilization are expected to have high conversion rates due to the generation of new surface area. Fragmentation of fuel particles immediately after the introduction into the combustion environment has been attributed to the thermal shock or stress created by the temperature gradient (Dacombe et al. 1999; Krishnamoorthy et al. 2017; Senneca et al. 2017b; Zhang et al. 2002), which often result in a large number of fragments. Fragmentation events occurring in later stages of devolatilization are due to the mechanical stresses created by the evolution of volatile matter at high temperatures (Chirone and Massimilla 1989; Dakic et al. 1989; Paprika et al. 2013). Primary fragmentation behaviour depends on the volatile content and the mechanical strength of the coal particles (Chirone et al. 1991), as well as the operating parameters such as particle size and temperature. The compressive strength and the porosity of the individual coal particles help in understanding the initiation and the extent of fragmentation (Dacombe et al. 1999; Syred et al. 2007). In literature, primary fragmentation of various solid fuels have been widely studied in conventional air fluidized bed combustion environments (Chirone et al. 1988, 1991; Chirone and Massimilla 1991; Cui et al. 2015; Kosowska-golachowska 2010; Prins et al. 1989; Stubington and Moss 1995), using irregular shaped fuel particles and sand as the bed material (Chirone et al. 1982; Chirone and Massimilla 1991; Dakic et al. 1989; Prins et al. 1989; Stubington and Linjewile 1989; Sundback et al. 1984). As opposed to conventional combustion environments, the use of steam as

fluidization medium in CLC is expected to influence the fragmentation and favourably the char reactivity (Khan and Hshieh 1989). Steam could probably modify the pore structures, which would alter the fragmentation behaviour of fuel particles in the CLC environment. In this chapter, the primary fragmentation behaviour of the fuels is investigated and related to their compressive strength and porosity (in terms of Pore Resistance Number), indicating their degree of influence. Additionally, the volumetric changes in the fuel particles are analysed.

## 6.2 Experiments

The primary fragmentation characteristics of the fuel particles tested are determined at different residence times during devolatilization, as described in Chapter 3. To understand the relation between the number of fragments and mechanical strength, compressive strengths of coal and biomass samples are tested using a computerized Universal Testing Machine (Shimadzu AG-X plus – 100 kN) at a loading rate of 1 mm/min. Since shaping the fuel particle creates cracks in the microstructure, and alters the compressive strength, fuel particles are tested without shaping, which is a more realistic approach (Zhong et al. 2014). Except for wood particles, particles of other fuels are used in irregular forms. The compressive strengths of coal samples are tested in the direction perpendicular to the bedding plane, whereas for the biomass, it has been tested along the grain direction. Compressive strength (stress) has been calculated following a similar procedure reported by Zhong et al. (2014).

## 6.3 Results and discussion

The results of the primary fragmentation behaviour of four types of fuels are expressed in terms of percentage of fragmentation, number of fragments, frequency of fragmentation, timing interval of fragmentation events, fragmentation index, and particle size distribution of fuel particles.

### 6.3.1   Percentage of fragmentation events

The percentage of fragmentation events (PF) gives information on the probability of the fragmentation event to occur and is defined by Equation 6.1.

$$PF = \frac{Number\ of\ particles\ that\ fragmented}{Total\ number\ of\ particles\ studied\ for\ fragmentation} * 100\ \% \ldots\ldots\ldots\ldots(6.1)$$

Figures 6.1 and 6.2 show the percentage of fragmentation events for different fuels studied at different operating conditions. The percentage of particles that undergo fragmentation during devolatilization increases with the increase in temperature for all the fuel types studied. This behaviour may be attributed to the thermal shock experienced by the particle. Fragmentation percentage is found to raise with increase in particle diameter (Dacombe et al. 1999), but with few exceptions.
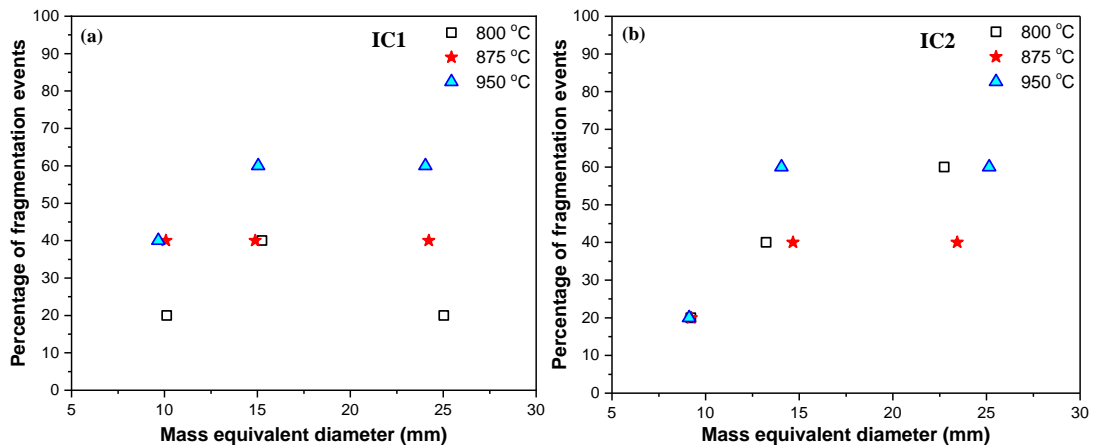


*Figure 6.1 Percentage of fragmentation events of (a) IC1 and (b) IC2.*
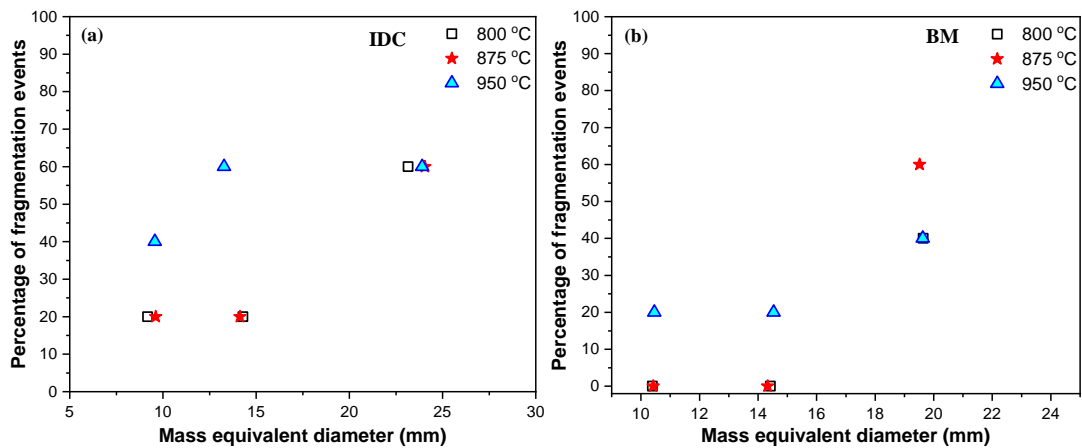


*Figure 6.2 Percentage of fragmentation events of (a) IDC and (b) BM.*

As larger fuel particles have higher temperature gradient compared to that of the smaller ones (Syred et al. 2007), the effect of particle size on PF is significant. Thus, a larger fuel particle experiences more thermal shock (Dacombe et al. 1999) and this phenomenon is closely related to the fuel's homogeny. Figure 6.3 illustrates the differences in heterogeny between a small and a large particle of IC2 coal. Cross-section of the sample shows that the number of stripes (layers of coal formation) are more in a large particle. Another side of the sample shows an interspersed pattern of

grey and white matter. The stratified structure of coal, as well as different zones of conversion, offers thermal resistance to heat transfer, and at each layer, the thermal conductivity and thermal expansion co-efficient continue to change(Chern and Hayhurst 2006; Dacombe et al. 1999; Paprika et al. 2013; Zhong et al. 2018). Thus, it may result in increased thermal stress, making the particle susceptible to failure at high temperatures.

It means if a fuel particle has non-uniformity in structure and composition, then with the increase in particle size, the non-homogeneity gets compounded, resulting in increased thermal stress (Stanmore et al. 1996). Finally, the particle tends to crack severely and produce daughter fragments. If the particle is more homogenous, the effect of particle size is less pronounced. This can be substantiated by the results of relatively more homogenous and non-homogenous fuel particles i.e. biomass particle and coal particle respectively. As known, the coal is a complex formation compared to the woody biomass whose composition is relatively more consistent. The non-homogenous compostion of coals results in deformations in particle structure due to devolatilization reactions, as an example, the white stripes featuring in IC2 particles (Figure 6.3) are found to be the zone of volatile release and tend to disintegrate with an initial crack formation along this plane.. Particles of all coal types have a minimum of 20% to a maximum of 60% chances of fragmentation, where the maximum chances are most likely at higher bed temperatures.
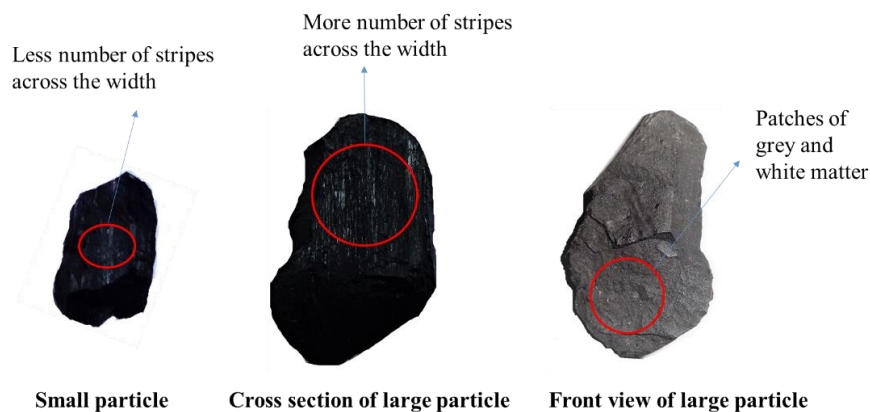


*Figure 6.3 Heterogenous formation in a coal fuel (IC2).*

Dacombe et al. (1999) noted that the particle's propensity to fragment increases with the increase in fixed carbon and mineral matter of the fuel. Indian coals behave in

line with this observation, as evidenced from Figure 6.1. They fragmented more severely than other fuels in this study. Among the coal types, IC1 is found to have the maximum probability of fragmentation, since particles in all sizes fragment. Figure 6.4 shows the surface morphology of coal particles, where the homogeneity is mapped to uniform and shining texture. IC1 particle appears shiny but has a rough texture (showing weakness in structure), IC2 has uniform texture but non-shiny and also patches of white and grey spots showing the heterogenous nature. The IDC particle is both shiny and has an even texture (possibly due to its high vitrinite). IDC particles are relatively less likely to fragment, and this property is owing to the fuel's composition and homogenous nature (Figure 6.4). Similar observations, to that of IDC, are made with the highly porous biomass samples, whose 10 and 15 mm particles do not fragment at low temperatures.
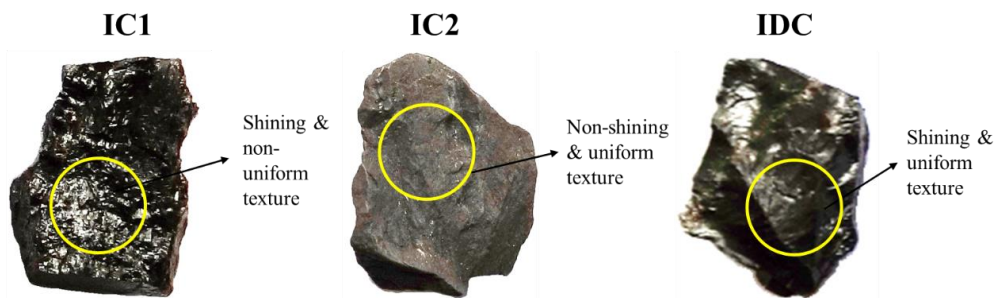


*Figure 6.4 Morphology of cross-sections of coal particles.*

*Table 6.1* **Pore resistance number (PRN) of fuels used in this study**

| *Fuel* | *Pore Resistance Number* | *Critical diameter (mm) for fragmentation by definition of Dakic et al. (1989)* | *Minimum particle size (mm) to get fragmented (Present experiments)* |
|---|---|---|---|
| Indian Coal 1(IC1) | 4.08 | 7.41 | 8 |
| Indian Coal 2 (IC2) | 5.15 | 6.19 | 8 |
| Indonesian Coal (IDC) | 6.412 | 5.48 | 8 |
| Biomass (BM) | 8.96 | 4.46 | 20 |

Dakic et al. (1989) relate the pore resistance number (PRN) with the critical diameter of fragmentation. PRN of a fuel is defined as the ratio of the volatile matter

content to the equilibrium moisture content. Critical diameter ($D_{crit}$) is defined as the diameter of the largest particle for which the probability of fragmentation (PF) is least or nil. In the present study, PF corresponding to $D_{crit}$ is experimentally found to be 10% or even less for IC2, IDC, and it is nil for IC1. With no exceptions to the PRN relationship with critical diameter for fragmentation, all fuel particles of sizes larger than the defined critical diameter (Table 6.1) are seen to have fragmented. However, PRN relation may not always assure 100 % chances of fragmentation.

### 6.3.2 Number of fragments

The number of fragments (NF) or particle multiplication factor or fragmentation ratio can be defined as the ratio of the number of particles at the end of devolatilization or at specified residence time to the initial number of particles (Equation 6.2).

$$NF= \frac{Number\ of\ particles\ present\ at\ a\ specified\ residence\ time}{Number\ of\ particles\ introduced\ initially\ into\ the\ combustor} \dots\dots\dots\dots\dots(6.2)$$

Since the present study deals with single-particle experiments, NF is directly the particle count at a particular residence time. If a particle does not fragment, the number of fragments remains one; when a particle fragments, the number of fragments would be a minimum of two. The effects of operating parameters on the number of fragments of various fuel particles at different residence times during devolatilization can be interpreted from Figures 6.5 and 6.6. The data points represent the average number of fragments at that specified residence time. Also, considering the stochastic nature of the fragmentation phenomenon, each of the data points is marked with bars, indicating the minimum and maximum NF obtained at that particular residence time. Among the different kinds of fuels, namely coal and biomass, it can be observed that at all bed temperatures and particle sizes, the NF generated by coals are higher than biomass.

Coals used in this study typically generated up to 6 fragments on an average, during the course of devolatilization, while the biomass particles generated less than 3 fragments under various conditions of operation. Biomass, compared to coal exhibited a very consistent fragmentation behaviour, as can be seen from Figures 6.5 and 6.6. The biomass particles hardly fragment and only the 20 mm particles are found to produce fragments of an average count of 3. This considerable difference in the behaviour between coal and biomass can be attributed to their difference in fuel properties namely

porosity, thermal conductivity and particle density (Coal: 1300 to 1900 kg/m$^3$, Wood: 800 kg/m$^3$). Coal with relatively higher density (1900 kg/m$^3$) and lower porosity (5-10 %), tend to fragment severely (Kosowska-Galachowska et al. 2009) than biomass. Also, the thermal diffusivity of the coals (about $1.5*10^{-7}$ m$^2$/s) differs considerably from biomass (about $4*10^{-7}$ m$^2$/s), which is an important reason for their different fragmentation behaviour. The fragment count in conventional combustion is comparably higher than that in the present case (for higher sizes at 950 $^o$C), even at lower bed temperatures of 850 $^o$C (Sudhakar et al. 2008). This indicates a noticeable effect of the fluidization medium/combustion environment on the fragmentation phenomenon.

Among the different coals studied, IC1 displayed a consistent trend of increase in number of fragments with the increase in residence time in the combustor. While IC2 and IDC occasionally deviated from their behaviour slightly at certain residence times. For instance, consider the case of IC2 of 20-25 mm at 950 $^o$C in Figure 6.5, the NF decrease gradually with increasing residence time, which appears counter intuitive. However, this gradual decrease can happen due to the following reasons.

(i)  Fragments generated in a previous quarter may generate relatively smaller fragments in the following quarter, of sizes small enough that elutriates out of the basket/bed, resulting in complete loss of original small fragments.

(ii)  Coals in specific, during different quarters of devolatilization, especially in the later quarters (3$^{rd}$,4$^{th}$) generate large number of very small fragments (flakes $\approx$ 2 mm) which are not considered for NF, thus decreasing the NF in the later quarters of devolatilization. However, the mass of these smaller fragments generated is taken into account for other relevant parameters, e.g. conversion calculations.
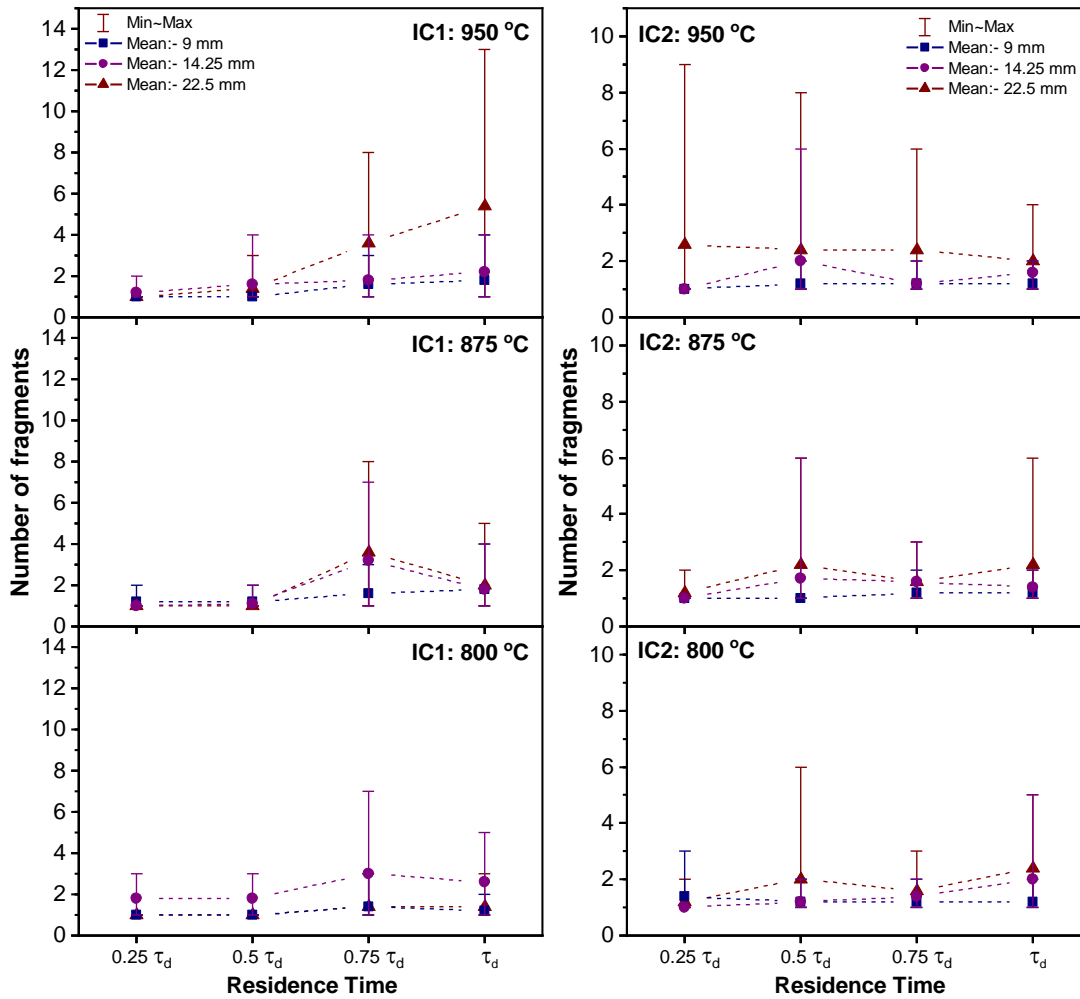
*Figure 6.5 Number of fragments of IC1 and IC2 observed at different residence times during devolatilization.*

IC1 particles of 22.5 mm generated a maximum of 13 fragments at 950 °C and the average NF is 6. The smaller sized particles of 9 mm and 14.25 mm yielded an average of around 2 and 3 fragments respectively. The IC2 particles of 22.5 mm size produced 9 fragments at the maximum, while the averages lie in the range of 2 to 3. Indonesian coal (IDC) particles of largest size generated a highest count of 8 fragments with averages between 2 and 4, and the smaller particles have 1 to 2 particle fragments.
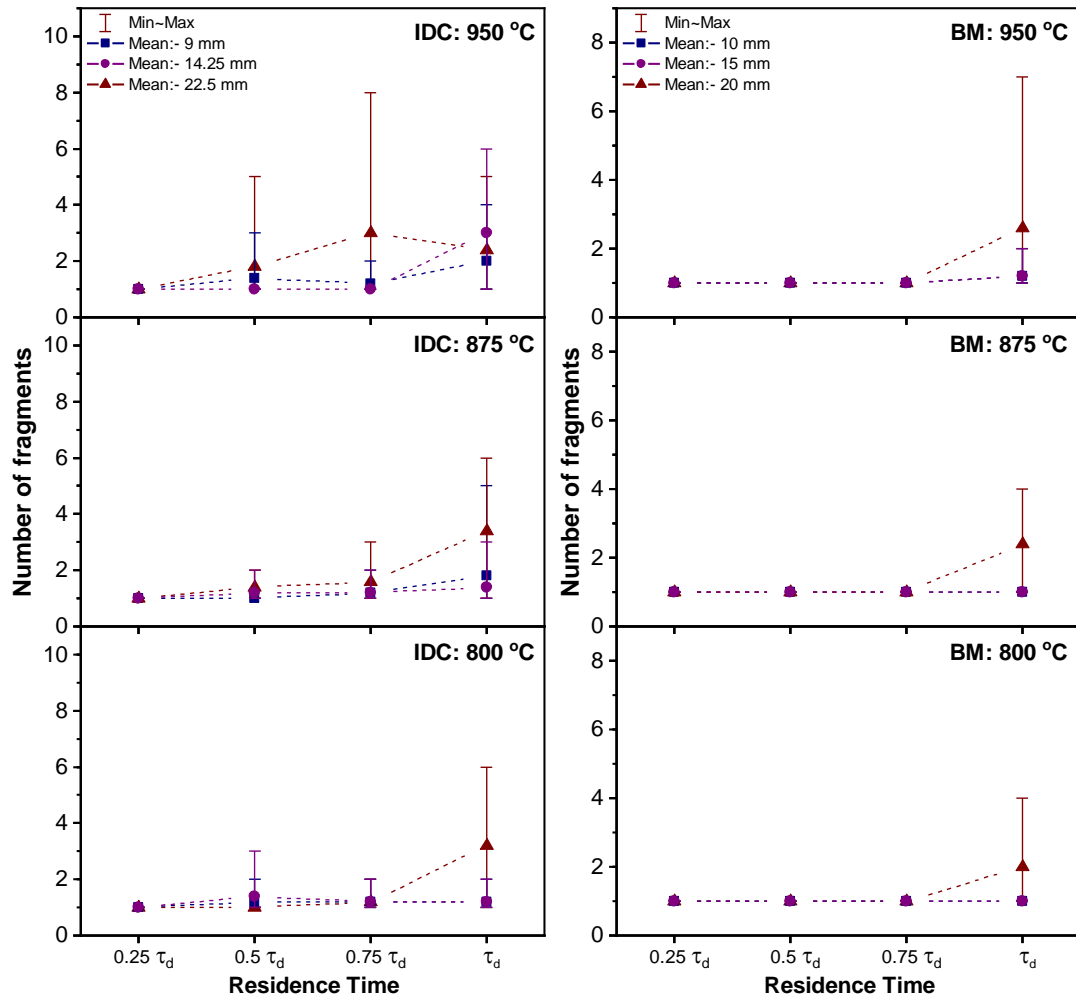
***Figure 6.6 Number of fragments of IDC and BM observed at different residence times during devolatilization.***

The extent of fragmentation in all fuels tested is found to increase with the increase in particle size, as noticed in earlier works conducted in air-FB experiments (Dacombe et al. 1999; Kosowska-golachowska 2010; Li et al. 2014). Also, it is to be noted that high-volatile coals (IDC) yield a lesser number of fragments compared to the medium-volatile types (IC1 and IC2) (Dacombe et al. 1999). In a study by Kosowska-Galachowska et al. (Kosowska-Galachowska et al. 2009) in air environment, 10-12 mm particles of Polish coal with similar properties that of IDC exhibited a comparable degree of fragmentation (about 7) to that of 20-25 mm IDC particles in the present study. It may be the steam environment in CLC which favoured a lower degree of fragmentation for this type of coal in smaller particle sizes.

The number of fragments is found to increase with the increase in particle size irrespective of the fuel nature and operating bed temperature. The maximum average NF of 8-10, 12.5-16, and 20-25 mm particles are 2, 3 and 6 particles respectively. The number of fragments increases by a factor of 2 to 3 when the particle size increases from 8 to 25 mm.

For a particular sized fuel particle, the largest number of fragments are found with samples devolatilised at the highest temperature studied i.e. 950 $^{o}$C, similar to the conventional air combustion experiments (Baizhong et al. 2009). Moreover, it can be noticed that the NF increases with the increase in residence time at 950 $^{o}$C for all fuel types of different sizes, with few exceptions. But, at lower temperatures, the NF does not show a consistent pattern.
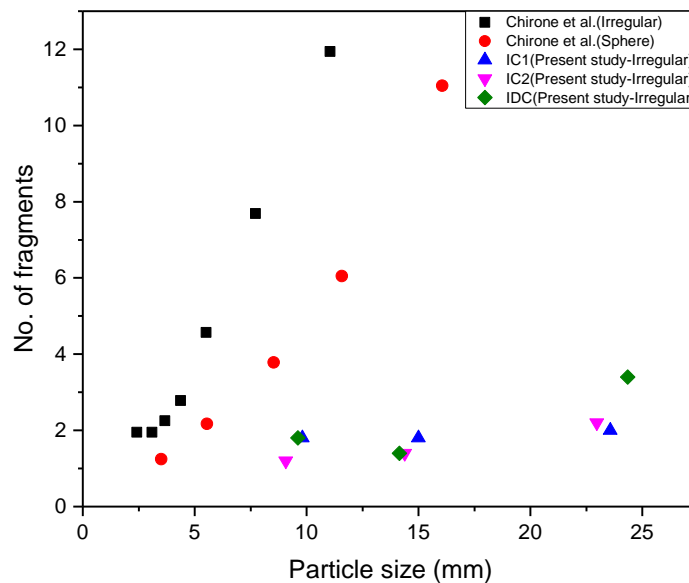


*Figure 6.7 Comparison of number of fragments obtained in air (Chirone et al. 1988) at 850 $^{o}$C and in CLC environments at 875 $^{o}$C.*

Among the fuels, IC1 and IC2 are found to generate more number of fragments in the third and second quarters respectively, whereas the IDC and biomass particles produce more fragments in the last quarter. In Figure 6.7, comparison of the number of fragments (particle multiplication factor) obtained in air (Chirone et al. 1988) and CLC combustion environments shows that the air environment promotes fuel fragmentation. In CLC environment, the degree of fragmentation is relatively lower (about 5 times)

than that during air combustion. However, for the fuel with higher fixed carbon content (IDC), the number of fragments is noticeably higher in CLC experiments.

### 6.3.3 Relationship of physical properties of fuels to their fragmentation characteristics

A fuel's fragmentation characteristic can be related to its physical properties such as strength, porosity, density, size etc. In literature, the number of fragments is related to diameter (Dacombe et al. 1999), compressive strength (Dacombe et al. 1999), porosity (Sasongko et al. 2017) etc. individually to NF. Equations 6.3 and 6.4 are defined to express the fragmentation characteristic of coal and biomass respectively in terms of number of fragments, with the physical properties such as diameter and compressive strength.

$$NF_{coal} = 0.81d^{0.379}\sigma_c^{-0.116} \dots\dots\dots\dots\dots\dots\dots\dots\dots\dots\dots\dots\dots\dots\dots(6.3)$$

$$NF_{biomass} = 1.2d^{0.924}\sigma_c^{-0.559} \dots\dots\dots\dots\dots\dots\dots\dots\dots\dots\dots\dots\dots(6.4)$$

where 'd' is the fuel particle diameter (mass equivalent) in mm, '$\sigma_c$' is the compressive strength in MPa.

The correlation coefficients ($R^2$) of Equations 6.3 and 6.4 are 0.77 and 0.84 respectively. It can be inferred that particles size is the dominant influencing factor of NF, followed by compressive strength. It can be observed that the number of fragments increases with the increase in particle diameter, whereas it is inversely related to the compressive strength, as also can be noticed from Table 6.2.

*Table 6.2 Compressive strength of fuel particles*

| Fuel | Compressive Strength (MPa) | | | Average number of fragments | | |
|------|-----------|------------|------------|----------|-----------|----------|
| | +8-10 mm | +12-16 mm | +20-25 mm | +8-10 mm | +12-16 mm | +20-25 mm |
| IC1 | $5.73 \pm 0.51$ | $3.27 \pm 0.37$ | $1.11 \pm 0.44$ | 1.6 | 2.2 | 2.93 |
| IC2 | $5.55 \pm 1.23$ | $2.74 \pm 0.65$ | $1.05 \pm 0.25$ | 1.2 | 1.7 | 2.4 |
| IDC | $1.73 \pm 0.77$ | $1.30 \pm 0.45$ | $0.56 \pm 0.03$ | 1.7 | 1.9 | 3 |
| BM | $71.78 \pm 2.46$ | $52.24 \pm 7.17$ | $32.46 \pm 5.24$ | 1.07 | 1.07 | 2.33 |

On the fuel side, biomass has the least number of fragments as expected, whose compressive strength is the highest among all these fuels. Among the coals, the compressive strength decreases with the increase in coal's volatile matter, when compared across coals with low to medium volatile matter (Dacombe et al. 1999). On this basis, IDC has the least compressive strength as it has the highest volatile matter among the coal types and thus has the highest average number of fragments at the end of devolatilization.

### 6.3.4 *Frequency and timing of fragmentation*

Timing of fragmentation (TF) can be defined as the time slot or simply as one or more quarters of total devolatilization time, in which the fragmentation events occur. It influences the further rate of fuel conversion, fines generation and the other parameters like gas species concentration etc. for e.g., if a particle fragments in the first two quarters, the fragmentation event has a high influence over the fuel conversion rate and when it fragments in later quarters, the fragmentation become less influential. A particular residence time is considered for mapping into TF only when a particle fragments afresh in that quarter, mainly based on the number of fragments in a quarter. For example, if the NF of a fuel in the first, second, third and fourth quarters are 2,2,3 and 2, then TF is marked in the first and third quarters.

The frequency of fragmentation (FF) is defined as the number of instances a fuel particle fragments in the entire devolatilization period and is calculated from the sum of TF markings in the entire devolatilization period at specific operating conditions (Figure 6.8 and 6.9). It is a significant characteristic of a fuel getting converted at certain operating conditions, which influence the devolatilization times and conversion rates i.e. if a fuel has high FF, it will apparently have lesser devolatilization time, and probably higher fines generation.

IC1 particles fragment in the second and third quarters of devolatilization at 800 °C. However, they start to fragment in the very first quarters at higher temperatures. IC2 particles tend to fragment in the first and second quarters, with some exceptions. Indonesian coal (IDC) fragments mostly in the third and fourth quarters but it fragments even in the second quarter at higher temperatures. Biomass particles of 20 mm fragment

in the fourth quarter at all temperatures of study. However, the smaller sized particles fragment only at 950 °C in the final quarter of devolatilization.
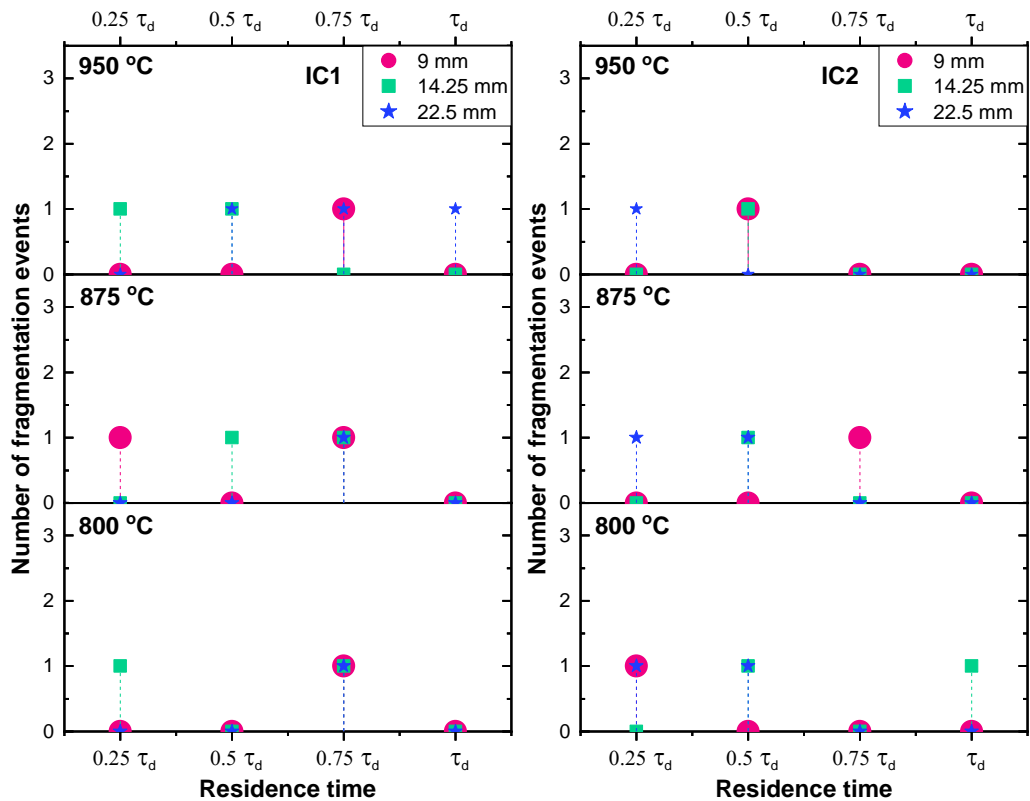


*Figure 6.8 Timing and frequency of fragmentation events in (a) IC1 and (b) IC2.*

Overall, it can be noticed that IC1 particles start fragmenting in very early stages (first and second quarters) of the devolatilization process, whereas the biomass particles are the least fragmenting, which fragment only in the last quarter. The compressive strengths of coal particles are also found to influence the timing of fragmentation (Syred et al. 2007), where the coal with a higher strength fragments quicker. This means that stronger coals tend to develop cracks or fragments in the earlier stages, due to the mounting of pressure build-up during the volatile release process. If the particles fragment in the first and second quarters, size reduction helps increase in surface area and subsequent fuel conversion. Fuel particle that generates fragments in the last quarter does not have much influence on the devolatilization time as well as the overall conversion time. The increase in temperature is found to shift the fragmentation time interval to an earlier quarter of devolatilization in all fuel types, except for a very few cases.
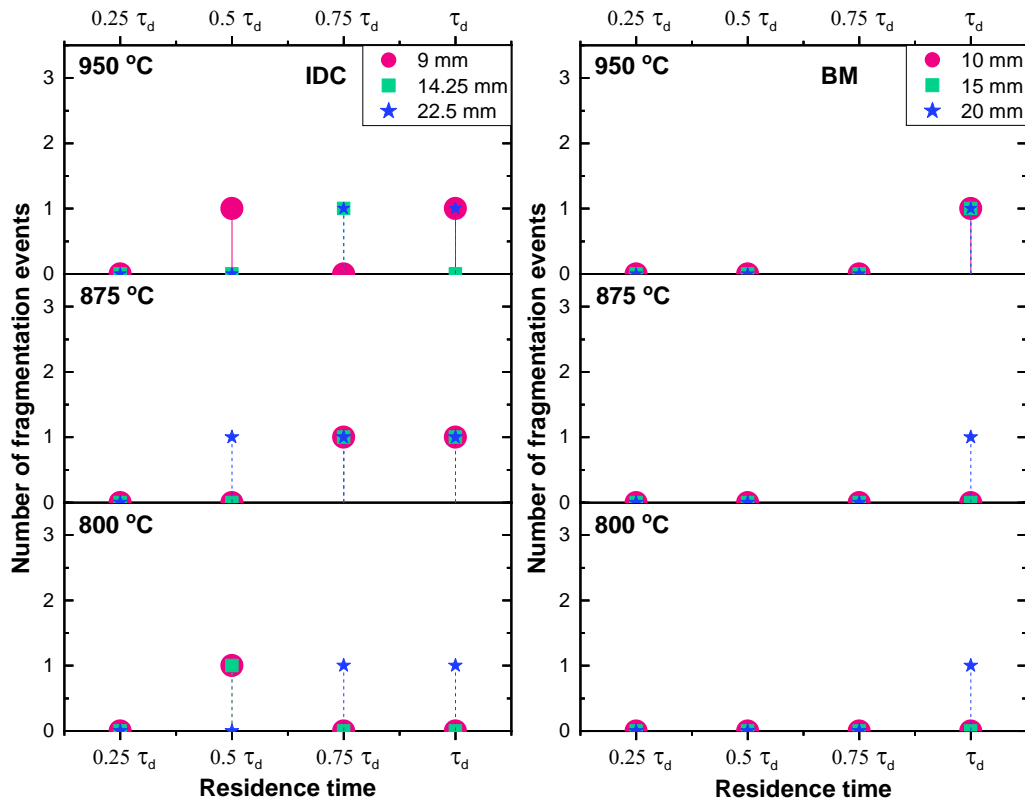
*Figure 6.9 Timing and frequency of fragmentation events in (a) IDC and (b) BM.*

The highest frequency of fragmentation events is found in IC1 and IDC fuel particles, which fragmented 3 times during devolatilization. This behaviour may be due to the higher volatile content of these two fuels. The least frequency of fragmentation is found in the case of biomass particles, with almost no fragmentation at lower temperatures. The fragmentation frequency of the same wood particles studied under conventional air-FBC (Sudhakar et al. 2008) is higher than in FB-CLC, hinting the probable influence of steam atmosphere. A study by Molina-Sabio et al. (2006) shows that the porosity of char has been improved by using steam for activation. The steam may probably enlarge the pores of the particle, leading to reduction in pressure build-up within the particle. The improved porous nature of the fuel may aid easier volatile release, thus reducing the fragmentation events.

In all the fuel types, frequency of fragmentation events either increases or stays as such with the increase in particle size, except for fuel IC1. The particles of largest sizes tend to fragment many times, which might be due to the thermal stress they experience (Kosowska-golachowska 2010). A different behaviour can be observed in

92

the case of IC1, whose 22.5 mm (average) particles do not exhibit a second instance of fragmentation till the bed temperature is raised to 950 °C. This shows that additional thermal energy is needed for a larger particle of such fuel to undergo thermal stress and break apart. With the increase in temperature, FF increases, and the highest frequencies are observed for all fuels at 950 °C, except IC2. The reason for this exceptional behaviour of IC2 may be due to a condition in which the first instance of fragmentation itself has developed enough room to vent the pressure created by volatile evolution (Figure 6.17). On an average, all fuel types other than biomass have fragmentation frequency of 2. Biomass particles fragment only at 950 °C but with a maximum frequency of 1. IDC particles of all sizes have a relatively higher frequency of fragmentation at 875 °C compared to other temperatures of study.

### 6.3.5   Fragmentation index

Fragmentation index is defined as the ratio of the number of fragments to the variation factor of the feed particles (Zhang et al. 2002), as shown in Equations 6.5 and 6.6.

$$\textbf{Fragmentation index, FI} = \frac{No. of\ fragments\ (NF)}{Variation\ factor\ of\ feed\ particles\ (F_d)} \ldots\ldots\ldots\ldots(6.5)$$

$$F_d = \sum_{i=1}^{n} \frac{X_i d_i}{d_a} \ldots\ldots\ldots\ldots\ldots\ldots\ldots\ldots\ldots\ldots\ldots\ldots(6.6)$$

where $X_i$ is the mass fraction of particle fragment of diameter, $d_i$; $d_a$ = average particle diameter of the particles subjected to devolatilization.

The fragmentation indices (FI) for various fuels in different particle sizes at three bed temperatures are shown in Figures 6.10 and 6.11. The FI value depends mainly on the $F_d$ value. $F_d$ would always be less than 1 if the fuel is of non-swelling type and when the fuel is of swelling nature, the $F_d$ will be ≥1 (Paprika et al. 2015). Since FI is inversely proportional to $F_d$, the FI value will be ≤ 1 for swelling types and ≥1 for non-swelling and shrinking types.

From Figure 6.10, it can be seen that the maximum changes in the particle size occur in the third quarter for the fuel type IC1. During this period, the particle is either losing its mass drastically or the number of fragments increases hugely or both. Also, it is noticed that IC1 has its least devolatilization time at 950 °C because of increased surface area, which is reflected from the relatively higher FI. IC2 particles of 22.5 mm

always have their peak FI values in the second quarter at all temperatures studied. Whereas, for the smaller particles, the occurrence of maximum FI is one quarter earlier with an increase in bed temperature from 800 to 950 °C; at the highest temperature, maximum FI value is recorded in the second quarter (Figure 6.10). Indonesian coal (IDC) of all particle sizes have maximum size variations in the last quarter, which indicates the occurrence of more than one instance of fragmentation event (Figure 6.11). But smaller particles of 9 and 14.25 mm have their maximum FI in the second quarter at 800 °C. Biomass particles of all sizes have maximum FI in the last quarter, since the onset of fragmentation occurs just before the endpoint of devolatilization (Figure 6.11).
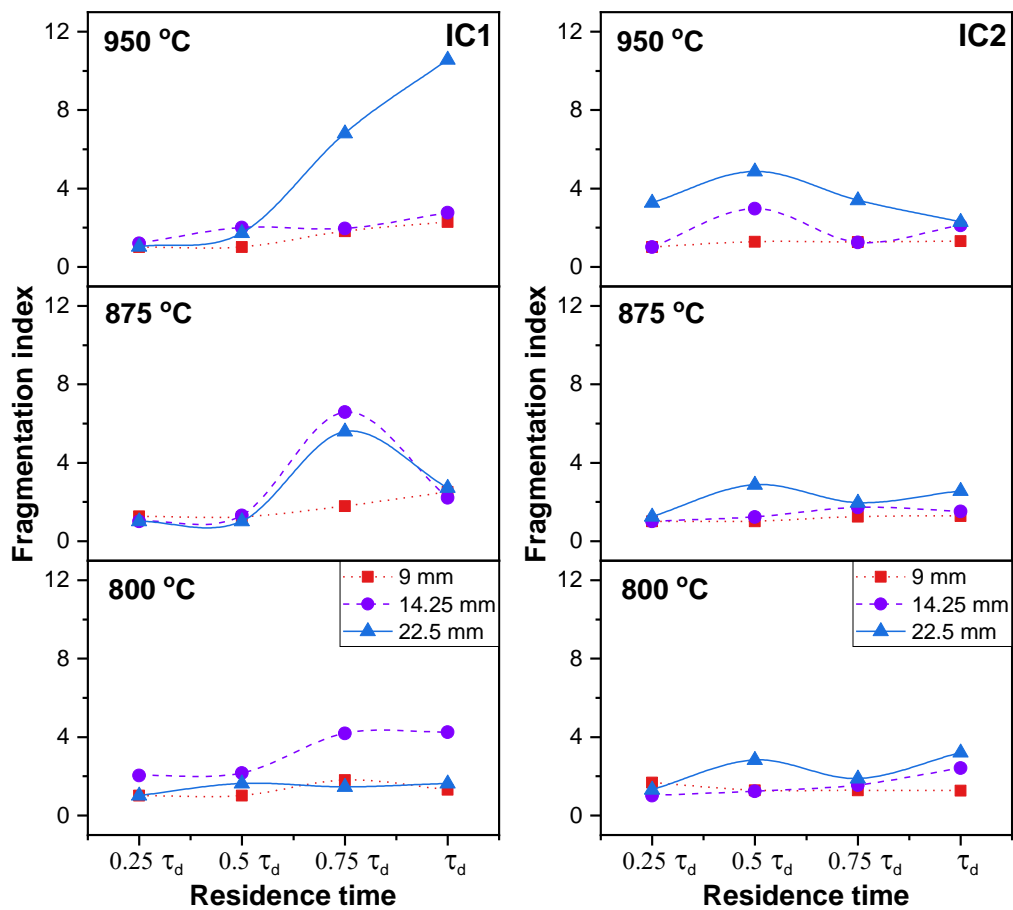


*Figure 6.10 Fragmentation index of IC1 and IC2 particles at different operating conditions.*
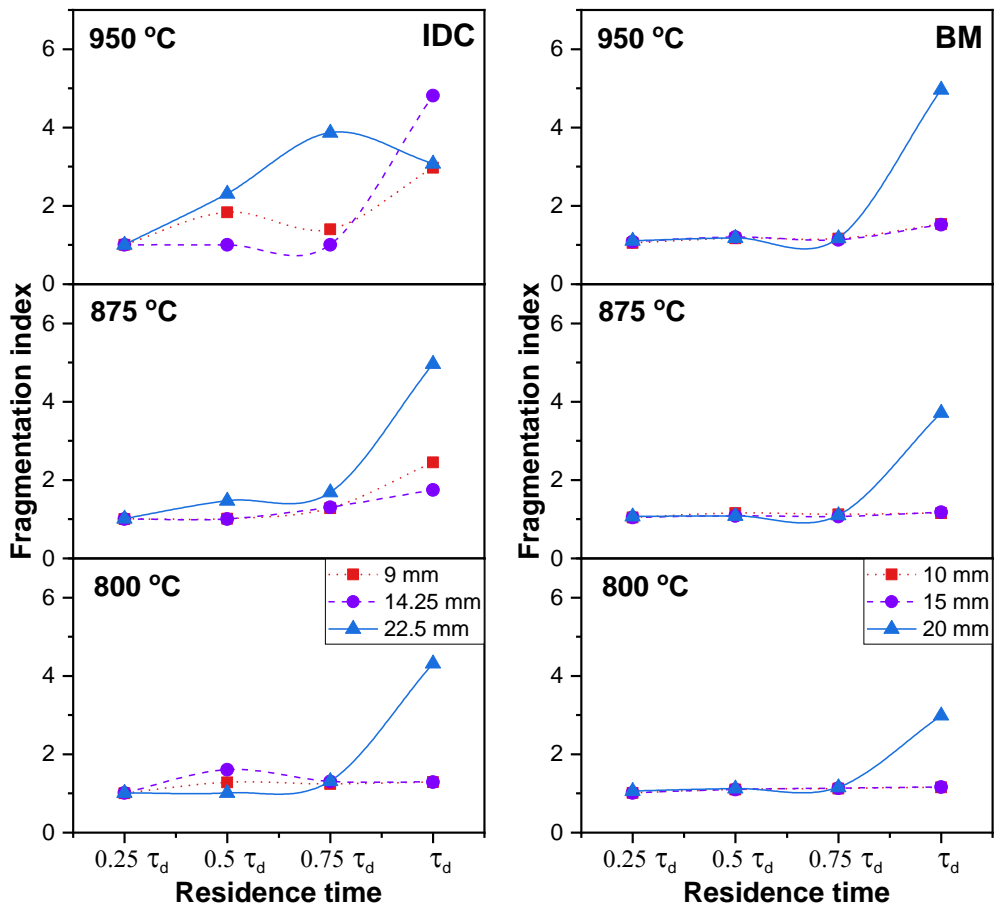
*Figure 6.11 Fragmentation index of IDC and BM particles at different operating conditions.*

Overall, volatile-rich fuel particles (IDC and BM) have the peak size/mass variation in the last quarter and it is the second/third quarter for other fuels (Indian coals) where the maximum FI is found. Similarly, in air combustion experiments, Zhang et al. (Zhang et al. 2002) found that the fragmentation index is maximum for the coal with the highest volatile content. The maximum FI values noticed in IC1, IC2, IDC and BM are 10.57, 4.87, 4.96 and 4.96 respectively, all observed for the largest particle sizes studied (except few cases where 12.5-16 mm particles have maximum FI). Among all the fuels, IC1 is found to undergo much size variations, which can be seen from Figure 6.10. Biomass registers a considerable FI (3-5) only for the highest size (20 mm) studied, that too at the end of devolatilization time (implying less significance). But for the other sizes, regardless of the operating conditions, BM exhibits the lowest FI (viz. 1 to 1.5) compared to all other fuels studied, indicating a relatively lesser size changes due to fragmentation.

From the particle size point of view, the fragmentation index is always higher for larger particle sizes, as observed in conventional combustion systems (Li et al. 2014; Zhang et al. 2002) and similarly, bed temperature has a proportional influence on FI. Observations in line with the present study are noticed in literature findings on air-FBC (Baizhong et al. 2009; Li et al. 2014; Senneca et al. 2011). In the order of influence on FI, the operating parameters can be arranged as fuel type > particle size > bed temperature.

### 6.3.6  *Particle size distribution*

If a particle fragments in the combustor, the particle size distribution (PSD) gives the entire picture of the particle sizes formed out of fragmentation. For every quarter of the devolatilization time, PSD is represented in terms of cumulative mass fraction. The PSD of all fuels of three sizes at 950 $^{o}$C are given as Figures 6.12 to 6.15 and the PSD at temperatures 800 and 875 $^{o}$C are provided in Figures A1 to A8. As a common trend, two kinds of patterns emerge from PSD observations, as follows.

(i)   If a particle fragments in the first two quarters, the smaller particles generated tend to get converted and escape out of the basket/reactor and only the large particle fragments are left behind in the combustor, in the later quarters [more likely in Indian coals].

(ii)  If a particle fragments in the third/fourth quarter, the PSD shows the presence of smaller particle fragments near the end of devolatilization [mostly in IDC and biomass particles].

During fragmentation experiments, processes such as coarse particles undergoing only conversion without fragmentation, coarse particle fragmenting into smaller particles and complete conversion of smaller fines, followed by elutriation are observed in the present study. Similar observations are found in conventional air combustion of biomass as well (Sudhakar et al. 2008). The originating location of fractures or fissures in the particle determines the particle size distributions in a fragmentation process. If the crack develops in the inner radial positions of the fuel structure (due to the high volatile content of the fuel), it results in the formation of a larger daughter particle (Senneca et al. 2011). The fracture originating in the outer radial locations due to the thermal stresses leads to exfoliation of outer layers, resulting in generation of large

amount of fines (Paprika et al. 2015, 2013). Thus, it can be understood that if most of the resulting fragments lie in the smaller particle size range, it denotes that the thermal stresses are predominant in creating fragments. If the mass fraction is higher for larger particle sizes, the fragmentation cause could be the outburst due to excessive internal pressure developed at high temperatures.

For all of the fuel types, at all bed temperatures, the larger fuel particles generated more fragments as well as fines. As a general pattern, fragments generated in the earlier quarters are not retained until the end of devolatilization, because of subsequent fragmentation into very small fines which may either escape the basket or due to further conversion and elutriation. Sometimes, particles which fragment in earlier quarters may show a trend of reduced number of particles in the next quarter, and again have their fragments increase in the subsequent quarter. This is because of another instance of fragmentation event witnessed by a larger particle (fragment) from the earlier quarter. At any given temperature for any particle size of a fuel, a concurrent increase in the mass loss with residence time is reflected from the decreasing mass equivalent diameter of the largest fragment, that can be noticed from all PSD figures. Compared to other coal types, IC1 generated relatively larger fraction of smaller fragments and fines, which also lead to an increase in the particle fragment count (Figures 6.12, A1, and A2). Meanwhile, IDC produced relatively lesser fractions of smaller particles (Figures 6.14, A5, and A6), which may be attributed to the coal's plastic nature and polymerization reactions during the devolatilization that prevented the particle from fragmenting. Though the cracks are fully developed, they are held together by thin joints (Figure 6.18). The biomass particles fragment rarely and most of the particles stay as such from the time of introduction till the end of devolatilization. In cases where BM fragments, the daughter particles are usually of sizes above half of the original diameter of the parent particle (Figures 6.15, A7, and A8). PSD of all coal types show decrements in the mass fractions of smaller sized fragments with the increase in temperature. The probable cause for this type of phenomena could be the conversion of the smaller sized fragments due to fines generation and their conversion followed by elutriation/ basket escape incidents, as discussed earlier.

*Figure 6.12 Particle size distribution of IC1 particles of (a) 8-10 mm, (b) 12.5-16 mm and (c) 20-25 mm at the end of various quarters of devolatilization at 950 ºC.*



*Figure 6.13 Particle size distribution of IC2 particles of (a) 8-10 mm, (b) 12.5-16 mm and (c) 20-25 mm at the end of various quarters of devolatilization at 950 ºC.*
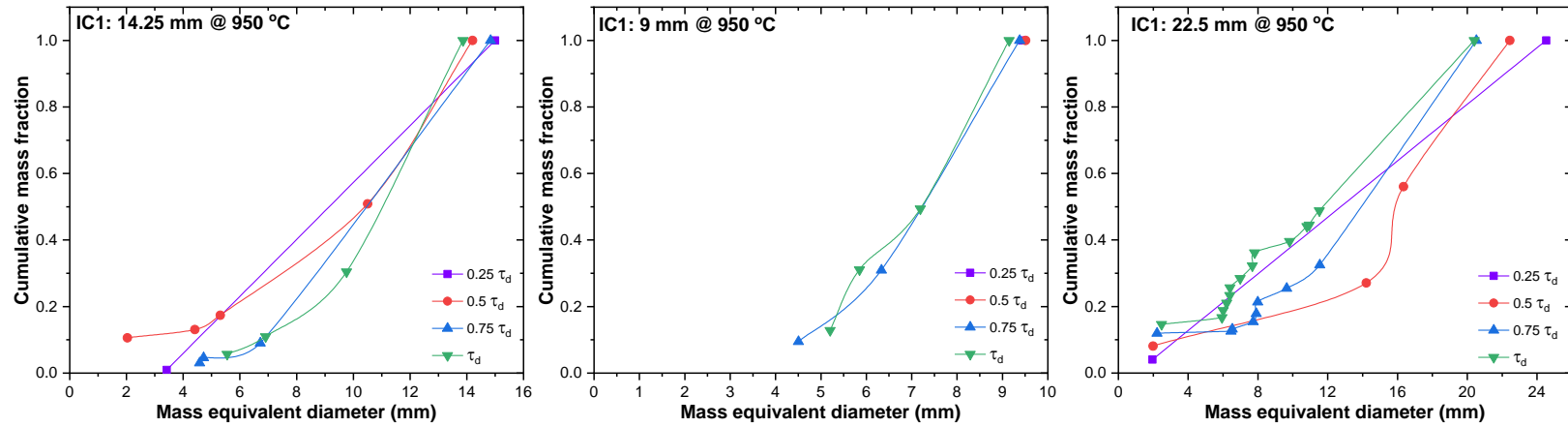
*Figure 6.14 Particle size distribution of IDC particles of (a) 8-10 mm, (b) 12.5-16 mm and (c) 20-25 mm at the end of various quarters of devolatilization at 950 °C.*
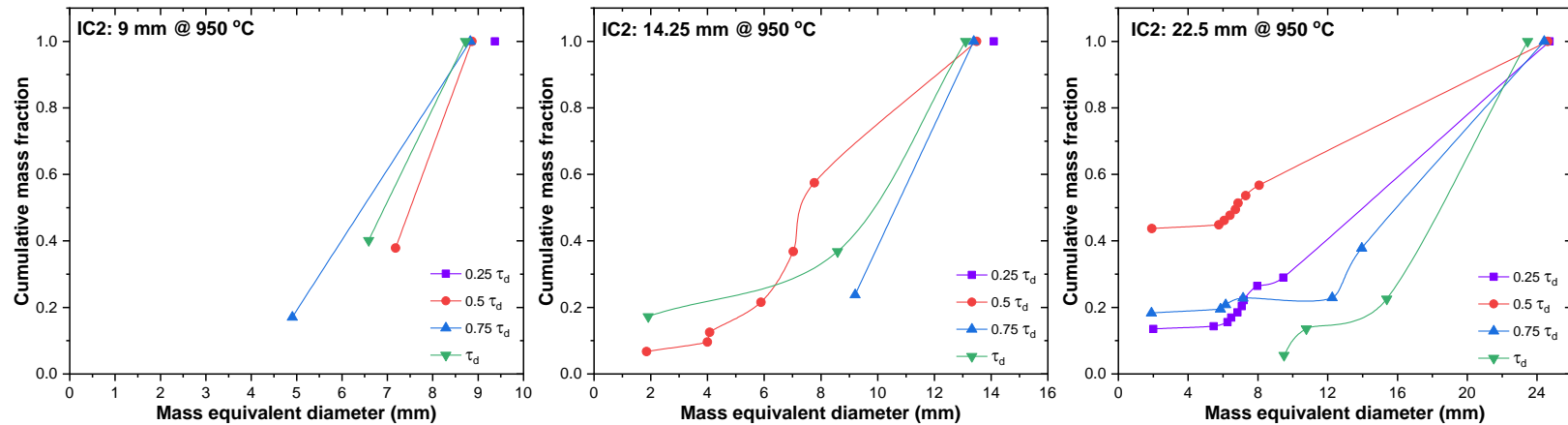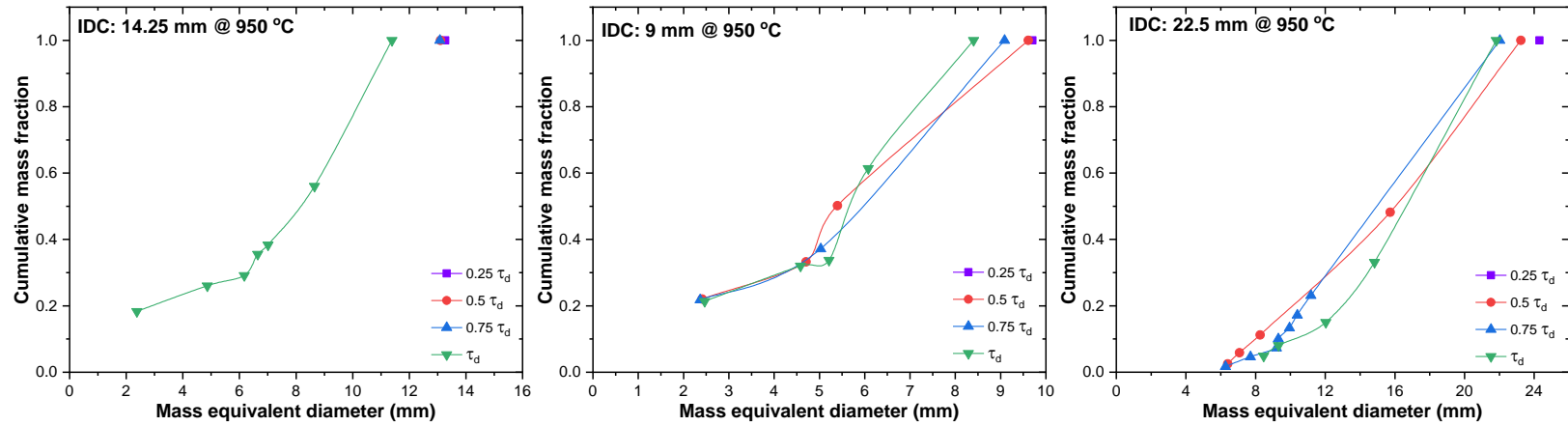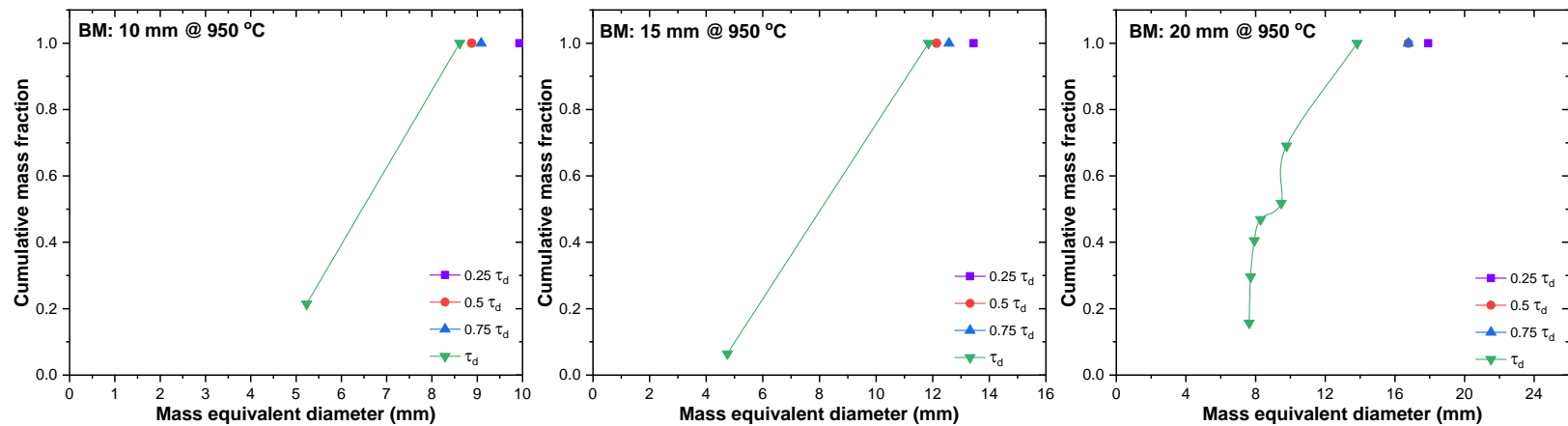


*Figure 6.15 Particle size distribution of biomass particles of 10 (a), 15 (b) and 20 mm (c) at the end of various quarters of devolatilization at 950 °C.*

### 6.3.7 Modes of fragmentation

For generalizing the qualitative pattern of the fragmentation phenomenon, fuel particles retrieved from the bed at different residence times during devolatilization are further analysed. The crack patterns can be observed from the images of various fuels given in Figures 6.16 to 6.20. Changes to the particle geometry for all tested solid fuels are listed in Table 6.3.

In the case of coal particles, they fragment mostly in a systematic manner of crack formation, crack propagation followed by particle breakage. In some instances, Indian coal particles exhibited stochastic fragmentation behaviour as discussed earlier in the number of fragments and fragmentation index sections. This may be characterized by the fragmentation events occurring in the earlier quarters of devolatilization. In such particles, the degree of non-homogeneity may be relatively higher than other particles of the same fuel, which results in increased thermal stress within the particle leading to random failures.



*Figure 6.16 Crack formation and fragmentation pattern of IC1 particles (12.5 - 16 mm) during various stages of devolatilization.*



*Figure 6.17 Crack formation and fragmentation pattern of IC2 particles (12.5 - 16 mm) during various stages of devolatilization.*

IC1 samples (Figure 6.16) develop multiple sub-surface cracks in the first quarter and then they split into larger fragments and few smaller fragments. In the subsequent quarter, larger fragments may undergo a second instance of fragmentation, resulting in smaller fragments. In the last quarter, the fines are lost, and larger fragments stay as such, only undergoing further conversion. IC2 samples as seen in Figure 6.17, undergo fragmentation in a very methodical way. The crack initiation starts along the bedding plane (the plane of organic matter deposition during coal formation). As devolatilization continues, samples develop into layered wafer-like or finger-like structures as a result of crack propagation. Then, they produce fragments along a well-developed crack, in the form of thin sheets and flakes. A flat surface is usually noticed in the interface of crack, which denotes the crack propagation in a parallel direction to the bedding plane (Chirone and Massimilla 1989).
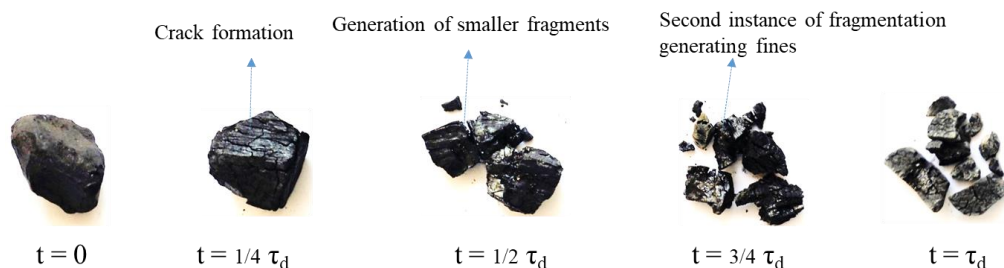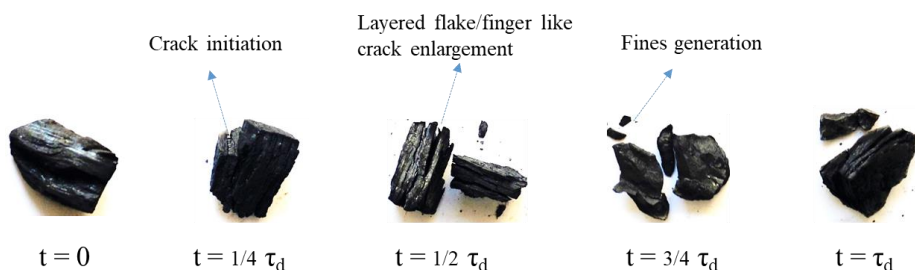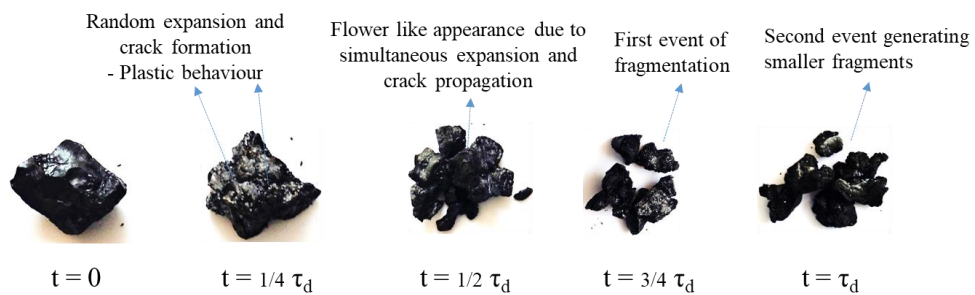


*Figure 6.18 Crack formation and fragmentation pattern of IDC particles (12.5 - 16 mm) during various stages of devolatilization.*
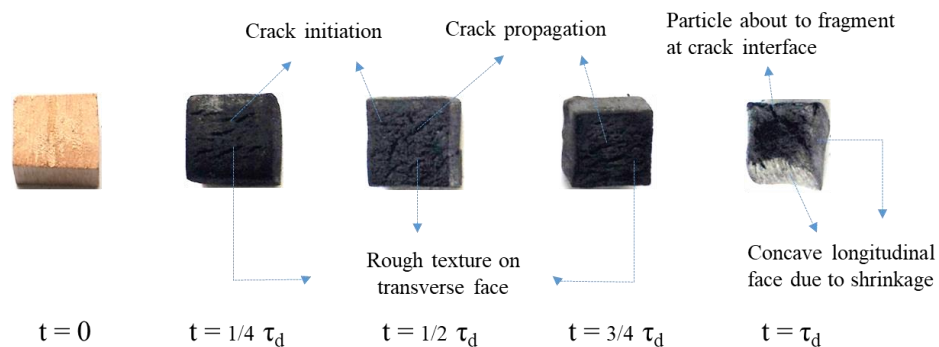


*Figure 6.19 Crack patterns over the transverse face of biomass particles (15 mm) during various stages of devolatilization.*
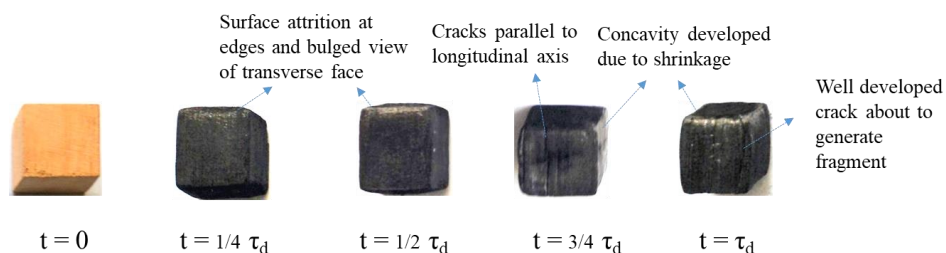
*Figure 6.20 Crack patterns over the longitudinal face of biomass particles (15 mm)*
*during various stages of devolatilization.*

*Table 6.3 Summary of changes to particle geometry during primary fragmentation*

| Parameters* | IC1 | IC2 | IDC | BM |
|---|---|---|---|---|
| **Fragmentation mode** | At particle centre | Exfoliation into flakes | At particle centre with plasticity | Exfoliation |
| **Sphericity** | Decrease | Decrease heavily | Decrease moderately | Decrease |
| **Symmetry** | Decrease moderately | Maintained constant | Decrease moderately | Maintained constant |
| **B/L ratio** | Decrease moderately | Nearly constant | Nearly constant | Nearly constant |
| **Convexity** | Nearly constant | Decrease heavily | Expands to a concave structure | Cube shrinks to form concave sides |

*adapted from Cui et al.(2015)

IDC samples show a stochastic crack formation pattern, but the crack propagation and particle split-up process are systematic and sequential. As expected from the PRN relation with fragmentation, the IDC particles with the highest PRN among coals have the maximum crack formations. Even though the cracks are well developed to result in a fragmentation event, it is observed that they are held together by thin bridges for a longer time. Concurrent expansion and crack propagation in IDC give the particle, a flower-like structure (Figure 6.18). At the end of devolatilization, the fuel fragments cleave apart once the carbon bridges between them weaken.

The biomass particles seem to form initially sub-surface cracks (Dhanarathinam and Kolar 2013) that later develop into bigger cracks leading to fragmentation. The transverse sides of biomass particles show cracks parallel (and continuous) to the

longitudinal axis i.e. along the grain direction (Figure 6.20). Whereas, the top and bottom faces (plane perpendicular to the longitudinal axis) have cracks propagating radially in a discontinuous manner. These observations match the literature findings by Dhanarathinam and Kolar (2013) in air-FB combustion environment. Figures 6.19 and 6.20 show the particle shrinkage leading to crack propagation (due to thermal strain). The particle at the end of devolatilization time appears to be on the verge of failure by fragmentation, which is a combined effect of crack development, shrinkage and weakening of the fuel particle. Except IC1, all other fuel types show a systematic fragmentation process. Thus, depending on the fuel nature, the processes of crack formation, propagation and fragmentation vary.

### 6.3.8    *Swelling and shrinkage in fuels during devolatilization*

During the process of devolatilisation, the volatile-rich fuels have a tendency to swell/shrink depending upon the porosity and composition of other constituents like fixed carbon and ash matter. The implications of changes in fuel particle volume during conversion help determining the reactor size as well as the fuel loading. Indian coals (Figures 6.16 and 6.17) do not show any significant change in the volume as an individual particle or as a fragment (apart from fragmentation or attrition). But the Indonesian coal particles exhibit thermoplastic expansion randomly at different locations (Figure 6.18). Usually, bituminous and sub-bituminous coals exhibit thermoplastic behaviour, which are analysed for their caking properties and their suitability in combustion processes (Fermoso et al. 2010; Lu et al. 2013). The free swelling index determined by ASTM D720/D720M-15 for the fuels IC1, IC2, and IDC respectively are 1, 0, and $1\frac{1}{2}$. This means that IC2 produces non-coherent residue while IC1 and IDC form coherent residue after the tests. Only IDC exhibits a very mild swelling behaviour (Figure 6.18) that does not have a considerable effect on the volume of fuel particles.
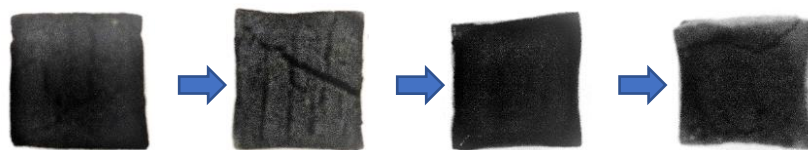


*Figure 6.21 Shrinkage in biomass particles during the course of devolatilization from first to last quarter (from left to right).*

The woody biomass exhibit shrinkage, affecting the particle volume to a great extent. The biomass particles (Figure 6.21) show a continuous but gradual shrinkage during the course of devolatilisation. The shrinkage pattern is characterised by convex appearance along the transverse direction. As residence time increases, the middle region along the sides of the particle tends to shrink throughout the devolatilization period. But the edges do not exhibit such characteristic. Rather, the edges appear to be blunt and smooth due to attrition. Sometimes, the longitudinal centre of the fuel particles appears to have bulged (Figure 6.21), though they do not actually bulge. This bulged appearance is because of the char loss around the edges due to conversion and attrition (Sudhakar et al. 2008).

*Table 6.4 Level of shrinkage in different directions and volume of biomass particles*

| Size | 10 mm | | 15 mm | | 20 mm | |
|---|---|---|---|---|---|---|
| Domain / Shrinkage | Min. (%) | Max. (%) | Min. (%) | Max. (%) | Min. (%) | Max. (%) |
| Longitudinal direction | 10.41 | 15.48 | 14.17 | 15.87 | 13.86 | 15.06 |
| Transverse direction | 11.88 | 16.27 | 20.83 | 23.75 | 16.88 | 24.69 |
| Volume | 31.31 | 40.71 | 44.64 | 50.47 | 40.55 | 51.86 |

As the biomass particles are shaped, the volumetric change can be measured easily. On average, percentage volumetric shrinkage of 10, 15, and 20 mm particles respectively are 36.01, 47.55, and 46.2. The largest particle size studied (20 mm) experiences the maximum volumetric shrinkage as well as directional shrinkage. The shrinkage levels of biomass particles in transverse, longitudinal directions and in volume is provided in Table 6.4. When particle size increases from 10 to 20 mm, volumetric shrinkage percentage also increases in a range of 6-11%, depending upon the bed temperature. When the temperature is increased from 800 to 950 ºC, shrinkage increases by 7% for 10 mm particles and by 10% for the largest size studied (20 mm). The particles have a maximum reduction in the volume of about 52% of their original volume at 950 ºC.
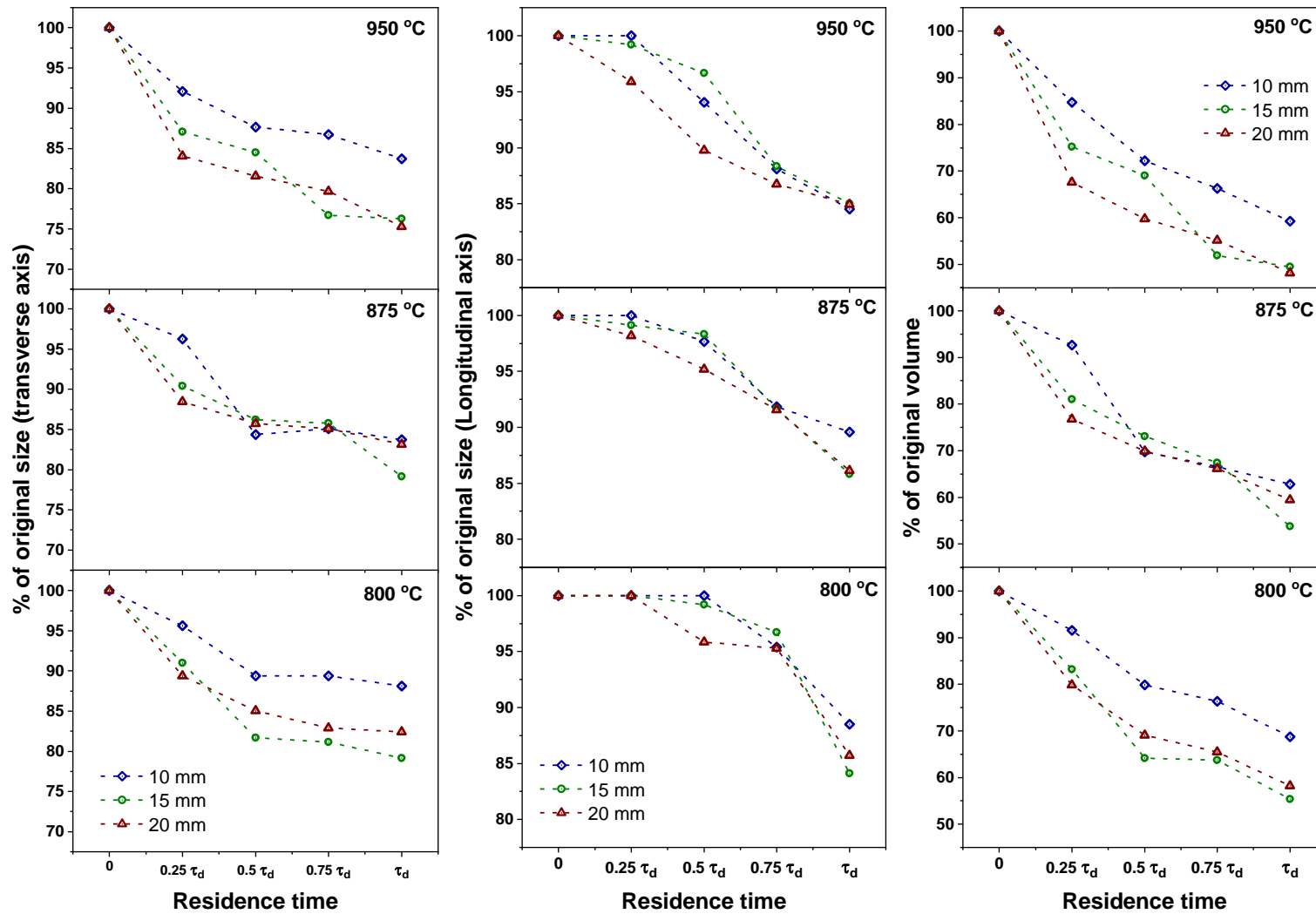
*Figure 6.22 Transverse, longitudinal and volumetric shrinkage of various sized BM particles at different bed temperatures.*

Volumetric change in biomass particle is highly dependent on the changes in dimensions along transverse direction since two sides of the cube are covered in this direction. Shrinkage in the transverse direction is relatively higher than in the longitudinal direction. Longitudinal shrinkage is limited to a maximum of 15% for all particle sizes (Figure 6.22). Maximum shrinkage in the transverse direction is found to be in the range of 16.27 - 24.69%. Hence, shrinkage in biomass is advantageous in maintaining the volume occupied by fuel particles, for a better control of overall solids inventory.

## 6.4 Closure

The primary fragmentation behaviour of four different fuel particles at different operating conditions is investigated during different residence times of devolatilization process in CLC, using various indicators of fragmentation. The minimum particle diameter for fragmentation to occur is validated with the pore resistance number relationship. Correlations between the compressive strength of fuels and the number of primary fragments generated, are developed. The modes in which each fuel type undergo fragmentation are discussed in detail, varying from structured to unstructured crack formation and their propagation leading to failures. A significant shrinkage behaviour observed in the woody biomass is analysed and reported.

# CHAPTER 7

# 7 CHAR CONVERSION AND SECONDARY FRAGMENTATION OF FUELS UNDER CLC CONDITIONS

## 7.1 Introduction

Devolatilization phase is followed by char conversion by steam gasification. In parallel to char conversion, secondary fragmentation of char particles is witnessed. Char conversion and char fragmentation are considered to be significant, owing to the longer residence times of fuel particles during this phase of conversion (Scala et al. 2006; Senneca et al. 2017b). In combustion environments like CLC, long residence times of chars in the absence of direct oxygen promotes char fragmentation.

Char fragmentation is relatively more significant in gasification conditions (because of intrinsic kinetic control) than in the combustion case (Senneca et al. 2017b), it becomes a rate-controlling phenomenon in char conversion during iG-CLC. Thus, understanding these comminution phenomena provides clear insights on the fuel size changes, consequent changes in conversion kinetics, effects on bed aerodynamics by the fuel particles and maintaining the reactor inventory during the reactor operations, particularly in newer combustion environments like CLC. This chapter presents the results of the investigation of char conversion time and the concurrent comminution phenomenon of various fuel particles under fluidized bed CLC environment.

## 7.2 Experimental

Char conversion time ($\tau$cc) is calculated from the difference between the total fuel conversion time and the devolatilization time. The devolatilization time is determined using the colour indistinction method (Pragadeesh and Sudhakar 2019). After devolatilization, char particles of all fuel types reappear as tiny white spots spattered across the bed. During the conversion regime, char particles typically tend to disappear in bed as they turn into ash (both fly ash and bottom ash). The completion of char conversion of each fuel is visualized differently as follows.

a)   IC1 particles exhibit intensive fragmentation behaviour and are difficult to track during most of the instances but they can be noticed while disappearing in the bed and seen as elutriated sparkles in the freeboard during the final stages of conversion.

b) In the case of IDC and BM, comparably large particles undergoing conversion are visible throughout char conversion regime and are observed as sparkles like IC1 particles during the completion of char conversion.

c) IC2 particles which have the highest ash content, remain visible as large particles/fragments until complete conversion. This aids easy monitoring of the particles and they are observed as objects with bright (white) periphery with reddish-orange core. As the conversion progresses, the bright zone expands towards the centre of the particle. Char conversion is considered complete once a completely bright particle (coherent ash skeleton) is observed without any reddish-orange patch.

For IC1, IDC and BM, completion of char conversion is determined by the time at which the last particle or sparkle appeared. Char fragmentation observed in fuel chars is quantified using the same indicators followed by Pragadeesh and Sudhakar (Pragadeesh and Sudhakar 2018).

## 7.3 Results and discussion

### 7.3.1 Char conversion time

Char conversion times of various sized fuel particles studied at different bed emperatures are presented in Figures 7.1 and 7.2. Among the fuels, IC2 char particles consume the longest time for conversion while the BM chars are the quickest to get converted (Figure 7.2). As earlier noted in the literature (Arena et al. 1994) of conventional combustion, all the fuel types exhibit increased char conversion times with the increase in particle size and a decrease in bed temperature. The magnitude of changes observed in char conversion time with increasing particle size and bed temperature are summarized in Table 7.1. IC1 and BM are found to be the most influenced fuels by the changes in particle size but are least affected by changes in temperature. The effect of particle size on char conversion time decreases with the increase in operating bed temperature, as noticed clearly from the largest sized particles in all coals tested at 950 $^\circ$C. In contrast to coals, particle size effect in biomass chars is amplified with the increase in bed temperature. A possible reason for this phenomenon could be a higher degree of fragmentation as a result of longer residence times of char at lower temperatures. Amongst all fuels, wide variations in the char conversion time

108

are observed in the largest sized samples tested at 800 ºC. This is due to the higher degree of variation in the inhomogeneity within the fuel particles with the increase in particle size (Pragadeesh and Sudhakar 2018). This would lead to changes in temperature gradient, residual thermal stresses and porosity during conversion, which consequently reflected-on as variations in fragmentation events (Krishnamoorthy et al. 2017; Sreekanth et al. 2008a). Also, as the char residence times are longest at 800 ºC, variations in the factors causing fragmentation resulted in a broad range of char conversion time, especially in the larger sized particles studied.



*Figure 7.1 Char conversion times of IC1 and IC2 of various sizes at three different bed temperatures.*



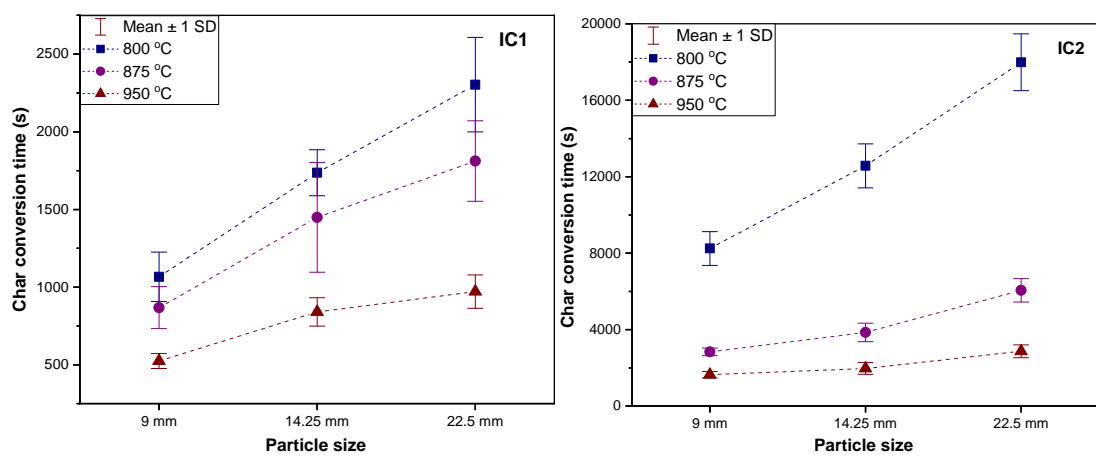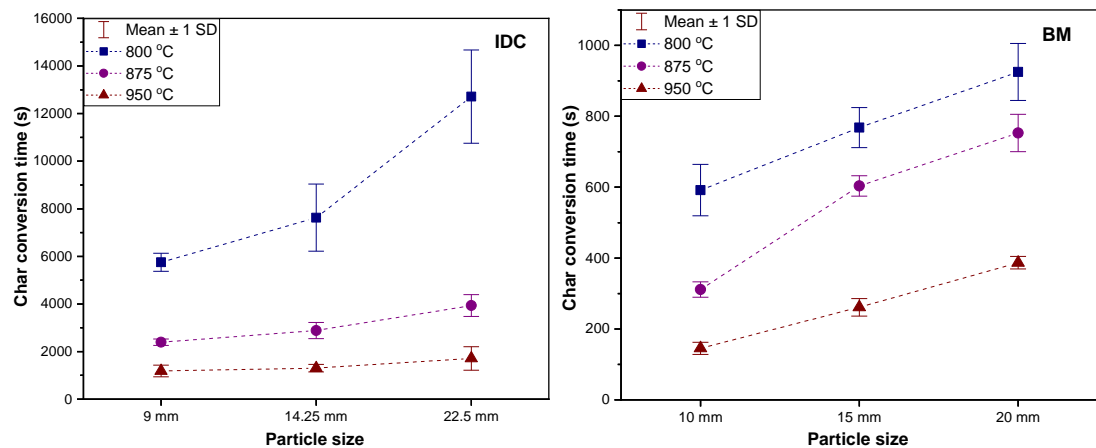*Figure 7.2 Char conversion times of IDC and BM of various sizes at three different bed temperatures.*

The conversion times reduced drastically for fuels with high fixed carbon (IC2 and IDC), with the increase in bed temperature. IDC appears to be the most affected fuel by the changes in bed temperature i.e. a maximum reduction in char conversion

time by 86 % is observed when the bed temperature is increased from 800 to 950 °C. This behaviour of the fuels is attributed to the fixed carbon content of the chars of each fuel. When the fixed carbon in the char is sparsely distributed in the coherent ash skeleton (like in IC2), only the exposure to higher temperatures enables faster oxidation of carbon, either by crack formation or pore network expansion, eventually reducing the conversion time. The above-mentioned phenomenon can be substantiated by the higher thermal conductivity of carbon in char (0.01 to 2000 W/mK (Balandin 2011; Mokhena et al. 2018; Neumann and Wallisch 1983; Renteria et al. 2014), depending on the mix of amorphous and crystalline forms) than the aluminosilicate ash component (0.5 to 1.5 W/mK (Chern and Hayhurst 2006; Kwiatkowski et al. 2014; Mason et al. 2016)). Fixed carbon in the chars of IC1 and BM are exposed for conversion, respectively by means of smaller fragments and highly porous structure.

*Table 7.1 Changes in char conversion time with respect to the changes in operational parameters*

| Fuel | % increase in $\tau_{cc}$ with increase in particle size from 8 to 25 mm | | | % decrease in $\tau_{cc}$ with increase in bed temperature from 800 to 950 °C | | |
|---|---|---|---|---|---|---|
| | *800 °C* | *875 °C* | *950 °C* | *+8-10 mm* | *+12.5-16 mm* | *+20-25 mm* |
| IC1 | 216 | 209 | 185 | 51 | 52 | 58 |
| IC2 | 219 | 216 | 169 | 80 | 84 | 85 |
| IDC | 227 | 169 | 159 | 80 | 84 | 86 |
| BM | 156 | 242 | 266 | 75 | 66 | 58 |

The magnitude of char conversion time can be directly related to the amount of fixed carbon present in the char, only if the fixed carbon (FC) value is far greater than the ash content (as in the case of IDC and BM). Based on the quantity of fixed carbon and ash content of the fuel, the following scenarios are possible.

(i)   If FC > ash value, fragmentation occurs, and the char conversion times come down. e.g. IC1;

(ii)    When FC < ash value, chars do not fragment, resulting in longer conversion times. e.g. IC2.

Therefore, the conversion time is clearly a characteristic of the fuel composition.

### 7.3.2    Char conversion levels at various residence times

The extent of char conversion is expressed in terms of mass loss percentage with respect to the initial sample mass, at various residence times of fuel char in the fluidized bed (Figures 7.3 and 7.4). The mass loss at char conversion time is denoted as 100% (except for IC2), since finer ash particles could not be retrieved using the basket technique. IC1 particles tested at 800 $^o$C show that the mass loss of 14.25 mm particles at any quarter of $\tau_{cc}$ is the highest and for 9 mm is the least. The 14.25 mm particles experience mass loss of about 30% in the first quarter of char conversion time itself. This is most probably due to the fragmentation of char immediately after devolatilization. In contrast, 9 mm particles lose much of their mass in the final quarter. Only moderate changes are observed when the operating bed temperature is varied. At 800 $^o$C, differences in the conversion levels among various sizes are observed at respective quarters. For higher bed temperatures, conversion levels rise steadily, without much differences irrespective of particle size. At 950 $^o$C, char conversion happens at a minimal rate for all sizes in the last quarter since 70% of the mass is lost by the end of second quarter and 90 % mass loss by the end of the third quarter. This implies that higher bed temperatures diminish the particle size effect and becomes a significant operational parameter when scale-up is considered.

In contrast to IC1, 14.25 mm of IC2 particles are the slowest ones to convert at all the bed temperatures and 9 mm particles exhibit faster conversion rates. The maximum mass loss experienced by IC2 is about 70% in the smallest size studied (9 mm) at 800 and 950 $^o$C and  about 15% mass loss is observed in the first quarter, which could probably be due to fragmentation since they do not fragment during devolatilization. Though fragmentation at 800 $^o$C is less favoured, longer residence times could support this comminution phenomenon, by means of impact on the reactor walls. As a result, particles of all sizes exhibit a mass conversion of more than 65% at 800 $^o$C. At 950 $^o$C, 14.25 and 22.5 mm particles experience mass loss of only about

60% (while the remained ash mass almost equals the stoichiometric ash quantity) at the end of char conversion time, evidently due to the short residence times of char particles.



*Figure 7.3 Char conversion of different sized IC1 and IC2 particles during various residence times at three different bed temperatures.*

Similar to the IC2 case, 9 mm particles of IDC also experience a higher conversion in the first quarter of char conversion time. 14.25 mm particles show a steady conversion at all bed temperatures, whereas the 22.5 mm particles show a higher slope of mass loss in the second quarter. A maximum deviation in $\tau_c$ at 800 °C between the smallest and largest size at end of any quarter is 11% which reduces to 8% at 875 °C. At 950 °C, the particle size effect on conversion time is almost non-existent, as observed clearly from Figure 7.4. Since IDC is a low ash fuel, the ash in the final quarter

could not be retrieved using the basket. The bottom ash or ash mixing in bed could be absent, providing a similar advantage as that of using pulverized fuel in combustion(Zhang 2013).
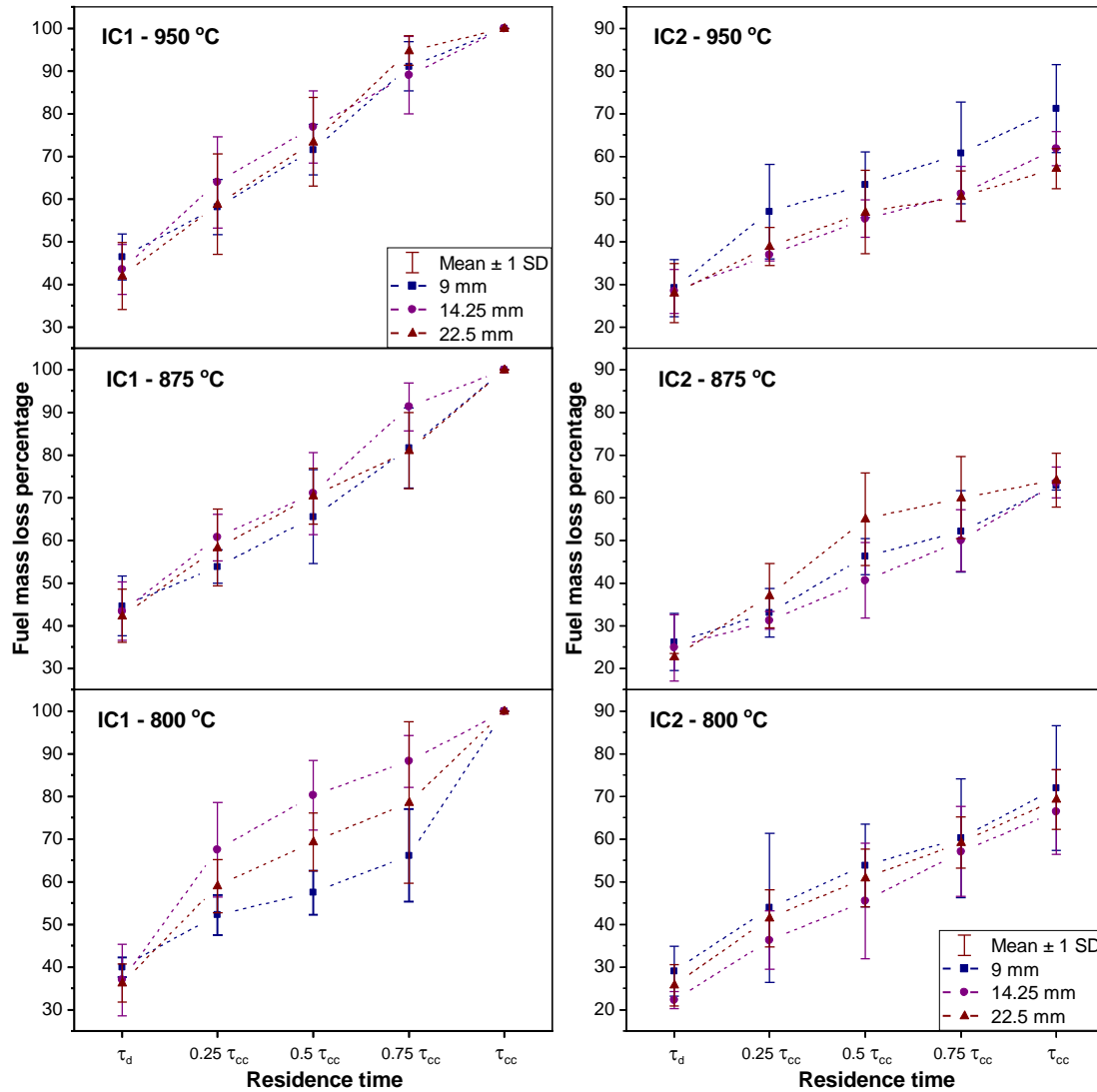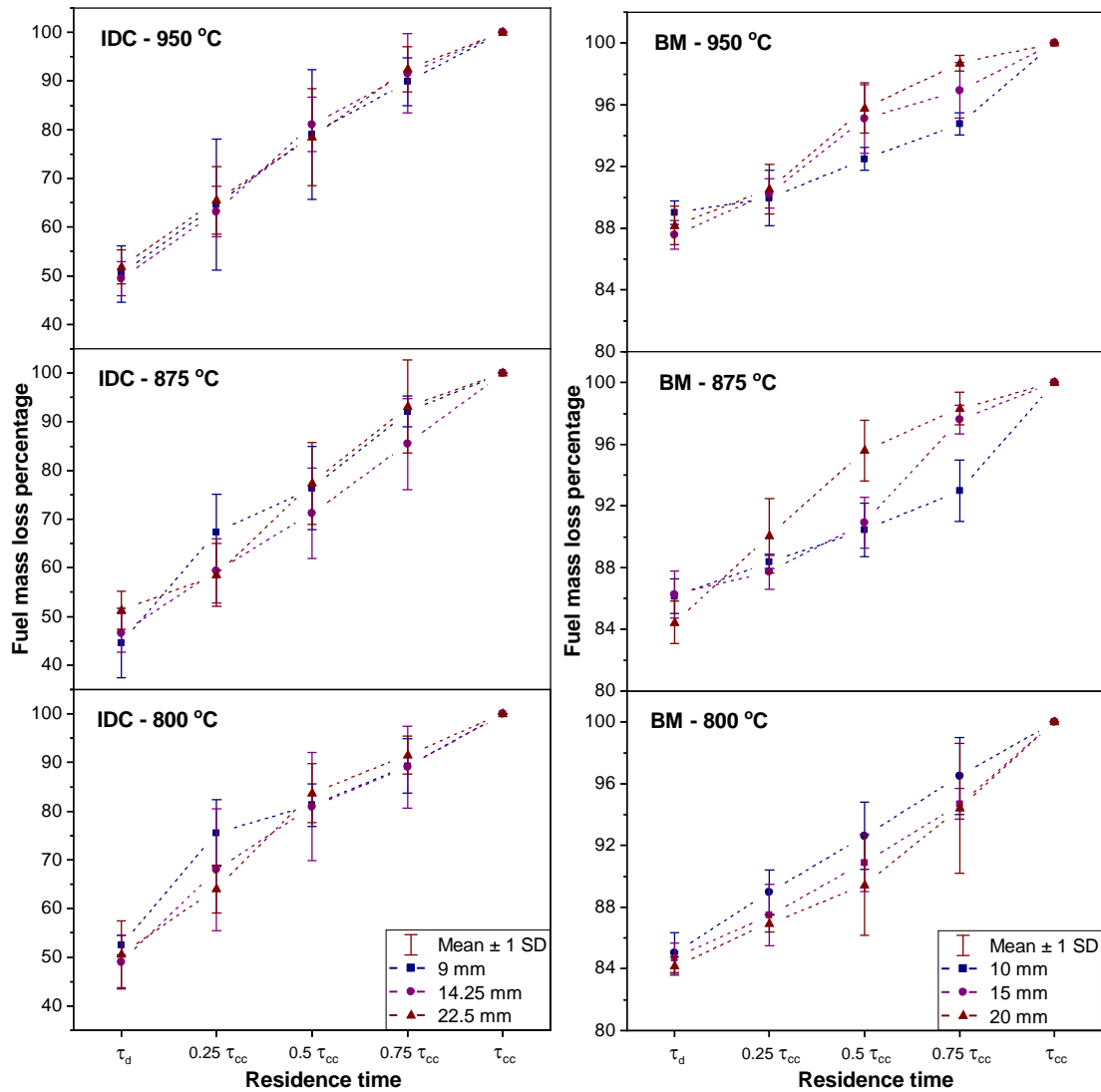


*Figure 7.4 Char conversion of different sized IDC and BM particles during various residence times at three different bed temperatures.*

Biomass particles exhibited limitations in char conversion with an increase in particle size at 800 $^{\circ}$C i.e. larger particles show relatively slower conversion. At higher bed temperature, the observation is contrary to the aforementioned pattern. Conversion levels of 14.25 mm chars tested at 875 $^{\circ}$C are comparable to that of 9 mm particles till the end of the second quarter, which later becomes closer to that of 22.5 mm chars. At the highest temperature, 22.5 mm particles exhibit higher levels of conversion

113

compared to other sizes, from the second quarter of char conversion time till the end of conversion. Being a low-density and low-ash fuel, biomass samples do not produce any bottom ash, and only fly ash fines are elutriated due to the attrition of fragments. The inherently high porous nature of the char and the increase in bed temperature enable higher conversion rates compared to coals.

For achieving a conversion of 50% of the fixed carbon present in char, IC1 particles spends the first two quarters of the char conversion time at 950 $^{\circ}$C. Whereas, at the lowest temperature, 50% conversion is reached only in the third or the fourth quarter. For IC2 particles, it occurs somewhere between the second and third quarter, while it mostly occurred in the second quarter for IDC. The 50% carbon conversion in biomass chars is achieved in the second quarter at 950 $^{\circ}$C and in the third quarter at 800, 875 $^{\circ}$C. Conversion levels at lower temperatures are controlled by particle size for all the fuel types. At 950 $^{\circ}$C, the effect of particle size is diminished, and a faster conversion rate is achieved at various stages of conversion.

### 7.3.3 Char Fragmentation

Alongside the carbon consumption, the ash skeleton continuously disintegrates into smaller particles, which further advances the char conversion rate. Char fragmentation unlike primary fragmentation (which happens out of intraparticular pressure build-up) is a phenomenon arising out of the deformation of carbon bridges that hold the char particle intact. As the fixed carbon is consumed by steam to form carbon monoxide and hydrogen, the weakest link becomes the point of crack initiation and this further propagates with progressing conversion and collision impacts. To represent the aspects of char fragmentation, the indicators which are used earlier in the primary fragmentation study (Pragadeesh and Sudhakar 2018) are borrowed.

### 7.3.3.1 Percentage of fragmentation

The likeliness of a fragmentation event for a fuel sample during char conversion time during a particular time interval is expressed by the percentage of fragmentation (PF). PF is defined as the ratio of the number of samples getting fragmented to the total number of samples tested (Equation 7.1). Although PF could be seen less than 100 % during certain time intervals, all the fuel samples tested in this study experienced

fragmentation event at least in one or the other quarters of char conversion time. Figures 7.5 and 7.6 show the percentage of fragmentation events that occur during various conditions of char conversion.

$$PF = \frac{Number\ of\ samples\ that\ undergone\ fragmentation}{Total\ number\ of\ samples\ tested\ at\ particular\ operating\ conditions}\ x\ 100\%.........(7.1)$$
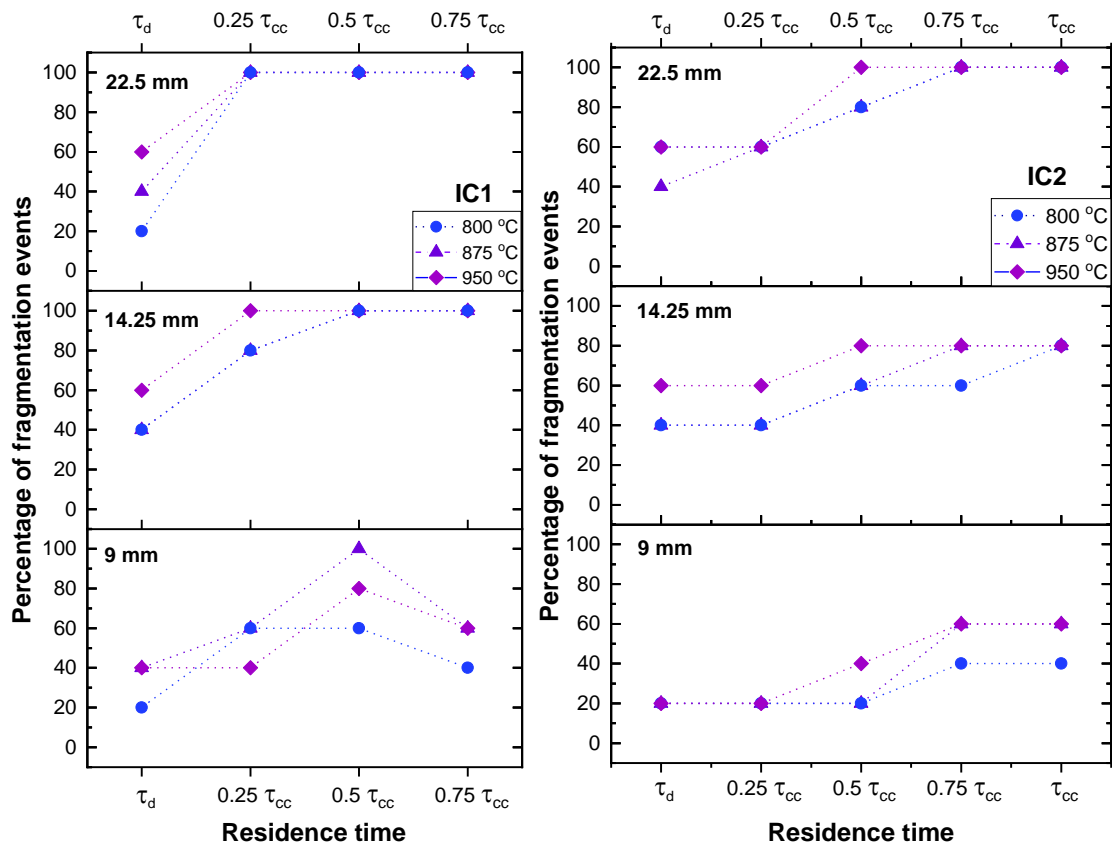


**Figure 7.5 Percentage of fragmentation events during char conversion of IC1 and IC2 of various sizes at three different bed temperatures.**

The occurrence of char fragmentation events is more likely with the increase in residence time, particle size and moderately with respect to increasing bed temperature. The 9 mm particles of IC1 achieve PF of 100% only at 950 °C during the second quarter. The effect of bed temperature in 9 mm particles is highest for 875 °C, which is aided by longer residence time. All the higher sized particles fragment in the first quarter itself but with an exception to 14.25 mm samples at 800 °C. It is noticed that PF decreases in their respective subsequent quarters, after a 100% mark in an earlier quarter. This is because of the complete burnout of smaller char particles and the

number of fragments generated by successive fragmentation does not cross the maximum count reached earlier.
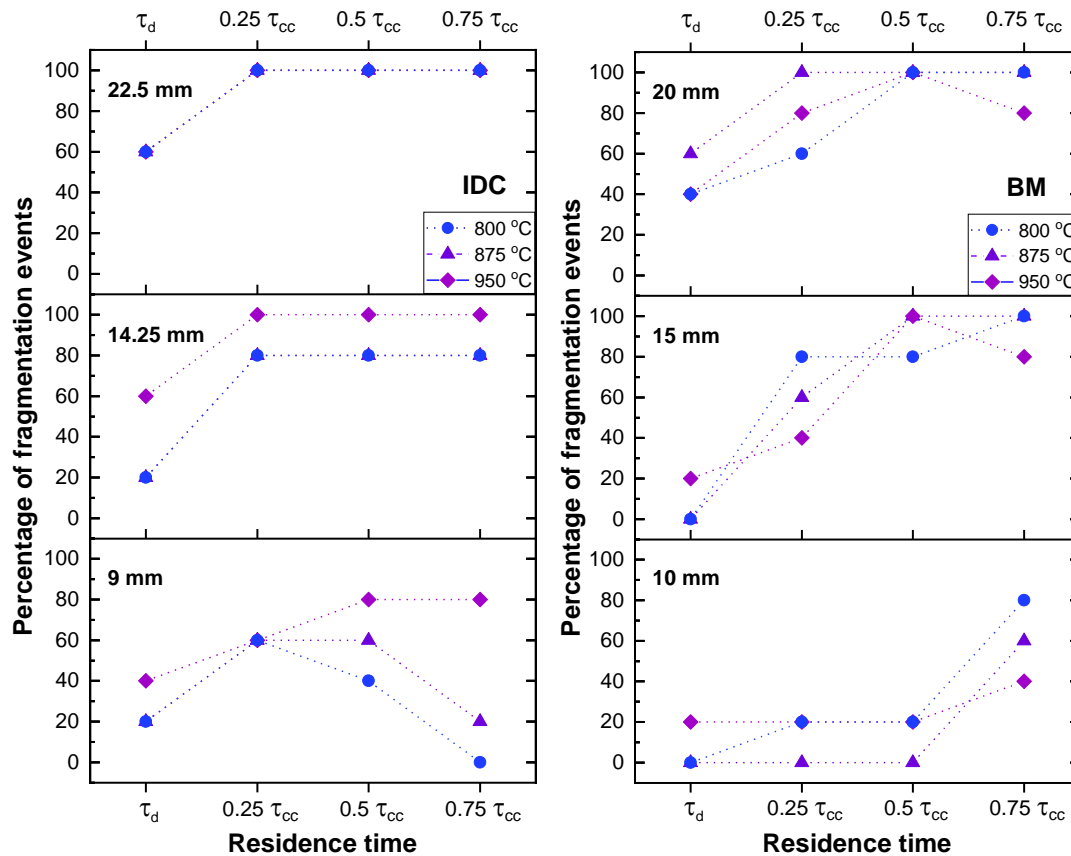


***Figure 7.6 Percentage of fragmentation events during char conversion of IDC and BM of various sizes at three different bed temperatures.***

The maximum PFs observed in IC2 are 60, 80 and 100%, respectively in 9, 14.25 and 22.5 mm particles. For 9 mm particles, the maximum value is recorded during the third and fourth quarters, whereas it is the second quarter for larger particles. The maximum PF of 14.25 mm samples is observed in the last quarter at 800 °C, which prepones to an earlier quarter at 875 °C, eventually moving to the second quarter for the highest temperature of 950 °C. Similarly, PF of 22.5 mm particles at 950 °C reaches their maximum in one quarter earlier than their low-temperature counterparts. This implies that temperature is the most influencing parameter for the char fragmentation of IC2.

The PF trends of IDC resembles IC1 but with an exception for 9 mm particles. The smallest sized samples do not have a 100% chance of fragmentation at any of the

bed temperatures and a maximum of only 80% fragmentation is observed, only at 950 $^{\circ}$C. The 14.25 mm particles achieve 100% fragmentation only at 950 $^{\circ}$C, whereas all the 22.5 mm particles undergo fragmentation in the first quarter itself and continue to fragment till the last quarter irrespective of changes in bed temperature. For IDC chars, particle size heavily influences the fragmentation probability, whereas the influence of bed temperature is severe in smaller sized particles.

The PF of the porous biomass chars are in contrast to that of the coals i.e. 950 $^{\circ}$C appears to be the least influencing bed temperature and samples at 800 $^{\circ}$C show the maximum PF values. This might be due to one or more of the following causes viz. (a) longer conversion times at low temperatures, resulting in the generation of irretrievable char fines, (b) quick conversion favoured by high temperature. Chars of 10 mm size are likely to follow the case (a) since very fine chars are easily produced by smaller sized chars, and the higher sized chars follow the case (b) till the third quarter. A maximum of 80% PF is noticed in 10 mm samples in the third quarter and the samples of 15 and 20 mm sizes achieve 100% PF in the second quarter at 950 $^{\circ}$C. The PF values of the later sizes at 950 $^{\circ}$C in the subsequent quarter after they reach the maximum, whose cause is the earlier mentioned case (b). All 20 mm particles fragment in the second quarter irrespective of the bed temperature. The common observation among all the fuels is that the largest sized particles completely undergo fragmentation irrespective of the bed temperature, while the effect of bed temperature is observed more in the smaller particles, which have the least chances of getting fragmented.

### 7.3.3.2 Frequency and timing of fragmentation

Frequency of fragmentation (FF) denotes the number of times the char gets fragmented during the char conversion phase. The timing of fragmentation (TF) details the time interval in which the fragmentation event occurs. The FF and TF values of various fuels are given in Figures 7.7 and 7.8. The sum of the number of fragmentation events in each plot gives the frequency. IC1 particles of all sizes have a frequency of 2 at 875 and 950 $^{\circ}$C within the first two-quarters of $\tau_{cc}$, whereas at 800 $^{\circ}$C, only 22.5 mm particles have a frequency of 2 in the same time interval. The smaller sized particles at 800 $^{\circ}$C fragment only in the first quarter. Thus, char fragmentation of IC1 occurs in the initial stages of the char conversion phase.

***Figure 7.7 Frequency and the timing of fragmentation during char conversion of IC1 and IC2 of various sizes at three different bed temperatures.***

From Figure 7.7, all IC2 particles are observed to fragment in the first quarter of char conversion time at all bed temperatures, confirming the 15% mass loss in 9 and 14.25 mm particles observed in the first quarter. The largest sized particles (22.5 mm) at any given condition have a fragmentation frequency of 3, which occurs during first, third, and fourth quarters. This implies that devolatilization induced crack formation results in the first event of breakage in the first quarter of char conversion time. Then, the carbon bridges become too weak to dissociate the particles only in the later quarters of char conversion time. The smaller sized ones have a maximum frequency of 2 at all bed temperatures. The second fragmentation event of 9 mm particles prepones from last quarter at 800 ℃ to third quarter at 875 ℃ and then to the second quarter at 950 ℃. Hence, the particle size holds a good influence over TF and FF whereas the effect of change in bed temperature is recognised only in 9 mm samples, alike the case of PF.
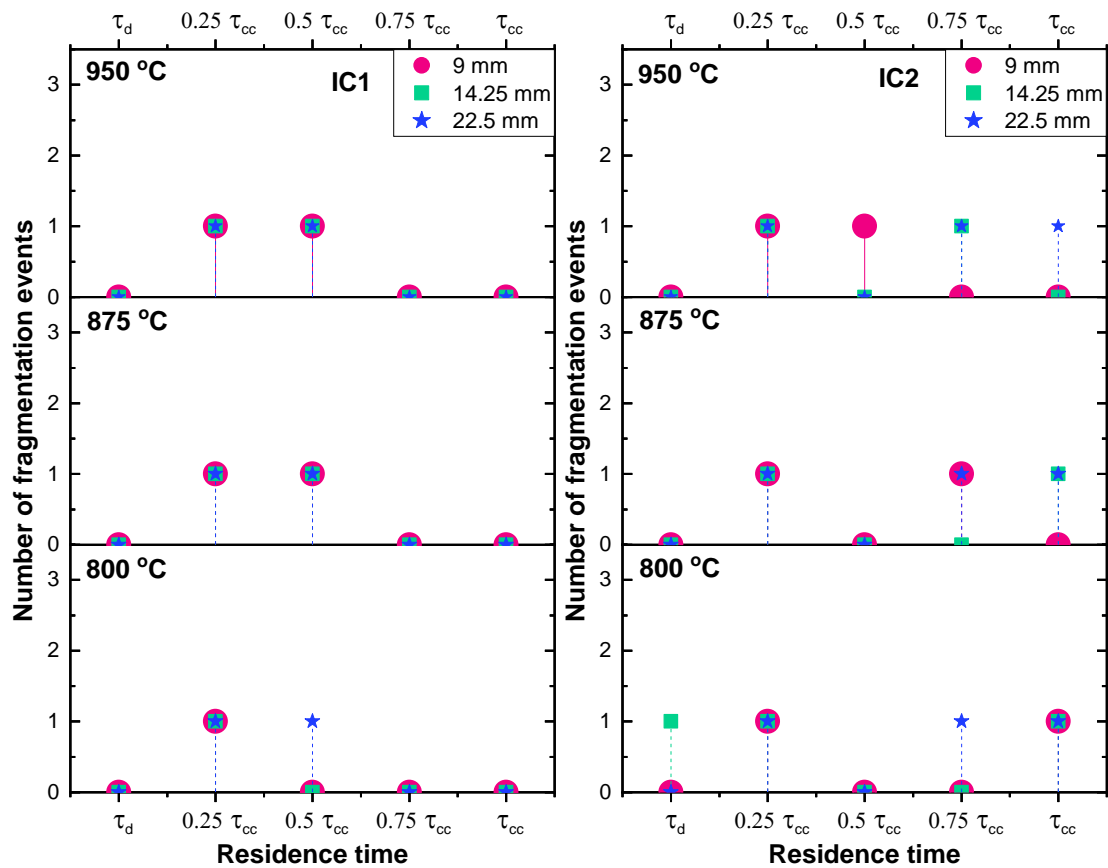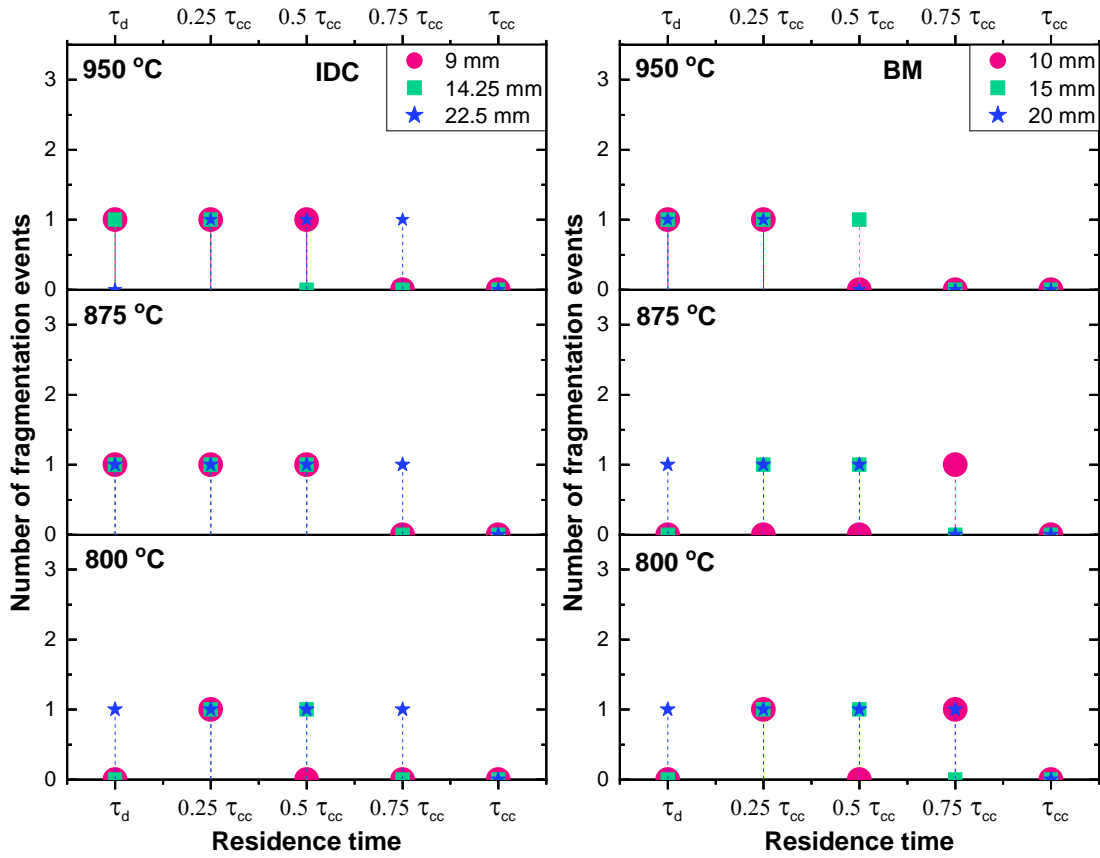
*Figure 7.8 Frequency and the timing of fragmentation during char conversion of IDC and BM of various sizes at three different bed temperatures.*

The largest-sized IDC particles, like IC2, also have a constant frequency of 3 and timing of fragmentation (first three quarters) at all temperatures of study. 9 mm particles have only one event during the first quarter at 800 °C, and the FF increases to 2 in the second quarter at higher temperatures. The medium-sized ones have a maximum FF of 2, only at 875 °C, and a value of 1 in other conditions. These results indicate that bed temperature has a mild effect on FF, meanwhile particle size has a greater influence on both FF and TF.

Similar to coals, 20 mm biomass chars have a maximum FF of 3 at the lowest temperature of study and decrease by the value of 1 for each higher temperature. Also, fragmentation occurs in the first three quarters while it is limited to the second and first quarters at 875 and 950 °C respectively. The 15 mm chars are consistent in both FF (of 2) and TF (first 2 quarters) at all temperatures. The 10 mm chars fragment only once in the first quarter at 950 °C and in the third quarter at 875 °C. But an FF of 2 (first and

third) is observed for 800 °C because of the longer residence times and no event of primary fragmentation. Compared to the devolatilization phase, smaller fuel particles are observed to fragment more during char conversion (Pragadeesh and Sudhakar 2018). This is attributed to the fact that a relatively lower thermal stress developed in smaller particles than the larger-sized particles during devolatilization, deferring the fragmentation event to the char conversion regime (Syred et al. 2007). Bed temperature is the most influencing factor of fragmentation frequency of biomass particles whereas the particle size greatly affects the timing of fragmentation.

### 7.3.3.3 Number of fragments

The number of fragments (NF) or the particle multiplication factor is defined by Equation 7.2 as follows.

$$NF = \frac{Number\ of\ particles\ present\ at\ a\ specified\ residence\ time}{Number\ of\ particles\ introduced\ initially\ into\ the\ combustor} \dots\dots\dots\dots\dots\dots(7.2)$$

The number of fragments (NF) generated by the fuels tested is given in Figures 7.9 and 7.10. As observed in primary fragmentation studies (Pragadeesh and Sudhakar 2018), an increase in NF with the increase in particle size is noticed, which is further boosted by the increase in bed temperature. Table 7.2 quantifies the increment of NF with respect to increase in particle size and bed temperature. The larger sized samples fragment relatively more at 950 °C than at 800 °C, when compared to the smaller sized ones. This behaviour of smaller particles can be attributed to the relatively lesser residence time than at lower temperatures. Nevertheless, the contrasting trend of 22.5 mm samples could be due to the tertiary fragmentation events occurring in the secondary daughter fragments.

As the IC1 particles reach half of their $\tau_{cc}$, they fragment further into smaller fractions which mostly get converted quickly. After the maximum NF is observed at a certain time interval, the subsequent decrease in NF cannot be interpreted as no event of further fragmentation. After this point of time, percolative fragmentation is more likely to happen, which is inferred from the number of fines (as sparkles) elutriating to the freeboard during the experiments, but not always from the counts using the basket retrieval technique. This is the primary reason for the observation in largest sized

particles (22.5 mm) yielding high NF in almost all fuels, as the size of the fragments is large enough to be retained in the basket.



***Figure 7.9 Number of fragments generated during char conversion of IC1 and IC2 of various sizes at three different bed temperatures.***

Among the coals, IC2 displays a different trend in NF values during char conversion. Either a constant or a gradually increasing slope in NF for increasing residence time is observed in all sizes of IC2 and biomass at all bed temperatures, till the NF is maximum (Figures 7.9 and 7.10). Biomass particles have a unique characteristic of lower NF count at the highest bed temperature, probably due to the generation of numerous fines and their immediate conversion. IDC is found to be the most sensitive fuel (in terms of char fragmentation) to the changes in particle size and

bed temperature. Also, it generates the highest number of char fragments, owing to its high carbon and low ash composition. IC2, despite having a high fixed carbon, does not disintegrate much because of its uniformly distributed mineral matter throughout the char structure(Pragadeesh and Sudhakar 2018).
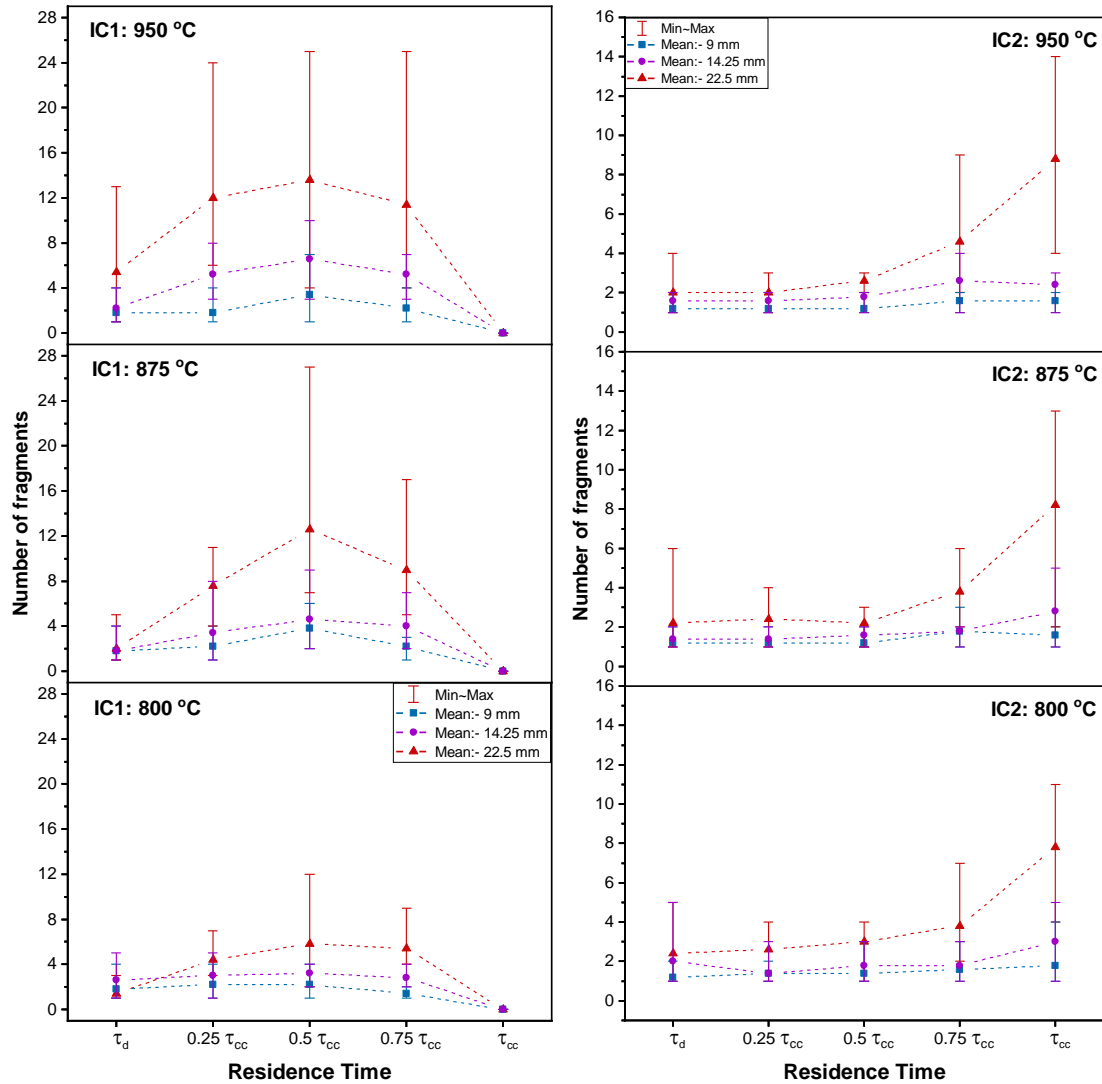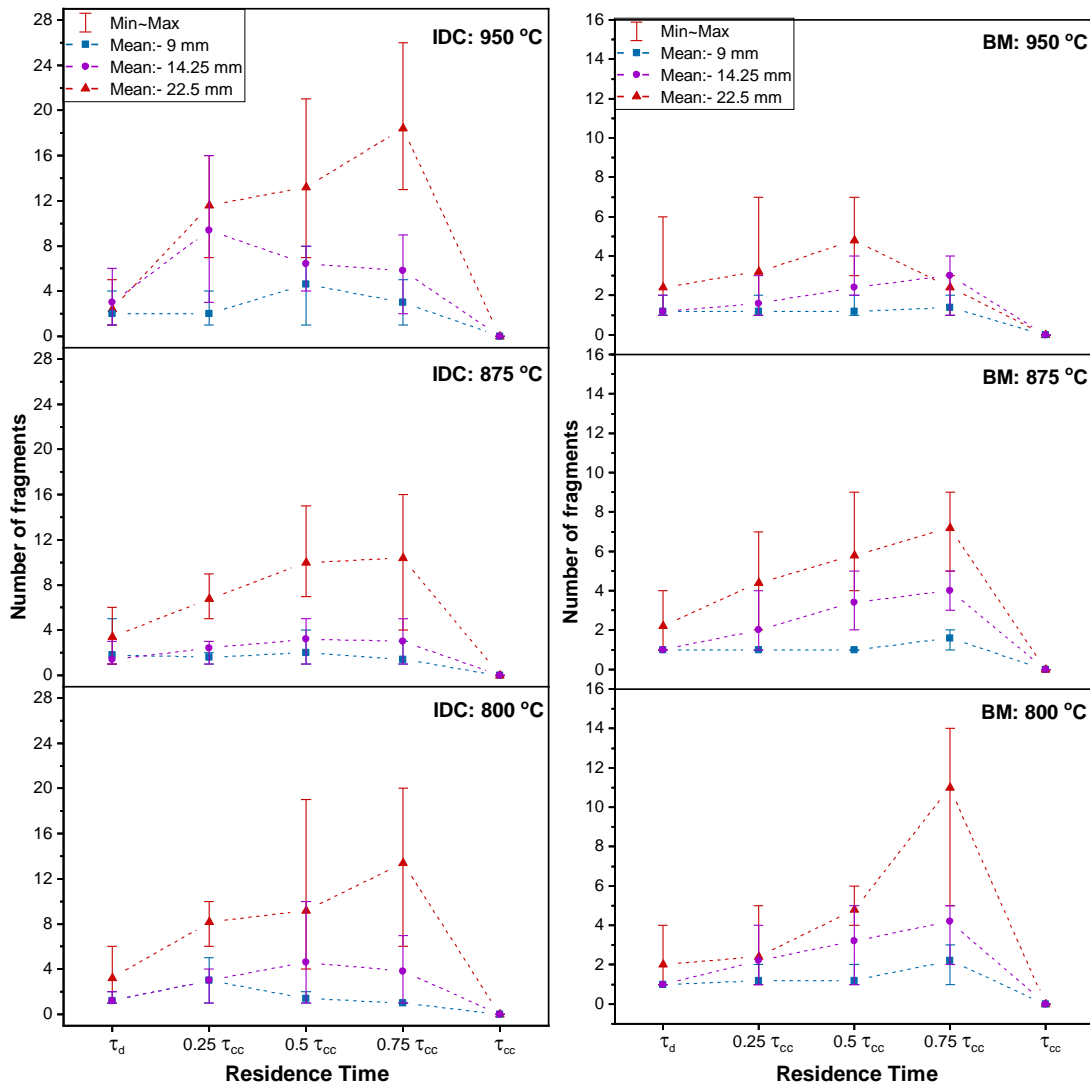


***Figure 7.10 Number of fragments generated during char conversion of IDC and BM of various sizes at three different bed temperatures.***

*Table 7.2 Changes in number of fragments generated with respect to the changes in operational conditions.*

| Fuel | No. of folds increase in NF with increase in particle size from 9 to 22 mm | No. of folds increase in NF with increase in bed temperature from 800 to 950 $^{\bullet}C$ | Maximum NF (average) | Residence time quarter of the maximum NF |
|---|---|---|---|---|
| IC1 | 2.64 – 5.67 | 1.57 – 2.34 | 14 | Q2 |
| IC2 | 1.67 – 5.5 | 1.13 – 1.3 | 9 | Q4 (Q3 for 9 mm at 875 $^{o}$C and 14.25 mm at 950 $^{o}$C) |
| IDC | 4 – 8.2 | 1.71 – 2.94 | 18 | Q1 for 9 mm at 800 $^{o}$C and 14.25 mm at 950 $^{o}$C; Q2 for 9 and 14.25 mm; Q3 for 22.5 mm particles |
| BM | 2 – 5 | 1.2 – 2.29 | 11 | Q3 (Q2 for 20 mm at 950 $^{o}$C) |

### 7.3.3.4 Fragmentation index

Fragmentation index (FI) is an important indicator of fragmentation which combines the effect of number of fragments and the particle size of fragments generated. It is given by the following Equations 7.3 and 7.4, as

$$\textbf{\textit{Fragmentation index, FI}} = \frac{No.of\ fragments\ (NF)}{Variation\ factor\ of\ feed\ particles\ (F_d)}\dots\dots\dots(7.3)$$

$$F_d = \sum_{i=1}^{n} \frac{X_i d_i}{d_a}\dots\dots\dots\dots\dots\dots\dots\dots(7.4)$$

where $X_i$ is the mass fraction of particle fragment of diameter, $d_i$; $d_a$ = average particle diameter of the particles subjected to devolatilization.

Though the trends of FI are analogous to NF, they express the tangible impact of the fragmentation phenomenon on the char conversion process. The calculated FI

values of the fuels tested at various conditions are presented in Figures 7.11 and 7.12. Inferring from all the indicators defined, the larger particles display a higher degree of comminution. The principal cause of this behaviour is the relatively higher thermal stress accumulated in the large particles, resulting in stronger dissociating forces during the initial instants of fuel conversion (Krishnamoorthy et al. 2017; Sreekanth et al. 2008a). The development of high thermal stress with an increase in bed temperature favours the fragmentation process in most cases (Chirone et al. 1988, 1991).



*Figure 7.11 Fragmentation index of different sized IC1 and IC2 particles during various residence times at three different bed temperatures.*

The magnitude of changes to the original size of the char due to fragmentation is highest for IDC (~80), followed by IC1 (~50), BM (~35), and IC2 (~20). The increase in bed temperature has a positive influence on FI in IC1 and IDC while its effects are opposite in IC2 and BM. Since the ash skeleton in the former is not strong enough to

124

hold the particle intact, it disintegrates at the weaker spots created during carbon conversion. Biomass particles also follow the same suit which is apparently observed in 800 ºC. Since higher bed temperatures aid an easier consumption of fixed carbon in the highly porous char particles, the surface carbon gets converted spontaneously when contacted with the oxidising environment. This leads to an interpretation that no new char fragments are formed, and thus, low FI are obtained at 875 and 950 ºC for IC1 and IDC samples during the final char conversion quarter. Thus, char fragmentation is dominantly influenced by particle, followed by the bed temperature.
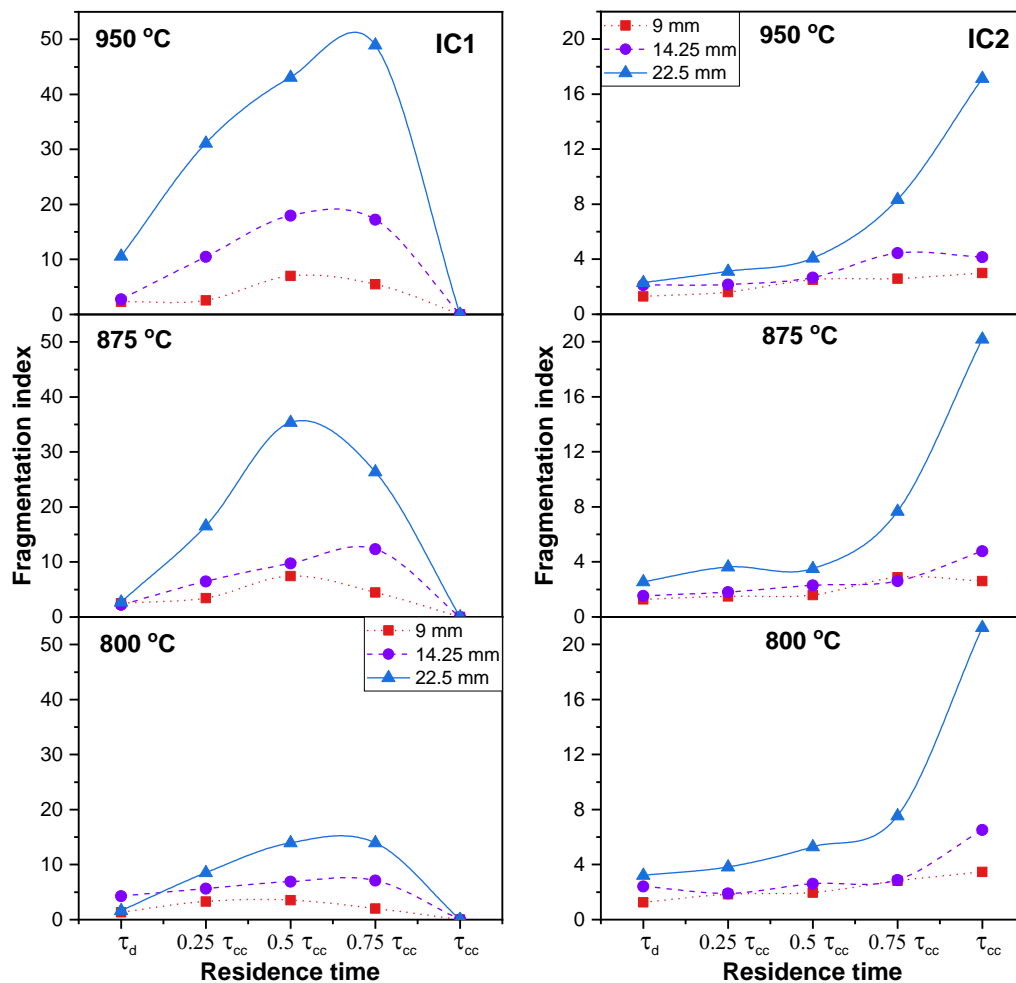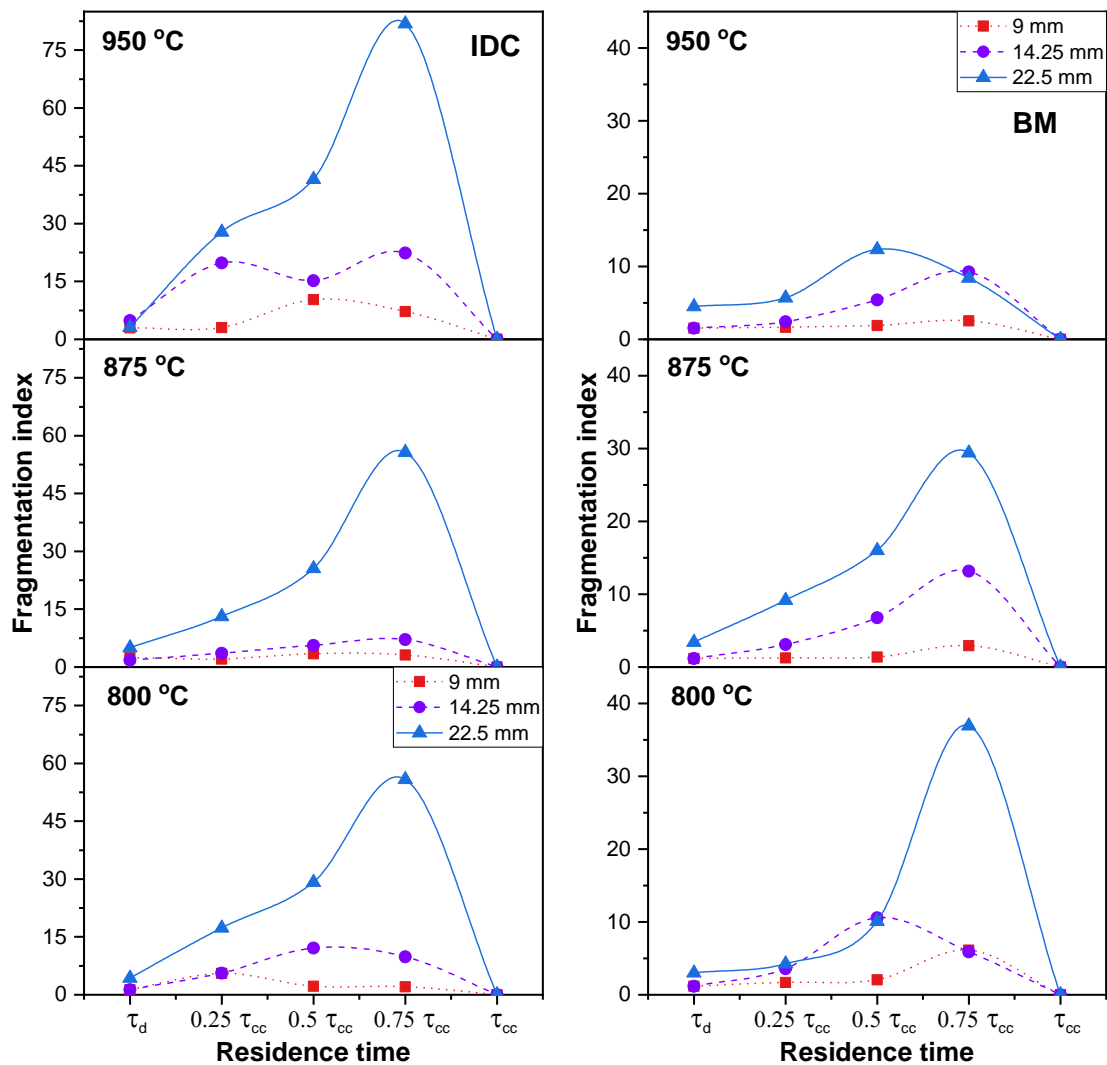


***Figure 7.12 Fragmentation index of different sized IDC and BM particles during various residence times at three different bed temperatures.***

### 7.3.3.5 Particle size distribution

The particle size distributions of fragments generated during the char conversion period of IC1, IC2, IDC and BM at 950 °C are presented in Figures 7.13, 7.14, 7.15 and 7.16 respectively, and the PSD corresponding to the bed temperatures of 800 and 875 °C are provided in Figures A10 to A16. The particle sizes of char fragments are represented in terms of mass equivalent diameter (Sudhakar et al. 2008). As reported in the earlier sections on PF and NF, an increase in particle size increases the number of fragments, while most of the fragments generated fall into sizes less than 50% of the original size of actual fuel introduced. Among all the fresh fuel chars obtained at the end of devolatilization, the largest char fragments of 9 and 22.5 mm particles retain almost 60-70% of the original size, at the lowest bed temperature (800 °C). As the conversion progresses and with the increase in bed temperature, a continuous decrease in the char fragment size is observed.

Size distribution plots of IC1 show that the 9 mm particles have reduced to half of their original size in the second quarter itself and even the largest particle at the end of the third quarter is less than 50% size. The largest fragment in the final quarter of 14.25 mm set is found at its 40% size, while that for 22.5 mm is just 35% of the original. These 22.5 mm particles generated a larger number of smaller fragments compared to the lower sized feed samples. The largest particle of fresh chars from 14.25 and 22.5 mm feed particles reduces to their half sizes by the end of the first quarter. As IC2 chars are noticed to fragment less, they generate a majority of fragments in sizes more than 50% of their original, till the end of char conversion. At all bed temperatures, the largest sized particles show significant size change in the first quarter after devolatilization, whereas the smaller sized samples show significant size change in the last quarter of char conversion time. In contrary to the comminution behaviour of other fuels studied, the largest fragments in the final quarter are bigger at a higher temperature, retaining about 60-70% of their original sizes. At 800 °C, the char conversion time is longer than those at other temperatures which lead to the massive breakdown of particles, particularly in 22.5 mm sizes. These types of high ash Indian coals have to be reduced to less than 10 mm for their use as fuel in CLC. The ash particles generated by IC2 are mostly non-elutriable and stay as such in the bed without considerable comminution,

which could cause problems in fluidisation and difficulty in separating them from the oxygen carrier bed. Thus, the size reduction range must be optimised for easier ash segregation during CLC operation using IC2.

IDC chars reduce to nearly about their half sizes in the first two-quarters of char conversion. After this point of time, char fragments generated are in the size range of the immediate lower feed size (fragments of 14.25 mm for 22.5 mm feed). However, as the particle numbers are large, the time taken for conversion for these smaller fragments (fragments of 22.5 mm in ~14.25 mm size) is found to be more than that of the original smaller size feed char (14.25 mm feed char). This is inevitable because of the lacking reactant concentration, as the particle count increases. In these conditions, the conversion rate could be improved by a higher velocity of oxidizing agent (steam) and as well as by altering the fuel feed rate, depending on the particle size. An increase in bed temperature significantly affects the fragment size distribution only in the smallest sized (9 mm) samples. Hence, it can be perceived that the bed temperature has a meagre influence on the fragmentation of IDC.

As a fuel of different nature, BM chars produce fines larger than 2 mm only till the second quarter. The retrieved fragments during the third quarter are of near sizes (4-6 mm). As the char conversion times are longer at 800 $^{o}$C compared to other bed temperatures, the small and medium-sized particles experience more breakage. But the chars of 20 mm samples at 950 $^{o}$C tend to reduce in size about the same extent as that of the smaller sizes at 800 $^{o}$C. This behaviour favours the usage of these large-sized particles in the reactor without size reduction.

*Figure 7.13 Particle size distribution of IC1 particles of three different sizes during various residence times at 950 °C.*

***Figure 7.14 Particle size distribution of IC2 particles of three different sizes during various residence times at 950 ºC.***
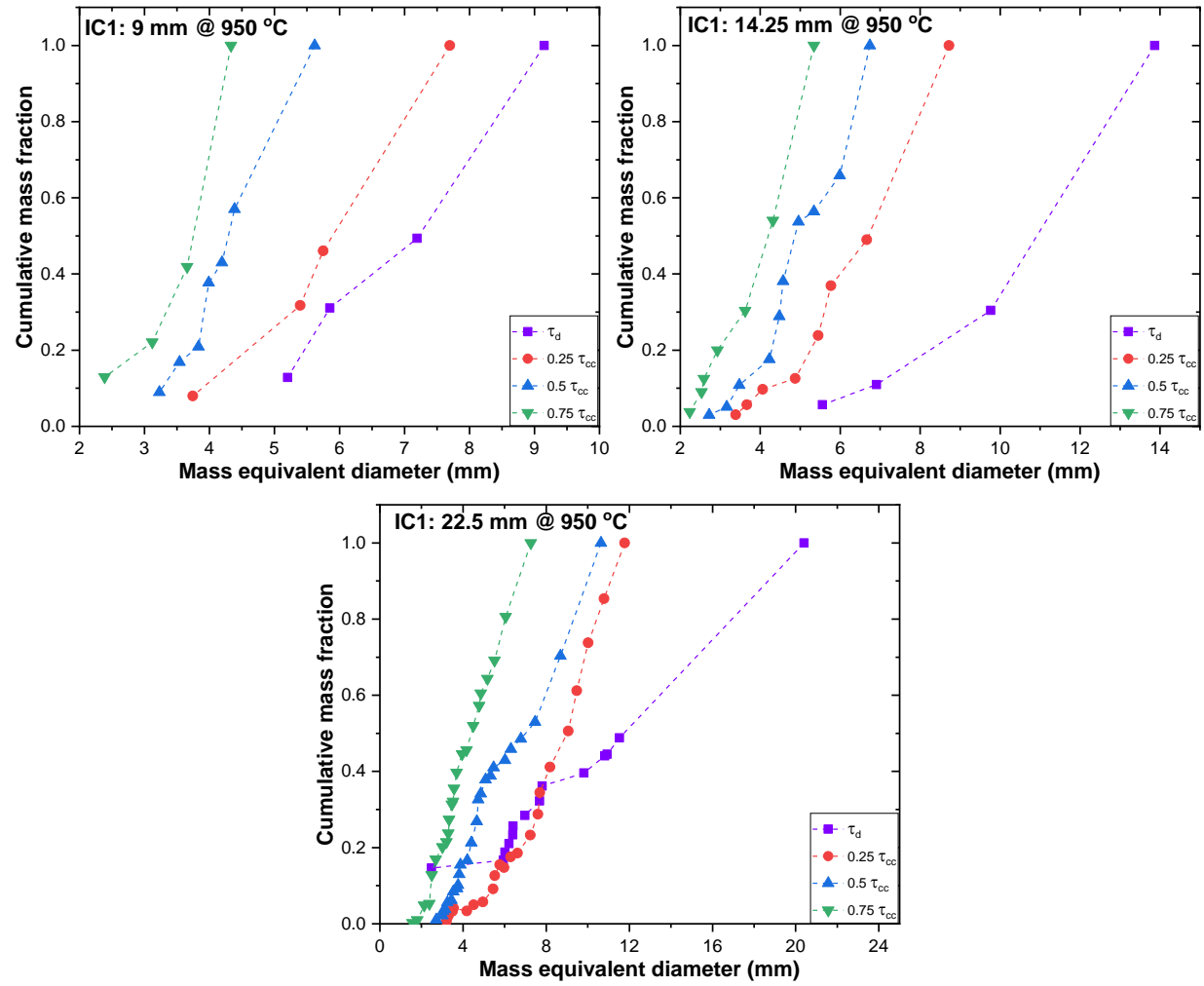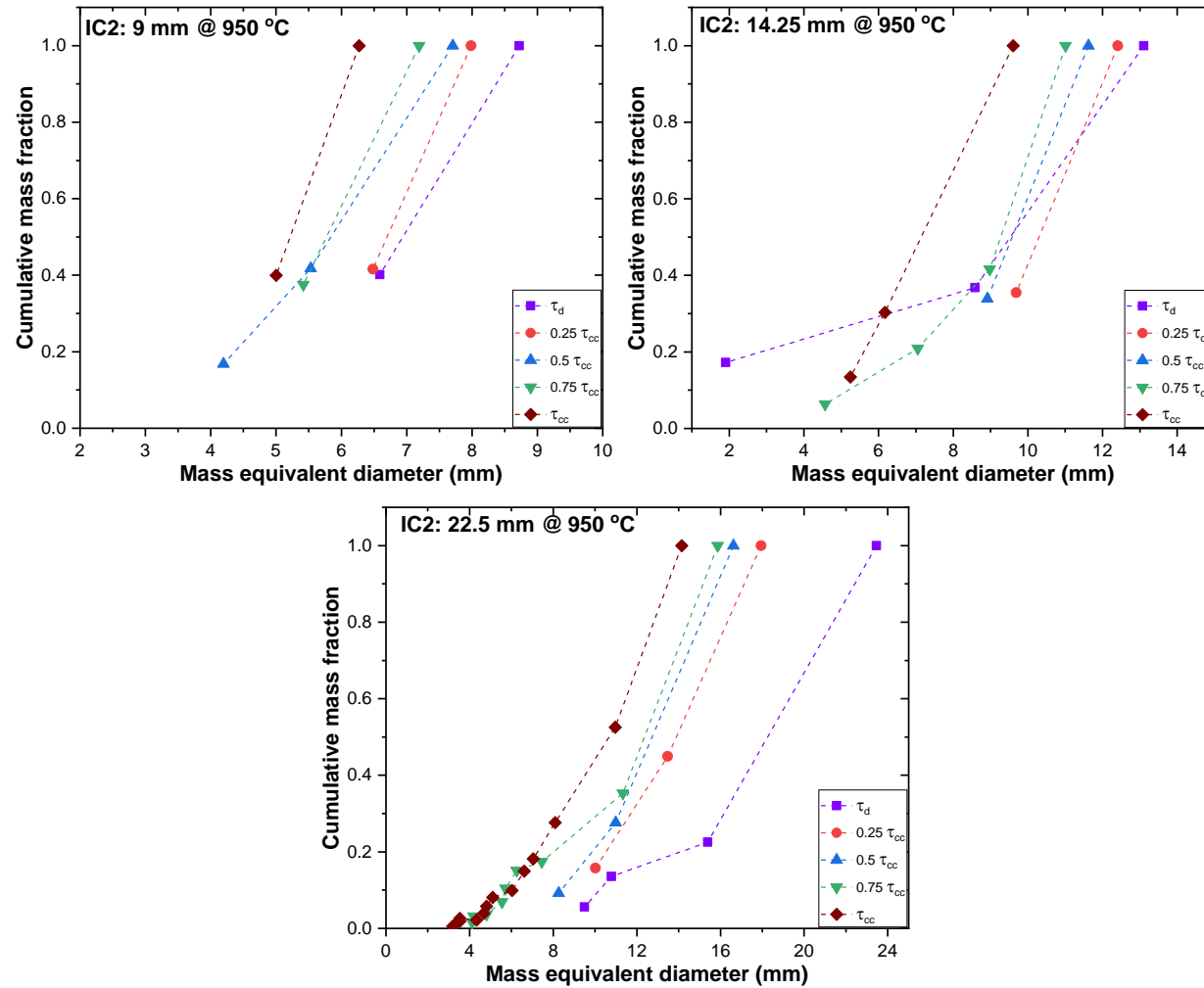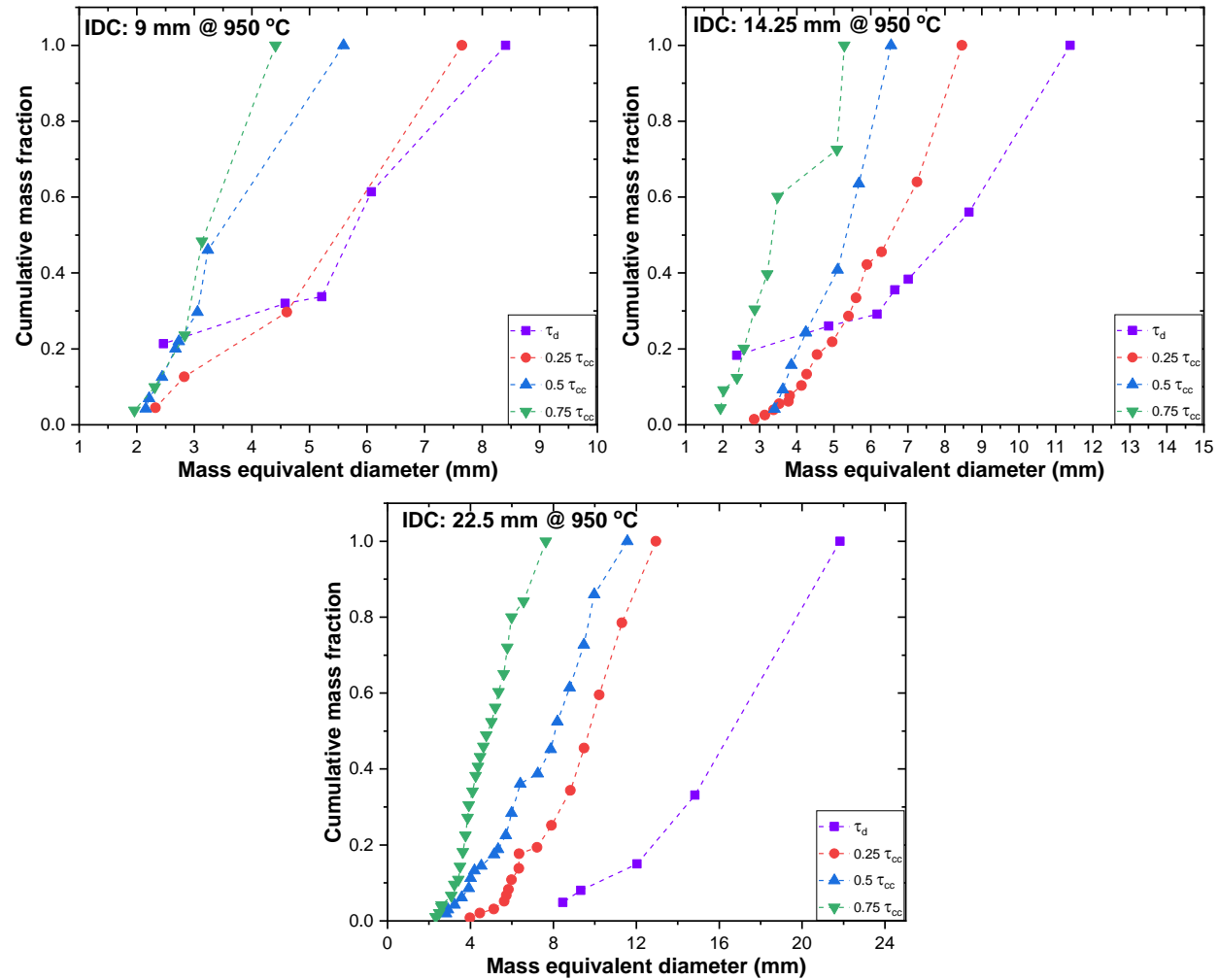
*Figure 7.15 Particle size distribution of IDC particles of three different sizes during various residence times at 950 °C.*
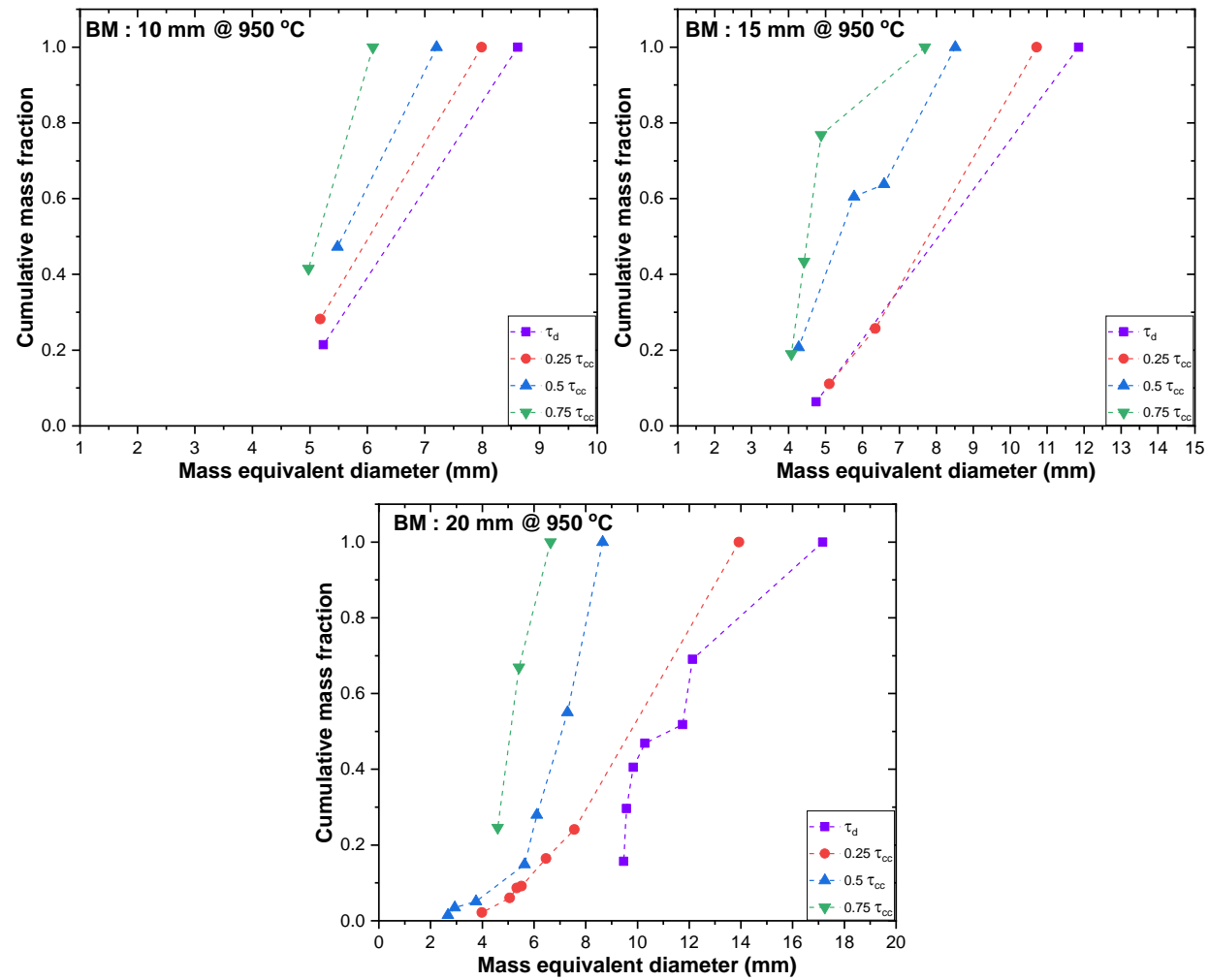
*Figure 7.16 Particle size distribution of BM particles of three different sizes during various residence times at 950 °C.*

It is observed that coals with high volatile content that generate more fragments in the primary fragmentation continue to fragment similarly in the char conversion regime as well. Though biomass does not fragment much during devolatilization, the char fragmentation is significantly visible after its first quarter of char conversion time. But, the IC2 is too hard to get fragmented (Pragadeesh and Sudhakar 2018), making it an unfavourable fuel type for its application in larger sizes. All the other fuels can be used in CLC operations at higher temperatures (say 950 °C) irrespective of their sizes depending on the oxygen carrier and the gas composition (ratio of gasification agents) requirements. As most of the tested fuel particles (except that of IC2) reduce to less than half of their initial sizes within the first two quarters due to fragmentation, the rate of char conversion is effectively increased. This in-process size reduction improves the conversion efficiency and allows to increase the fuel feeding rate. However, in cases where the char conversion rate becomes too slow, the fuel inventory should be increased accordingly, by keeping in account of the resulting changes of fluid dynamics and the overall solid inventory.

Results of this study suggest the existence of a critical minimum fragment size below which the char fragmentation by impact event is not feasible. In this study, it is considered as the size of the largest particle in the last quarter of char conversion where particles are retrievable. The critical size for IC1 is about 4.4 – 7.3 mm, and 4.4 – 7.6 mm for IDC, 6.1 – 7.7 mm for biomass, where the lower and higher values correspond to the smallest and largest feed sizes, respectively. Distinctive critical values are obtained in the case of IC2 particles i.e. 6.3, 9.6, and 14.2 mm for 9, 14.25 and 22.5 mm feeds respectively, due to a possible fragmentation resistance created by its inherently high-ash nature.

Although feeding the large-sized fuel particles could minimise the loss in carbon capture efficiency, the unconverted finer char fragments are likely to escape from the fuel reactor without getting converted completely. The char escape could be handled using a carbon stripper between the fuel reactor and the air reactor, and as a result, the carbon capture efficiency is maintained. To ascertain the amount of unconverted carbon exiting the fuel reactor, further detailed investigation on the finer chars is necessary. In bubbling regime, like the case of the present study, the amount of unconverted fines in

fuel reactor exit might be relatively lesser than the turbulent transport regime, whose critical size of particle elutriation would be comparatively larger. Irrespective of the quantity of unconverted char entraining the fuel reactor, the presence of carbon stripper could enhance the carbon capture efficiency (Adánez et al. 2018). Also, Abad et. al (Abad et al. 2017) found that the bubbling bed fuel reactor could deliver a relatively higher degree of oxidation of gasification products than the volatile matter. When the bubbling bed fuel reactor is connected to a riser that transports solids to the carbon stripper, high carbon capture and combustion efficiencies are achieved, while provided with a high solids inventory (Lyngfelt and Linderholm 2017; Markstrom et al. 2014; Markström et al. 2013; Song and Shen 2018). Parallelly, circulating fluidized bed fuel reactors are preferred for a better degree of volatile matter conversion and their flexible nature(Abad et al. 2015; Adánez et al. 2018; Song and Shen 2018). Therefore, depending on initial fuel particle size, fuel's fragmentation behaviour and terminal settling velocity of solid particles, the fuel conversion and $CO_2$ capture efficiencies in the fuel reactor could be optimised by altering the fluidization velocity and the solids inventory(Song and Shen 2018). This would also necessitate design/operational changes in the carbon stripper and the oxygen polishing equipment accordingly.

### 7.3.3.6 Modes of char fragmentation

Fuel particles undergo primary fragmentation during devolatilization and further experience char fragmentation in a relatively more systematic way such as structural weakening and percolation. The fragmentation patterns observed in various types of fuels are shown in Figures 7.17, 7.18, 7.19 and 7.20. IC1 particles (Figure 7.17) which showed a primary fragmentation originating from the core due to volatile(Senneca et al. 2013), continue to break down into finer fragments and exfoliate into flakes(Bareschino et al. 2020). Further conversion weakens the particles and dismembers them into carbon islands. The fines generated in this process get converted spontaneously, while the ash gets elutriated. Additional cracks form across the surface and the aforementioned fragmentation pattern is noticed. The breakage by percolation takes place in the third and final quarters and the upsurge in the rate of conversion was observed due to the production of numerous fines.

IC2 particles experience the char fragmentation along the cracks formed along the fault planes, in the first quarter (Pragadeesh and Sudhakar 2018). Smaller fragments in the form of flakes or fines are generated correspondingly by chipping of the outer surface or by impacts and abrasion. Because of the high ash content, additional fragments are likely to form only in the zones of homogenous carbon distribution where the weak sites of fragmentation are created by carbon burn out. As the largest fragment nearing its complete conversion in the last quarter, the weaker-small fragments are broken apart by their impact on the reactor wall and by the abrasion during fluidisation.

Exfoliation into thin flakes and fines

Conversion of fines and weakening of structure with multiple cracks

Intensive fragmentation by percolation

$t = \tau_d$          $t = 1/4\ \tau_{cc}$          $t = 1/2\ \tau_{cc}$          $t = 3/4\ \tau_{cc}$
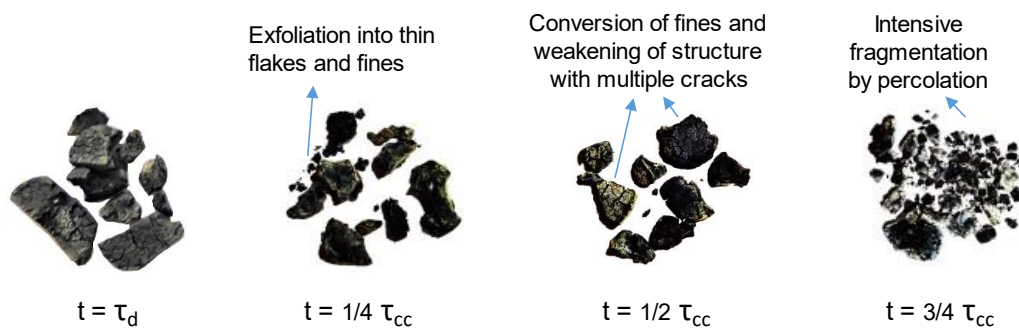
*Figure 7.17 Char fragmentation mode of IC1 particles at different residence times.*

Dissociation of fragments from plane of crack formation

Fines generation from impacts and abrasion

Attrition of fines and further breakage

Complete breakdown at various weak points as carbon bridges are depleted

$t = \tau_d$       $t = 1/4\ \tau_{cc}$       $t = 1/2\ \tau_{cc}$       $t = 3/4\ \tau_{cc}$       $t = \tau_{cc}$
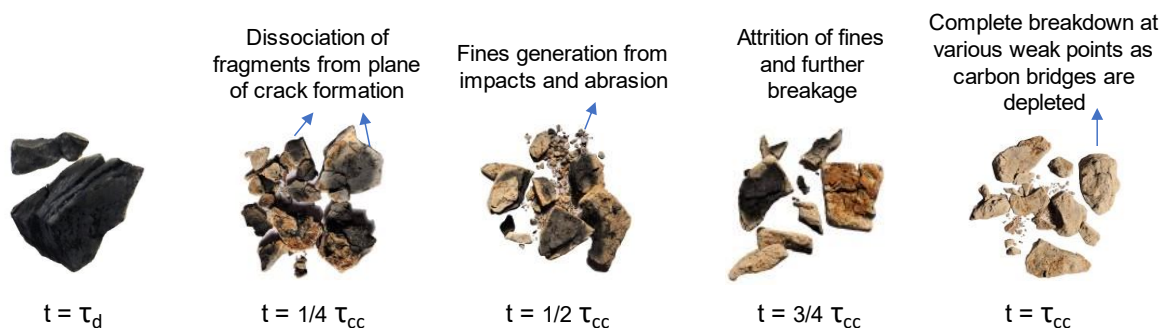
*Figure 7.18 Char fragmentation mode of IC2 particles at different residence times.*

Breakup of fragments weakly attached to core particle

Conversion and weakening of primary fragments

Peak of secondary fragmentation leading to complete burnout

$t = \tau_d$          $t = 1/4\ \tau_{cc}$          $t = 1/2\ \tau_{cc}$          $t = 3/4\ \tau_{cc}$

*Figure 7.19 Char fragmentation mode of IDC particles at different residence times.*

The loosely connected IDC char structures begin to wear out primarily by carbon conversion during the initial stage of the char conversion. The larger fragments undergo conversion in a shrinking core fashion (like that of IC2), while the ash on the char surface is instantly lost through the combustion-assisted mode of attrition and new surfaces are exposed for the reaction. The conversion occurs at a faster rate during the last two-quarters of conversion time as the weakened char structures form a large number of smaller fragments and fines.
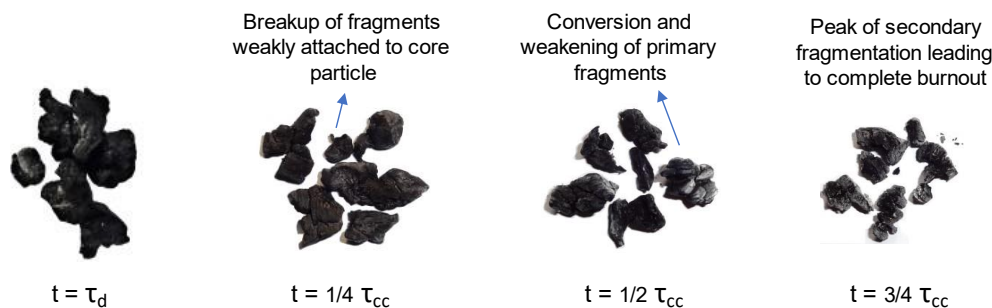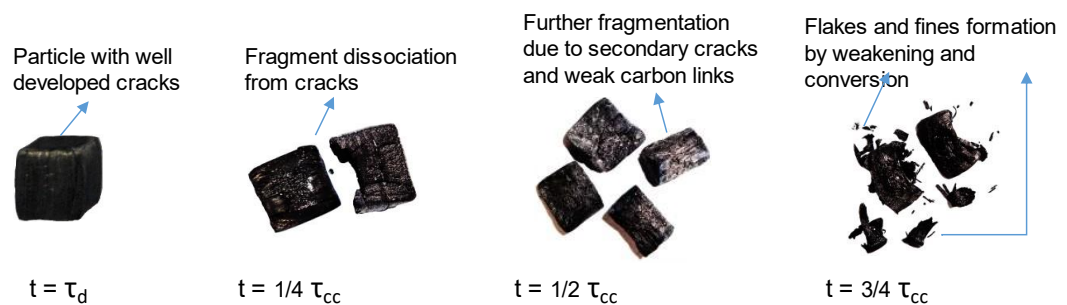


*Figure 7.20 Char fragmentation mode of BM particles at different residence times.*

Biomass chars start to disintegrate prominently during the char conversion period, through the cracks formed during devolatilization. The fragmentation initiates in these cracks during the first quarter, which then proliferates due to the structural weakening process. The breakage of carbon bridges is accompanied by percolative comminution during the final stages of conversion and the generated micron sized char fines further get converted in bed or elutriated. Thus, it is reiterated that the use of carbon stripper becomes vital to mitigate the loss of carbon capture efficiency during chemical looping combustion of fuels that extensively undergo percolative fragmentation.

## 7.4 Closure

A detailed investigation of the char conversion time and the secondary fragmentation phenomena of different sized coal and biomass particles in a CLC system, at various bed temperatures, is carried out. The range of char conversion times of various fuels are reported and the factors influencing the char conversion time are indicated in their order of influence. Using similar indicators employed for understanding the primary fragmentation, the characteristics of the secondary fragmentation phenomenon are assessed. Alike the defined minimum particle size to undergo primary fragmentation, a critical size below which char particles do not experience secondary fragmentation is

recognised. The modes of char fragmentation along with percolation are itemised comprehensively. The particle sizes suited for industrial scale CLC application are identified for each of the fuels tested.

# CHAPTER 8

# 8   ANALYSES OF CHAR REACTIVITY AND STRUCTURAL ASPECTS

## 8.1 Introduction

Char reactivity has been widely studied using $CO_2$, $O_2$, $H_2O$, and their mixtures at various component ratios(Li et al. 2017, 2018; Rathnam et al. 2009). Typically, char reactivity can be determined either by the fastest reaction involving direct oxidation of char using oxygen or the slowest reaction involving $CO_2$ gasification (Boudouard reaction). Since the slowest reaction is generally considered as the rate-determining step in a set of reactions, it would be ideal to study the reactivity of char using $CO_2$ (Peng et al. 1995). This part of the research study is focused on understanding the transient changes in fuel during conversion at certain operating conditions (like particle size, bed temperatures, and residence times). To understand the effect of inorganic mineral matter on char conversion, elemental analysis by Energy Dispersive X-ray spectroscopy (EDX) is performed. Since changes in the morphology of char microstructures and the crystallinity of char carbon have known influence on reactivity, various structural aspects of char samples are investigated. This chapter is aimed at

(i)    connecting the char reactivity data obtained using thermogravimetry with the detailed investigation of Raman spectroscopic information;

(ii)   detailing the structural and elemental variations in char at different stages of char conversion.

## 8.2 Experiments

### 8.2.1   Thermogravimetric analysis of char reactivity

Char samples obtained at different operating conditions are crushed to sizes less than 100 microns. About 5 to 10 mg of the sample is subject to test in a thermogravimetric analyser, by placing the sample over a Platinum or alumina crucible to make a thin bed in order to minimize the mass transfer resistance (Gomez and Mahinpey 2015). The highest bed temperature of 950 ℃ used in the char preparation is chosen to study the samples at isothermal conditions. Samples are heated to 950 ℃ at a rate of 30 ℃/min, with inert purging of nitrogen gas. Once 950 ℃ is achieved, nitrogen is replaced by $CO_2$ to conduct gasification and the temperature is maintained constant at 950 ℃ with a heating rate of 10 ℃/min. Experiments are carried out under the $CO_2$ atmosphere

until no weight loss is observed. Flow rates of the nitrogen purge stream and the $CO_2$ reactive stream are maintained at 100 mL/min. A pure stream of $CO_2$ (100%) is used in the experiments since the limiting reactant concentration of $CO_2:N_2$ is found to be 90:10, as followed in the literature (Sharma et al. 2012; Wang et al. 2015a).

### 8.2.2 Analysis of structural variations in char

Samples prepared for thermogravimetric study are used for surface-pore analysis and Raman spectroscopy. The electron micrographic investigation is carried out using Jeol JSM-6380 LA scanning electron microscopes (SEM) equipped with EDAX APEX Energy Dispersive X-ray spectroscopy (EDX) and ZEISS Sigma SEM 300 equipped with EDX (Oxford Instruments, Germany). Samples used in SEM analysis are uncrushed specimens retrieved at different conditions of the study. The surface characteristics and the pore parameters are analysed using the Quantachrome ASiQwin physisorption instrument. Structural variations in carbon formations in chars obtained at different operating conditions are characterised using Raman spectroscopy. Horiba - Jobin Yvon Lab RAM HR800 Raman spectrometer, equipped with an Nd:YAG LASER (excitation wavelength of 532 nm) is used to obtain the Raman data. The laser power is maintained at 5 mW and the beam of 2 μm diameter is exposed over the samples. Consistent Raman data obtained from multiple particles/spots for each sample are used in the analysis.

### 8.3 Results and discussion

The operating conditions that prevailed during the fluidised bed experiments are referred to as the sample preparation conditions in the following discussions on char reactivity, char structural changes and Raman spectroscopic analysis of char carbon.

### 8.3.1 Reactivity investigation of fuel chars by thermogravimetric analysis

Chars retrieved at different residence times during conversion at different operating conditions are tested for their $CO_2$ gasification reactivity and conversion time. The Gasification reactivity is given by Equation 8.1.

$$Reactivity = \frac{1}{m_0} * \frac{dm}{dt} \ min^{-1} \ \dots\dots\dots\dots\dots\dots\dots\dots\dots\dots\dots\dots\dots\dots\dots\dots(8.1)$$

where 'm$_o$' is the initial mass of loaded char and 'm' is the instantaneous mass recorded at the time 't'. The conversion ratio is defined as the ratio of the amount of carbon lost from the char to the total carbon present in the char (Equation 8.2).

$$Conversion\ ratio = \frac{Initial\ mass\ of\ char\ (m_i) - Instantaneous\ mass\ of\ char\ (m)}{Initial\ mass\ of\ char\ (m_i) - Final\ mass\ of\ char\ (m_f)} \dots\dots(8.2)$$

Figures 8.1-8.2, 8.3-8.4, 8.5-8.6 and 8.7-8.8 present the $CO_2$ conversion times and reactivity of char particles of IC1, IC2, IDC and BM respectively, of various sized samples prepared at 950 °C and the 22.5 mm samples prepared at different bed temperatures. All the coal chars show high reactivity during the earlier phase of conversion followed by low reactivity in the later stages, probably due to the formation of low reactive carbon. Whereas, the reactivity trend of biomass chars appears to be completely different to that of coals. But, on a closer look, it could be observed that the trend of biomass is similar to coals, till it reaches the peak char reactivity. After the peak reactive phase, the curve drops abruptly during the fag end of conversion, hinting at the absence of ash layer diffusional resistance. This characteristic is attributed to the low-ash and high-porous nature of biomass fuel.

Fresh IC1 chars (at $\tau_d$) prepared at 950 °C and the converted chars (during 0.75 $\tau_{cc}$) prepared at 800 and 875 °C have the least conversion time of about 10 min. A maximum conversion time of 50 min is observed in smaller sized samples prepared at 950 °C (during 0.75 $\tau_{cc}$) and conversely, the samples prepared from the largest sized particles show shorter conversion times and higher peak reactivities. When comparing the samples prepared at different operating bed temperatures, chars prepared at 875 °C is found to be the least reactive samples. Low surface availability in the less-fragmenting smaller sized particles might have reduced the diffusion of gasification agent ($H_2O$) during char preparation, and possibly limited the char reactivity. Char samples from low bed temperatures with higher reactivity are noticed only when they are retrieved at residence times of 0.5 and 0.75 $\tau_{cc}$. Peak reactivity of samples prepared at high bed temperatures, particularly those in the later conversion stages (Figure 8.2) is found within the 50% conversion regime. Thus, the reactivity increases with progressing conversion more evidently in 950°C samples, hinting that higher heating

rates favour faster conversion in the presence of steam(Megaritis et al. 1998; Mermoud et al. 2006; Reschmeier and Karl 2016).

Interestingly, IC2 samples exhibit similar trends in reactivity at all conditions of the study, with only variations in values of conversion time and reactivity with respect to particle size and temperature of char preparation (Figures 8.3 and 8.4). Though the nature of IC2 is heterogenous (Pragadeesh and Sudhakar 2018), each layer between the sandwiched structure of fault planes (volatile-rich zones where cracks are initiated) consists of a relatively more uniform spread of fixed carbon in the ash skeleton. Therefore, after the initial fragmentation event, the char structure becomes free of fault planes. The conversion time under the $CO_2$ atmosphere is directly proportional to the carbon content of the samples tested. This is evidenced by the fresh char samples having the maximum conversion time (90 min.) and 0.75 $\tau_{cc}$ samples having the minimum (25 min.). The highest reactivity is observed with the largest sized samples (about 0.09 $min^{-1}$) prepared at 950°C, like IC1.  This could be due to the increased porosity due to the formation of microporous and mesoporous formations due to high-temperature treatment, which is also evident from a study involving a high-ash coal (Liu et al. 2020). The lowest reactivity is noticed in the IC2 samples of 14.25 mm sized (at 950 °C) and those prepared at 875 °C (among bed temperatures) with about 0.015-0.025 $min^{-1}$, incidentally both being the middle range of the selected parameters. All the IC2 samples reach their peak reactivity before a 50% carbon conversion is achieved.

IDC samples show comparable reactivity trends to that of IC2. Chars from the earlier quarters of conversion time are found to be less reactive, consuming more time to get converted (90-120 min.). Chars obtained from the later quarters show higher reactivity values, possibly related to their high fragmentation index in the respective quarters. As observed from the particle size distribution of char particles in Chapter 7, chars from the later quarters are much smaller in size that could have exposed more surface area for reaction, as the carbon bridges in them are so weak and highly porous too. Samples of 9 mm size range (950 °C) and those prepared at 800 °C (22.5 mm) are the most reactive (0.04-0.05 $min^{-1}$), with the minimum conversion time of 65-70 min.

*Figure 8.1 CO₂ conversion time and reactivity of different sized chars of IC1 at 950 ºC, retrieved at various residence times.*



*Figure 8.2 CO₂ conversion time and reactivity of 22.5 mm chars of IC1 at different temperatures, retrieved at various residence times.*
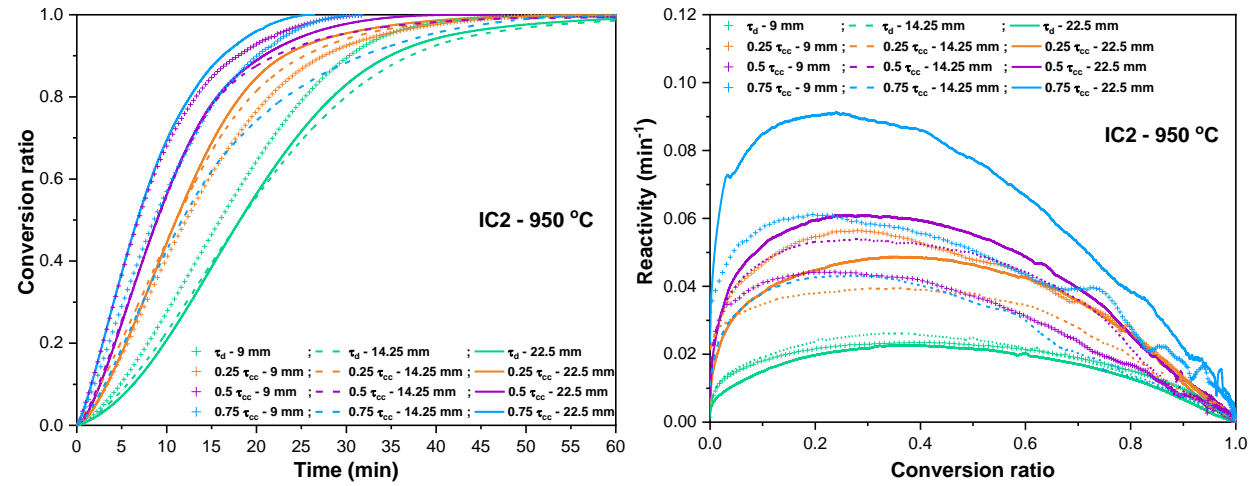
*Figure 8.3 CO₂ conversion time and reactivity of different sized chars of IC2 at 950 °C, retrieved at various residence times.*
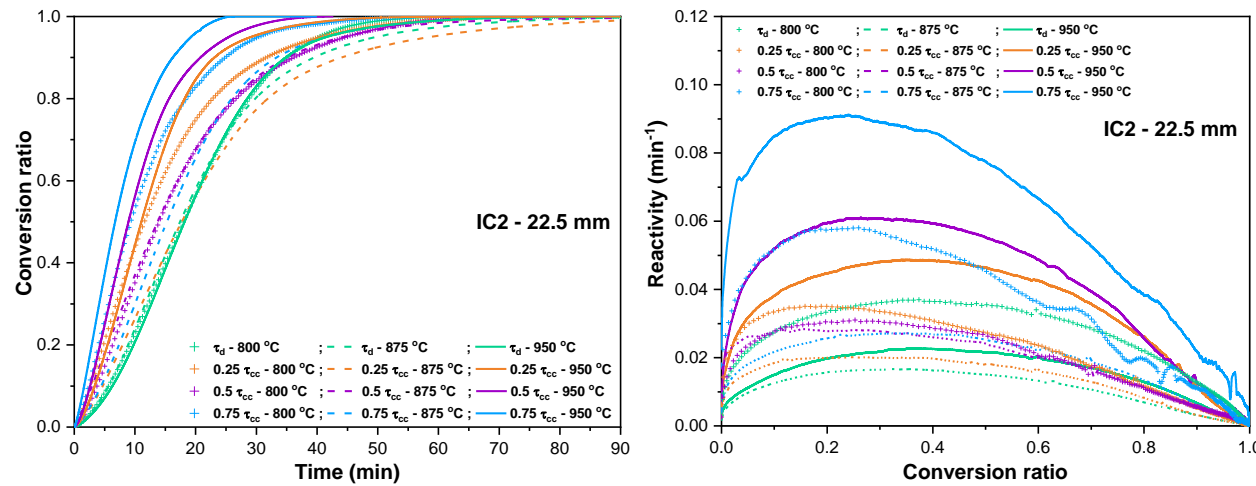


*Figure 8.4 CO₂ conversion time and reactivity of 22.5 mm chars of IC2 at different temperatures, retrieved at various residence times.*
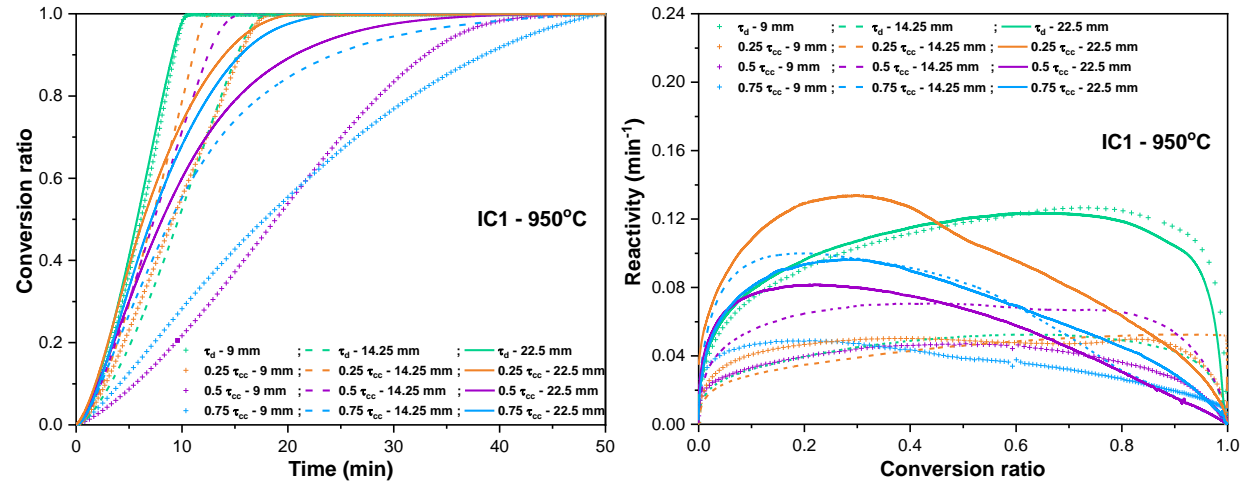
142

*Figure 8.5 CO₂ conversion time and reactivity of different sized chars of IDC at 950 ᵒC, retrieved at various residence times.*
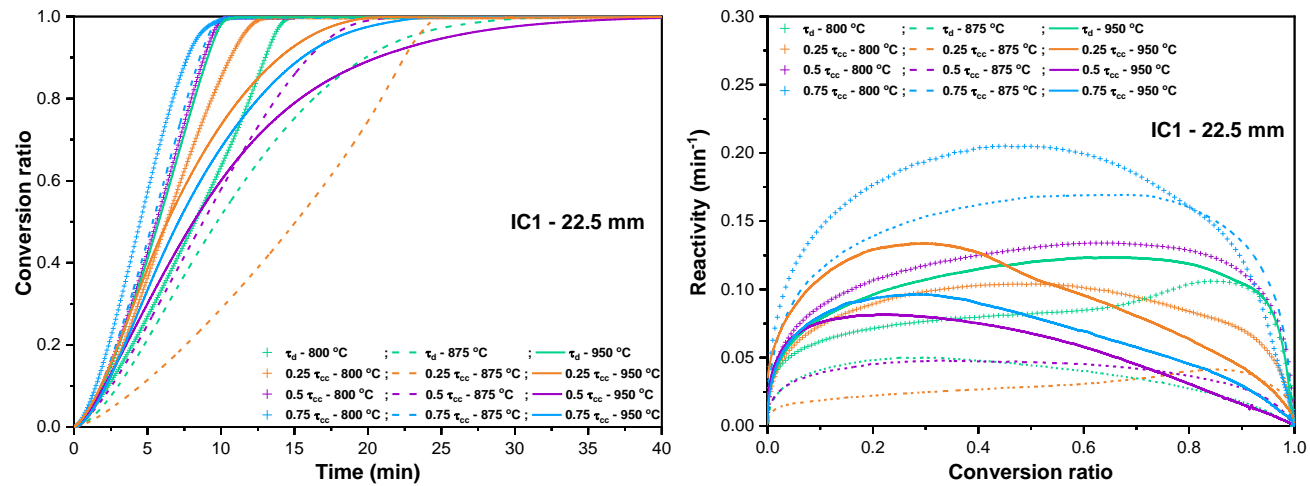


*Figure 8.6 CO₂ conversion time and reactivity of 22.5 mm chars of IDC at different temperatures, retrieved at various residence times*

*Figure 8.7 CO2 conversion time and reactivity of different sized chars of BM at 950 ᵒC, retrieved at various residence times.*



*Figure 8.8 CO₂ conversion time and reactivity of 22.5 mm chars of BM at different temperatures, retrieved at various residence times.*
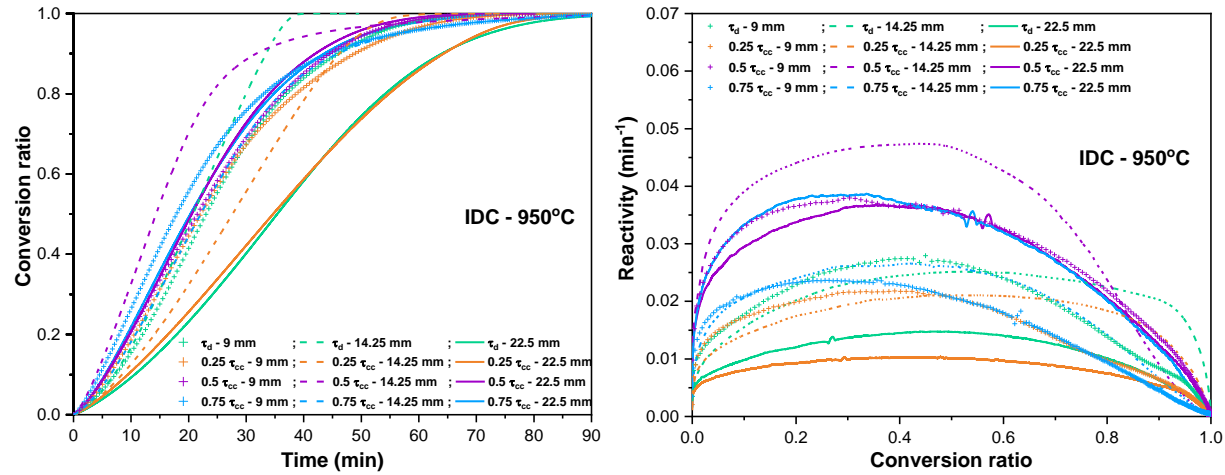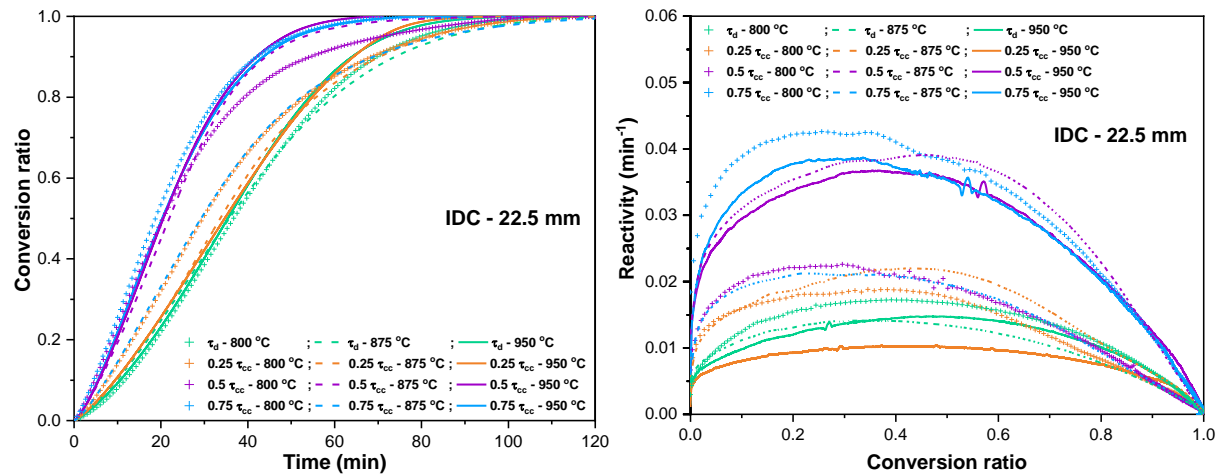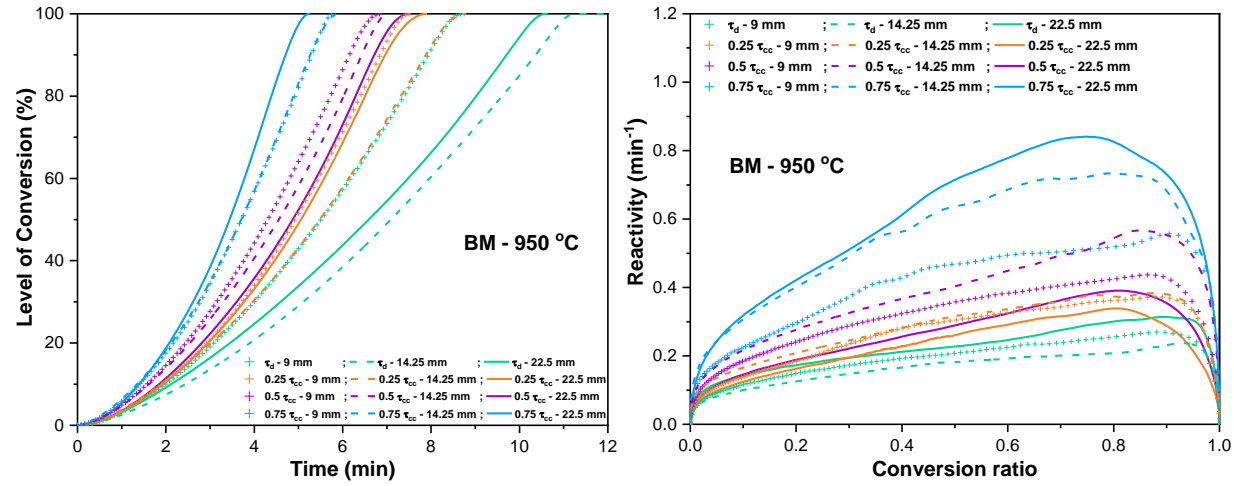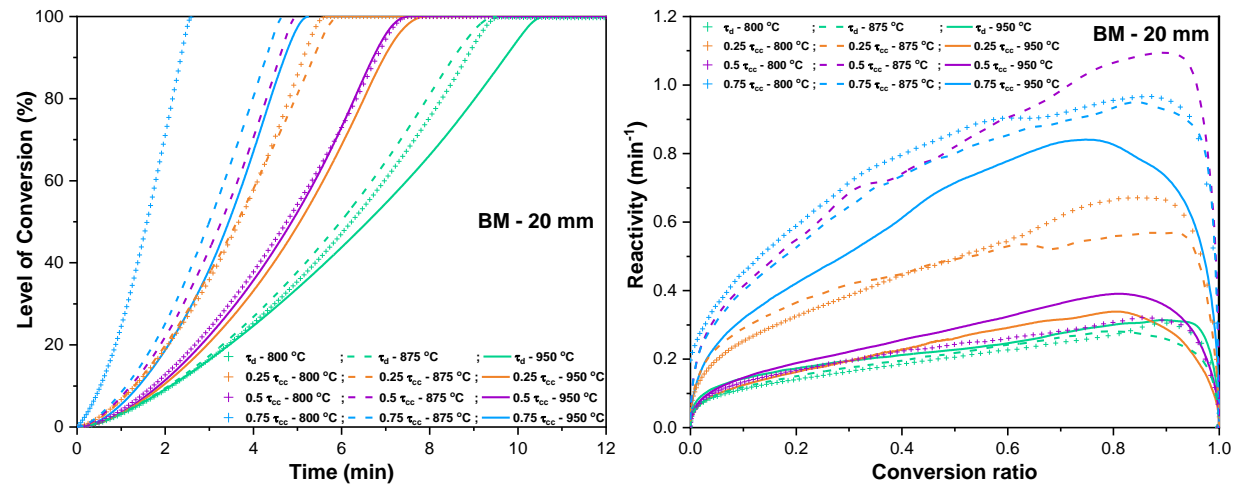
144

Char preparation in high volatile coals could produce a more reactive carbon at low temperatures (Hippo et al. 1979; Morin et al. 2018b), but high temperatures result in a more structured carbon (Keown et al. 2007; Xie et al. 2019). Owing to the low fragmentation probability with the smallest sized particles, the bed temperature effect on carbon structuring is limited, leaving the char more amorphous and accessible for reaction.

Known as a fuel of relatively less heterogenous composition, biomass samples exhibit relatively consistent and distinct behaviour. Unlike coals, the highly channelled biomass chars (Figure 8.11) of any size tested at any bed temperature have similar trends in conversion time and reactivity. Moreover, the longest TGA conversion time is observed only in their fresh char forms. As the conversion progresses, reactivity increases and thus, the char samples in the final stages of conversion have the least conversion time. Only about 30-35% of the mass is converted in half of the total conversion time. Whereas, all the coal types lose more than 70% mass within 50% of the TGA-$CO_2$ conversion times. Reactivity of these particles improves and achieve their peaks in the later stages of conversion (only after 70% mass conversion). An observation in biomass, common with that in coals is the size effect on the char reactivity i.e. the largest sized particles have the highest reactivity (0.8 - 1.1 $min^{-1}$). The samples prepared at lower temperatures are found to be the most reactive, as observed in IDC chars. Because, in both the volatile-rich and low-ash IDC and BM fuel particles, low temperatures possibly slowed down the condensation-polymerisation reactions. This could have aided in retaining the temperature-sensitive catalytic groups, amorphous and highly reactive O-containing groups (Lu et al. 2002; Meng et al. 2014) i.e. organic molecules that are rich in oxygen like carbonyl (C=O) and carboxylate groups (COOH).

Among the fuels tested, the most reactive is the biomass, followed by IC1, IC2 and IDC. Though IDC had the highest fixed carbon among coals, $CO_2$ gasification seems to be less selective towards the reacting sites in the carbon structure (Guizani et al. 2016). As coal and biomass have different conversion behaviour, suitable partial pressures of $CO_2$ and steam must be used to achieve high conversion rates while cofiring biomass with coal.

### 8.3.2 Micrographic interpretation of char structures

Electron micrographs of the chars of various fuels, at different stages of conversion (i.e. (a) raw fuel, (b) fresh char after devolatilization, (c) char at the end of the third quarter of char conversion time) are given as Figures 8.9 to 8.11 and 8.13. The surface characteristics of the char samples are tested in their fresh form and at the end of conversion (Tables 8.1 and 8.2). The specific surface area of all fuels remains almost constant before and after char conversion (Table 8.2). The raw fuel particle of IC1 shows an almost flat surface with multiple mounds, which develops into macroporous structures after devolatilization. Char at the later stage of conversion is seen to have well-developed mesopores (~3 nm) in the macroporous templates. This observation closely matches with the finding of Guizani et al. (2016) that steam gasification preferentially forming micropores that develop into mesopores upon conversion. The surface area and the pore volume show a slight improvement upon char gasification. These observations confirm the consumption of carbon bridges, and the multiple mesoporous formations indicate the likeliness of char to undergo percolative fragmentation.



***Figure 8.9 Electron micrographs of (a) IC1 raw fuel particle, (b) chars obtained after devolatilization and (c) at the end of Q3 of char conversion time at 950 ºC.***
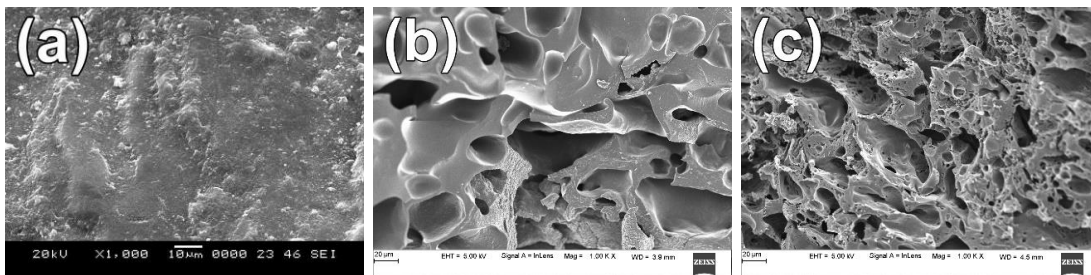


***Figure 8.10 Electron micrographs of (a) IC2 raw fuel particle, (b) chars obtained after devolatilization and (c) at the end of Q3 of char conversion time at 950 ºC.***

146
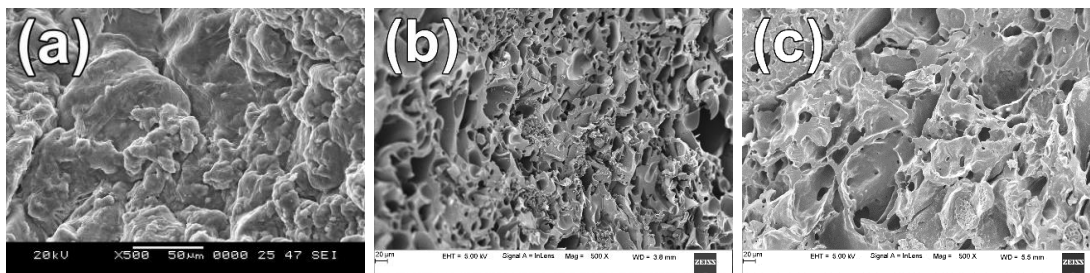
*Figure 8.11 Electron micrographs of (a) IDC raw fuel particle, (b) chars obtained after devolatilization and (c) at the end of Q3 at 950 °C.*

The feed IC2 particle has a rough non-porous surface, develops cracks at the end of devolatilization. The third quarter char shows propagated cracks, yet, holding the particle integrity, possibly resulting in the formation of a few fragments after char conversion (Pragadeesh et al. 2021). A 20% increase in pore surface area and the decrease in pore diameter indicate the increasing number of pores, upon char conversion. Meanwhile, the pore volume remains almost constant (Table 8.1), as the decrease in pore diameter is balanced by the increment in the number of pores.
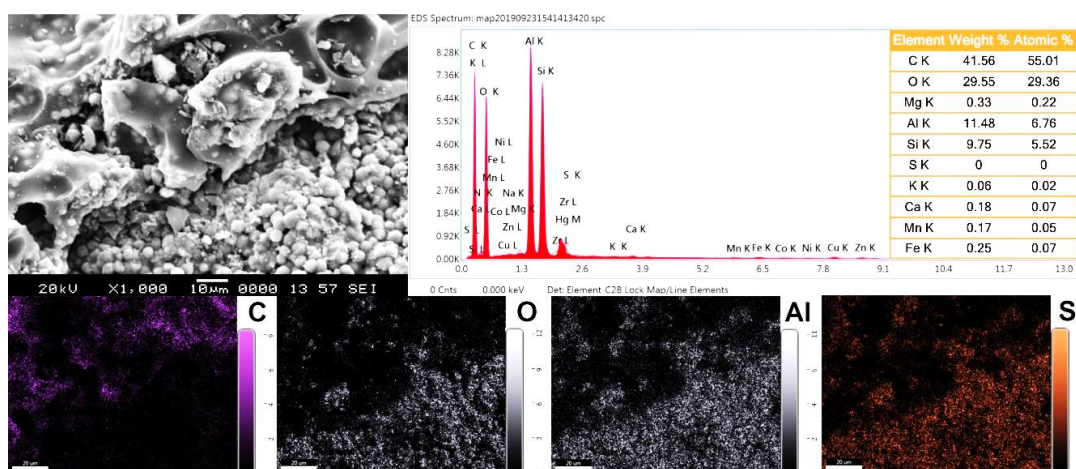


*Figure 8.12 Energy Dispersive X-ray (EDX) spectrograph and the elemental maps of major elements in IDC chars at the end of Q3 of char conversion time at 950 °C.*

The globular structure of the IDC sample is found to exhibit rough texture with multiple mounds over the surface, similar to IC1. The devolatilized fuel particle develops macropores and numerous mesoporous channels, which later collapses heavily during the conversion phase, due to the consumption of carbon bridges. The pore volume, pore surface area of IDC chars remains constant, but the pore diameter enlarged (Table 8.1). So, the pores enlarge and collapse resulting in a possible fusion of melting phases

147

alumina and silica along the cell walls and sintering of mesopores is interpreted. This is confirmed with a micrograph obtained with a different specimen of the same conversion level (Figure 8.12). Cenospheres (hollow inert spheres formed out of melting phases) of about 5 microns are seen in clumps and are characterised as aluminosilicate spheres from elemental mapping analysis. These particles end up in fly ash and have the propensity to get carried away in air and water bodies, due to their low density (Fenelonov et al. 2010). Carbon and Iron are not found to be distributed over these cenospheres, hinting that the ash formed does not interact with the oxygen carrier (hematite) and thus, non-magnetic in nature. Inertinite dominated macerals are recognised from the char structures of IC1 and IDC possessing honeycomb-like pockets and networks. Cenosphere formation in IDC chars suggests the vitrinite maceral combination with inertinite. The honeycomb structured chars are expected to have higher reactivity than the cenospheric chars and the flat solid types(Juniper and Schumacher 2013).
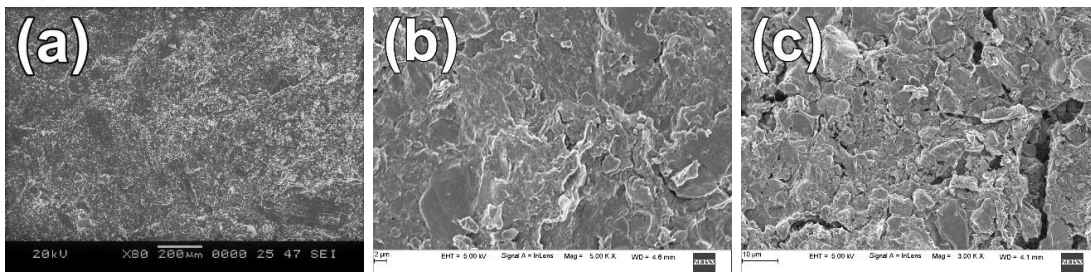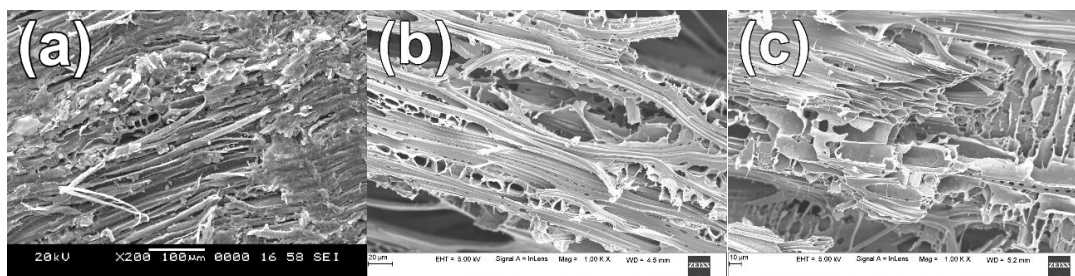


*Figure 8.13 Electron micrographs of (a) BM raw fuel particle, (b) chars obtained after devolatilization and (c) at the end of Q3 of char conversion time at 950 ºC.*

By nature, wood particles have a good network of pores owing to their fluid vessels (Figure 8.13). The devolatilized wood char shows disrupted vessels due to volatile release and an array of mesoporous channels is seen. Char particle in the later stages of conversion also has a similar structure to that of fresh char but with well-developed macroporous structures evolved from mesopore enlargement. The BJH pore characteristics of third-quarter char also exist unchanged from its freshly devolatilized form. This corroborates the previous observations of the mode of char comminution in biomass chars in Chapter 7, where, only the outer layer of the char is dislodged by attrition leaving the parent particle almost unaffected.

*Table 8.1. BJH surface pore parameters of char samples*

| | IC1 | | IC2 | | IDC | | BM | |
|---|---|---|---|---|---|---|---|---|
| | *Fresh char* | *Char at Q3* | *Fresh char* | *Char at Q3* | *Fresh char* | *Char at Q3* | *Fresh char* | *Char at Q3* |
| Pore Surface Area (m²/g) | 316 | 323 | 338 | 402 | 336 | 336 | 331 | 324 |
| Pore Volume (cc/g) | 0.30 | 0.31 | 0.33 | 0.36 | 0.33 | 0.33 | 0.33 | 0.32 |
| Pore Diameter (nm) | 3.47 | 3.50 | 3.53 | 2.15 | 2.86 | 3.56 | 3.57 | 3.56 |

*Note:* Q - char conversion Quarter

*Table 8.2 Surface BET parameters of char samples*

| | IC1 | | IC2 | | IDC | | BM | |
|---|---|---|---|---|---|---|---|---|
| | *Fresh char* | *Char at Q3* | *Fresh char* | *Char at Q3* | *Fresh char* | *Char at Q3* | *Fresh char* | *Char at Q3* |
| Slope | 13.4 | 13.8 | 13.4 | 13.0 | 13.4 | 13.3 | 13.6 | 13.8 |
| Intercept | 0.2 | 0.2 | 0.2 | 0.2 | 0.2 | 0.2 | 0.2 | 0.2 |
| Constant | 69.9 | 75.4 | 69.1 | 63.2 | 78.2 | 73.6 | 71.9 | 83.8 |
| Surface Area (m²/g) | 256.9 | 249.5 | 256.6 | 263.2 | 256.7 | 257.4 | 253.0 | 249.1 |

### 8.3.3 *Elemental variation in char during various stages of conversion*

To understand the role of elements during conversion, the semi-quantitative EDX analyses are carried out. Comparison of elemental profiles of fresh and third quarter chars of IC1 (Figure 8.14) reveals the interaction of Fe of the oxygen carrier with the char particle, not significant though. Calcium and Sulphur in the char are retained throughout the conversion process, due to a plausible interaction with aluminosilicates during the high temperature process (Hurley and Schobert 1993), and could become a component of bed ash.
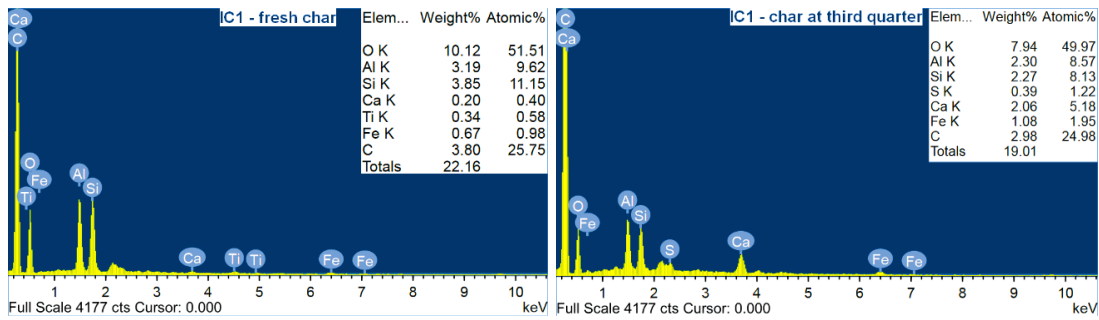
*Figure 8.14 EDX plots of IC1 chars at the initial and final stages of conversion.*
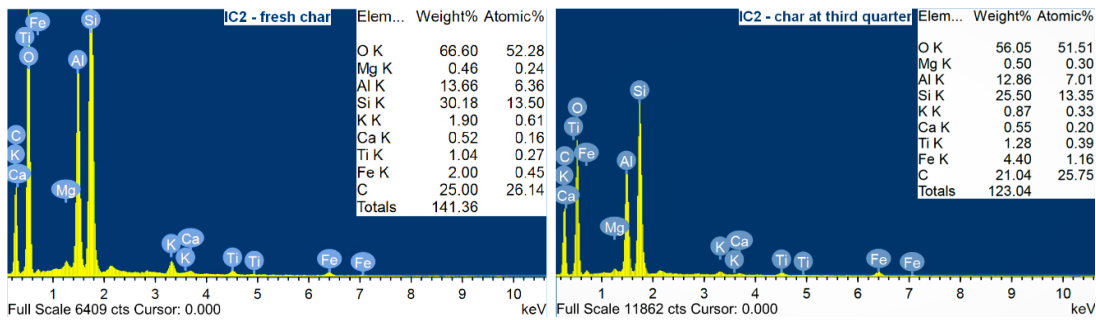


*Figure 8.15 EDX plots of IC2 chars at the initial and final stages of conversion.*
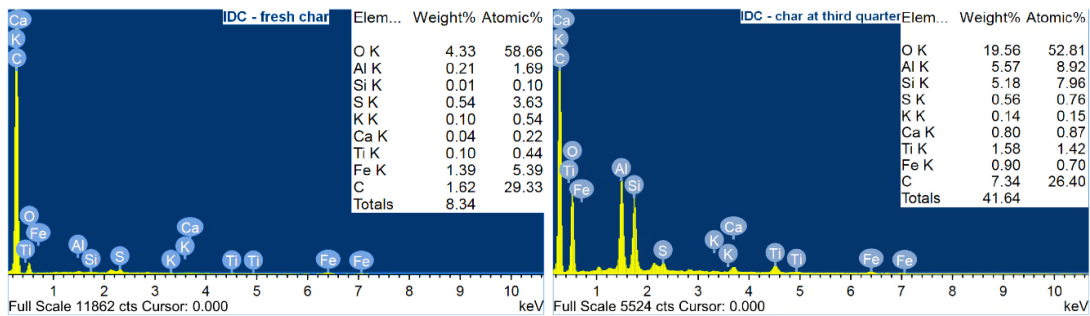


*Figure 8.16 EDX plots of IDC chars at the initial and final stages of conversion.*
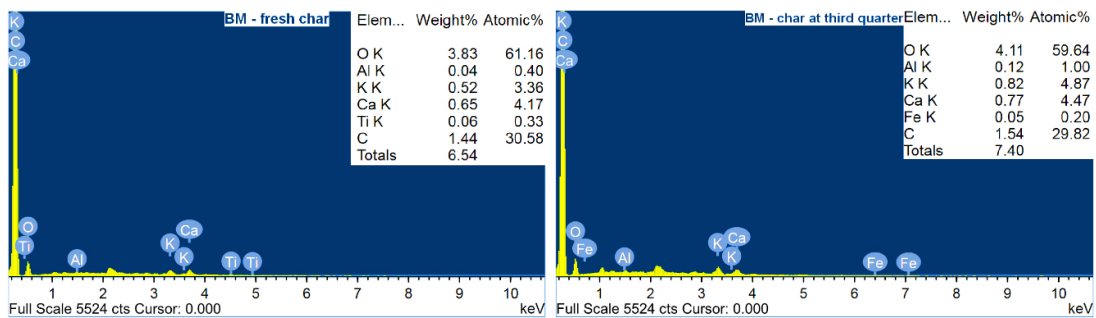


*Figure 8.17 EDX plots of BM chars at the initial and the final stages of conversion.*

Since the elemental composition of the IC2 char surface does not contain any carbon (Figure 6.18), the unconverted zone is analysed. The conversion front of the char in the later stages of conversion is found to have similar elemental composition to that of fresh char (Figure 8.15). This hints that conversion proceeds in a shrinking core

150

fashion, because of the less porous nature of IC2. IDC chars, as noticed from SEM images, form melt phase agglomerate spheres composed of Al and Si (Figure 8.12). But the carbon percentage does not vary much (Figure 8.16), as the ash components detach from the char continuously. Sulphur is lost during conversion and likely entered the flue stream, which may get dissolved into water while condensing steam. Biomass chars retain Al, K, and Ca till the end of conversion (Figure 8.17). The oxidising medium (steam) encounters new surfaces containing carbon, all along the conversion period, alike IDC.

### 8.3.4 *Raman spectroscopic analyses of carbon formations*

The obtained Raman bands are split into primary (800-2000 $cm^{-1}$) and secondary bands (2200-3400 $cm^{-1}$) for convenience. Deconvolution of Raman bands is performed by curve fitting procedure in Origin 2016 software. The Gaussian function is chosen for fitting, since it produced the most fitting line shape when compared to the Lorentzian function, for classifying the bands corresponding to defects in non-homogenous materials like coal and biomass(Cuesta et al. 1994; Smith et al. 2016). Typical Raman spectra with deconvoluted bands for first and second-order regions are provided in Figures 8.18 and 8.19 respectively. The band assignments for various carbonaceous formations are given in Tables 8.3 and 8.4.

On deconvolution of primary Raman spectrum obtained in the visible range gives rise to two major peaks namely the graphitic (G) band and the defective (D) band (Dresselhaus and Eklund 2000; Lin-Vien et al. 1991; Tuinstra and Koenig 1970). As the peak positions of these bands are known to shift with respect to the excitation wavelength (Wang et al. 1990), 532 nm source produces D band peaks in the range of 1300-1350 $cm^{-1}$ and the G band around 1580-1600 $cm^{-1}$. The G band is typical of a graphitic structure with a characteristic of the aromatic quadrant ring breathing in highly ordered materials, whereas the naturally formed biomass and the coals are found to have CH deformations, semi-graphitic structures such as graphene sheets and micro-crystalline graphite under heat treatment (Emmerich 1995; Zaida et al. 2007). A critical way to identify the high order of graphitization is by the presence of a defective band shoulder around the 1620 $cm^{-1}$ region (Cuesta et al. 1994; Schuepfer et al. 2020).

*Table 8.3 First-order Raman band assignments and their characteristics (adapted from Lin-Vien et al. (1991) and Li et al. (2006))*

| Band name | Band position, cm$^{-1}$ | Description | Bond type | References |
|---|---|---|---|---|
| $G_l$ | 1700-1730 | Carbonyl group C=O; alkene C=C | sp$^2$ | (Lin-Vien et al. 1991) |
| G | 1580-1600 | Graphite $E_2{}^2{}_g$; aromatic ring quadrant breathing; alkene C=C | sp$^2$ | (Tuinstra and Koenig 1970) |
| $G_r$ | 1520-1550 | Aromatics with 3–5 rings; amorphous carbon structures | sp$^2$ | (Li et al. 2006) |
| $V_l$ | 1460-1495 | Methylene or methyl; semi-circle breathing of aromatic rings; amorphous carbon structures | sp$^2$, sp$^3$ | (Schwan et al. 1996) |
| $V_r$ | 1370-1390 | Methyl group; semi-circle breathing of aromatic rings; amorphous carbon structures | sp$^2$, sp$^3$ | (Lin-Vien et al. 1991) |
| D | 1300-1350 | Defects in highly ordered carbonaceous materials; C–C between aromatic rings and aromatics with not less than 6 rings | sp$^2$ | (Wang et al. 1990) |
| $S_l$ | 1230-1250 | Aryl–alkyl ether; para-aromatics | sp$^2$, sp$^3$ | (Li et al. 2006) |
| S | 1150-1185 | $C_{aromatic}$–$C_{alkyl}$; aromatic (aliphatic) ethers; C–C on hydroaromatic rings; hexagonal diamond carbon sp$^3$; C–H on aromatic rings | sp$^2$, sp$^3$ | (Nemanich et al. 1988; Schwan et al. 1996) |
| $S_r$ | 1060-1080 | C–H on aromatic rings; benzene (ortho-di-substituted) ring | sp$^2$ | (Lin-Vien et al. 1991) |

*Table 8.4 Second-order Raman band assignments and their characteristics (adapted from Wang et al.* (2015b) *and Xu et al. (2017))*

| Band name | Band position, $cm^{-1}$ | Description | Bond type | References |
|---|---|---|---|---|
| $(2G)_L$ | 3300-3330 | Overtone of the band at 1670 $cm^{-1}$, carbonyl group C=O | $sp^2$ | (Li et al. 2006; Xu et al. 2016) |
| 2G | 3180-3200 | Overtone of the G band at 1590 $cm^{-1}$, aromatic rings | $sp^2$ | (Lee 2004; Wang et al. 2015b) |
| $(2G)_R$ | 3030-3060 | Aryl C−H stretch vibration | $sp^2$ | (Colangeli et al. 1992; Lin-Vien et al. 1991; Wang et al. 2015b) |
| D + G | 2860-2925 | Combination of $D_1$ band and G band, large aromatic rings system | $sp^2$ | (Antunes et al. 2006; Lee 2004; Wang et al. 2015b; Zaida et al. 2007) |
| $(2D)_L$ | 2650-2750 | Mix of C−H stretch of methyl and methylene, small aromatic rings and amorphous carbon structures | $sp^2$ ;$sp^3$ | (Lin-Vien et al. 1991; Wang et al. 2015b) |
| 2D | 2480-2560 | Overtone of the $D_1$ band, C−C between aromatic rings, large aromatic rings system | $sp^2$ | (Antunes et al. 2006; Lee 2004; Wang et al. 2015b; Zaida et al. 2007) |
| 2S | 2290-2330 | Overtone of the S band at 1150 $cm^{-1}$, $C_{aromatic}$-$C_{alkyl}$, C=O structures, large aromatic rings system | $sp^2$ ;$sp^3$ | (Li et al. 2006; Xu et al. 2016) |
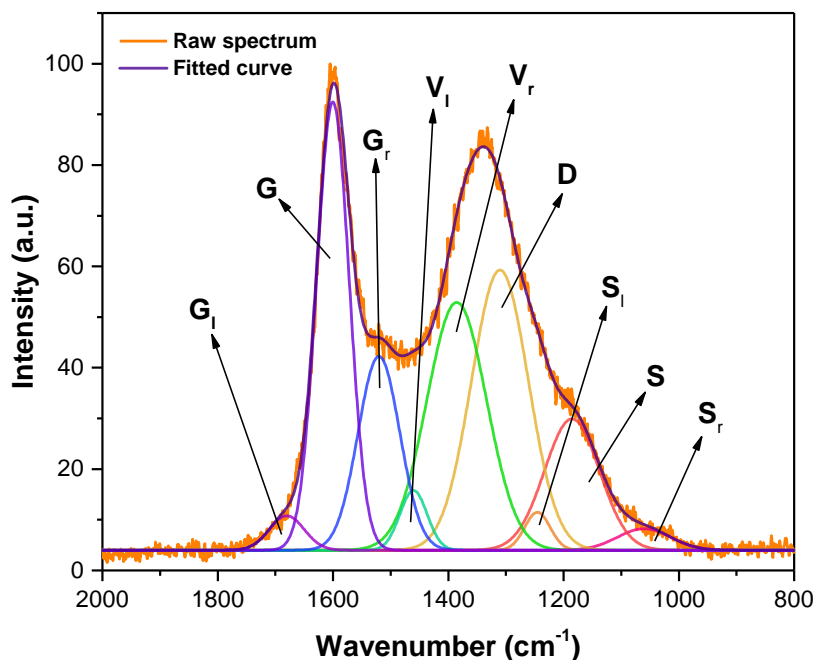
*Figure 8.18 Deconvoluted first-order region of a Raman spectrum (IC2:9 mm fresh char prepared at 950 ºC).*

Raman spectra of raw samples of IC1 and IDC show a bump near the G band hinting at the highly-ordered carbon than IC2 and BM. Carbon in IC1 and IDC are otherwise known to be more structured from their high reflectance nature owing to the presence of microcrystalline graphite (Li et al. 2019; Pragadeesh and Sudhakar 2018). Only IC2 and BM samples prepared from the highest temperature (i.e. 950 ºC), exhibit bleak shoulders around 1610-1620 cm$^{-1}$. Thus, the G band represents the $E_2^{2g}$ graphitic mode in IC1, IDC and in the samples of IC2 and BM prepared at 950 ºC, while this band in the rest of the samples represents aromatic ring breathing and alkenes. If the G band is of graphitic nature, the respective D band defines the in-plane imperfections in the graphitic lattice, else the D band is that of an aromatic system with more than 6 fused benzene rings (Sheng 2007).

In addition to these major bands, curve-fitting of the raw spectrum gives rise to large amounts of residuals which are usually assigned to three bands namely, $G_r$ (Right of G band), Vr (valley right), and $V_l$ (valley left). As a whole, these three bands represent the semi-quadrant aromatic ring breathing in systems with 3-5 fused rings, particularly in amorphous carbon structures (Li et al. 2006). $V_r$ and $V_l$ indicate the carboxylates and aliphatics, while $G_r$ represents the small ring systems. As $V_r$ and $V_l$

154

get consumed during high temperature cross-linking process (Asadullah et al. 2010), only $G_r$ finds its largest proposition. Another band $G_l$ assigned in the region around 1700 cm$^{-1}$ is attributed to carbonyl structures like aliphatic ketones. A band at 1150 cm$^{-1}$ represent structures with mixed sp$^2$-sp$^3$ nature (Bacsa et al. 1993) and a nearby band in the range of 1170-1180 cm$^{-1}$ is known for sp$^3$ structures (Nemanich et al. 1988; Schwan et al. 1996). This sp$^3$ band is designated as S band and to its left is the $S_l$ band at 1230 cm$^{-1}$ and at right is the $S_r$ band at 1060 cm$^{-1}$, of para- and ortho-disubstituted benzene structures respectively (Lin-Vien et al. 1991).
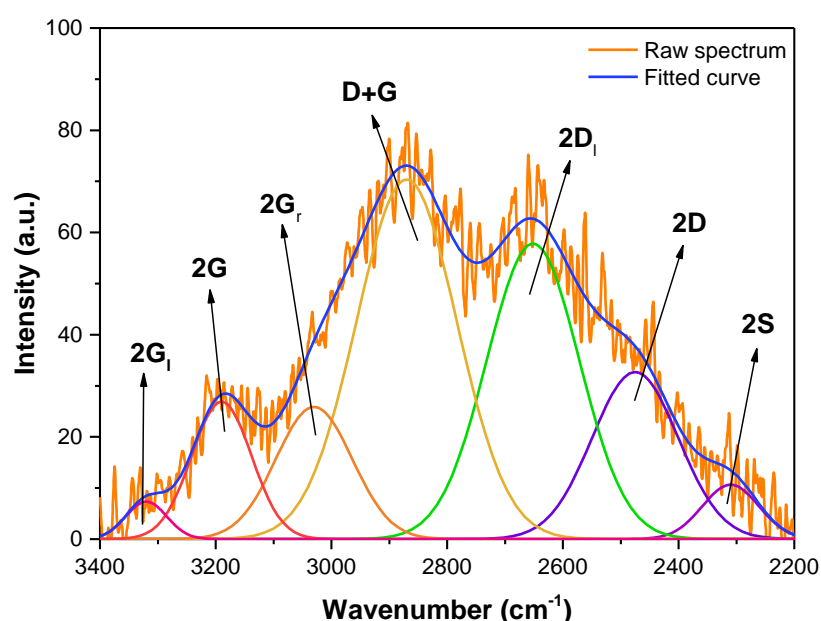


*Figure 8.19 Deconvoluted second order region of a Raman spectrum (IC1:9 mm char in 3rd quarter prepared at 950 °C).*

The respective major second-order bands in the spectrum are 2D, 2G and 2D$_l$. The overtone of the D band occurs around 2450-2560 cm$^{-1}$ arising from the 2 iTO phonons near the k point of the unit cell (Antunes et al. 2006; Wang et al. 2015b). For a highly ordered carbon, it represents the number of graphene layers, whereas, it is related to the defects in graphitic lattice containing large aromatic rings in amorphous carbon matter. 2G band around 3180-3240 cm$^{-1}$ is the overtone of the G band corresponding to the aromatic ring structures. A minor band 2G$_l$ around 3320 cm$^{-1}$ is the overtone of the carbonyl group band at 1700 cm$^{-1}$. Bands arising out of the region from 2650-2810 cm$^{-1}$ is attributed to the overtone of CH stretching vibration in aryl, methyl functional groups and Poly-Aromatic Hydrocarbons (PAH) found in non-

graphitic structures and represent the small aromatic ring systems(Wang et al. 2015b; Xu et al. 2017). Due to the complexity in deconvolution and understanding this region, $2V_r$ assignment found in literature is ignored and is collectively termed as $2D_l$. It also represents the C=C bonds in the graphitic lattice of highly ordered carbon(Wang et al. 1990). $2G_r$ band around 3060 cm$^{-1}$ is analogous to $2D_l$, representing the CH stretching vibration of aromatic ring structures such as PAH in amorphous carbon(Cuesta et al. 1994; Ramsteiner and Wagner 1987). D+G band around 2860-2950 cm$^{-1}$ is the D and G band combination from the first-order spectrum. The band information is similar to that of the D band, revealing large aromatic structures. The overtone band of sp$^3$ rich structures is found around 2300-2350 cm$^{-1}$, representing C≡C stretching and bending modes of vibration (Larkin 2011).



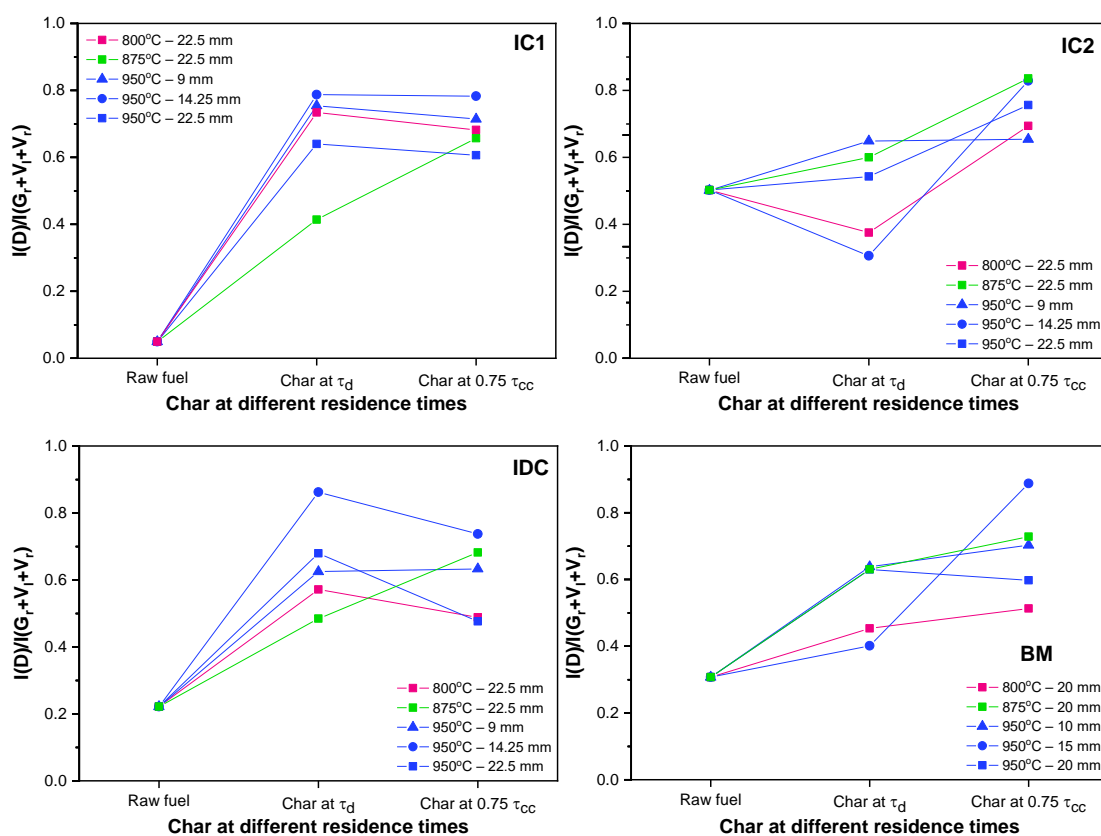Figure 8.20 Primary band area ratios of large to small aromatic rings in chars of different fuels at different stages of conversion

The first-order Raman spectra are analysed under three classes such as the band area ratios of large to small aromatic rings ($I_D/I(G_r+V_l+V_r)$), total Raman area, Raman parameter ($R_G = W_G/W_D$ i.e. full width – half maxima ratio between graphitic ($W_G$) and

deformed carbon peaks ($W_D$)) and the band area ratio of amorphous aryl-alkyl linkages to the graphitic carbon i.e. reactive to non-reactive structures ($I_S/I_G$). The second-order Raman spectra are also studied under similar aspects (Figures A19 to A23).

Figure 8.20 shows the band area ratios between large to small aromatic ring groups in different fuels. All raw fuel particles show the lowest value of $I_D/I(G_r+V_l+V_r)$. Under heat treatment during devolatilization, the larger aromatic rings increased due to the condensation of the 3-5 ring systems, enabled by ring-opening in the presence of steam (Asadullah et al. 2009). This usually results in the formation of polycyclic aromatic ring systems. IC1 and IDC show relatively more developed larger rings than IC2 and biomass chars. On char conversion, IC1 and IDC show a slight and medium decrease in the ratio respectively, and IC2 samples show a better increment than biomass particles. The probable reason for this observation could be the inverse relationship with $I_S/I_G$ (Figure A17). New smaller rings ($I(G_r+V_l+V_r)$) are formed at the expense of the electron-rich O-containing groups such as carboxylates, ethers, and the aryl-alkyl linkages in char, enhancing the cross-linking density ($I_S$). This denotes that with the increase in available S band structures, smaller ring groups are also continuously formed. As the $sp^2/sp^3$ rich disorder phases modify during heat treatment, $sp^2$ phases in the graphitic network domain are formed (Takai et al. 2003). These $sp^2$ structures support the small ring systems, and simultaneous increment in the D band values is noticed from $I_D/I_G$ and $I_{2D}/I_{2G}$ (Figures A18 and A23). But for IC2 and biomass samples, no new formation of aryl-alkyl linkages is noticed, thus expending only the available $G_r+V_l+V_r$ structures to form a larger aromatic system. With the particle size increasing, the formation of S band structures is limited over the period of conversion, yielding a low quantity of small rings. As noticed previously that char yield in larger particles is larger due to the recondensed volatiles in char without much thermal cracking. Volatile reabsorption in char is more prevalent in low temperature heat treatment, paving the way to hold more O containing groups in large fuel particles. This leads to a considerable reduction of the S band structures over char conversion to form smaller aromatics. Consequently, the $I_D/I(G_r+V_l+V_r)$ values of low temperature samples reduce to a greater extent than the samples prepared at 950 °C, which is the reason for the volatile-rich and low-ash fuels like IDC and biomass to show increased reactivity in char prepared at low temperatures.

157
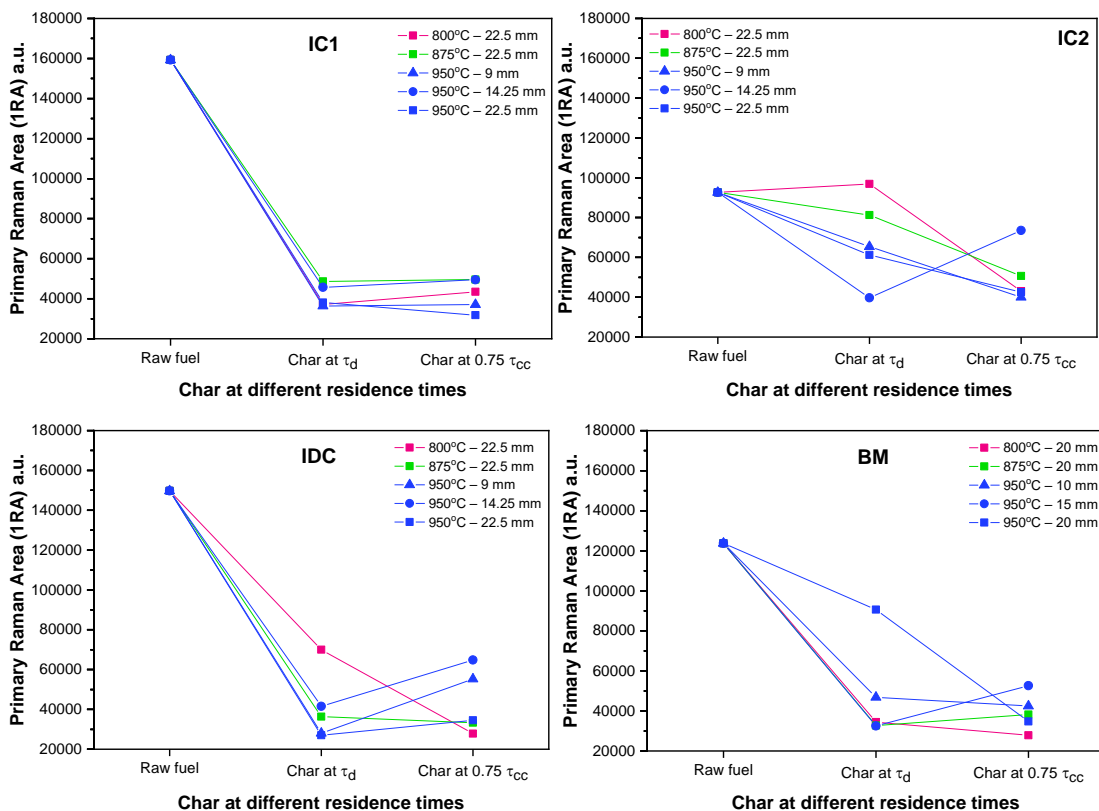
*Figure 8.21 Primary total Raman area in the primary bandwidth in chars of different fuels at different stages of conversion.*

Irrespective of the fuel type, fresh char particles undergo ring condensation at all operating conditions, progressing towards graphitization (Figure A18). The band ratios of large to small ring systems ($I(2D+(D+G)/(2G_r+2D_l))$) in the second-order region reveals no significant information (Figure A19). Fuel samples show an increase in values upon devolatilization which then drops back almost to that of the raw samples. A possible course of events could be the initial consumption of smaller ring-groups and the development of these groups from $sp^2/sp^3$ phases during char conversion, which is supported by the decrement in the S band intensity values (Figure A22).

The total Raman area of the first order region (1RA) of IC2 and BM samples tends to decrease as the conversion progresses (Figure 8.21). In IC1, no significant changes are noticed in the total area, whereas in IDC, the increase in area is noticed. Chars of IC2 and BM in the third quarter of conversion have the least value, particularly the lowest temperature samples (of 800 $^o$C). This is an indication of the increased order of crystallinity, with most of the samples having achieved the graphene planar structure

158

with defects (D band). Since the D band is rich in $sp^2$ structures, and their high light-absorbing nature results in an overall reduction in Raman intensity i.e. low Raman area(Keown et al. 2007, 2008; Li et al. 2006). Increase in the Raman area of IDC hints at the probability of formation of 3-5 ring systems till the end of char conversion, with D band intensities not varying much during this regime (Figure A17). Lower sized char samples and those prepared at 950 °C show a relatively higher Raman area than the rest. The secondary Raman area (2RA in Figure A20) shows no significant difference between the values of fresh and converted chars, whereas, raw IC2 samples show very low values like that in the primary region.

The Raman parameter, $R_G$ is an indicating parameter of the char graphitization i.e. increase in $R_G$ means an increase in graphitic structures or reduction in crystal disorder in char (Sekine et al. 2006). $R_G$ of various fuels tested exhibit decremental trends as the residence time increases, which has different causes in each fuel type, as understood from the values other band ratios.

- In the case of IC1, G band intensity has evidently increased after fuel devolatilization leading to a drop in $R_G$ values, which later is found to not vary much because of the balanced depletion of all carbon structures throughout the char conversion period.

- IC2 chars, which have a homogenous distribution of fixed carbon, show low $R_G$ in raw form, which then continuously acquire D band carbon by expending the low order carbon structures until char conversion is complete. During char conversion, all forms of carbon are depleted at almost in a balanced mode, except the faster depleted graphitic structures (G band).

- The initial decreasing trend of $R_G$ in IDC samples till devolatilization is due to the initial formation of structures related to the D band, where the later dropping during char conversion is because of the G band consumption by steam. Though depletion of D band structures is also noticed, D band intensity is maintained by continuous condensation of lower ordered carbons during char conversion regime.

- Raw biomass samples tend to form more D band structures expending all forms of lower order carbons, to form an almost equal amount of G band ($I_D/I_G$ =1). During char conversion, depletion of both D and G bands is noticed. However, G band

depletion is predominant under the steam environment, and the lower order carbon forms are retained throughout char conversion.
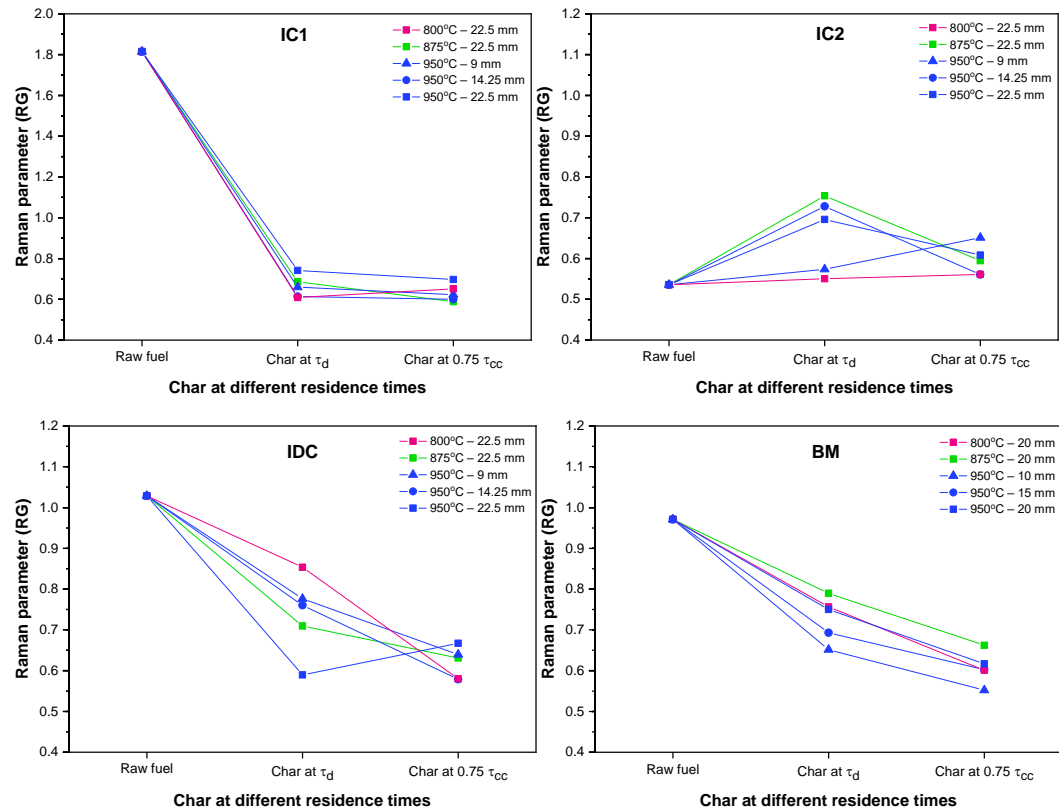


*Figure 8.22 Primary Raman parameter of chars of different fuels at different stages of conversion.*

Thus, Raman spectroscopic analyses of samples retrieved from FB experiments reveals that the chars of high-volatile fuels retain D band carbon till the end of conversion. The graphitic carbon structures (G-band) in char samples are found to be more selectively converted by the steam atmosphere. This also leaves a clue that the $CO_2$-rich gasification medium may suit only the non-graphitic (amorphous) carbon forms, which is earlier hinted at by Guizani et al. (2016). Further, the steam atmosphere enables micropore formations in smaller sizes (say 1 nm) compared to that in the $CO_2$ atmosphere. At the same time, $CO_2$ has lower diffusivity compared to $H_2O$. Thus, it may not be advantageous to use $CO_2$ as the only gasification agent for CLC processes (Aranda et al. 2016; Guizani et al. 2016). Remarkable depletion of D band carbons in IC1 and BM (D-band rich) during char conversion substantiates the earlier-indicated (in subsection 3.3) catalytic activity by alkali species.

### 8.3.5 *Relationship between char reactivity and Raman bands*

A variety of reactivity indices are utilized for scaling the samples' reactive nature to the gasification medium. Few of the definitions include the half time of conversion i.e. $t_{0.5}$ and the corresponding reactivity, $R_{0.5}$ (Álvarez et al. 1995; Wu et al. 2008), $0.5/t_{0.5}$ (Al-Qayim et al. 2017; Huo et al. 2014; Takarada et al. 1985), $2/t_{0.5}$ (Shenqi et al. 2011), and the sample temperature at 20% conversion (Sheng 2007; Zhang et al. 2015). As the present reactivity study is carried out in isothermal conditions, sample temperature at various conversion levels could not be taken as a measure of reactivity index. In all other indices defined, $t_{0.5}$ is the principal parameter expressed either as an inverse function or simply as such. Thus, it is suitable to simply follow Álvarez et al. (1995), by considering the half time of conversion and reactivity at half time.

Figure 8.23 presents the $t_{0.5}$ and $R_{0.5}$ values varying with respect to $I_D/I_G$ of char samples. In general, it is desirable that $t_{0.5}$ is minimum, thus a higher reactivity. All fuels show a decreasing trend of half-time with the increment in $I_D/I_G$ value viz. IC1 and IDC exhibit a linear trend while IC2 and BM exhibit exponential decay. As a support, the trends of $I_D/I_G$ of IC1 and IDC chars (Figure A18) show a slight increment while the trends of IC2 and BM chars increased rapidly. The reactivity at half-time increases with respect to the increase in $I_D/I_G$, in all the fuels tested (Xu et al. 2015). This is in line with the published literature finding that the sample temperature at 20% conversion levels decreases with increasing D band intensity (Sheng 2007). As noted earlier, the intensity of the S band in IDC samples could influence the char reactivity, apart from the D band. As the D band values of IC2 particles ramps up with the level of char conversion, reactivity at half time takes an exponential course of increment when $I_D/I_G$ is greater than 1. Thus, it is generally observed that the higher ratio of $I_D/I_G$ increases the char reactivity. Char preparation at high temperature (950 °C) is found to yield higher $I_D/I_G$ values. Thus, a higher bed temperature is proved to enhance the overall conversion rate.

161
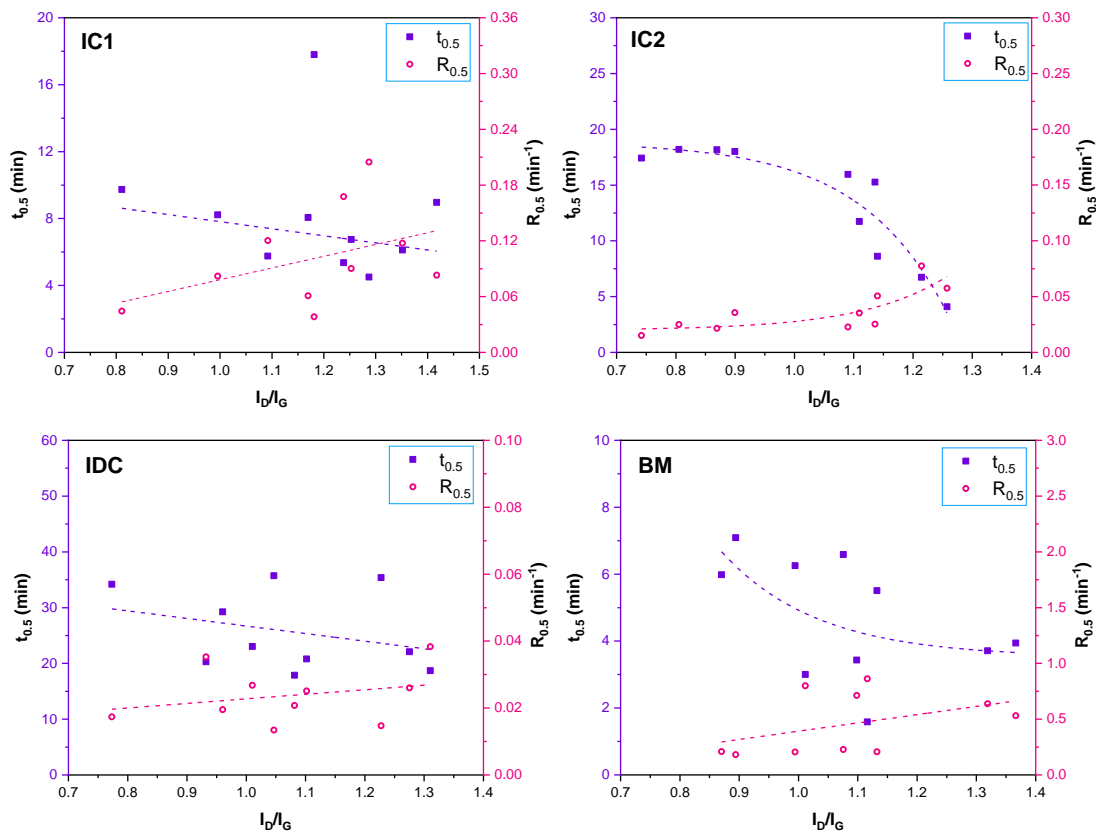
*Figure 8.23 Half-time of char conversion in TGA and reactivity at half-time for various fuels and their corresponding band intensity ratios of D to G.*

## 8.4 Closure

Reactivities of various fuel chars obtained from different testing conditions are analysed using thermogravimetry under $CO_2$ atmosphere. Peak char reactivities are investigated, and the operational parameters of char preparation that favoured high char reactivates are determined. Char microstructures are examined to ascertain the changes that contributed to changes in char reactivity values. Further, the prospective catalytic elements that took part in the char conversion processes are identified. The evolution of char carbon crystallinity and the influence of various chemical groups on char reactivity during conversion are studied using Raman spectroscopy. The selectivity of carbon structures for the reaction towards gasification environments are qualitatively understood, and the suitable gasification environments for the tested fuels are suggested.

# CHAPTER 9

# 9 SUMMARY AND CONCLUSIONS OF THE THESIS

## 9.1 Summary of the thesis

Experiments were conducted to understand the thermophysical and thermochemical behaviour of large-sized solid fuels, particularly Indian coals, India's majorly imported Indonesian coal and one type of carbon-neutral woody biomass during FB-CLC. Five interlinked studies have been carried out, namely (i) the development of a new technique to determine devolatilization time in CLC conditions, (ii) detailed investigation of devolatilization, (iii) primary fragmentation, (iv) char conversion studies along with secondary fragmentation, and (v) the char reactivity investigation clubbed with the analysis of structural variations during various stages of fuel conversion under FB-CLC conditions. The study-wise summary of the research findings is as follows.

### *9.1.1 Colour Indistinction Method for devolatilization time determination*

A new method named 'Colour Indistinction Method' is developed, validated and compared with other methods available in the literature for determining devolatilization times of large particles of different fuels during chemical looping combustion. The significant inferences while establishing this method are as follows.

❖ For both the fuel types studied, CIM compares well with the FET method, in terms of the accuracy of devolatilization time determination.

❖ The CIM determined values very well matches with other accurate methods, such as PCT measurements, with an error range of -7.57 to +3.70 %.

❖ The devolatilization times of coal and biomass particles determined using CIM is found to differ from FET observations by about +30% and +15% respectively, which can be attributed to the difference in the environment of conventional fluidized bed (inert sand and air medium) and the CLC (reactive oxygen carrier and steam medium), there forth necessitating the use of CIM as a new specific technique for the devolatilization time determination in FB-CLC systems.

Thus, CIM is found to be a valid, quick, easy, and convenient technique for determining devolatilization times of fuel particles in FB-CLC environment. It is

recommended that this method can also be applied for devolatilization time measurements of high moisture fuels even in oxidizing air atmospheres.

### 9.1.2 Devolatilization time of large fuel particles

❖ The devolatilization times of fuels are found to increase with the increase in particle size and decrease with the increase in operating bed temperature, analogous to the qualitative trend observed in the conventional fluidized bed combustion.

❖ Indonesian coal has the longest devolatilization time among the coals studied, with biomass having the least devolatilization time. Also, IDC is the most influenced fuel type, by the changes in operating parameters because of its highest combustible matter composition.

❖ Coal flakes are found to have 60% lesser devolatilization time than the near-rounded particles, indicating the importance of the shape effect to be considered in modeling of devolatilization and design of FB-CLC system.

❖ Larger coal particles always have higher char yields than smaller particles, whereas the size effect on char yields of biomass particles are found to be insignificant.

❖ The following correlations for devolatilization time of coals (Equation 9.1) and biomass particles (Equation 9.2) in CLC conditions are developed, with a satisfactory value of the coefficient of determination of around 0.95.

$$\tau_d = 10421 . d_p^{1.536} . T^{-1.266} . \varphi^{0.376} \dots\dots\dots\dots\dots\dots\dots\dots\dots(9.1)$$

$$\tau_d = 293 . d_p^{1.615} . T^{-0.799} \dots\dots\dots\dots\dots\dots\dots\dots\dots\dots(9.2)$$

### 9.1.3 Primary fragmentation behaviour of fuels

❖ Out of all the studied fuel particles, 20 to 60 percent of the particles tend to fragment, in all fuel types.

❖ Among the studied fuels, Indian coals are more likely to fragment while considering all operating conditions, especially IC1 (which also produces the highest number of fragments).

❖ The Indian coals are found to fragment very early in the initial quarters of devolatilization, whereas IDC and BM fragment in the later quarters of devolatilization, indicating a stronger influence and higher importance of fragmentation in the case of Indian coals on its conversion.

- The number of fragments is found to be relatively high for the large-sized fuel particles and also at higher bed temperatures.
- Coal particles have a fragmentation frequency of 2 to 3 while the biomass particles have a maximum frequency of one.
- IC1 has the maximum fragmentation index (FI) and the least FI is observed with biomass particles, reflecting the considerable difference due to the nature of fuel.

It is also established that the compressive strength proportionally influences the number of fragments. It is understood that each of the fuels tested exhibits different modes of fragmentation which would significantly affect the rate-controlling char conversion phase during CLC.

### 9.1.4 Char conversion and secondary fragmentation behaviour of fuels

- The char conversion time and the extent of char fragmentation are primarily dependent on the fuel type, followed by particle size and the bed temperature in decreasing order.
- Conversion times are found to be proportionally related to the quantity of fixed carbon, for chars whose ash to fixed carbon ratio is <1. Among the fuels studied, the high-ash IC2 has the longest char conversion time, preceding IDC chars which have the highest fixed carbon.
- Increasing the particle size from 8 to 25 mm rises the char conversion times by 60 to 170 %, for all fuel types. Whereas, increasing the operating bed temperature results in the reduction of conversion time by at least 42% (in IC1) to a maximum of 86% (in IDC).
- Chars of all fuels fragment in the very first quarter of residence time, affecting the overall char conversion time significantly. Barring IC2, chars of other fuels exhibit a 100% probability of fragmentation by the end of the second quarter and the highest index of fragmentation is marked in the third quarter.
- Secondary fragmentation reduced the size of chars to less than half of their initial feed sizes within the first two quarters of char conversion time, in all the fuels except IC2.
- There exists a critical size for all fuel types below which the impact of the collisions is feeble, limiting the char fragmentation. This critical size of fragments

occurs in the range of 4.4 – 7.7 mm for all fuels, except IC2 for which it is found in the range of 6.3 - 14.2 mm.

❖ Percolative mode of fragmentation is observed to occur in the last quarter of char conversion time for all fuels except IC2.

❖ Comparing the intensity of char comminution, the fuels with higher fixed carbon content (IDC, IC1) experience more intensive fragmentation than those with lower fixed carbon (IC2 and BM).

### 9.1.5 *Reactivity and structural changes in fuel char during conversion*

Key findings from the investigation of reactivity and structural changes in chars through combined thermogravimetric and Raman spectroscopy, accompanied by electron microscopy and surface pore analysis are as follows.

❖ Chars of low volatile fuels like IC1 and IC2 are more reactive when they are prepared at high temperatures and from larger sizes. In contrast, high volatile fuels like IDC and biomass produce high reactive chars at the small size - low temperature and large size – low temperature conditions, respectively.

❖ The peak char reactivity values of coals are obtained during the initial quarters of char conversion time and within the fixed carbon conversion range of 20-30% under the $CO_2$ atmosphere. Unlike coals, peak char reactivity of biomass samples is observed in the later quarters of char conversion time as well as after 70% carbon conversion.

❖ Comparing the results of char conversion time and char reactivity experiments, woody biomass and IC1 are found to be the most reactive fuels under both steam and $CO_2$ atmospheres. IC2 is the least reactive fuel in the steam atmosphere, whereas IDC is the least reactive in the $CO_2$ atmosphere.

❖ Micrograph histories of fuel conversion show continuous pore network expansion in IC1 and IC2, and initial pore enlargement followed by sintering or collapse in IDC and BM samples. IDC chars show aluminosilicate melt formations during the later stages of conversion.

❖ Electron dispersive X-ray spectroscopy reveals that IC1 chars are found to retain Ca and S during the entire char conversion period, whereas biomass chars retain K and Ca, hinting at their probable role in catalytic activity.

166

❖ Raman spectroscopic investigation finds that IC1 and IDC produce highly ordered carbon ($\geq$6 rings) with defects, whereas IC2 and BM develop smaller aromatic ring groups (3-5 rings). Low temperature char preparation favours retention of O containing groups like ethers and substituted aromatics in larger particles, resulting in the formation of smaller ring structures.

❖ IDC chars, despite having defective carbon arrangement and amorphous ring groups, the factors like absence of catalytic phases, sintering of pores with aluminosilicate formations depreciate the reactiveness of char.

❖ Steam atmosphere is observed to favour the conversion of all forms of carbon (amorphous as well as high-ordered carbons), whereas $CO_2$ atmosphere is more selective towards low-ordered amorphous carbon forms that mostly have oxygen and hydrogen-containing groups.

## 9.2 Conclusions

The conception of using large fuel particles to ensure sustained volatile release for better $CO_2$ capture efficiency, to bring down the oxygen requirement in the freeboard oxygen polishing step, and thus reducing energy penalty in fluidized bed CLC systems is found to be feasible. A new method for the determination of devolatilization time for flameless combustion environments is needed and the proposed 'CIM' is available as an easy and reliable technique for this purpose. Under the scope of the study, the following conclusions are drawn.

❖ Particle comminution in large fuel particles enables in-process size reduction, improves conversion rate and thereby, helps to reduce the energy penalty involved in the chemical looping process. However, the high ash coal (IC2) produced larger ash particles that could end up in bed, possibly causing ash separation issues. Therefore, it is recommended that IC1, IDC and BM may be used in larger forms up to 25 mm in favour of the cut in fuel sizing costs and reduction of loss in carbon capture efficiency in fluidized bed CLC units. It is also understood that the high-ash IC2 in larger forms are not suitable for usage in fuel reactors and must be fed in sizes well below 10 mm for better conversion rates.

❖ Volatile-rich woody biomass particles are highly recommended for usage in larger forms to achieve higher carbon capture efficiency.

167

- ❖ Raman studies suggest that char rich in graphitic carbon may be selectively gasified using higher partial pressures of steam, while higher partial pressures of $CO_2$ (in a mixture with steam) may be preferred for chars rich in lower ordered carbon.

## 9.3 Scope and directions for future studies

- ➢ The present study is limited to testing single fuel particle studies to understand the fuel particle behaviour in an isolated manner. The next immediate step towards development in this research direction is to test the same fuels in batch operations consisting of larger particles and maximum feed size could be further refined. This may be further extended to continuous operation mode with a standalone air reactor in place to gain a better understanding of the reactor scale-up.

- ➢ The high-ash Indian coal 2 (IC2) along with a wide range of Indian coals (in terms of grades) need to be tested further in wide size ranges not larger than 10 mm, for their suitability in FB-CLC applications. Lignite and biomass which share few common properties may be tested for co-firing under CLC conditions.

- ➢ The study on char reactivity was primarily focussed to test the reactiveness of char obtained at different temperatures at isothermal conditions, which need to be extended to studying the reactivity of char particles at the same temperature as that of preparation temperature to bring out the kinetic parameters like pre-exponential factor and the activation energy. These parameters could then be used to test the suitability of existing kinetic models or to create new char kinetic models.

- ➢ To date, there exist very few fragmentation models that could predict particle comminution but with more limitations. Research may be driven towards this direction as well.

- ➢ Once a better fragmentation model is in place, the best kinetic models could be incorporated to bring a new thermo-physico-chemical kinetic model for predicting the entire fuel conversion regime with reasonable accuracy.

# APPENDIX 1

## APPENDIX 1 – SUPPLEMENTARY FIGURES



*Figure A1 Particle Size Distribution of IC1 of different sizes at 800 ºC during various quarters of devolatilization.*



*Figure A2 Particle Size Distribution of IC1 of different sizes at 875 ºC during various quarters of devolatilization.*

169

*Figure A3 Particle Size Distribution of IC2 of different sizes at 800 ⁰C during various quarters of devolatilization.*
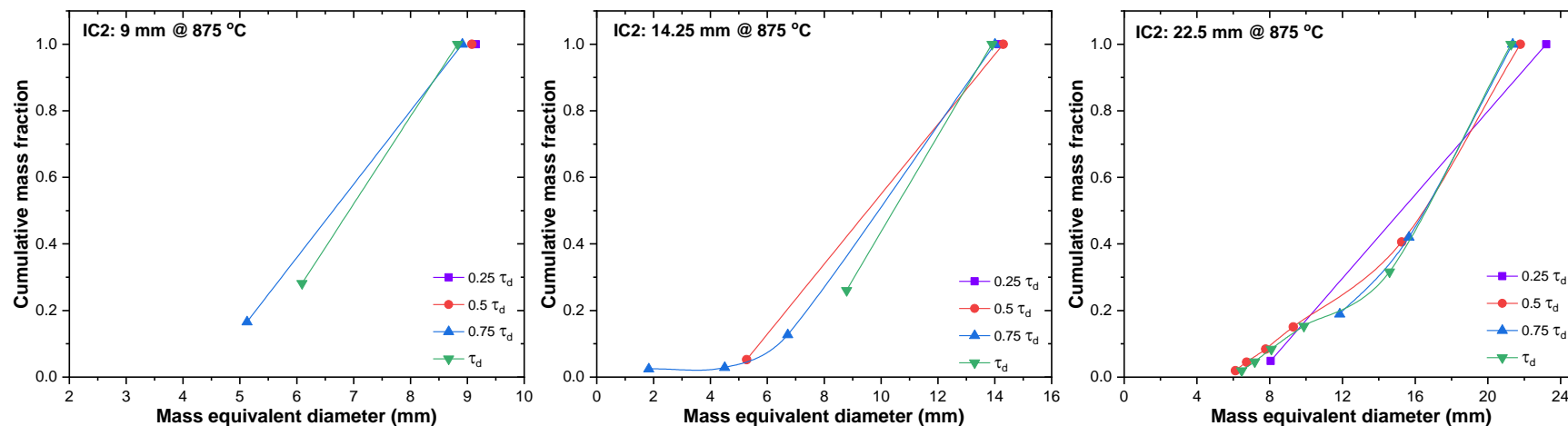


*Figure A4 Particle Size Distribution of IC2 of different sizes at 875 ⁰C during various quarters of devolatilization.*

*Figure A5 Particle Size Distribution of IDC of different sizes at 800 ⁰C during various quarters of devolatilization.*
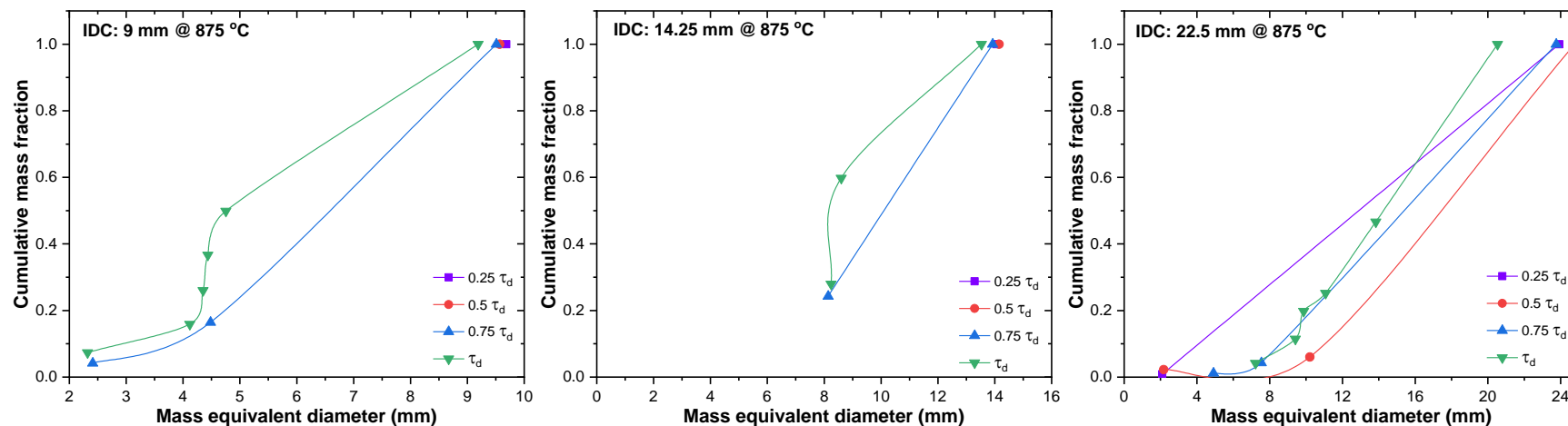


*Figure A6 Particle Size Distribution of IDC of different sizes at 875 ⁰C during various quarters of devolatilization.*

171

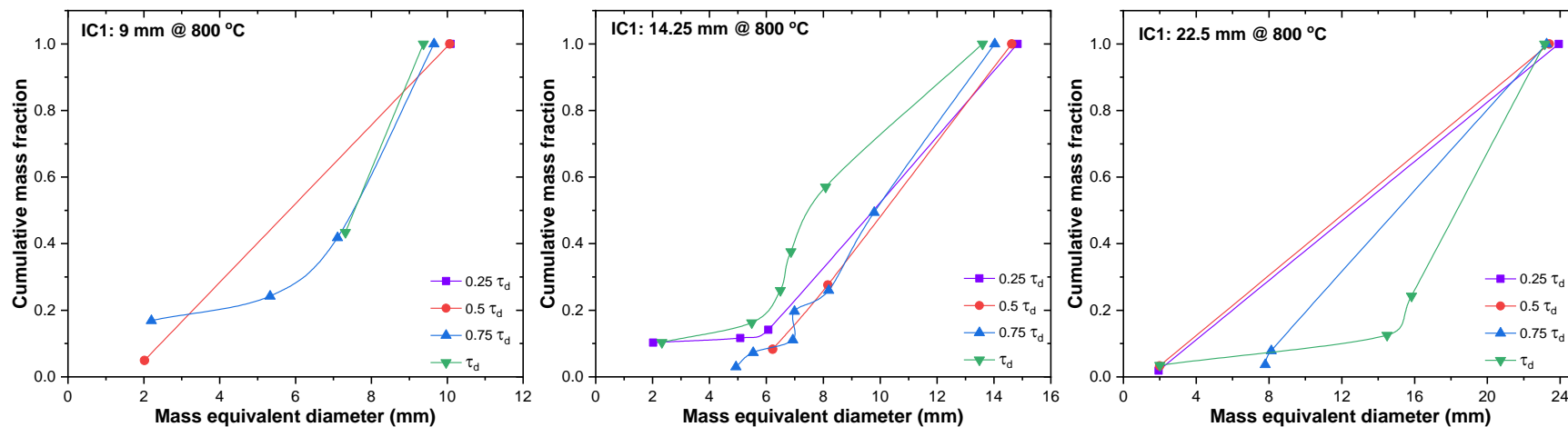*Particle size distribution of fuel particles during devolatilization*



*Figure A7 Particle Size Distribution of BM of different sizes at 800 ºC during various quarters of devolatilization.*
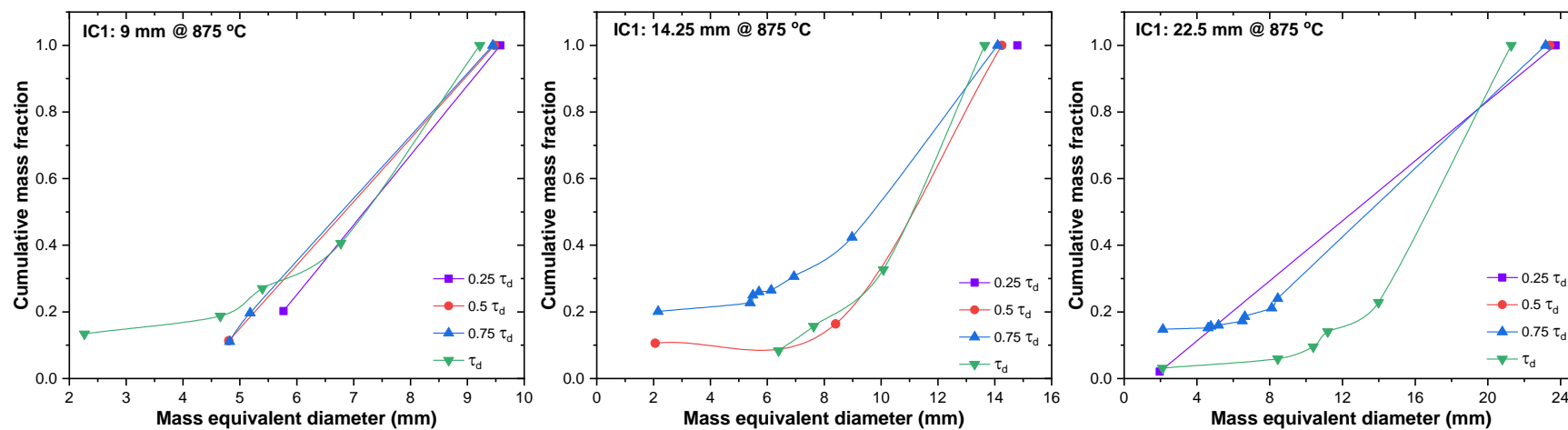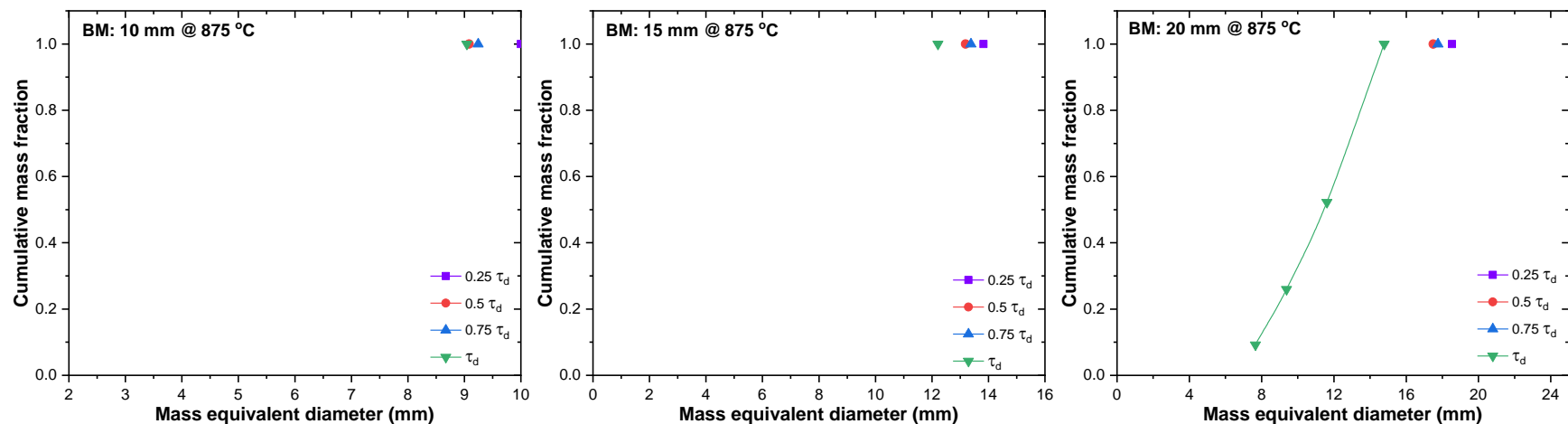


*Figure A8 Particle Size Distribution of BM of different sizes at 875 ºC during various quarters of devolatilization.*

*Particle size distribution of fuel particles during char conversion*



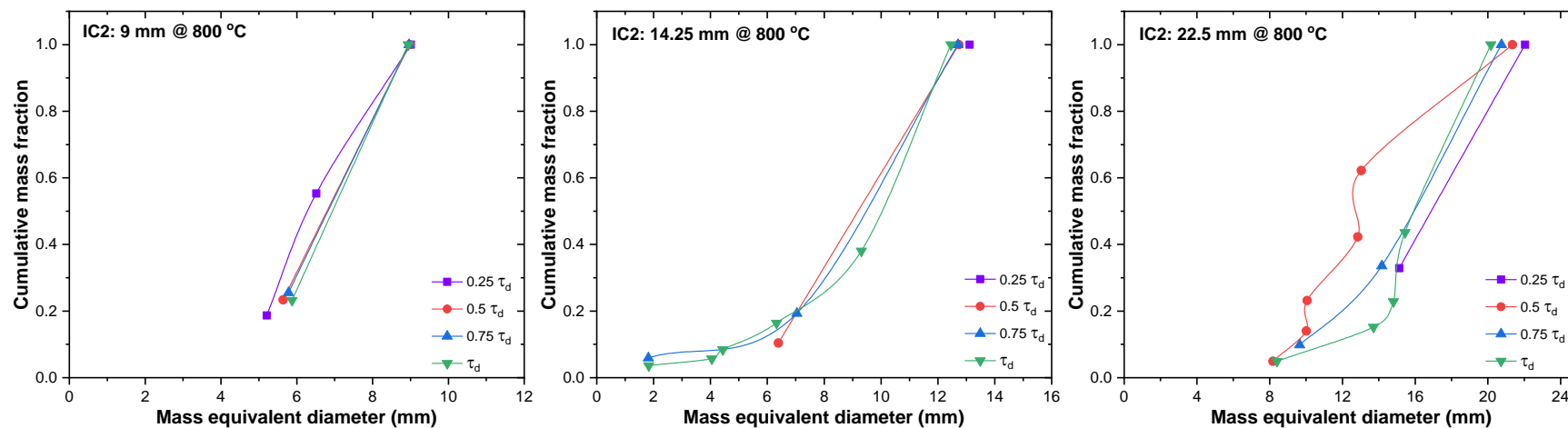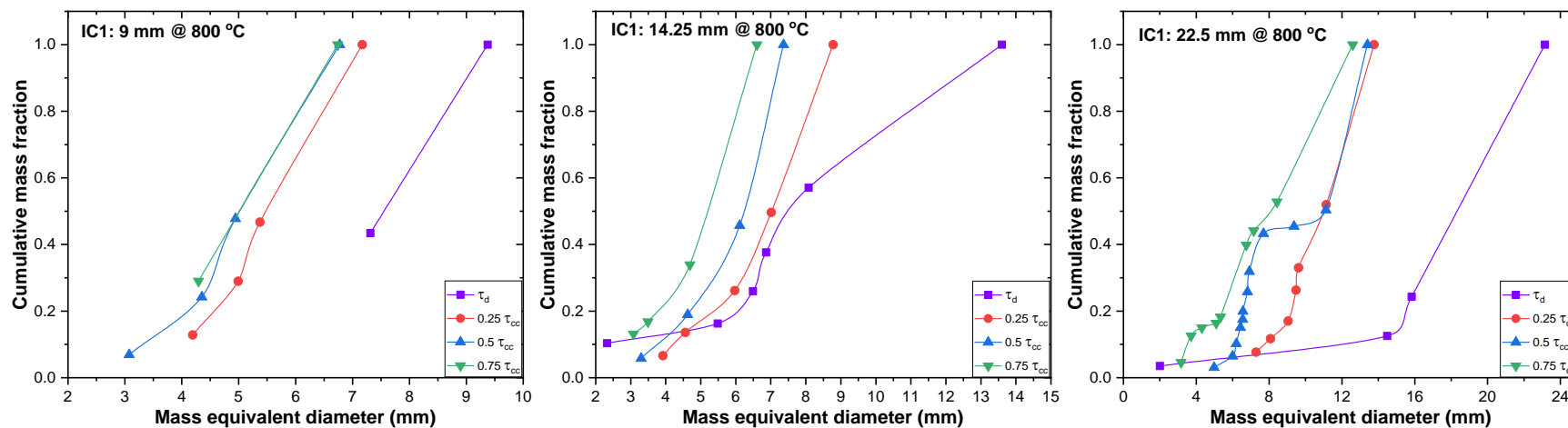***Figure A9 Particle size distribution of IC1 particles of three different sizes during various residence times at 800 °C.***
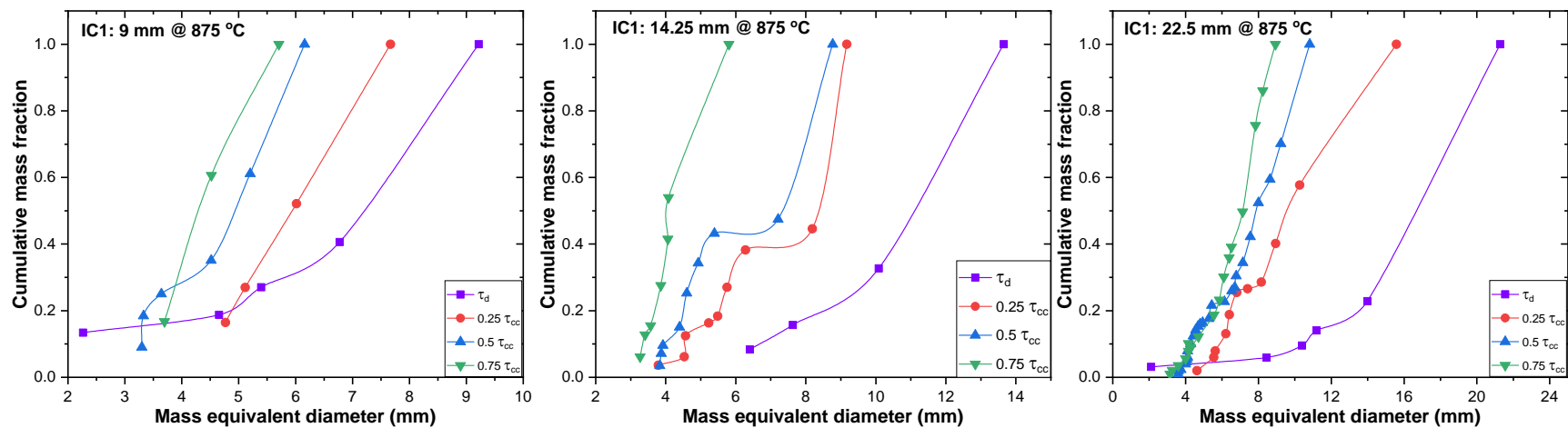


***Figure A10 Particle size distribution of IC1 particles of three different sizes during various residence times at 875 °C.***

*Particle size distribution of fuel particles during char conversion*
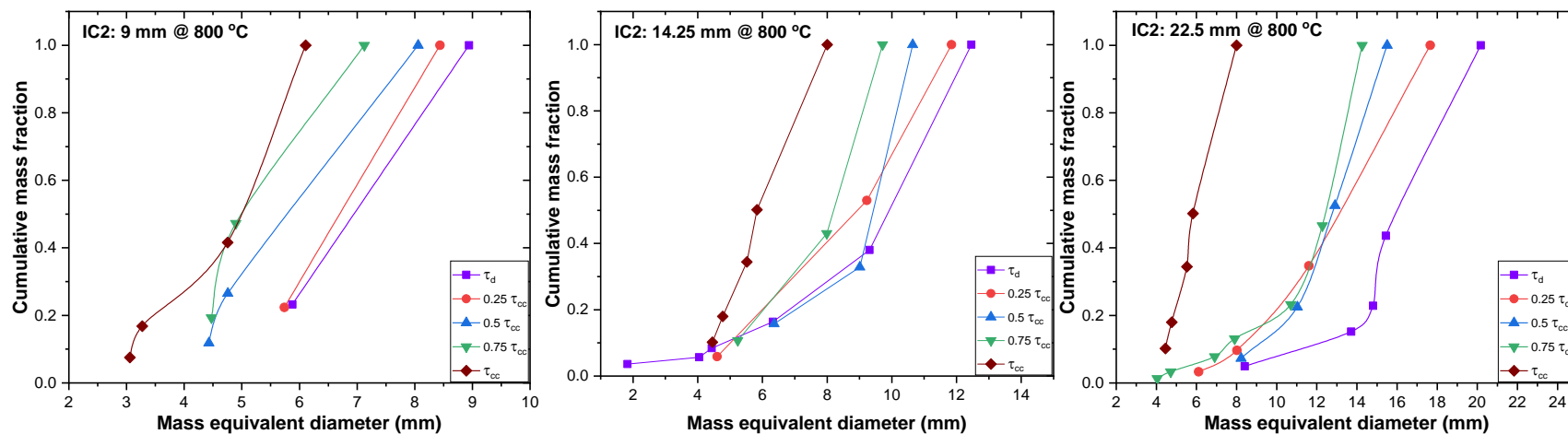


*Figure A11 Particle size distribution of IC2 particles of three different sizes during various residence times at 800 °C.*
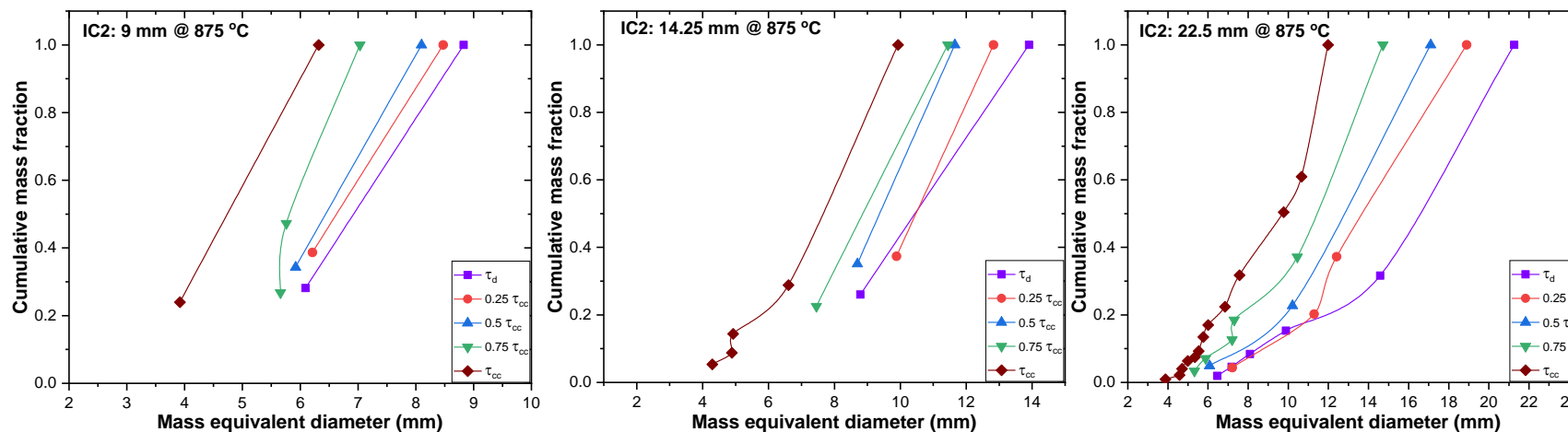


*Figure A12 Particle size distribution of IC2 particles of three different sizes during various residence times at 875 °C.*

174

*Particle size distribution of fuel particles during char conversion*
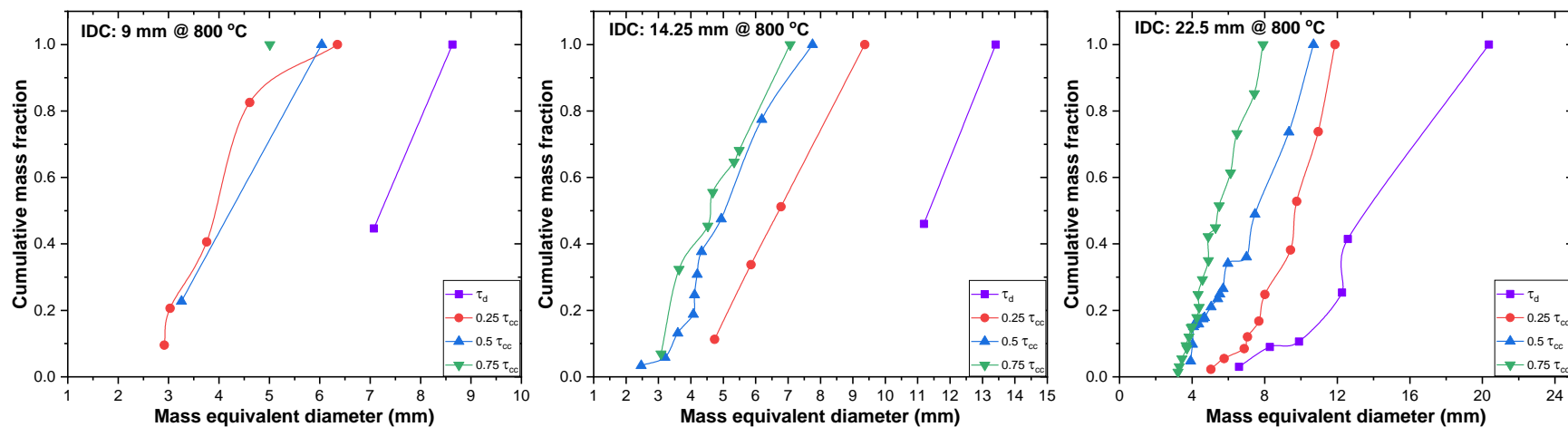


*Figure A13 Particle size distribution of IDC particles of three different sizes during various residence times at 800 ºC.*
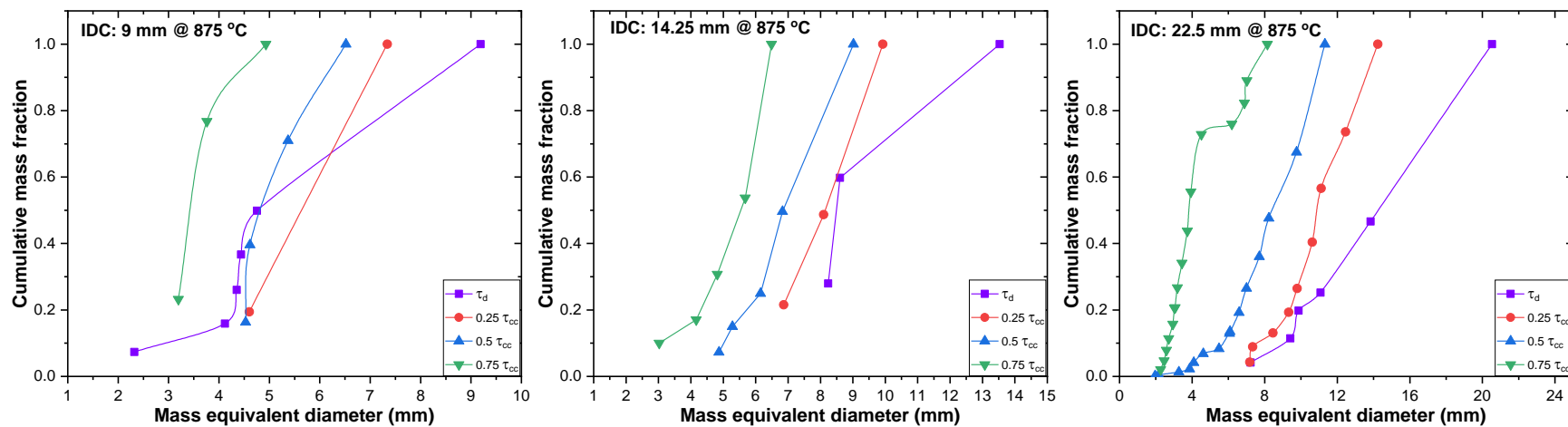


*Figure A14 Particle size distribution of IDC particles of three different sizes during various residence times at 875 ºC.*

*Particle size distribution of fuel particles during char conversion*



*Figure A15 Particle size distribution of BM particles of three different sizes during various residence times at 800 °C.*
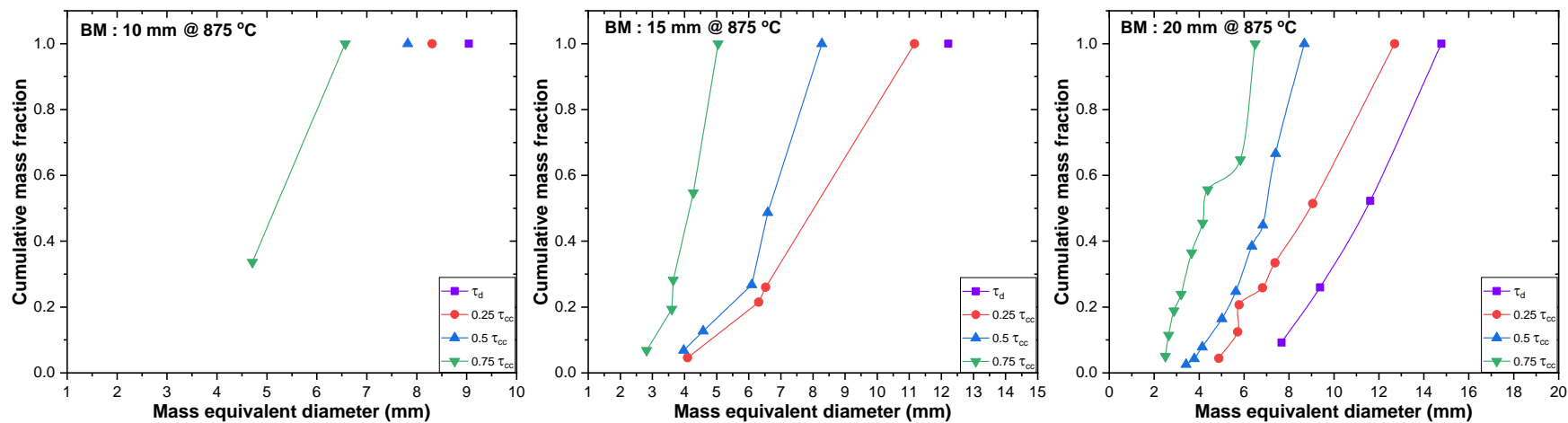


*Figure A16 Particle size distribution of BM particles of three different sizes during various residence times at 875 °C.*

*Raman spectroscopy – Secondary region (800-2000 cm$^{-1}$)*
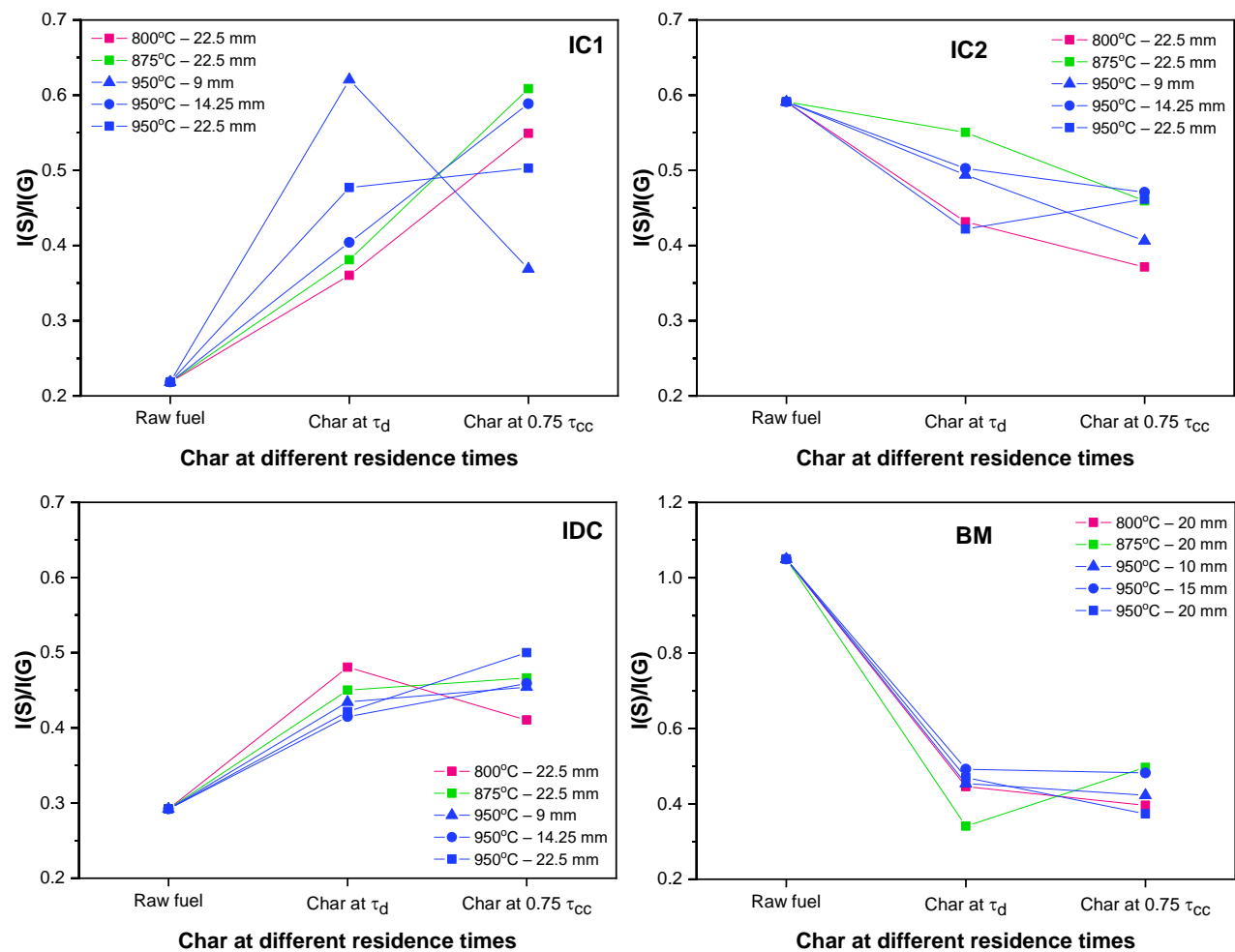


*Figure A17 Primary band area ratios of aryl-alkyl linkages to graphitic carbon in chars of different fuels at different stages of conversion.*
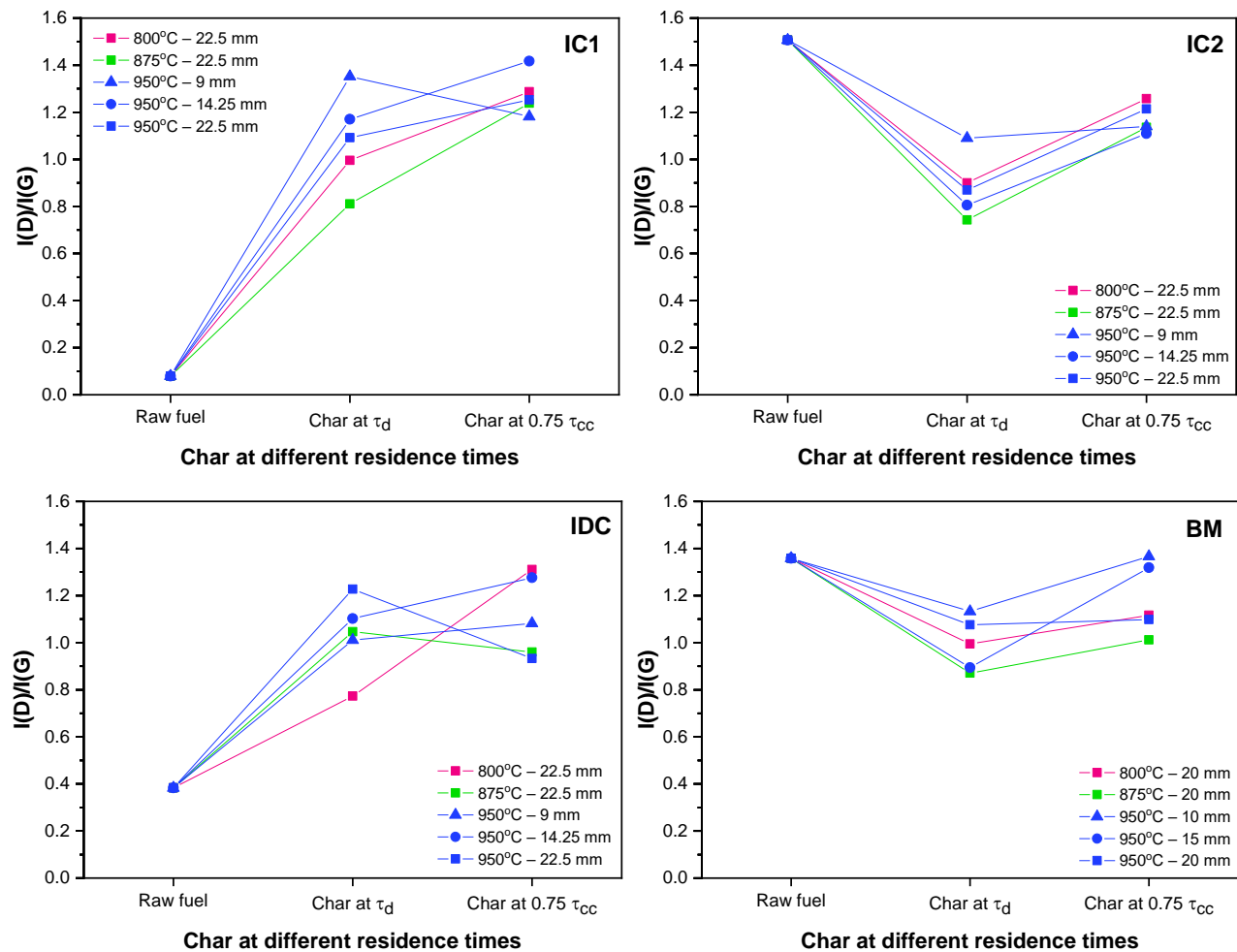
*Figure A18 Primary band area ratios of defective (D) to graphitic (G) regions in chars of different fuels at different stages of conversion.*
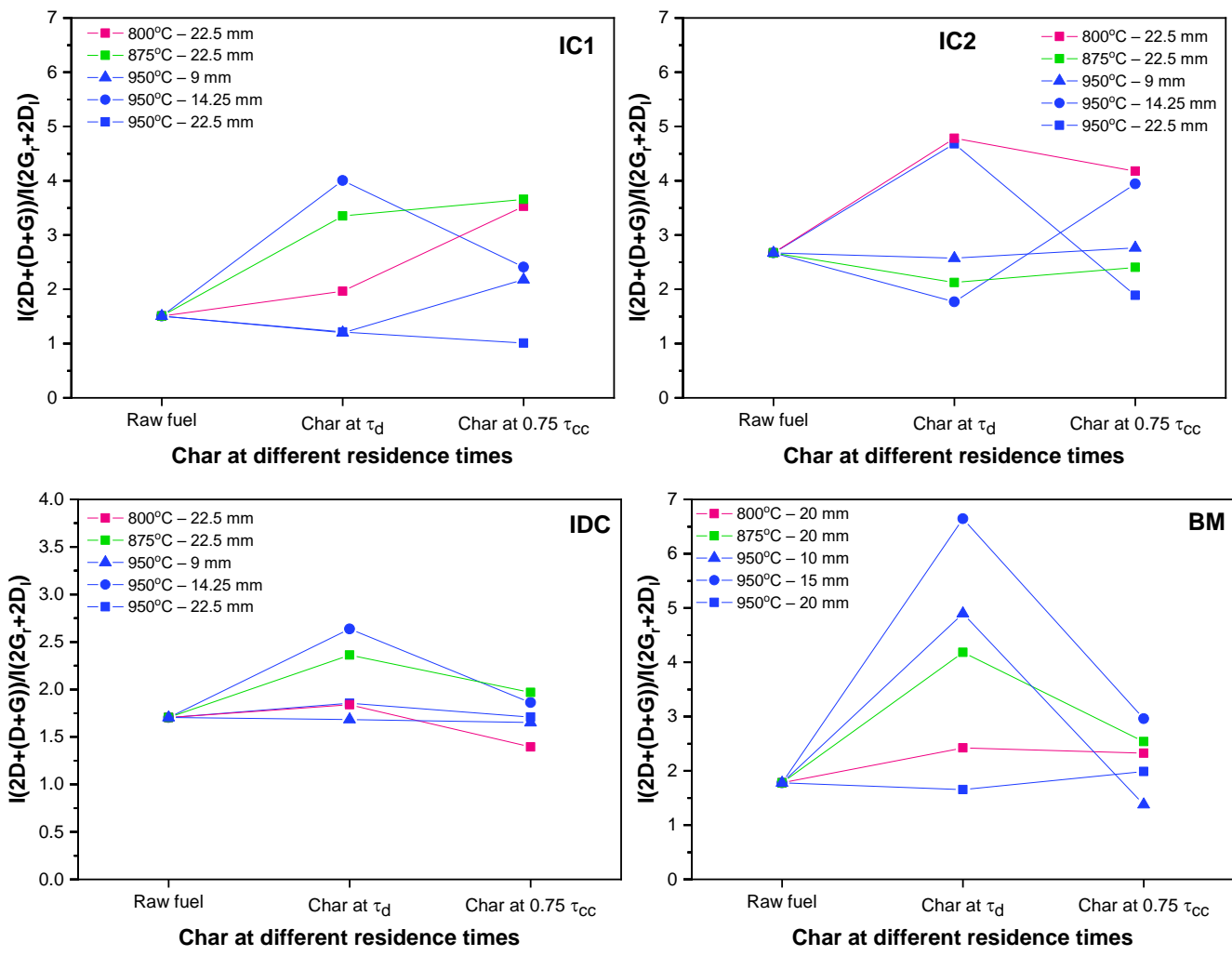
*Figure A19 Secondary band area ratios of large to small aromatic rings in chars of different fuels at different stages of conversion.*
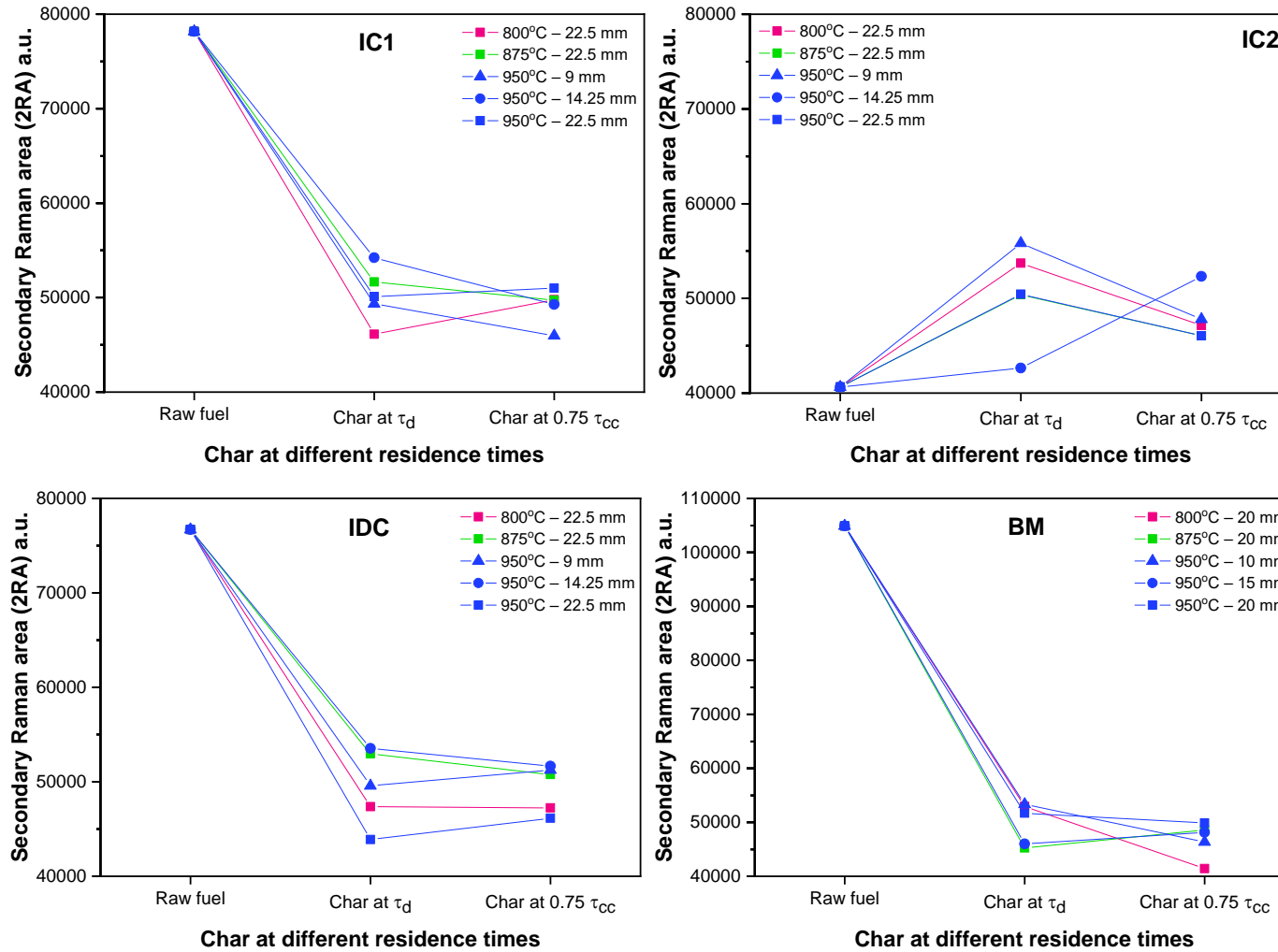
*Figure A20 Secondary total Raman area in chars of different fuels at different stages of conversion.*
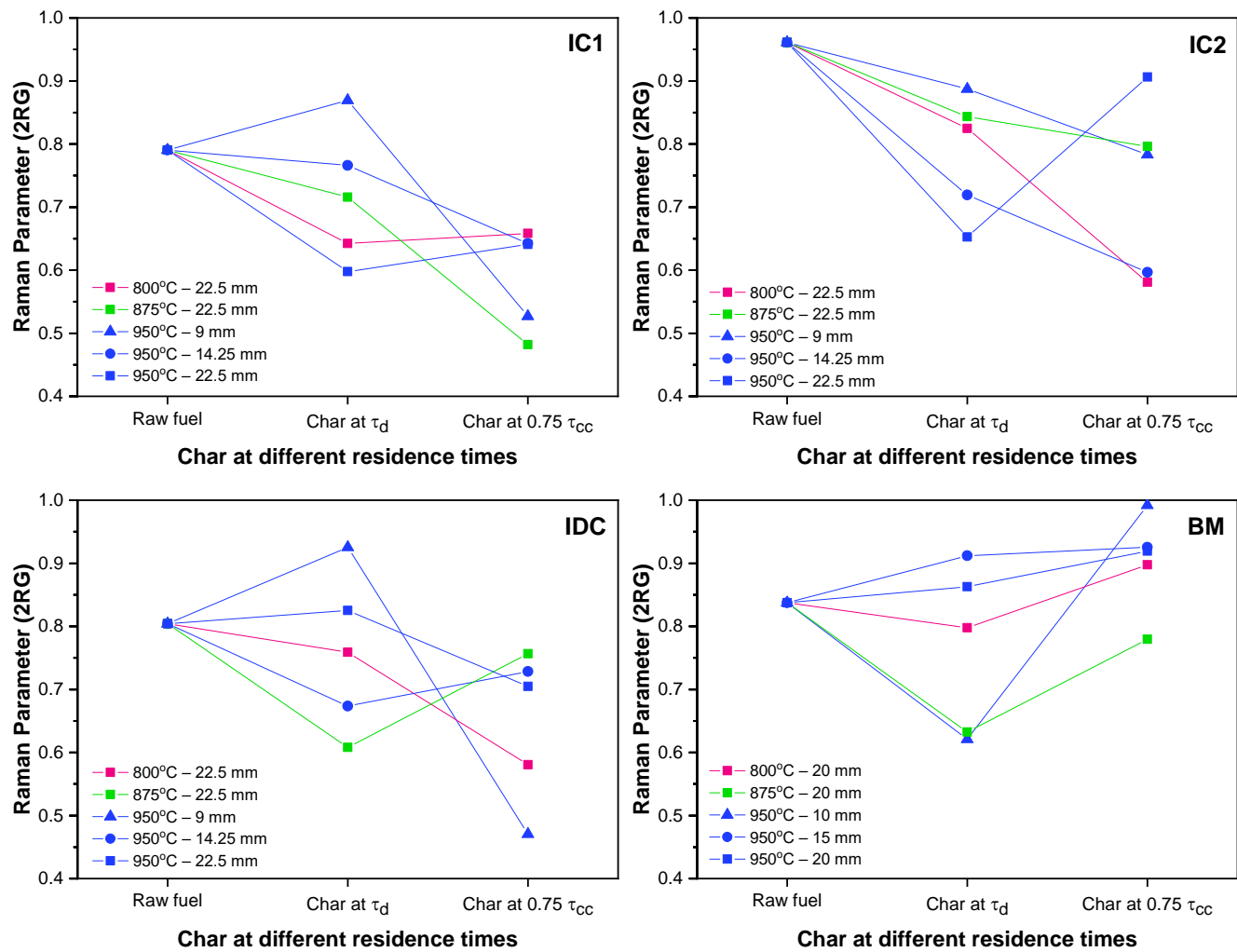
*Figure A21 Secondary Raman parameter of chars of different fuels at different stages of conversion.*
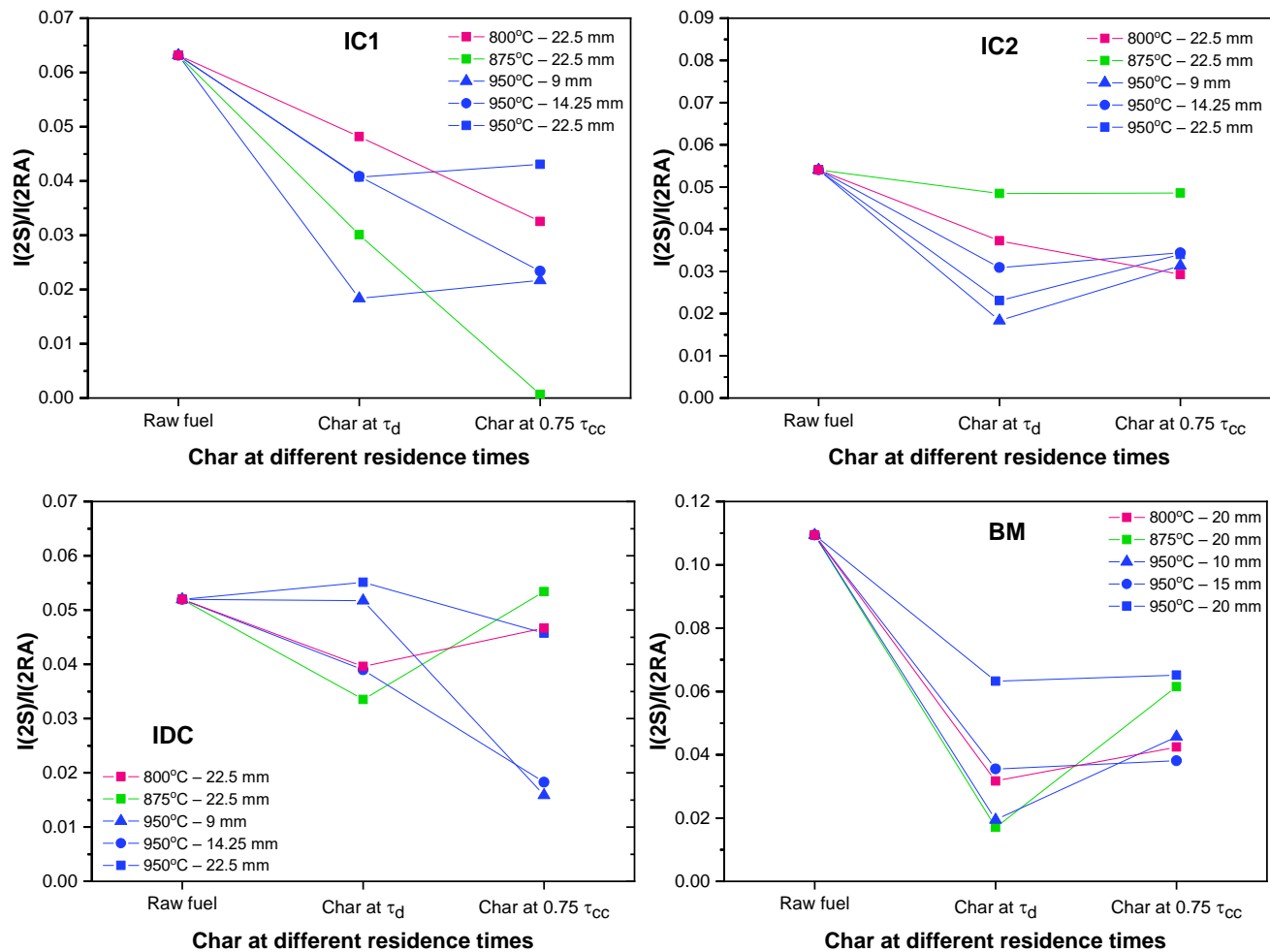
*Figure A22 Secondary band area ratios of aryl-alkyl linkages to graphitic carbon in chars of different fuels at different stages of conversion.*
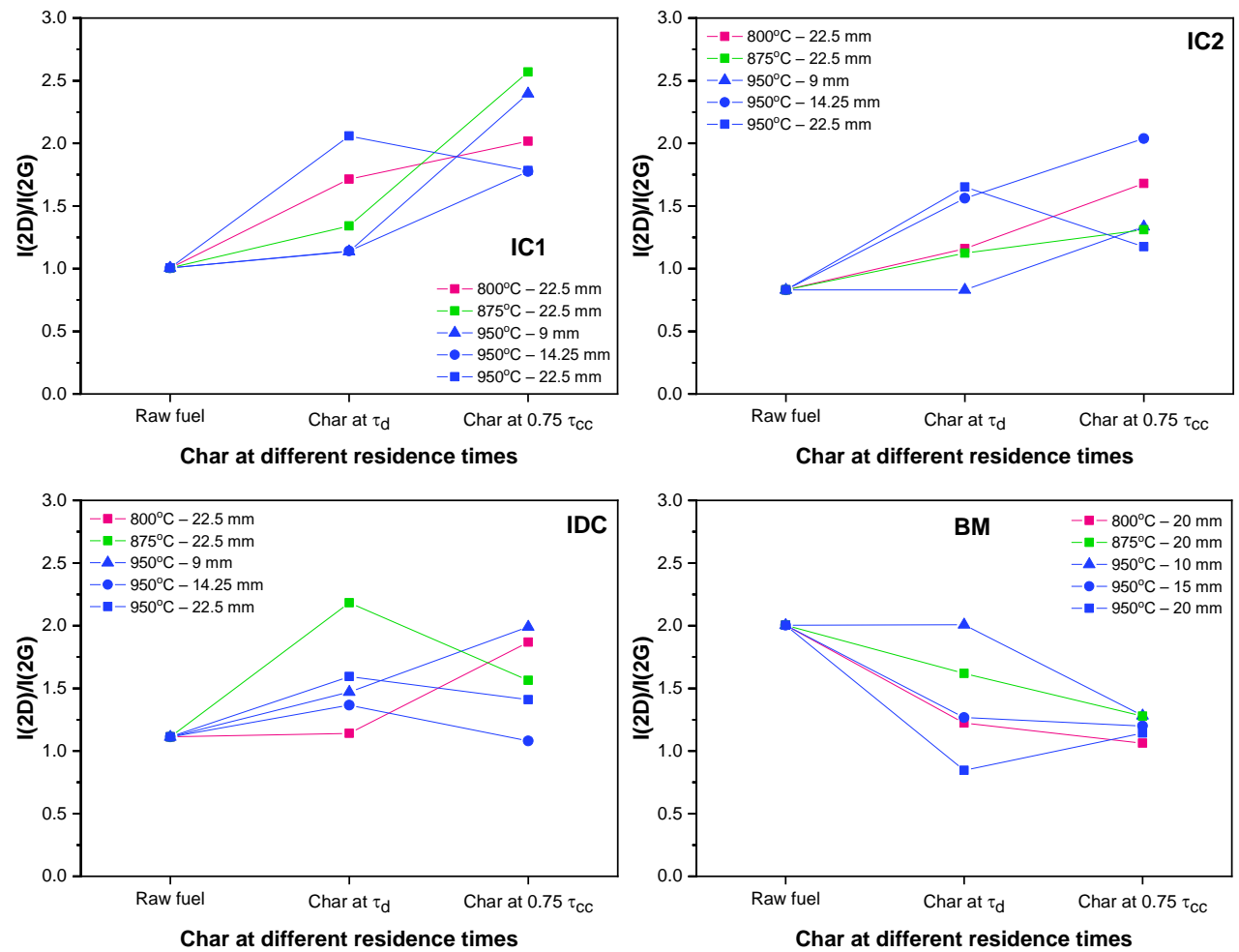
*Figure A23 Secondary band area ratios of defective (D) to graphitic (G) regions in chars of different fuels at different stages of conversion.*

# APPENDIX 2

## APPENDIX 2 – UNCERTAINTY ANALYSIS

### Introduction

The experiments in the thesis are carried out with utmost care, minimizing the occurrences of known errors. However, there are chances of inevitable experimental errors, that are being addressed as uncertainties in this section. Some of the uncertainties include errors in measurements such as flow velocities, pressure drop, size and shape of fuel particles, number of fragments, devolatilization and char conversion times, indicators of fragmentation, char reactivity and Raman measurements. The level of uncertainties in primary measurements and the associated errors from calculations based on the measured values are discussed in the following.

### Theory

Certain engineering experiments could not always be repeated several times to provide useful statistical information due to the extensive time involved or the cost of experiments. In most of these cases in research, single-sample uncertainty analysis has been used as a diagnostic tool for the development of experiments (Moffat 1988). In few cases, it is a set of few experiments called multiple-sample experiments alike the experiments in present. A statistical way to estimate the uncertainty for single-sample experiments was developed by Kline and McClintock(1953). In general, an experimental measurement ($X_i$) with uncertainty can be expressed as done in Equation A1.

$$X_i = X_i \ (measured) \pm \delta X_i \ldots\ldots\ldots\ldots\ldots\ldots\ldots\ldots\ldots\ldots\ldots.(A1)$$

Here, $X_i$ (measured) is the arithmetic mean and $\delta X_i$ being the uncertainty interval. The level of uncertainty is usually fixed by the experimenter, during the experimental plan and debugging stage. The value of $\delta X_i$ represents $2\sigma$ for a single-sample analysis, where $\sigma$ is the standard deviation of the experimental population from which the sample was taken. In the experiments carried out in the thesis i.e. multiple-sample experiments, $\delta X_i$ represents the random error components due to the heterogeneity amongst the samples (Equation A2).

$$\delta X_i = \frac{t.S(N)}{\sqrt{N}} \ldots\ldots\ldots\ldots\ldots\ldots\ldots\ldots\ldots\ldots\ldots\ldots\ldots\ldots\ldots.(A2)$$

In Equation A2, 't' represents the population statistic of the t-distribution with sample numbers less than 30, S(N) is the standard deviation for 'N number of samples. On applying the values of primary measurements of several variables from multiple sources/instruments in quantitating an entity, the errors involved in each of the individual sources would sum up to propagate the uncertainty. While estimating the uncertainty of a calculated result that is based on the uncertainty in primary measurements, the result (R) can be expressed as a function of independent variables such as $X_1$, $X_2$, $X_3$ etc., as in Equation A3.

$$R = R(X_1, X_2, X_3, \ldots\ldots X_N) \ldots\ldots\ldots\ldots\ldots\ldots\ldots\ldots\ldots (A3)$$

Kline and McClintock (1953) showed that the uncertainty in the calculated result could be estimated with reasonable accuracy using a root-sum-square(RSS) method. The uncertainty involved in a single measurement is defined by Equation A4.

$$\delta R_{X_i} = \frac{\partial R}{\partial X_i} \cdot \delta X_i \ldots\ldots\ldots\ldots\ldots\ldots\ldots\ldots\ldots\ldots\ldots\ldots (A4)$$

For the experiments with several independent variables, the error would be,

$$\delta R = \left[ \left( \frac{\partial R}{\partial X_1} \delta X_1 \right)^2 + \left( \frac{\partial R}{\partial X_2} \delta X_2 \right)^2 + \left( \frac{\partial R}{\partial X_3} \delta X_3 \right)^2 + \ldots + \left( \frac{\partial R}{\partial X_N} \delta X_N \right)^2 \right]^{1/2} \ldots (A5)$$

In Equation A5, the partial derivative of R with respect to a $X_i$ is the sensitivity co-efficient for result $R_{X_i}$. This equation is used to determine the uncertainty in the following sections.

**Uncertainty in Fluidization Velocity**

Pipe diameter, $d_1 = 53 \pm 0.025$ mm

Pipe area, $A_1 = \frac{\pi}{4} \left( \frac{53}{1000} \right)^2 = 2.206 \times 10^{-3} \text{m}^2$

*Uncertainty in Cross-Sectional Area:*

$A = \frac{\pi}{4} d^2$

$\frac{d(A)}{d(d^2)} = \frac{\pi}{4} \times 2d$

Uncertainty, $\delta R_A = \left[\left(\frac{d(A)}{d(d^2)} \times \delta R_g\right)^2\right]^{1/2} = \frac{\pi}{4} \times 2d \times 0.025 = 0.03925 \, d$

Uncertainty in pipe area, $\delta R_{A1} = 0.03925 \times 53 = 2.08 \, \text{mm}^2 = 2.08 \times 10^{-6} \, \text{m}^2 = 0.094\%$

### *Uncertainty in the Velocity in Pipe*

Uncertainty in mass flow measurement using rotameter $= \pm 1\%$ of full scale i.e. $0.00006$ $\text{m}^3/\text{s}$

Uncertainty in $\rho = 0.01 \, \text{kg/m}^3$

For a given mass flow rate ($m_a$) of $1.667 \times 10^{-3} \, \text{m}^3/\text{s}$,

Air velocity in pipe, $u_p = \frac{m_a}{\rho A_1} = \frac{1.667 \times 10^{-3}}{1.16 \times 2.206 \times 10^{-3}} = 0.6514 \, \text{m/s}$

Uncertainty in $u_p$:

$$\frac{du_p}{dm_a} = \frac{1}{\rho A_1} = \frac{1}{1.16 \times 2.206 \times 10^{-3}} = 390.78$$

$$\frac{du_p}{d\rho} = \frac{m_a}{A_1} \times \frac{-1}{\rho^2} = \frac{-1.667 \times 10^{-3}}{2.206 \times 10^{-3} \times 1.16^2} = 0.5615$$

$$\frac{du_p}{dA_1} = \frac{m_a}{\rho} \times \frac{-1}{A_1^2} = \frac{-1.667 \times 10^{-3}}{1.16 \times (2.206 \times 10^{-3})^2} = 295$$

$$\delta R_{u_p} = [(390.78 \times 0.00006)^2 + (0.5615 \times 0.01)^2 + (295 \times 2.08 \times 10^{-6})^2]^{\frac{1}{2}}$$

$$= 0.024 \, \text{m/s}$$

$$= 3.6 \, \%$$

### *Uncertainty in the Reactor Area*

Diameter of the reactor $= 130 \pm 0.01 \, \text{mm}$

Area of reactor $= \frac{\pi}{4} \left(\frac{130}{1000}\right)^2 = 0.0133 \, \text{m}^2$

Uncertainty in the reactor area, $\delta R_{w_r} = \frac{\pi}{4} \times 2 \times d \times 0.025 = \frac{\pi}{4} \times 2 \times 130 \times 0.025$

$$= 5.1 \, \text{mm}^2$$

$$= 5.1 \times 10^{-6} m^2$$

$$= 0.038\%$$

*Uncertainty in the Velocity inside the Reactor*

Velocity in the reactor, $u_r = \dfrac{m_a}{\rho_r A_r} = \dfrac{1.667 \times 10^{-3}}{0.315 \times 0.0133} = 0.397$ m/s

Uncertainty in $u_r$:

$$\frac{du_r}{dm_a} = \frac{1}{\rho_r A_r} = \frac{1}{0.315 \times 0.0133} = 238.69$$

$$\frac{du_r}{d\rho_r} = \frac{m_a}{A_r} \times \frac{-1}{\rho_r^2} = \frac{-1.667 \times 10^{-3}}{0.0133 \times (0.315)^2} = -1.263$$

$$\frac{du_r}{dA_r} = \frac{m_a}{\rho_r} \times \frac{-1}{(A_r)^2} = \frac{-1.667 \times 10^{-3}}{0.315 \times (0.0133)^2} = 29.917$$

Uncertainty in the velocity in the reactor,

$$\delta R_{u_r} = [(238.69 \times 0.00006)^2 + (1.263 \times 0.001)^2 + (29.917 \times 5.1 \times 10^{-6})^2]^{\frac{1}{2}}$$

$$= 19 \times 10^{-3} m/s$$

$$= 4.7\%$$

**Uncertainty in Measurement of Shrinkage**

Shrinkage is defined as

% Shrinkage$= \left[1 - \dfrac{\text{Instantaneous dimension}}{\text{Initial dimension}}\right] \times 100 = \left[1 - \dfrac{d_i}{d_0}\right] \times 100$

$d_0 = 10 \pm 0.025$ mm

$d_i = 8 \pm 0.025$ mm

$\% s = \left[1 - \dfrac{8}{10}\right] \times 100 = 20\%$

$$\frac{ds}{dd_i} = \frac{-100}{d_0} = \frac{-100}{10} = -10$$

$$\frac{ds}{dd_0} = -100d_i \times \frac{-1}{d_0^2} = 100 \times \frac{8}{10^2} = 8$$

Uncertainty in shrinkage, $\delta Rs = [(-10 \times 0.025)^2 + (8 \times 0.025)^2]^{1/2} = 0.32 = 1.6\%$

***Uncertainty in Volumetric Shrinkage***

$$\% \ s_v = \left[1 - \frac{\text{Instantaneous volume}}{\text{Initial volume}}\right] \times 100$$

For a cube/cuboid,

$$\% \ s_v = \left[1 - \frac{a_i b_i c_i}{a_0 b_0 c_0}\right] \times 100$$

$a_i = 8 \pm 0.025$ mm; $b_i = 7 \pm 0.025$ mm; $c_i = 9 \pm 0.025$ mm

$a_0 = 10 \pm 0.025$ mm; $b_0 = 10 \pm 0.025$ mm; $c_0 = 10 \pm 0.025$ mm

$$\% \ s_v = \left[1 - \frac{8 \times 7 \times 9}{10 \times 10 \times 10}\right] \times 100 = 49.6$$

$$\frac{ds_v}{da_i} = \frac{-100 \times b_i \times c_i}{a_0 \times b_0 \times c_0} = \frac{-100 \times 7 \times 9}{10 \times 10 \times 10} = -6.3$$

$$\frac{ds_v}{db_i} = \frac{-100 \times a_i \times c_i}{a_0 \times b_0 \times c_0} = \frac{-100 \times 8 \times 9}{10 \times 10 \times 10} = -7.2$$

$$\frac{ds_v}{dc_i} = \frac{-100 \times a_i \times b_i}{a_0 \times b_0 \times c_0} = \frac{-100 \times 8 \times 7}{10 \times 10 \times 10} = -5.6$$

$$\frac{ds_v}{da_0} = \frac{-100 \times a_i \times b_i \times c_i}{b_0 c_0} \times \frac{-1}{a_0^2} = \frac{-100 \times 8 \times 7 \times 9}{10^2 \times 10 \times 10} = -5.04$$

Similarly, $\frac{ds_v}{db_0} = \frac{ds_v}{dc_0} = -5.04$

Uncertainty in volume shrinkage,

$$\delta R_{s_v} = \left[\begin{array}{l}(-6.3 \times 0.025)^2 + (-7.2 \times 0.025)^2 + (-5.6 \times 0.025)^2 + \\ (-5.04 \times 0.025)^2 + (-5.04 \times 0.025)^2 + (-5.04 \times 0.025)^2\end{array}\right]^{1/2} = 0.35$$

$$= 0.705\%$$

**Uncertainty in Fragmentation Index (FI)**

Fragmentation Index, $FI = \dfrac{NF}{\frac{x_i d_i}{d_a}} = \dfrac{NF d_a}{x_i d_i}$

For an unfragmented (but shrunk) particle, i=1.

NF=1, $d_a$=10, $d_i$=8 ± 0.025 mm

$x_i$=1 ± 0.01

$FI = \dfrac{1 \times 10}{1 \times 8} = 1.25$

$\dfrac{dFI}{dNF} = \dfrac{d_a}{x_i d_i} = \dfrac{10}{1x8} = 1.25$

$\dfrac{dFI}{dd_a} = \dfrac{NF}{x_i d_i} = \dfrac{1}{1x8} = 1.25$

$\dfrac{dFI}{dx_i} = NF \dfrac{d_a}{d_i} X \dfrac{-1}{x_i^2} = 1X \dfrac{10}{8} X \dfrac{-1}{12} = 1.25$

$\dfrac{dFI}{dd_i} = NF \dfrac{d_a}{x_i} X \dfrac{-1}{d_i^2} = 1X \dfrac{10}{1} X \dfrac{-1}{8} = -0.156$

Uncertainty in FI,

$\delta R_{FI} = [(1.25 \times 0)^2 + (0.125 \times 0.025)^2 + (1.25 \times 0.01)^2 + (-0.156 \times 0.025)^2]^{\frac{1}{2}}$

$$= 0.01346$$

$$= 1.1\%$$

**Uncertainty in results of experimental measurements**

The uncertainty is intervals defined in the experimental results conform to a minimum confidence level of 90% in all the experiments. Statistic values of t-distribution are applied in declaring the error values corresponding to the fore mentioned confidence level and mostly, the values are equivalent to 1 standard deviation limit (1σ).

**Uncertainty in instrumental measurements**

The uncertainties involved in various instrumental measurements are summarized in Table A3.1

Table A3.1: Instruments and uncertainties

| S. No | Instrument | Least count | Uncertainty (±) |
|-------|-----------|-------------|-----------------|
| 1 | Vernier calipers (Mauser make) | 0.05 mm | 0.025 mm |
| 2 | Stopwatch (Casio make) | 0.01 s | 0.005 s |
| 3 | Thermocouple (k type) | 0.01 °C | 1.5 °C |
| 4 | DC ammeter (Agilent Technologies) | 4 mA | $5 \times 10^{-3}$ mA |
| 5 | Thermogravimeter (Hitachi TG/DTA 6300) | 0.2 µg | 0.1 µg |
| 6 | Differential Thermal Analyzer (Hitachi TG/DTA 6300) | 0.06 µV | 0.03 µV |

**Closure**

The uncertainty of various measurements made is found to be within reasonable limits.

## REFERENCES

Abad, A., Mendiara, T., Gayán, P., García-Labiano, F., Diego, L. F. F. De, Bueno, J. A. A., Pérez-Vega, R., and Adánez, J. (2017). "Comparative Evaluation of the Performance of Coal Combustion in 0.5 and 50 kWth Chemical Looping Combustion Units with Ilmenite, Redmud or Iron Ore as Oxygen Carrier." *Energy Procedia*, T. S. Dixon T. Laloui L., ed., Elsevier Ltd, 285–301.

Abad, A., Pérez-Vega, R., Diego, L. F. de, García-Labiano, F., Gayán, P., and Adánez, J. (2015). "Design and operation of a 50 kWth Chemical Looping Combustion (CLC) unit for solid fuels." *Appl. Energy*, 157, 295–303.

Abián, M., Abad, A., Izquierdo, M. T., Gayán, P., Diego, L. F. de, García-Labiano, F., and Adánez, J. (2017). "Titanium substituted manganese-ferrite as an oxygen carrier with permanent magnetic properties for chemical looping combustion of solid fuels." *Fuel*, 195, 38–48.

Adanez, J., Abad, A., Garcia-Labiano, F., Gayan, P., and Diego, L. F. de. (2012). "Progress in Chemical-Looping Combustion and Reforming technologies." *Prog. Energy Combust. Sci.*, 38(2), 215–282.

Adánez, J., Abad, A., Mendiara, T., Gayán, P., Diego, L. F. de, and García-Labiano, F. (2018). "Chemical looping combustion of solid fuels." *Prog. Energy Combust. Sci.*, 65, 6–66.

Agarwal, P. K., Genetti, W. E., and Lee, Y. Y. (1984). "Model for devolatilization of coal particles in fluidized beds." *Fuel*, 63(8), 1157–1165.

Al-Qayim, K., Nimmo, W., Hughes, K., and Pourkashanian, M. (2017). "Kinetic parameters of the intrinsic reactivity of woody biomass and coal chars via thermogravimetric analysis." *Fuel*, 210(August), 811–825.

Álvarez, T., Fuertes, A. B., Pis, J. J., and Ehrburger, P. (1995). "Influence of coal oxidation upon char gasification reactivity." *Fuel*, 74(5), 729–735.

Andrei, M. A., Sarofim, A. F., and Beér, J. M. (1985). "Time-resolved burnout of coal particles in a fluidized bed." *Combust. Flame*, 61(1), 17–22.

Anheden, M., and Svedberg, G. (1996). "Chemical-looping combustion in combination with integrated coal gasification-a way to avoid CO/sub 2/ emission from coal fired power plants without a significant decrease in net power efficiency." *IECEC 96. Proc. 31st Intersoc. Energy Convers. Eng. Conf.*, (P. R. K. Chetty and W. D. Jackson, eds.), 3, 2045–2050.

Anthony, D. B., and Howard, J. B. (1976). "Coal devolatilization and hydrogasification." *AIChE J.*, 22(4), 625–656.

Antunes, E. F., Lobo, A. O., Corat, E. J., Trava-Airoldi, V. J., Martin, A. A., and Veríssimo, C. (2006). "Comparative study of first- and second-order Raman spectra of MWCNT at visible and infrared laser excitation." *Carbon N. Y.*

Aranda, G., Grootjes, A. J., Meijden, C. M. van der, Drift, A. van der, Gupta, D. F., Sonde, R. R., Poojari, S., and Mitra, C. B. (2016). "Conversion of high-ash coal under steam and CO2 gasification conditions." *Fuel Process. Technol.*, 141, 16–30.

Arena, U., Cammarota, A., and Chirone, R. (1994). "Primary and secondary fragmentation of coals in a circulating fluidized bed combustor." *Symp. Combust.*, 25(1), 219–226.

Arena, U., Cammarota, A., Chirone, R., Massimilla, L., Naples, P. V. T., and Massimilla, L. (1992). "Secondary fragmentation of a char in a circulating fluidized bed combustor." *Symp. Combust.*, 24(1), 1341–1348.

Asadullah, M., Zhang, S., and Li, C.-Z. (2010). "Evaluation of structural features of chars from pyrolysis of biomass of different particle sizes." *Fuel Process. Technol.*, 91(8), 877–881.

Asadullah, M., Zhang, S., Min, Z., Yimsiri, P., and Li, C. Z. (2009). "Importance of biomass particle size in structural evolution and reactivity of char in steam gasification." *Ind. Eng. Chem. Res.*, 48(22), 9858–9863.

Babinski, P., Sciazko, M., and Ksepko, E. (2018). "Limitation of thermogravimetry for oxy-combustion analysis of coal chars." *J. Therm. Anal. Calorim.*, 133(1), 713–725.

Bacsa, W. S., Lannin, J. S., Pappas, D. L., and Cuomo, J. J. (1993). "Raman scattering of laser-deposited amorphous carbon." *Phys. Rev. B*, 47(16), 10931–10934.

Baizhong, S., Hong, Q., Qing, W., Jingru, B., Hongpeng, L., and Chunxia, J. (2009). "Experiment on Bituminous Coal Thermal Fragmentation." *2009 Int. Conf. Energy Environ. Technol.*, IEEE, 640–643.

Balandin, A. A. (2011). "Thermal properties of graphene and nanostructured carbon materials." *Nat. Mater.*, 10(8), 569–581.

Bareschino, P., Urciuolo, M., Scherer, V., Chirone, R., and Senneca, O. (2020). "Effect of O2/CO2 atmospheres on coal fragmentation." *Fuel*, 267, 117145.

Basile, A., Gugliuzza, A., Iulianelli, A., and Morrone, P. (2011). "Membrane technology for carbon dioxide (CO2) capture in power plants." *Adv. Membr. Sci. Technol. Sustain. Energy Environ. Appl.*, Elsevier Inc., 113–159.

Basu, P. (2006). *Combustion and Gasification in Fluidized Beds*. CRC Press.

Bayham, S., McGiveron, O., Tong, A., Chung, E., Kathe, M., Wang, D., Zeng, L., and Fan, L.-S. S. (2015). "Parametric and dynamic studies of an iron-based 25-kWth coal direct chemical looping unit using sub-bituminous coal." *Appl. Energy*, 145, 354–363.

Berguerand, N., and Lyngfelt, A. (2009). "Chemical-Looping Combustion of Petroleum Coke Using Ilmenite in a 10 kW th Unit−High-Temperature Operation." *Energy & Fuels*, 23(10), 5257–5268.

Bhui, B., and Vairakannu, P. (2019). "Experimental and kinetic studies on in-situ CO2 gasification based chemical looping combustion of low ash coal using Fe2O3 as the oxygen carrier." *J. CO2 Util.*, 29, 103–116.

Blamey, J., Anthony, E. J., Wang, J., and Fennell, P. S. (2010). "The calcium looping cycle for large-scale CO2 capture." *Prog. Energy Combust. Sci.*, 36(2), 260–279.

Blasi, C. Di, and Branca, C. (2003). "Temperatures of wood particles in a hot sand bed fluidized by nitrogen." *Energy and Fuels*, 17(1), 247–254.

Bliek, A., Poelje, W. M. Van, Swaaij, W. P. M. Van, and Beckum, F. P. H. Van. (1985).

"Effects of intraparticle heat and mass transfer during devolatilization of a single coal particle." *AIChE J.*, 31(10), 1666–1681.

Borah, R. C., Ghosh, P., and Rao, P. G. (2008). "Devolatilization of coals of North-Eastern India under fluidized bed conditions in oxygen-enriched air." *Fuel Process. Technol.*, 89(12), 1470–1478.

Borah, R. C., Ghosh, P., and Rao, P. G. (2011). "A review on devolatilization of coal in fluidized bed." *Int. J. Energy Res.*, 35(11), 929–963.

Borah, R. C., Rao, P. G., and Ghosh, P. (2010). "Devolatilization of coals of northeastern India in inert atmosphere and in air under fluidized bed conditions." *Fuel Process. Technol.*, 91(1), 9–16.

Bouraoui, Z., Jeguirim, M., Guizani, C., Limousy, L., Dupont, C., and Gadiou, R. (2015). "Thermogravimetric study on the influence of structural, textural and chemical properties of biomass chars on CO2 gasification reactivity." *Energy*, 88, 703–710.

BP p.l.c. (2019). *BP Energy Outlook 2019 edition*. *BP Energy Outlook 2019*.

Campos, D. C., Belkouch, J., Hazi, M., and Ould-Dris, A. (2013). "Reactivity Investigation on Iron-Titanium Oxides for a Moving Bed Chemical Looping Combustion Implementation." *Adv. Chem. Eng. Sci.*, 03(January), 47–56.

Canò, G., Salatino, P., and Scala, F. (2007). "A single particle model of the fluidized bed combustion of a char particle with a coherent ash skeleton: Application to granulated sewage sludge." *Fuel Process. Technol.*, 88(6), 577–584.

Chen, G., Yu, Q., Sjiistrm, K., and Sjöström, K. (1997). "Reactivity of char from pyrolysis of birch wood." *J. Anal. Appl. Pyrolysis*, 41, 491–499.

Chen, L., Kong, L., Bao, J., Combs, M., Nikolic, H. S., Fan, Z., and Liu, K. (2017). "Experimental evaluations of solid-fueled pressurized chemical looping combustion – The effects of pressure, solid fuel and iron-based oxygen carriers." *Appl. Energy*, 195, 1012–1022.

Chen, L., Zhang, Y., Liu, F., and Liu, K. (2015). "Development of a cost-effective oxygen carrier from red mud for coal-fueled chemical-looping combustion." *Energy and Fuels*, 29(1), 305–313.

Chern, J. S., and Hayhurst, A. N. (2006). "A model for the devolatilization of a coal particle sufficiently large to be controlled by heat transfer." *Combust. Flame*, 146(3), 553–571.

Chirone, R., Cammarota, A., D'amore, M., and Massimilla, L. (1982). "Elutriation of Attrited Carbon Fines in the Fluidized Combustion of a Coal." *Symp. Combust.*, 19(1), 1213–1221.

Chirone, R., and Massimilla, L. (1989a). "The application of Weibull theory to primary fragmentation of a coal during devolatilization." *Powder Technol.*, 57(3), 197–212.

Chirone, R., and Massimilla, L. (1989b). "Primary fragmentation of a coal in fluidized bed combustion." *Symp. Combust.*, 22(1), 267–277.

Chirone, R., and Massimilla, L. (1991). "Primary fragmentation in fluidised bed combustion of anthracites." *Powder Technol.*, 64(3), 249–258.

Chirone, R., Massimilla, L., and Salatino, P. (1991). "Comminution of carbons in fluidized bed combustion." *Prog. Energy Combust. Sci.*, 17(4), 297–326.

Chirone, R., Salatino, P., and Scala, F. (2000). "The relevance of attrition to the fate of ashes during fluidized-bed combustion of a biomass." *Proc. Combust. Inst.*, 28(2), 2279–2286.

Chirone, R., Salatino, P., Scala, F., Solimene, R., and Urciuolo, M. (2008). "Fluidized bed combustion of pelletized biomass and waste-derived fuels." *Combust. Flame*, 155(1–2), 21–36.

Coetzee, S., Neomagus, H. W. J. P., Bunt, J. R., Strydom, C. A., and Schobert, H. H. (2014). "The transient swelling behaviour of large (-20 + 16 mm) South African coal particles during low-temperature devolatilisation." *Fuel*, 136, 79–88.

Colangeli, L., Mennella, V., Baratta, G. A., Bussoletti, E., and Strazzulla, G. (1992). "Raman and infrared spectra of polycyclic aromatic hydrocarbon molecules of possible astrophysical interest." *Astrophys. J.*

Cuadrat, A., Abad, A., Diego, L. F. de, García-Labiano, F., Gayán, P., and Adánez, J. (2012a). "Prompt considerations on the design of Chemical-Looping Combustion of coal from experimental tests." *Fuel*, 97, 219–232.

Cuadrat, A., Abad, A., García-Labiano, F., Gayán, P., Diego, L. F. de, and Adánez, J. (2011). "Ilmenite as oxygen carrier in a chemical looping combustion system with coal." *Energy Procedia*, (J. Gale, C. Hendriks, and W. Turkenberg, eds.), 4, 362–369.

Cuadrat, A., Abad, A., García-Labiano, F., Gayán, P., Diego, L. F. de, and Adánez, J. (2012b). "Relevance of the coal rank on the performance of the in situ gasification chemical-looping combustion." *Chem. Eng. J.*, 195–196, 91–102.

Cuadrat, A., Abad, A., García-Labiano, F., Gayán, P., Diego, L. F. F. de, and Adánez, J. (2012c). "Effect of operating conditions in Chemical-Looping Combustion of coal in a 500Wth unit." *Int. J. Greenh. Gas Control*, 6, 153–163.

Cuesta, A., Dhamelincourt, P., Laureyns, J., Martínez-Alonso, A., and Tascón, J. M. D. (1994). "Raman microprobe studies on carbon materials." *Carbon N. Y.*, 32(8), 1523–1532.

Cui, T., Zhou, Z., Dai, Z., Li, C., Yu, G., and Wang, F. (2015). "Primary Fragmentation Characteristics of Coal Particles during Rapid Pyrolysis." *Energy and Fuels*, 29(10), 6231–6241.

Cui, Y., and Stubington, J. F. (2001). "In-bed char combustion of Australian coals in PFBC. 2. Char combustion without secondary fragmentation." *Fuel*, 80(15), 2235–2243.

Czechowski, F., and Kidawa, H. (1991). "Reactivity and susceptibility to porosity development of coal maceral chars on steam and carbon dioxide gasification." *Fuel Process. Technol.*, 29(1–2), 57–73.

Dacombe, P. J., Hampartsoumian, E., and Pourkashanian, M. (1994). "Fragmentation of large coal particles in a drop-tube furnace." *Fuel*, 73(8), 1365–1367.

Dacombe, P., Pourkashanian, M., Williams, A., and Yap, L. (1999). "Combustion-

induced fragmentation behavior of isolated coal particles." *Fuel*, 78(15), 1847–1857.

Dakic, D., Honing, G. van der, Valk, M., Dakič, D., Honing, G. van der, and Valk, M. (1989). "Fragmentation and swelling of various coals during devolatilization in a fluidized bed." *Fuel*, 68(7), 911–916.

DeFusco, J. P., McKenzie, P. a., and Stirgwolt, W. R. (2010). "A Comparison of Fluid-Bed Technologies for Renewable Energy Applications." *2010 Renew. Energy World Conf.*

Demirbas, A. (2004). "Combustion characteristics of different biomass fuels." *Prog. Energy Combust. Sci.*, 30(2), 219–230.

Dhanarathinam, R. S., and Kolar, A. K. (2013). "Visualization and characterization of thermo-physical behaviour of wood during devolatilization in a hot fluidized bed using X-ray radiography technique." *Fuel*, 112, 208–223.

Diego, L. . de, García-Labiano, F., Abad, A., Gayán, P., and Adánez, J. (2002). "Coupled drying and devolatilisation of non-spherical wet pine wood particles in fluidised beds." *J. Anal. Appl. Pyrolysis*, 65(2), 173–184.

Diego, L. F. de, García-Labiano, F., Abad, A., Gayán, P., and Adánez, J. (2003). "Effect of Moisture Content on Devolatilization Times of Pine Wood Particles in a Fluidized Bed." *Energy & Fuels*, 17(2), 285–290.

Diego, L. F. De, García-Labiano, F., Adánez, J., Gayán, P., Abad, A., Corbella, B. M., and Palacios, J. M. (2004). "Development of Cu-based oxygen carriers for chemical-looping combustion." *Fuel*, 83(13), 1749–1757.

Diego, L. F. de, Ortiz, M., Adánez, J., García-Labiano, F., Abad, A., and Gayán, P. (2008). "Synthesis gas generation by chemical-looping reforming in a batch fluidized bed reactor using Ni-based oxygen carriers." *Chem. Eng. J.*, 144(2), 289–298.

Diego, L. F. de, Serrano, A., García-Labiano, F., García-Díez, E., Abad, A., Gayán, P., and Adánez, J. (2016). "Bioethanol combustion with CO2 capture in a 1kWth Chemical Looping Combustion prototype: Suitability of the oxygen carrier." *Chem. Eng. J.*, 283, 1405–1413.

Dresselhaus, M. S., and Eklund, P. C. (2000). "Phonons in carbon nanotubes." *Adv. Phys.*, 49(6), 705–814.

Dubey, A. K., Saxena, V. K., Sarkar, P., and Samanta, A. (2014). "Chemical Looping Combustion of Indian Coal With Copper Oxide as Oxygen Carrier." *Chemcon-2014*, 1–2.

Dutta, S., Wen, C. Y., and Belt, R. J. (1977). "Reactivity of Coal and Char. 1. In Carbon Dioxide Atmosphere." *Ind. Eng. Chem. Process Des. Dev.*, 16(1), 20–30.

Eatough, C. N., and Douglas Smoot, L. (1996). "Devolatilization of large coal particles at high pressure." *Fuel*, 75(13), 1601–1605.

Emmerich, F. G. (1995). "Evolution with heat treatment of crystallinity in carbons." *Carbon N. Y.*, 33(12), 1709–1715.

Evdou, A., Zaspalis, V., and Nalbandian, L. (2016). "Ferrites as redox catalysts for chemical looping processes." *Fuel*, 165, 367–378.

Fan, L.-S., Kim, R., Bayham, S., and Luo, S. (2012). "Coal direct chemical looping combustion process: Bench and sub-pilot unit study for metallurigical coke conversion." *Abstr. Pap. Am. Chem. Soc.*, 244.

Fan, L. (2010). *Chemical Looping Systems for Fossil Energy Conversions*. Hoboken, NJ, USA: John Wiley & Sons, Inc.

Fenelonov, V. B., Mel'gunov, M. S., and Parmon, V. N. (2010). "The Properties of Cenospheres and the Mechanism of Their Formation During High-Temperature Coal Combustion at Thermal Power Plans." *KONA Powder Part. J.*, 28, 189–208.

Feng, B., and Bhatia, S. K. (2000). "Percolative Fragmentation of Char Particles during Gasification." *Energy & Fuels*, 14(2), 297–307.

Fennell, P., and Anthony, B. (2015). *Calcium and Chemical Looping Technology for Power Generation and Carbon Dioxide (CO2) Capture*. (P. Fennell and B. Anthony, eds.), Woodhead Publishing.

Fermoso, J., Gil, M. V., Borrego, A. G., Pevida, C., Pis, J. J., and Rubiera, F. (2010). "Effect of the Pressure and Temperature of Devolatilization on the Morphology and Steam Gasification Reactivity of Coal Chars." *Energy & Fuels*, 24(10), 5586–5595.

Feron, P. H. M., and Hendriks, C. a. (2005). "CO2 capture process principles and costs." *Oil Gas Sci. Technol.*, 60(3), 451–459.

García-Labiano, F., Diego, L. F. de, García-Díez, E., Serrano, A., Abad, A., Gayán, P., and Adánez, J. (2014). "Combustion and Reforming of Ethanol in a Chemical Looping Continuous Unit." *Energy Procedia*, 63, 53–62.

Ge, H., Shen, L., Gu, H., and Jiang, S. (2015a). "Effect of co-precipitation and impregnation on K-decorated Fe2O3/Al2O3 oxygen carrier in Chemical Looping Combustion of bituminous coal." *Chem. Eng. J.*, 262, 1065–1076.

Ge, H., Shen, L., Gu, H., Song, T., and Jiang, S. (2015b). "Combustion performance and sodium transformation of high-sodium ZhunDong coal during chemical looping combustion with hematite as oxygen carrier." *Fuel*, 159, 107–117.

Gómez-Barea, A., and Leckner, B. (2010). "Modeling of biomass gasification in fluidized bed." *Prog. Energy Combust. Sci.*, 36(4), 444–509.

Gomez, A., and Mahinpey, N. (2015). "Kinetic study of coal steam and CO 2 gasification: A new method to reduce interparticle diffusion." *Fuel*, 148, 160–167.

Gu, H., Shen, L., Zhong, Z., Zhou, Y., Liu, W., Niu, X., Ge, H., Jiang, S., and Wang, L. (2015). "Interaction between biomass ash and iron ore oxygen carrier during chemical looping combustion." *Chem. Eng. J.*, 277, 70–78.

Guizani, C., Jeguirim, M., Gadiou, R., Escudero Sanz, F. J., and Salvador, S. (2016). "Biomass char gasification by H2O, CO2 and their mixture: Evolution of chemical, textural and structural properties of the chars." *Energy*, 112, 133–145.

Guizani, C., Jeguirim, M., Valin, S., Limousy, L., and Salvador, S. (2017). "Biomass chars: The effects of pyrolysis conditions on their morphology, structure, chemical properties and reactivity." *Energies*, 10(6).

Gupta, A., Thengane, S. K., and Mahajani, S. (2018). "CO 2 gasification of char from

lignocellulosic garden waste: Experimental and kinetic study." *Bioresour. Technol.*, 263(April), 180–191.

Haus, J., Lyu, K., Hartge, E.-U., Heinrich, S., and Werther, J. (2016). "Analysis of a Two-Stage Fuel Reactor System for the Chemical-Looping Combustion of Lignite and Bituminous Coal." *Energy Technol.*, 4(10), 1263–1273.

Heidenreich, C. A., and Zhang, D. K. (1999). "Measuring the temperature response of large wet coal particles during heating." *Fuel*.

Hippo, E. J., Jenkins, R. G., and Walker, P. L. (1979). "Enhancement of lignite char reactivity to steam by cation addition." *Fuel*, 58(5), 338–344.

Huang, Z., He, F., Zhao, K., Feng, Y., Zheng, A., Chang, S., Zhao, Z., Li, H., Zhao, K., Zheng, A., Chang, S., Wei, G., Zhao, Z., and Li, H. (2014). "Natural iron ore as an oxygen carrier for biomass chemical looping gasification in a fluidized bed reactor." *J. Therm. Anal. Calorim.*, 116(3), 1315–1324.

Huijun, G., Laihong, S., Fei, F., and Shouxi, J. (2015). "Experiments on biomass gasification using chemical looping with nickel-based oxygen carrier in a 25 kWth reactor." *Appl. Therm. Eng.*, 85, 52–60.

Huo, W., Zhou, Z., Chen, X., Dai, Z., and Yu, G. (2014). "Study on $CO_2$ gasification reactivity and physical characteristics of biomass, petroleum coke and coal chars." *Bioresour. Technol.*, 159, 143–149.

Hurley, J. P., and Schobert, H. H. (1993). "Ash formation during pulverised subbituminous coal combustion. 2. Inorganic transformations during middle and late stages of burnout." *Energy & Fuels*, 7(4), 542–553.

Imtiaz, Q., Hosseini, D., Rüdiger, C., and Müller, C. R. (2013). "Review of Oxygen Carriers for Chemical Looping with Oxygen Uncoupling ( CLOU ): Thermodynamics, Material Development, and Synthesis." *Energy Technol.*, 1(11), 633–647.

International Energy Agency. (2019). *World Energy Outlook 2019 – Analysis - IEA. World Energy Outlook 2019*.

International Energy Agency. (2020). *India 2020: Energy Policy Review. IEA*.

Ishida, M., and Jin, H. (1994). "A new advanced power-generation system using chemical-looping combustion." *Energy*, 19(4), 415–422.

Ishida, M., Zheng, D., and Akehata, T. (1987). "Evaluation of a chemical-looping-combustion power-generation system by graphic exergy analysis." *Energy*, 12(2), 147–154.

J.-T., Yang, G.-G., W., Yang, J.-T., and Wang, G.-G. (1990). "The Effect of Heat Transfer on Coal Devolatilization." *J. Heat Transfer*, 112(1), 192.

Jand, N., and Foscolo, P. U. (2005). "Decomposition of wood particles in fluidized beds." *Ind. Eng. Chem. Res.*, 44(14), 5079–5089.

Jayaraman, K., and Gokalp, I. (2015). "Thermogravimetric and evolved gas analyses of high ash Indian and Turkish coal pyrolysis and gasification." *J. Therm. Anal. Calorim.*, 121(2), 919–927.

Jayaraman, K., Gökalp, I., and Jeyakumar, S. (2017). "Estimation of synergetic effects

of CO2 in high ash coal-char steam gasification." *Appl. Therm. Eng.*, 110, 991–998.

Jia, L., Becker, H. A., and Code, R. K. (1993). "Devolatilization and char burning of coal particles in a fluidized bed combustor." *Can. J. Chem. Eng.*, 71(1), 10–19.

Jin, H. G., Okamoto, T., and Ishida, M. (1999). "Development of a novel chemical-looping combustion: Synthesis of a solid looping material of NiO/NiAl2O4." *Ind. Eng. Chem. Res.*, 38(1), 126–132.

Juniper, L., and Schumacher, G. (2013). "Advances in pulverised fuel technology: Understanding coal comminution, combustion and ash deposition." *Coal Handb. Towar. Clean. Prod.*, Elsevier Inc., 312–351.

Jüntgen, H., and Heek, K. H. Van. (1979). "An update of german non-isothermal coal pyrolysis work." *Fuel Process. Technol.*, 2(4), 261–293.

Kanniche, M., Moullec, Y. Le, Authier, O., Hagi, H., Bontemps, D., Neveux, T., and Louis-Louisy, M. (2017). "Up-to-date CO 2 Capture in Thermal Power Plants." *Energy Procedia*, (T. S. Dixon T. Laloui L., ed.), 114, 95–103.

Keller, M., Arjmand, M., Leion, H., and Mattisson, T. (2014). "Interaction of mineral matter of coal with oxygen carriers in chemical-looping combustion (CLC)." *Chem. Eng. Res. Des.*, 92(9), 1753–1770.

Keown, D. M., Hayashi, J. I., and Li, C. Z. (2008). "Drastic changes in biomass char structure and reactivity upon contact with steam." *Fuel*, 87(7), 1127–1132.

Keown, D. M., Li, X., Hayashi, J. I., and Li, C. Z. (2007). "Characterization of the structural features of char from the pyrolysis of cane trash using Fourier transform-Raman spectroscopy." *Energy and Fuels*, 21(3), 1816–1821.

Khan, J., and Wang, T. (2013). "Implementation of a Demoisturization and Devolatilization Model in Multi-Phase Simulation of a Hybrid Entrained-Flow and Fluidized Bed Mild Gasifier." *Int. J. Clean Coal Energy*, 02(03), 35–53.

Khan, M. R., and Hshieh, F. Y. (1989). "Influence of Steam on Coal Devolatilization and on the Reactivity of the Resulting Char." *Prepr. Pap. Am. Chem. Soc. Div. Fuel Chem.*, 34(4), 1245–1255.

Kim, H. R., Wang, D., Zeng, L., Bayham, S., Tong, A., Chung, E., Kathe, M. V., Luo, S., McGiveron, O., Wang, A., Sun, Z., Chen, D., and Fan, L.-S. (2013). "Coal direct chemical looping combustion process: Design and operation of a 25-kWthsub-pilot unit." *Fuel*, 108, 370–384.

Kline, S. J., and McClintock, F. A. (1953). "Describing Uncertainties in Single-Sample Experiments." *Mech. Eng.*

Kobayashi, H., Howard, J. B., and Sarofim, A. F. (1977). "Coal devolatilization at high temperatures." *Symp. Combust.*, 16(1), 411–425.

Kök, M. V., and Yildirim, B. (2020). "Gasification kinetics of Thrace region coal by thermogravimetry analysis." *J. Pet. Sci. Eng.*, 188(September 2018).

Kosowska-Galacbowska, M., and Luckos, A. (2009). "An Experimental Investigation into the Fragmentation of Coal Particles in a Fluidized-Bed Combustor." *Proc. 20th Int. Conf. Fluid. Bed Combust.*, Berlin, Heidelberg: Springer Berlin Heidelberg, 330–

334.

Kosowska-golachowska, M. (2010). "Experimental investigations into primary fragmentation of large coal particles." *27th Annu. Int. Pittsburgh Coal Conf. PCC 2010.*

Krishnamoorthy, V., Tchapda, A. H., and Pisupati, S. V. (2017). "A study on fragmentation behavior, inorganic melt phase formation, and carbon loss during high temperature gasification of mineral matter rich fraction of Pittsburgh No. 8 coal." *Fuel*, 208, 247–259.

Kumar, R. R., Kolar, A. K., and Leckner, B. (2006). "Shrinkage characteristics of Casuarina wood during devolatilization in a fluidized bed combustor." *Biomass and Bioenergy*, 30(2), 153–165.

Kuo, Y. L., Hsu, W. M., Chiu, P. C., Tseng, Y. H., and Ku, Y. (2013). "Assessment of redox behavior of nickel ferrite as oxygen carriers for chemical looping process." *Ceram. Int.*, 39(5), 5459–5465.

Kwiatkowski, K., Bajer, K., Celińska, A., Dudyński, M., Korotko, J., and Sosnowska, M. (2014). "Pyrolysis and gasification of a thermally thick wood particle - Effect of fragmentation." *Fuel*, 132, 125–134.

Lahijani, P., Zainal, Z. A., Mohammadi, M., and Mohamed, A. R. (2015). "Conversion of the greenhouse gas CO2 to the fuel gas CO via the Boudouard reaction: A review." *Renew. Sustain. Energy Rev.*, Elsevier Ltd.

Larkin, P. (2011). *Infrared and Raman Spectroscopy; Principles and Spectral Interpretation. Infrared Raman Spectrosc. Princ. Spectr. Interpret.*

Lee, Y.-J. J. (2004). "The second order Raman spectroscopy in carbon crystallinity." *J. Nucl. Mater.*, 325(2–3), 174–179.

Leion, H., Mattisson, T., and Lyngfelt, A. (2009). "Using chemical-looping with oxygen uncoupling (CLOU) for combustion of six different solid fuels." *Energy Procedia*, 1(1), 447–453.

Lewis, W. K., and Gilliland, E. R. (1954). "Production of pure carbon dioxide." United States.

Li, C., Xia, Z. X., Qiao, X. L., Li, W. B., and Fang, M. X. (2014). "The Investigation on Fragmentation Behavior of Lignite Coal during Fluidized Bed Pyrolysis." *Adv. Mater. Res.*, 953–954, 1254–1260.

Li, K., Rimmer, S. M., Liu, Q., and Zhang, Y. (2019). "Micro-Raman Spectroscopy of Microscopically Distinguishable Components of Naturally Graphitized Coals from Central Hunan Province, China." *Energy & Fuels*, research-article, 33(2), 1037–1048.

Li, T., Zhang, L., Dong, L., Wang, S., Song, Y., Wu, L., and Li, C.-Z. Z. (2017). "Effects of char chemical structure and AAEM retention in char during the gasification at 900 °C on the changes in low-temperature char-O2reactivity for Collie sub-bituminous coal." *Fuel*, 195, 253–259.

Li, X., Hayashi, J., and Li, C.-Z. (2006). "FT-Raman spectroscopic study of the evolution of char structure during the pyrolysis of a Victorian brown coal." *Fuel*, 85(12–13), 1700–1707.

Li, Z., Jiang, L., Ouyang, J., Cao, L., Luo, G., and Yao, H. (2018). "A kinetic study on char oxidation in mixtures of O2, CO2 and H2O." *Fuel Process. Technol.*, 179, 250–257.

Lin-Vien, D., Colthup, N. B., Fateley, W. G., and Grasselli, J. G. (1991). *The handbook of infrared and Raman characteristic frequencies of organic molecules*. Academic Press.

Linderholm, C., Lyngfelt, A., Cuadrat, A., and Jerndal, E. (2012). "Chemical-looping combustion of solid fuels – Operation in a 10kW unit with two fuels, above-bed and in-bed fuel feed and two oxygen carriers, manganese ore and ilmenite." *Fuel*, 102, 808–822.

Linderholm, C., Schmitz, M., Knutsson, P., Kallen, M., Lyngfelt, A., Källén, M., and Lyngfelt, A. (2014). "Use of Low-Volatile Solid Fuels in a 100 kW Chemical-Looping Combustor." *Energy & Fuels*, 28(9), 5942–5952.

Liu, H., Luo, C., Toyota, M., Kato, S., Uemiya, S., Kojima, T., and Tominaga, H. (2003). "Mineral reaction and morphology change during gasification of coal in CO2 at elevated temperatures." *Fuel*, 82(5), 523–530.

Liu, L., Kong, B., Yang, J., Liu, Q., and Liu, X. (2020). "CO2 Gasification Kinetics and Structural Characteristics of Tri-High Coal Char Prepared at Elevated Temperature." *ACS Omega*, 5(1), 507–517.

Lorenz, H., Carrea, E., Tamura, M., and Haas, J. (2000). "Role of char surface structure development in pulverized fuel combustion." *Fuel*, 79(10), 1161–1172.

Lu, L., Devasahayam, S., and Sahajwalla, V. (2013). "Evaluation of coal for metallurgical applications." *Coal Handb. Towar. Clean. Prod.*, Elsevier, 352–386.

Lu, L., Kong, C., Sahajwalla, V., and Harris, D. (2002). "Char structural ordering during pyrolysis and combustion and its influence on char reactivity." *Fuel*, 81(9), 1215–1225.

Luo, M., Wang, S., Wang, L., and Lv, M. (2014a). "Reduction kinetics of iron-based oxygen carriers using methane for chemical-looping combustion." *J. Power Sources*, 270, 434–440.

Luo, S., Bayham, S., Zeng, L., McGiveron, O., Chung, E., Majumder, A., and Fan, L.-S. (2014b). "Conversion of metallurgical coke and coal using a Coal Direct Chemical Looping (CDCL) moving bed reactor." *Appl. Energy*, 118, 300–308.

Lyngfelt, A. (2010). "Oxygen-Carriers for Chemical-Looping Combustion - Operational Experience." *1st Int. Conf. Chem. Looping*, 17–19.

Lyngfelt, A. (2014). "Chemical-looping combustion of solid fuels - Status of development." *Appl. Energy*, 113, 1869–1873.

Lyngfelt, A. (2020). "Chemical Looping Combustion: Status and Development Challenges." *Energy & Fuels*, 34(8), 9077–9093.

Lyngfelt, A., and Leckner, B. (2015). "A 1000 MWth boiler for chemical-looping combustion of solid fuels - Discussion of design and costs." *Appl. Energy*, 157, 475–487.

Lyngfelt, A., Leckner, B., and Mattisson, T. (2001). "A fluidized-bed combustion process with inherent CO2 separation; application of chemical-looping combustion." *Chem. Eng. Sci.*, 56(10), 3101–3113.

Lyngfelt, A., and Linderholm, C. (2014). "Chemical-looping Combustion of Solid Fuels – Technology Overview and Recent Operational Results in 100kW Unit." *Energy Procedia*, (T. Dixon, H. Herzog, and S. Twinning, eds.), 63, 98–112.

Lyngfelt, A., and Linderholm, C. (2017). "Chemical-Looping Combustion of Solid Fuels – Status and Recent Progress." *Energy Procedia*, 114, 371–386.

Lyngfelt, A., Mattisson, T., Linderholm, C., and Rydén, M. (2016). "Chemical-Looping combustion of solid fuels–what is needed to reach full-scale." *4th Int. Conf. Chem. Looping*, Nanjing, China.

Markstrom, P., Linderholm, C., and Lyngfelt, A. (2014). "Operation of a 100 kW chemical-looping combustor with Mexican petroleum coke and Cerrejon coal." *Appl. Energy*, 113, 1830–1835.

Markström, P., Linderholm, C., and Lyngfelt, A. (2013). "Chemical-looping combustion of solid fuels – Design and operation of a 100kW unit with bituminous coal." *Int. J. Greenh. Gas Control*, 15, 150–162.

Mason, P. E., Darvell, L. I., Jones, J. M., and Williams, A. (2016). "Comparative Study of the Thermal Conductivity of Solid Biomass Fuels." *Energy & Fuels*, 30(3), 2158–2163.

Mattisson, T., Adánez, J., Mayer, K., Snijkers, F., Williams, G., Wesker, E., Bertsch, O., and Lyngfelt, A. (2014). "Innovative Oxygen Carriers Uplifting Chemical-looping Combustion." *Energy Procedia*, 63, 113–130.

Mattisson, T., Jing, D., Lyngfelt, A., and Rydén, M. (2016). "Experimental investigation of binary and ternary combined manganese oxides for chemical-looping with oxygen uncoupling (CLOU)." *Fuel*, 164, 228–236.

Mattisson, T., Keller, M., Linderholm, C., Moldenhauer, P., Rydén, M., Leion, H., and Lyngfelt, A. (2018). "Chemical-looping technologies using circulating fluidized bed systems: Status of development." *Fuel Process. Technol.*, 172(December 2017), 1–12.

Mattisson, T., Lyngfelt, A., and Leion, H. (2009). "Chemical-looping with oxygen uncoupling for combustion of solid fuels." *Int. J. Greenh. Gas Control*, 3(1), 11–19.

Megaritis, A., Zhuo, Y., Messenböck, R., Dugwell, D. R., and Kandiyoti, R. (1998). "Pyrolysis and gasification in a bench-scale high-pressure fluidized-bed reactor." *Energy and Fuels*, 12(1), 144–151.

Mei, D., Abad, A., Zhao, H., Adánez, J., and Adanez, J. (2015). "Characterization of a sol–gel derived CuO/CuAl2O4 oxygen carrier for chemical looping combustion (CLC) of gaseous fuels: Relevance of gas–solid and oxygen uncoupling reactions." *Fuel Process. Technol.*, 133, 210–219.

Mei, D., Zhao, H., Ma, Z., Fang, Y., and Zheng, C. (2013). "Experimental study on chemical looping with oxygen uncoupling using copper based oxygen carrier and different volatiles contained coal chars." *Zhongguo Dianji Gongcheng Xuebao/Proceedings Chinese Soc. Electr. Eng.*, 33(11), 14–21.

Mendiara, T., Diego, L. F. de, García-Labiano, F., Gayán, P., Abad, A., and Adánez, J. (2013a). "Behaviour of a bauxite waste material as oxygen carrier in a 500Wth CLC unit with coal." *Int. J. Greenh. Gas Control*, 17, 170–182.

Mendiara, T., García-Labiano, F., Gayán, P., Abad, A., Diego, L. F. De, and Adánez, J. (2013b). "Evaluation of the use of different coals in Chemical Looping Combustion using a bauxite waste as oxygen carrier." *Fuel*, 106, 814–826.

Mendiara, T., Gayán, P., Abad, A., Diego, L. F. de, García-Labiano, F., and Adánez, J. (2013c). "Performance of a bauxite waste as oxygen-carrier for chemical-looping combustion using coal as fuel." *Fuel Process. Technol.*, 109, 57–69.

Meng, F., Yu, J., Tahmasebi, A., Han, Y., Zhao, H., Lucas, J., and Wall, T. (2014). "Characteristics of chars from low-temperature pyrolysis of lignite." *Energy and Fuels*, 28(1), 275–284.

Mermoud, F., Salvador, S., Steene, L. Van de, and Golfier, F. (2006). "Influence of the pyrolysis heating rate on the steam gasification rate of large wood char particles." *Fuel*, 85(10–11), 1473–1482.

Min, F., Zhang, M., Zhang, Y., Cao, Y., and Pan, W. P. (2011). "An experimental investigation into the gasification reactivity and structure of agricultural waste chars." *J. Anal. Appl. Pyrolysis*, 92(1), 250–257.

Moffat, R. J. (1988). "Describing the uncertainties in experimental results." *Exp. Therm. Fluid Sci.*

Mokhena, T. C., Mochane, M. J., Sefadi, J. S., Motloung, S. V., and Andala, D. M. (2018). "Thermal Conductivity of Graphite-Based Polymer Composites." *Impact Therm. Conduct. Energy Technol.*, InTech.

Moldenhauer, P., Rydén, M., Mattisson, T., Jamal, A., and Lyngfelt, A. (2017). "Chemical-looping combustion with heavy liquid fuels in a 10 kW pilot plant." *Fuel Process. Technol.*, 156, 124–137.

Molina-Sabio, M., Sanchez-Montero, M. J., Juarez-Galan, J. M., Salvador, F., Rodrı́guez-Reinoso, F., and Salvador, A. (2006). "Development of porosity in a char during reaction with steam or supercritical water." *J. Phys. Chem. B*, 110(25), 12360–12364.

Morin, M., Pécate, S., and Hémati, M. (2018a). "Experimental study and modelling of the kinetic of biomass char gasification in a fluidized bed reactor." *Chem. Eng. Res. Des.*, 131, 488–505.

Morin, M., Pécate, S., and Hémati, M. (2018b). "Kinetic study of biomass char combustion in a low temperature fluidized bed reactor." *Chem. Eng. J.*, 331(May 2017), 265–277.

Morris, J. P., and Keairns, D. L. (1979). "Coal devolatilization studies in support of the Westinghouse fluidized-bed coal gasification process." *Fuel*, 58(6), 465–471.

Morris, R. M. (1993). "Effect of particle size and temperature on evolution rate of volatiles from coal." *J. Anal. Appl. Pyrolysis*, 27(2), 97–107.

Mukherjee, S., Kumar, P., Yang, A., and Fennell, P. (2015). "Energy and exergy

204

analysis of chemical looping combustion technology and comparison with pre-combustion and oxy-fuel combustion technologies for $CO_2$ capture." *J. Environ. Chem. Eng.*, 3(3), 2104–2114.

Nandy, A., Loha, C., Gu, S., Sarkar, P., Karmakar, M. K., and Chatterjee, P. K. (2016). "Present status and overview of Chemical Looping Combustion technology." *Renew. Sustain. Energy Rev.*, 59, 597–619.

Nemanich, R. J., Glass, J. T., Lucovsky, G., and Shroder, R. E. (1988). "Raman scattering characterization of carbon bonding in diamond and diamondlike thin films." *J. Vac. Sci. Technol. A Vacuum, Surfaces, Film.*, 6(3), 1783–1787.

NETL. (2011). *Cost and Performance Baseline for Fossil Energy Plants; Volume 3a: Low Rank Coal to Electricity: IGCC Cases*.

NETL. (2012). "Membrane-based CO2 Capture Systems for Coal-fired Power Plants." (September), 1–29.

Neumann, W., and Wallisch, K. (1983). "Determination of the thermal conductivity of graphite and high-temperature alloys by the laser-flash method." *Measurement*, 1(4), 204–208.

Niksa, S., Heyd, L. E., Russel, W. B., and Saville, D. A. (1985). "On the role of heating rate in rapid coal devolatilization." *Symp. Combust.*, 20(1), 1445–1453.

Ohlemüller, P., Busch, J.-P., Reitz, M., Ströhle, J., and Epple, B. (2016). "Chemical-Looping Combustion of Hard Coal: Autothermal Operation of a 1 MW th Pilot Plant." *J. Energy Resour. Technol.*, 138(4), 042203.

Oka, S. (2003). *Fluidized bed combustion*. CRC press.

Pans, M. A., Gayán, P., Diego, L. F. de, García-Labiano, F., Abad, A., Adánez., J., and Adánez, J. (2015). "Performance of a low-cost iron ore as an oxygen carrier for Chemical Looping Combustion of gaseous fuels." *Chem. Eng. Res. Des.*, 93(July), 736–746.

Paprika, M. J., Komatina, M. S., Dakić, D. V., and Nemoda, S. C. D. S. Đ. (2013). "Prediction of Coal Primary Fragmentation and Char Particle Size Distribution in Fluidized Bed." *Energy & Fuels*, 27(9), 5488–5494.

Paprika, M., Komatina, M., Dakić, D., Živković, G., and Mladenović, M. (2015). "Experimental and Numerical Investigation of the Primary Fragmentation of a Lignite during Fluidized-Bed (FB) Devolatilization." *Energy & Fuels*, 29(5), 3394–3398.

Peng, F. F., Lee, I. C., and Yang, R. Y. K. (1995). "Reactivities of in situ and ex situ coal chars during gasification in steam at 1000-1400°C." *Fuel Process. Technol.*, 41(3), 233–251.

Pragadeesh, K. S., Regupathi, I., and Ruben Sudhakar, D. (2021). "Insitu gasification – chemical looping combustion of large coal and biomass particles: Char conversion and comminution." *Fuel*, 292, 120201.

Pragadeesh, K. S., and Sudhakar, D. R. (2018). "Primary Fragmentation Behavior of Indian Coals and Biomass during Chemical Looping Combustion." *Energy & Fuels*, 32(5), 6330–6346.

Pragadeesh, K. S., and Sudhakar, D. R. (2019). "Color Indistinction Method for the Determination of Devolatilization Time of Large Fuel Particles in Chemical Looping Combustion." *Energy & Fuels*, 33(5), 4542–4551.

Prins, W., Siemons, R., Swaaij, W. P. M. M. Van, and Radovanovic, M. (1989). "Devolatilization and ignition of coal particles in a two-dimensional fluidized bed." *Combust. Flame*, 75(1), 57–79.

Rajendran, S., Zhang, S., Xiao, R., and Bhattacharya, S. (2015). "Use of synthetic oxygen carriers for Chemical Looping Combustion of Victorian brown coal." *Proc. Combust. Inst.*, 35(3), 3619–3627.

Raman, P. P., Walawender, W. P., Fan, L. T., and Howell, J. a. (1981). "Thermogravimetric Analysis of Biomass. Devolatilization Studies on Feedlot Manure." *Ind. Eng. Chem. Process Des. Dev.*, 20(4), 630–636.

Ramsteiner, M., and Wagner, J. (1987). "Resonant Raman scattering of hydrogenated amorphous carbon: Evidence for π-bonded carbon clusters." *Appl. Phys. Lett.*

Rangel, N., and Pinho, C. (2010). "Fragmentation effect on batches of pine wood char burning in a fluidized bed." *Energy and Fuels*, 24(1), 318–323.

Rathnam, R. K., Elliott, L. K., Wall, T. F., Liu, Y., and Moghtaderi, B. (2009). "Differences in reactivity of pulverised coal in air (O2/N2) and oxy-fuel (O2/CO2) conditions." *Fuel Process. Technol.*, 90(6), 797–802.

Redko, T., Volford, A., Marek, E. J., Scott, S. A., and Hayhurst, A. N. (2020). "Measurement of the times for pyrolysis and the thermal diffusivity of a pyrolysing particle of wood and also of the resulting char." *Combust. Flame*, 212, 510–518.

Renteria, J., Nika, D., and Balandin, A. (2014). "Graphene Thermal Properties: Applications in Thermal Management and Energy Storage." *Appl. Sci.*, 4(4), 525–547.

Reschmeier, R., and Karl, J. (2016). "Experimental study of wood char gasification kinetics in fluidized beds." *Biomass and Bioenergy*, 85, 288–299.

Richter, H. J., and Knoche, K. F. (1983). "Reversibility of Combustion Processes." *ACS Symp. Ser. Am. Chem. Soc. Washington, DC, 1983*, 71–85.

Ross, D. P. P., Heidenreich, C. A., and Zhang, D. K. (2000). "Devolatilisation times of coal particles in a fluidised-bed." *Fuel*, 79(8), 873–883.

Rubel, A., Zhang, Y., Neathery, J. K., and Liu, K. (2012). "Comparative study of the effect of different coal fly ashes on the performance of oxygen carriers for chemical looping combustion." *Energy and Fuels*, 26(6), 3156–3161.

Russell, N. V., Beeley, T. J., Man, C. K., Gibbins, J. R., and Williamson, J. (1998). "Development of TG measurements of intrinsic char combustion reactivity for industrial and research purposes." *Fuel Process. Technol.*, 57(2), 113–130.

Rydén, M., Lyngfelt, A., and Mattisson, T. (2008). "Chemical-looping combustion and chemical-looping reforming in a circulating fluidized-bed reactor using Ni- based oxygen carriers." *Energy & Fuels*, 22, 2585–2597.

Rydén, M., Lyngfelt, A., and Mattisson, T. (2011a). "Combined manganese/iron oxides as oxygen carrier for chemical looping combustion with oxygen uncoupling (CLOU)

in a circulating fluidized bed reactor system." *Energy Procedia*, 4, 341–348.

Rydén, M., Lyngfelt, A., and Mattisson, T. (2011b). "CaMn0.875Ti0.125O3 as oxygen carrier for chemical-looping combustion with oxygen uncoupling (CLOU)-Experiments in a continuously operating fluidized-bed reactor system." *Int. J. Greenh. Gas Control*, 5(2), 356–366.

Salam, T. F., Shen, X. L., and Gibbs, B. M. (1988). "A technique for determining devolatilization rates of large coal particles in a fluidized bed combustor." *Fuel*, 67(3), 414–419.

Sarkar, D. K. (2015). "Fluidized-Bed Combustion Boilers." *Therm. Power Plant*, Elsevier, 159–187.

Sasongko, D., Rasrendra, C. B., and Indarto, A. (2017). "Fragmentation model of coal devolatilisation in fluidised bed combustion." *Int. J. Ambient Energy*, 0(0), 1–8.

Sasongko, D., and Stubington, J. F. (1996). "Significant factors affecting devolatilization of fragmenting, non-swelling coals in fluidized bed combustion." *Chem. Eng. Sci.*, 51(16), 3909–3918.

Saxena, S. C. (1990). "Devolatilization and combustion characteristics of coal particles." *Prog. Energy Combust. Sci.*, 16(1), 55–94.

Scala, F., Chirone, R., and Salatino, P. (2006). "Combustion and attrition of biomass chars in a fluidized bed." *Energy and Fuels*, 20(1), 91–102.

Scala, F., Chirone, R., and Salatino, P. (2013). "Attrition phenomena relevant to fluidized bed combustion and gasification systems." *Fluid. Bed Technol. Near-Zero Emiss. Combust. Gasif.*, Elsevier, 254–315.

Schuepfer, D. B., Badaczewski, F., Guerra-Castro, J. M., Hofmann, D. M., Heiliger, C., Smarsly, B., and Klar, P. J. (2020). "Assessing the structural properties of graphitic and non-graphitic carbons by Raman spectroscopy." *Carbon N. Y.*, 161, 359–372.

Schwan, J., Ulrich, S., Batori, V., Ehrhardt, H., and Silva, S. R. P. (1996). "Raman spectroscopy on amorphous carbon films." *J. Appl. Phys.*

Scott, S. A., Davidson, J. F., Dennis, J. S., and Hayhurst, A. N. (2007). "The devolatilisation of particles of a complex fuel (dried sewage sludge) in a fluidised bed." *Chem. Eng. Sci.*, 62(1–2), 584–598.

Sekine, Y., Ishikawa, K., Kikuchi, E., Matsukata, M., and Akimoto, A. (2006). "Reactivity and structural change of coal char during steam gasification." *Fuel*, 85(2), 122–126.

Senneca, O., Bareschino, P., Urciuolo, M., and Chirone, R. (2017a). "Prediction of structure evolution and fragmentation phenomena during combustion of coal: Effects of heating rate." *Fuel Process. Technol.*, 166, 228–236.

Senneca, O., Russo, S., and Chirone, R. (2009). "Primary fragmentation of coal particles at high heating rate." *Chem. Eng. Trans.*, 18, 569–574.

Senneca, O., Scala, F., Chirone, R., and Salatino, P. (2017b). "Relevance of structure, fragmentation and reactivity of coal to combustion and oxy-combustion." *Fuel*, 201, 65–80.

Senneca, O., Urciuolo, M., and Chirone, R. (2013). "A semidetailed model of primary fragmentation of coal." *Fuel*, 104, 253–261.

Senneca, O., Urciuolo, M., Chirone, R., and Cumbo, D. (2011). "An experimental study of fragmentation of coals during fast pyrolysis at high temperature and pressure." *Fuel*, 90(9), 2931–2938.

Serrano, A., García-Labiano, F., Diego, L. F. de, Gayán, P., Abad, A., and Adánez, J. (2017). "Chemical Looping Combustion of liquid fossil fuels in a 1 kW th unit using a Fe-based oxygen carrier." *Fuel Process. Technol.*, 160, 47–54.

Shafiefarhood, A., Stewart, A., and Li, F. (2015). "Iron-containing mixed-oxide composites as oxygen carriers for Chemical Looping with Oxygen Uncoupling (CLOU)." *Fuel*, 139, 1–10.

Sharma, H. N., Pahalagedara, L., Joshi, A., Suib, S. L., and Mhadeshwar, A. B. (2012). "Experimental Study of Carbon Black and Diesel Engine Soot Oxidation Kinetics Using Thermogravimetric Analysis." *Energy & Fuels*, 26(9), 5613–5625.

Shen, L., Wu, J., Xiao, J., Song, Q., and Xiao, R. (2009). "Chemical-looping combustion of biomass in a 10 kWth reactor with iron oxide as an oxygen carrier." *Energy and Fuels*, 23(5), 2498–2505.

Sheng, C. (2007). "Char structure characterised by Raman spectroscopy and its correlations with combustion reactivity." *Fuel*, 86(15), 2316–2324.

Shenqi, X., Zhijie, Z., Jie, X., Guangsuo, Y., and Fuchen, W. (2011). "Effects of alkaline metal on coal gasification at pyrolysis and gasification phases." *Fuel*, 90(5), 1723–1730.

Shimizu, T., Hirama, T., Hosoda, H., Kitano, K., Inagaki, M., and Tejima, K. (1999). "A Twin Fluid-Bed Reactor for Removal of CO2 from Combustion Processes." *Chem. Eng. Res. Des.*, 77(1), 62–68.

Sims, I., Lay, J., and Ferrari, J. I. (2019). "Concrete aggregates." *Lea's Chem. Cem. Concr.*, Elsevier, 699–778.

Smith, M. W., Dallmeyer, I., Johnson, T. J., Brauer, C. S., McEwen, J.-S. S., Espinal, J. F., and Garcia-Perez, M. (2016). "Structural analysis of char by Raman spectroscopy: Improving band assignments through computational calculations from first principles." *Carbon N. Y.*, 100, 678–692.

Solimene, R., Chirone, R., and Salatino, P. (2012). "Characterization of the devolatilization rate of solid fuels in fluidized beds by time-resolved pressure measurements." *AIChE J.*, 58(2), 632–645.

Song, T., and Shen, L. (2018). "Review of reactor for chemical looping combustion of solid fuels." *Int. J. Greenh. Gas Control*, 76, 92–110.

Song, T., Zheng, M., Shen, L., Zhang, T., Niu, X., and Xiao, J. (2013). "Mechanism investigation of enhancing reaction performance with CaSO4/Fe2O3oxygen carrier in chemical-looping combustion of coal." *Ind. Eng. Chem. Res.*, 52(11), 4059–4071.

Sreekanth, M., Kolar, A. K., and Leckner, B. (2008a). "A semi-analytical model to predict primary fragmentation of wood in a bubbling fluidized bed combustor." *J. Anal.*

*Appl. Pyrolysis*, 83(1), 88–100.

Sreekanth, M., Sudhakar, D. R., Prasad, B. V. S. S. S., Kolar, A. K., and Leckner, B. (2008b). "Modelling and experimental investigation of devolatilizing wood in a fluidized bed combustor." *Fuel*, 87(12), 2698–2712.

Sreenivasulu, B., Gayatri, D. V., Sreedhar, I., and Raghavan, K. V. (2015). "A journey into the process and engineering aspects of carbon capture technologies." *Renew. Sustain. Energy Rev.*, 41, 1324–1350.

Stainton, H., Ginet, A., Surla, K., and Hoteit, A. (2012). "Experimental investigation of CLC coal combustion with nickel based particles in a fluidized bed." *Fuel*, 101, 205–214.

Stanmore, B. R., Brillard, A., Gilot, P., and Delfosse, L. (1996). "Fragmentation of small coal particles under fluidized-bed combustor conditions." *Symp. Combust.*, 26(2), 3269–3275.

Ströhle, J., Orth, M., and Epple, B. (2014). "Design and operation of a 1MWth chemical looping plant." *Appl. Energy*, 113, 1490–1495.

Stubington, J. F. F., Chui, T. Y. S. Y. S., and Saisithidej, S. (1992). "Experimental Factors Affecting Coal Devolatilization Time in Fluidized Bed Combustion." *Fuel Sci. Technol. Int.*, 10(3), 397–419.

Stubington, J. F., Huang, G., and Scaroni, A. W. (1991). "Devolatilization times of mm-size coal particles." *Fuel*, 70(9), 1105–1108.

Stubington, J. F., and Linjewile, T. M. (1989). "The effects of fragmentation on devolatilization of large coal particles." *Fuel*, 68(2), 155–160.

Stubington, J. F., and Moss, B. (1995). "On the Timing of Primary Fragmentation During Bituminous Coal Particle Devolatilisation in a Fluidized Bed Combustor." *Can. J. Chem. Eng.*, 73(4), 505–509.

Stubington, J. F., Ng, K. W. K., Moss, B., and Peeler, P. K. (1997). "Comparison of experimental methods for determining coal particle devolatilization times under fluidized bed combustor conditions." *Fuel*, 76(3), 233–240.

Stubington, J. F., and Sasongko, D. (1998). "On the heating rate and volatile yield for coal particles injected into fluidised bed combustors." *Fuel*, 77(9–10), 1021–1025.

Stubington, J. F., and Sumaryono. (1984). "Release of volatiles from large coal particles in a hot fluidized bed." *Fuel*, 63(7), 1013–1019.

Subramanian, P., and Arunachalam, V. (1980). "A Simple Device for the Determination of Sphericity Factor." *Ind. Eng. Chem. Fundam.*, 19(4), 436–437.

Sudhakar, D. R., and Kolar, A. K. (2010). "Transient Three-Dimensional Mathematical Model and Experimental Investigation of a Wet Devolatilizing Wood in a Hot Fluidized Bed." *Energy & Fuels*, 24(9), 4820–4832.

Sudhakar, D. R., Reddy, K. S., Kolar, A. K., and Leckner, B. (2008). "Fragmentation of wood char in a laboratory scale fluidized bed combustor." *Fuel Process. Technol.*, 89(11), 1121–1134.

Sundback, C. A., Beer, J. M., and Sarofim, A. F. (1984). "Fragmentation Behavior of

Single Coal Particles in a Fluidized Bed." *Twent. Symp. Combust.*, 1495–1503.

Suresh, P. V., Menon, K. G., Prakash, K. S., Prudhvi, S., and Anudeep, A. (2015). "Thermodynamic analysis of in situ gasification-chemical looping combustion (iG-CLC) of Indian coal." *Environ. Sci. Pollut. Res.*, 23(20), 1–9.

Syred, N., Kurniawan, K., Griffiths, T., Gralton, T., and Ray, R. (2007). "Development of fragmentation models for solid fuel combustion and gasification as subroutines for inclusion in CFD codes." *Fuel*, 86(14 SPEC. ISS.), 2221–2231.

Takai, K., Oga, M., Sato, H., Enoki, T., Ohki, Y., Taomoto, A., Suenaga, K., and Iijima, S. (2003). "Structure and electronic properties of a nongraphitic disordered carbon system and its heat-treatment effects." *Phys. Rev. B - Condens. Matter Mater. Phys.*, 67(21), 1–11.

Takarada, T., Tamai, Y., and Tomita, A. (1985). "Reactivities of 34 coals under steam gasification." *Fuel*, 64(10), 1438–1442.

Thon, A., Kramp, M., Hartge, E.-U. U., Heinrich, S., and Werther, J. (2014). "Operational experience with a system of coupled fluidized beds for chemical looping combustion of solid fuels using ilmenite as oxygen carrier." *Appl. Energy*, 118, 309–317.

Thunman, H., Davidsson, K., and Leckner, B. (2004). "Separation of drying and devolatilization during conversion of solid fuels." *Combust. Flame*, 137(1–2), 242–250.

Tian, H., Guo, Q., Yue, X., and Liu, Y. (2010). "Investigation into sulfur release in reductive decomposition of calcium sulfate oxygen carrier by hydrogen and carbon monoxide." *Fuel Process. Technol.*, 91(11), 1640–1649.

Tomeczek, J., and Palugniok, H. (1996). "Specific heat capacity and enthalpy of coal pyrolysis at elevated temperatures." *Fuel*, 75(9), 1089–1093.

Trahan, J., Graziani, A., Goswami, D. Y., Stefanakos, E., Jotshi, C., and Goel, N. (2014). "Evaluation of Pressure Drop and Particle Sphericity for an Air-rock Bed Thermal Energy Storage System." *Energy Procedia*, 57, 633–642.

Tsai, C. Y., and Scaroni, A. W. (1987). "Reactivity of bituminous coal chars during the initial stage of pulverized-coal combustion." *Fuel*, 66(10), 1400–1406.

Tuinstra, F., and Koenig, J. L. (1970). "Raman Spectrum of Graphite." *J. Chem. Phys.*, 53(3), 1126–1130.

Urciuolo, M., Solimene, R., Chirone, R., and Salatino, P. (2012). "Fluidized bed combustion and fragmentation of wet sewage sludge." *Exp. Therm. Fluid Sci.*, 43, 97–104.

Urkan, M. K., and Arikol, M. (1994). "Burning times of volatiles from Turkish coals during fluidized bed combustion." *Fuel*, 73(5), 768–772.

Walsh, P. M., and Li, T. (1994). "Fragmentation and attrition of coal char particles undergoing collisions during combustion at temperatures from 900 to 1100 K." *Combust. Flame*, 99(3–4), 749–757.

Wang, G., Zhang, J., Shao, J., Li, K., and Zuo, H. (2015a). "Investigation of non-isothermal and isothermal gasification process of coal char using different kinetic

model." *Int. J. Min. Sci. Technol.*, 25(1), 15–21.

Wang, M., Roberts, D. G., Kochanek, M. A., Harris, D. J., Chang, L., and Li, C.-Z. Z. (2014). "Raman Spectroscopic Investigations into Links between Intrinsic Reactivity and Char Chemical Structure." *Energy & Fuels*, 28(1), 285–290.

Wang, S., Li, T., Wu, L., Zhang, L., Dong, L., Hu, X., and Li, C. Z. (2015b). "Second-order Raman spectroscopy of char during gasification." *Fuel Process. Technol.*, 135, 105–111.

Wang, Y., Alsmeyer, D. C., and McCreery, R. L. (1990). "Raman Spectroscopy of Carbon Materials: Structural Basis of Observed Spectra." *Chem. Mater.*, 2(5), 557–563.

Wang, Y., and Bell, D. A. (2017). "Competition between H 2 O and CO 2 during the gasification of Powder River Basin coal." *Fuel*, 187, 94–102.

Wang, Y. G., Chen, X. J., Yang, S. S., He, X., Chen, Z. D., and Zhang, S. (2015c). "Effect of steam concentration on char reactivity and structure in the presence/absence of oxygen using Shengli brown coal." *Fuel Process. Technol.*, 135, 174–179.

Wang, Y. L., Zhu, S. H., Gao, M. Q., Yang, Z. R., Yan, L. J., Bai, Y. H., and Li, F. (2016). "A study of char gasification in H2O and CO2 mixtures: Role of inherent minerals in the coal." *Fuel Process. Technol.*, 141, 9–15.

Wu, S., Gu, J., Zhang, X., Wu, Y., and Gao, J. (2008). "Variation of carbon crystalline structures and CO2 gasification reactivity of Shenfu coal chars at elevated temperatures." *Energy and Fuels*, 22(1), 199–206.

Xiao, R., Song, Q., Song, M., Lu, Z., Zhang, S., and Shen, L. (2010). "Pressurized chemical-looping combustion of coal with an iron ore-based oxygen carrier." *Combust. Flame*, 157(6), 1140–1153.

Xie, Y., You, J., Lu, L., Wang, M., and Wang, J. (2019). "Raman spectroscopic study of coal samples during heating." *Appl. Sci.*, 9(21), 1–9.

Xu, G., Jin, H., Yang, Y., Xu, Y., Lin, H., and Duan, L. (2010). "A comprehensive techno-economic analysis method for power generation systems with CO2 capture." *Int. J. Energy Res.*, 34(4), 321–332.

Xu, J., Su, S., Sun, Z., Qing, M., Xiong, Z., Wang, Y., Jiang, L., Hu, S., and Xiang, J. (2016). "Effects of steam and CO2 on the characteristics of chars during devolatilization in oxy-steam combustion process." *Appl. Energy*, 182, 20–28.

Xu, J., Tang, H., Su, S., Liu, J., Han, H., Zhang, L., Xu, K., Wang, Y., Hu, S., Zhou, Y., and Xiang, J. (2017). "Micro-Raman Spectroscopy Study of 32 Kinds of Chinese Coals: Second-Order Raman Spectrum and Its Correlations with Coal Properties." *Energy & Fuels*, 31(8), 7884–7893.

Xu, K., Hu, S., Su, S., Xu, C., Sun, L., Shuai, C., Jiang, L., and Xiang, J. (2013). "Study on Char Surface Active Sites and Their Relationship to Gasification Reactivity." *Energy & Fuels*, 27(1), 118–125.

Xu, L., Edland, R., Li, Z., Leion, H., Zhao, D., and Cai, N. (2014). "Cu-Modified Manganese Ore as an Oxygen Carrier for Chemical Looping Combustion." *Energy & Fuels*, 28(11), 7085–7092.

Xu, X., Wang, Y., Chen, Z., Chen, X., Zhang, H., Bai, L., and Zhang, S. (2015). "Variations in char structure and reactivity due to the pyrolysis and in-situ gasification using Shengli brown coal." *J. Anal. Appl. Pyrolysis*, 115, 233–241.

Yan, X., Hu, J., Zhang, Q., Zhao, S., Dang, J., and Wang, W. (2020). "Chemical-looping gasification of corn straw with Fe-based oxygen carrier: Thermogravimetric analysis." *Bioresour. Technol.*, 303, 122904.

Yang, Y. B., Sharifi, V. N., Swithenbank, J., Ma, L., Darvell, L. I., Jones, J. M., Pourkashanian, M., and Williams, A. (2008). "Combustion of a Single Particle of Biomass." *Energy & Fuels*, 22(1), 306–316.

Zaida, A., Bar-Ziv, E., Radovic, L. R., and Lee, Y.-J. J. (2007). "Further development of Raman Microprobe spectroscopy for characterization of char reactivity." *Proc. Combust. Inst.*, 31(2), 1881–1887.

Zhang, D. (2013). "Introduction to advanced and ultra-supercritical fossil fuel power plants." *Ultra-Supercritical Coal Power Plants*, 1–20.

Zhang, H., Cen, K., Yan, J., and Ni, M. (2002). "The fragmentation of coal particles during the coal combustion in a fluidized bed." *Fuel*, 81(14), 1835–1840.

Zhang, J. Q., Becker, H. A., and Code, R. K. (1990). "Devolatilization and combustion of large coal particles in a fluidized bed." *Can. J. Chem. Eng.*, 68(6), 1010–1017.

Zhang, S., Xiao, R., and Zheng, W. G. (2014). "Comparative study between fluidized-bed and fixed-bed operation modes in pressurized chemical looping combustion of coal." *Appl. Energy*, 130, 181–189.

Zhang, W., Jiang, S., Hardacre, C., Goodrich, P., Wang, K., Shao, H., and Wu, Z. (2015). "A Combined Raman Spectroscopic and Thermogravimetric Analysis Study on Oxidation of Coal with Different Ranks." *J. Anal. Methods Chem.*, 2015, 1–8.

Zhao, H., Wang, K., Fang, Y., Ma, J., Mei, D., and Zheng, C. (2014). "Characterization of natural copper ore as oxygen carrier in chemical-looping with oxygen uncoupling of anthracite." *Int. J. Greenh. Gas Control*, 22, 154–164.

Zhong, S., Baitalow, F., and Meyer, B. (2018). "Experimental investigation on fragmentation initiation of mm-sized coal particles in a drop-tube furnace." *Fuel*, 234, 473–481.

Zhong, S., Baitalow, F., Nikrityuk, P., Gutte, H., and Meyer, B. (2014). "The effect of particle size on the strength parameters of German brown coal and its chars." *Fuel*, 125, 200–205.

Zhu, X., Imtiaz, Q., Donat, F., Müller, C. R., and Li, F. (2020). "Chemical looping beyond combustion-a perspective." *Energy Environ. Sci.*, 13(3), 772–804.

Zolin, A., Jensen, A., Pedersen, L. S., Dam-Johansen, K., and Tørslev, P. (1998). "A comparison of coal char reactivity determined from thermogravimetric and laminar flow reactor experiments." *Energy and Fuels*, 12(2), 268–276.

# PUBLICATIONS BASED ON THE THESIS

1. Pragadeesh, K. S., and Sudhakar, D. R. (2018). "Primary Fragmentation Behavior of Indian Coals and Biomass during Chemical Looping Combustion." *Energy & Fuels*, 32(5), 6330–6346.

2. Pragadeesh, K. S., and Sudhakar, D. R. (2019). "Color Indistinction Method for the Determination of Devolatilization Time of Large Fuel Particles in Chemical Looping Combustion." *Energy & Fuels*, 33(5), 4542–4551.

3. Pragadeesh, K. S., Regupathi, I., and Sudhakar, D. R. (2020). "Study of devolatilization during chemical looping combustion of large coal and biomass particles." *J. Energy Inst.*, 93(4), 1460–1472.

4. Pragadeesh, K. S., Regupathi, I., and Ruben Sudhakar, D. (2021). "Insitu gasification – chemical looping combustion of large coal and biomass particles: Char conversion and comminution." *Fuel*, 292, 120201.

*Conference proceedings*

1. Pragadeesh, K. S., and Sudhakar, D. R. (2018). "Experimental investigation of devolatilisation of Indian coal and biomass in Chemical Looping Combustion." First Int. Conf. Energy Environ. Glob. Challenges, 26.

*Article under preparation*

1. Pragadeesh, K. S., Regupathi, I., and Ruben Sudhakar, D. (2021). *Investigation of Reactivity and Structural Aspects of Coal and Biomass Chars Produced Under iG-CLC Environment*.

<div align="center">

**BIO-DATA**

</div>

**PRAGADEESH K S**

**Email address**       : pragadeeshsekar@gmail.com

**Contact number**     : +91-9486085060

**Permanent address** **:** 5-82, Komaranallipalayam,

                           Irugalur Post, Sangagiri Taluk,

                           Salem, Tamilnadu - 637103

                           India

**Educational qualification:**

- M.Tech. in Environmental Engineering (8.3/10), 2012-2014

  Pondicherry Engineering College,

  Pillaichavady, Puducherry.

- B.Tech. in Biotechnology (8.25/10), 2008-2012

  Arunai Engineering College,

  Tiruvannamalai, Tamilnadu.

**Research publications:**

[1]     Pragadeesh KS, Regupathi I, Ruben Sudhakar D. Insitu gasification – chemical looping combustion of large coal and biomass particles: Char conversion and comminution. Fuel 2021;292:120201. https://doi.org/10.1016/j.fuel.2021.120201.

[2]     Pragadeesh KS, Regupathi I, Sudhakar DR. Study of devolatilization during chemical looping combustion of large coal and biomass particles. J Energy Inst 2020;93:1460–72. https://doi.org/10.1016/j.joei.2020.01.008.

[3]     Pragadeesh KS, Sudhakar DR. Color Indistinction Method for the Determination of Devolatilization Time of Large Fuel Particles in Chemical Looping Combustion. Energy & Fuels 2019;33:4542–51. https://doi.org/10.1021/acs.energyfuels.8b04310.

[4]     Pragadeesh KS, Sudhakar DR. Primary Fragmentation Behavior of Indian
        Coals and Biomass during Chemical Looping Combustion. Energy & Fuels
        2018;32:6330–46. https://doi.org/10.1021/acs.energyfuels.8b00640.

[5]      Kumar RPP, Bharathiraja B, Pragadeesh KS, Chozhavendhan S, Johnson
        AWW. Utilization of cassava sago waste for bioethanol production by co-
        fermentation of starch degrading bacteria and *Saccharomyces cerevisiae*. Asian
        J Microbiol Biotechnol Environ Sci 2014;16:627–32.

[6]     Gnanamangai BM, Ponmurugan P, Yazhini R, Pragadeesh SK. PR Enzyme
        Activities of *Cercospora theae* Causing Bird's Eye Spot Disease in Tea Plants
        (*Camellia sinensis (L.) O.kuntze*). Plant Pathol J 2011;10:13–21.
        https://doi.org/10.3923/ppj.2011.13.21.

*Conference proceedings:*

[1]     Pragadeesh KS, Sudhakar DR. Experimental investigation of devolatilisation of
        Indian coal and biomass in Chemical Looping Combustion. First Int. Conf.
        Energy Environ. Glob. Challenges, 2018, p. 26.

[2]     Sekar PK, Velan M, Sundararajan T, Saravanane R. Municipal Wastewater
        Reclamation by Microalgae in Productive Ways. First Annu. Conf. Innov. Dev.
        Civ. Eng. ACIDIC-2014, NITK, Surathkal, India, 2014.

**Areas of interest:**

➢ Chemical looping technology, production of alternate fuels like methanol, hydrogen
  and others.
➢ Conversion of waste to value-added products and energy

**Declaration:**

I hereby declare that the above written particulars are true to the best of my knowledge.

Place: Surathkal, India

Date: 20-07-2021

K. S. Pragadeesh

(PRAGADEESH K S)